GRAVITY in the galactic center : exploring the central parsec through optical interferometry

Gustavo Rodríguez Coira de La Peña

▶ **To cite this version:**

Gustavo Rodríguez Coira de La Peña. GRAVITY in the galactic center : exploring the central parsec through optical interferometry. Astrophysics [astro-ph]. Université Paris sciences et lettres, 2020. English. NNT : 2020UPSLO013 . tel-03278335

HAL Id: tel-03278335

https://theses.hal.science/tel-03278335

Submitted on 5 Jul 2021

HAL is a multi-disciplinary open access archive for the deposit and dissemination of scientific research documents, whether they are published or not. The documents may come from teaching and research institutions in France or abroad, or from public or private research centers.

L'archive ouverte pluridisciplinaire **HAL**, est destinée au dépôt et à la diffusion de documents scientifiques de niveau recherche, publiés ou non, émanant des établissements d'enseignement et de recherche français ou étrangers, des laboratoires publics ou privés.

PSL
UNIVERSITÉ PARIS

THÈSE DE DOCTORAT
DE L'UNIVERSITÉ PSL

Préparée à l'Observatoire de Paris

GRAVITY in the Galactic Center: exploring the central parsec through optical interferometry

Préparée par

Gustavo RODRÍGUEZ COIRA DE LA PEÑA

Soutenue le 30-11-2020

École doctorale n°127

Astronomie et Astrophysique d'Île-de-France

Spécialité

Astronomie-Astrophysique

Composition du jury :

M. Éric GOURGOULHON Observatoire de Paris	*Président*
M. Pierre CRUZALÈBES Observatoire de la Côte d'Azur	*Rapporteur*
Mme. Maud LANGLOIS Observatoire de Lyon	*Rapporteuse*
Mme. Jihane MOULTAKA Institut de Recherche en Astrophysique et Planétologie	*Examinatrice*
M. Stephen T. RIDGWAY National Optical Astronomical Observatory	*Examinateur*
M. Guy PERRIN Observatoire de Paris	*Directeur de thèse*
M. Thibaut PAUMARD Observatoire de Paris	*Directeur de thèse*
M. Frédéric VINCENT Observatoire de Paris	*Invité*

l'Observatoire de Paris | PSL

"*So Einstein was wrong when he said, 'God does not play dice.' Consideration of black holes suggests, not only that God does play dice, but that he sometimes confuses us by throwing them where they cannot be seen.*"

Stephen W. Hawking

Acknowledgements

To begin with, I would like to thank you, dear reader, for your interest on this document which collects three years of work. It was September 18^{th}, 2017 when I arrived in France to start this thesis project, and it is impressive how things have changed since then. I would like to thank the Observatoire de Paris and École doctorale 127 for the opportunity they gave me by granting me this doctoral contract. Thanks to Jacques Le Bourlot, Thierry Fouchet and Alain Doressoundiram, who have always been there for helping me and evaluating my advances. I want also to thank Pierre Drossart and Gérard Rousset for their guidance and support as members of my *comité de suivi*. Thanks also to LESIA, for allowing me to prepare this thesis project. I would like to thank Pierre Cruzalèbes and Maud Langlois for having accepted to be the referees of this thesis work. I want to thank also Éric Gourgoulhon, Jihane Moultaka and Stephen T. Ridgway for accepting to be part of the jury and validating this thesis work.

A big thanks to my advisors Guy Perrin, Thibaut Paumard, and Frédéric Vincent for believing in me and for their support. Their immense patience, help and lessons have made me grow personally and professionally, and bringing out the best in me. I would like to thank also Odele Straub, who was part of the LESIA team during my first year, for her help and support, especially when I was a total newcomer. Thanks to Vincent Lapeyrere for all of his help regarding not only the calibration of the data, but also his help in everyday work life. Thanks also to Cris Dupont, for her patience solving all the paperwork issues I could have during our trips. I would like to thank also all of our colleagues from the galactic centers meetings which have helped me with my research (and presenting skills): Daniel Rouan, Pierre Vermot, Lam Nguyen, Lucas Grosset. I would like to thank also the cleaning staff, and specially Rui, for their work making the offices comfortable and accessible. During my doctoral contract I had the opportunity to teach three courses in Université Paris 7 Diderot, and that would not have been possible without the support and the help of Marc Huertas, Julien Girard and Simona Mei. Thank you.

Having worked as part of the GRAVITY Collaboration has been the greatest honour for me. For this reason I would like to thank, in addition to the LESIA team, our collaborators from the other teams which I had the opportunity to directly work with: thanks to Reinhard Genzel, Frank Eisenhauer, Stefan Gillessen, Oliver Pfuhl, Idel Waisberg, Jason Dexter, Feng Gao, Felix Widmann, Andreas Eckart and Matthew Horrobin for the fruitful discussions that lead to the new measurements of the orbit of S2, to which I have contributed dedicating a major part of this thesis work. Thanks also to the rest of the GRAVITY collaboration for making this possible.

This work has an important observational part. The data collection would have not been possible without the help of the staff of ESO Paranal. A big thanks to the cleaning, restoration, logistics and medical staff. For the work in the telescopes, I want to thank the telescope operations team (and especially Andrés Pino) for their help. Thanks also to the support astronomers who I had the opportunity to work with: Konrad Tristram, Pedro Figueira, Linda Schmidtobreick, Claudia Paladini.

Despite not being directly involved in the thesis work, I would like to thank Colegio de España in Cité Universitaire de Paris for accepting me as a resident. Their cultural environment has truly inspired me during my two-year stay. A big thanks to all the friends I made there, especially for keeping me afloat during the hardest times of the thesis: Aroa, Inés, Luis, Mariela, Mendia, Raquel.

Unfortunately, due to the health measures as a result of the 2020 pandemic, the defense of this thesis had to be held totally remote from home. In this situation, it is difficult not to feel completely alone while defending it, but I feel very lucky to be able to count on a group of people that were (and always are) present remotely. For this reason, I would like to thank here all of my friends who attended or watched the remote defense. In addition to the ones mentioned above, thanks to: Abel, Álex, Álvaro, Carlos, Carlos, Carmen, Cela, Clara, Elena, Eva, Felipe, Jaime, Javi, Jesu, Juan, Laura, Lucía, Mara, Melvin, Miguel, Miguel Ángel, Moisés, Nacho, Pablo, Pablo, Paco, Patri, Rodri, Sara, Sergio, Silvia, Silvia. If there is anything positive that came out of this situation, it is that if the defense would not have been held remotely, then not all of them would have been able to attend.

I would like to thank all my family (including those who left too early) for their unconditional love, care and support, even more in these challenging times. Although I am physically far from all of you, I have you in my thoughts every day. I want to have a few words here for my uncle (and godfather), as he is probably the only member of my family who understands what this thesis is about. Thank you for all your advice and all the physics discussions we have every time we see each other. Finally, thanks to my parents and my brother. This thesis is one of many outcomes of all the effort you have always put towards me and my personal development.

My last acknowledgement is for you, Morgan, for always believing in me and having the energy I sometimes lacked to keep pushing forward, especially this last year. I am looking forward for what the future will have in store for us.

A todos ellos, gracias.

Abstract

GRAVITY in the Galactic Center: exploring the central parsec through optical interferometry

by Gustavo RODRÍGUEZ COIRA DE LA PEÑA

The central parsec is one of the most interesting regions of our Galaxy. It is populated by a nuclear stellar cluster where massive, energetic and young stars coexist with colder evolved stars, hot plasma and streams of interstellar matter. A compact object called SgrA* with a mass of several million solar masses lies in its center becoming the closest supermassive black hole candidate, but being fainter in all wavelengths than other galactic nuclei. One of the closest stars to SgrA*, S2, completes an orbit around it in just 16 years and is bright enough to be used as a robust probe the gravitational potential of the central source by orbit tracking. In the infrared, SgrA* presents a quiescent emission with random short episodes called flares where its brightness sharply increases up to a factor 4, lasting several hours before dimming. The origin of these flares is likely due to the presence of accretion processes in the close environment of the black hole and their study can provide essential information about the exotic nature of SgrA*. Unfortunately, these events are random and require a sufficiently sampled monitoring over time.

The GRAVITY instrument, part of the second generation of VLTI, enables the use of optical interferometry to study the Galactic Center. It is able to track the orbit of the star S2 with unprecedented accuracy, up to 10 micro-arcseconds. This thesis work is focused on the data analysis of the first products of the GRAVITY instrument in the Galactic Center.

In the first part of the thesis, the astrometry of the star S2 is obtained by the use of the first two years of GRAVITY observations, in which I have actively participated. For that purpose, a binary star model is used to reproduce the interferometric data. Right before and after the pericenter passage, who took place in 2018, I have obtained the positions of S2 with respect to SgrA* reaching an astrometric accuracy of 30 micro-arcseconds, comparable with the expected size of the shadow of the supermassive black hole. In addition, I have obtained a new light curve of SgrA* which complements the data already published and confirms the quiescent-flare scenario. The results obtained are part of a larger study involving orbit fitting where several tests of General Relativity have been successfully performed, as well as interpretations of the flares as a product of accretion processes in the near SgrA* orbit.

The second part of the thesis is focused on an evolved star called GCIRS 7, which is also located in the central parsec and serves as a reference for GRAVITY observations. This star, which has a large variability in the infrared, is known to contribute to the interstellar medium of the Galactic Center. By complementing GRAVITY archival data from 2017 with observations I have taken in 2019, I have implemented an atmosphere model, widely used for the study of other advanced stars, to explain the visibility curves of GCIRS 7 obtained by GRAVITY. The model consists of a photosphere and a thin molecular shell. The results show that the data can be interpreted as a photosphere with the same diameter for both epochs, but with a shell being colder and larger in 2019 compared to 2017. An estimation of the density of the thin shell reveals a saturation of the model for 2017 due to a high density, but 2019 data is partially reproduced. The results can be explained by a layer expansion and cooling perhaps due to an episode of mass loss.

Contents

Chapter 1

Introduction

The centers of galaxies harbor some of the most powerful gravitational fields in the universe, due to the presence of supermassive black holes; a class of compact bodies containing masses equivalent to several million times the mass of the Sun. Unfortunately, a black hole does not emit light by definition, which makes them extremely elusive as they can be detected only by the influence they exert to their surroundings (or by gravitational radiation). Despite the overwhelming physical size of these objects (comparable to, or even greater than the Solar System itself), the greatest obstacle to explore the gravitational fields in their close environments relies in the immense distances where they are located at.

The closest supermassive black hole candidate can be found at the center of our own galaxy, at 8 kpc away (around 25000 light years). The current technical capabilities make its surroundings observable in the near infrared domain with very high angular resolution (less than a light year scale). The high density of stars in its immediate environment and their high proper motion make it one of the best laboratories to study gravity in the whole sky. The study of the motion of these stars and its interstellar medium can give invaluable knowledge not only about General Relativity, but also about the History of the Galaxy itself.

1.1 The center of our Galaxy

As the largest structure observable in the night sky (Figure 1.1), the Milky Way is known since antiquity, but it was not until the 20^{th} century that it was identified as a Spiral Galaxy which the Solar System is part of. The location of its center constitutes the most dense region of the disk with abundant interstellar medium, which highly increases light extinction on the line of sight. As a consequence, the galactic center is not observable in the visible spectrum (the extinction reaches 27 magnitudes at $\lambda = 550$ nm, Becklin and Neugebauer, 1968) but it is accessible in X-ray, in the infrared spectrum and in radio wavelengths, being known to be the first extra-terrestrial radio source ever detected Jansky (1933). The most prominent substructures that can be seen while approaching the central object are presented in this section.

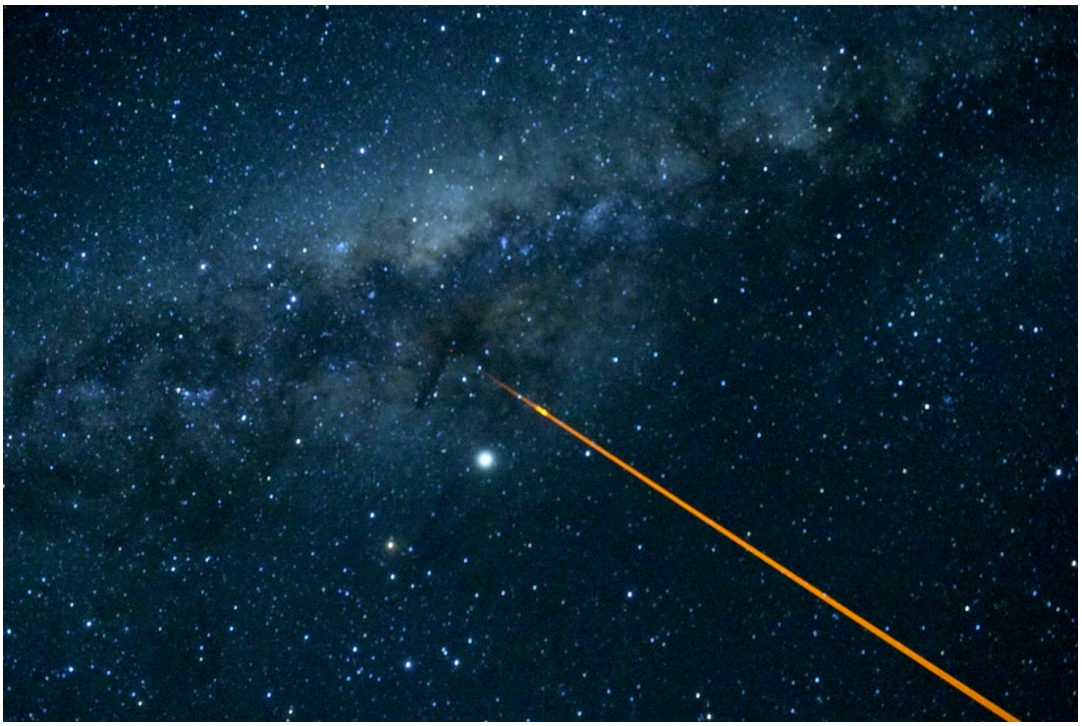

FIGURE 1.1: Picture of the Milky Way as seen from La Residencia (ESO, Paranal Observatory) during night observations. The four adaptive optics facility (AOF) lasers of UT4 point towards the location of the Galactic Center.

1.1.1 The central molecular zone

A region dominated by molecular gas with several substructures can be found by exploring the inner 4° of the galaxy (corresponding to 600 parsecs in physical distance). It is known as the Central Molecular Zone (CMZ), and with a total $M \approx 10^7 M_\odot$ it accounts for 10% of the neutral mass content of the whole galaxy (Güsten, 1989; Dahmen et al., 1998). Its molecular clouds present temperatures of $T \approx 70$ K (Morris et al., 1983) and an estimated density of $n \approx 10^4$ cm^{-3} (Stark et al., 1989), typically higher than the density of other molecular clouds in the galactic disk ($n \approx 10^2 - 10^3$). The turbulence of its molecular clouds, with supersonic internal velocities $v \gtrsim 15 - 50$ km s^{-1} and especially the shape of the CMZ suggest this structure has evolved from an AGN torus, revealing that the nucleus of the Milky Way could have been active in the past (Ponti et al., 2013, and references therein).

An image of the CMZ obtained by Kassim et al. (1999) is displayed in Figure 1.2. The gas distribution is heterogeneous, presenting several spherical clouds as a product of the supernova explosions of massive stars (labelled SNR in the picture, from Super Nova Remnant). Other substructures such as filaments reveal the presence of large scale magnetic fields and star formation processes (André et al., 2014; Federrath et al., 2016). Aligned with the galactic equator, three giant molecular clouds stand out: SgrC, SgrB (also subdivided in the clouds B1 and B2) and finally SgrA, the largest and more prominent of them.

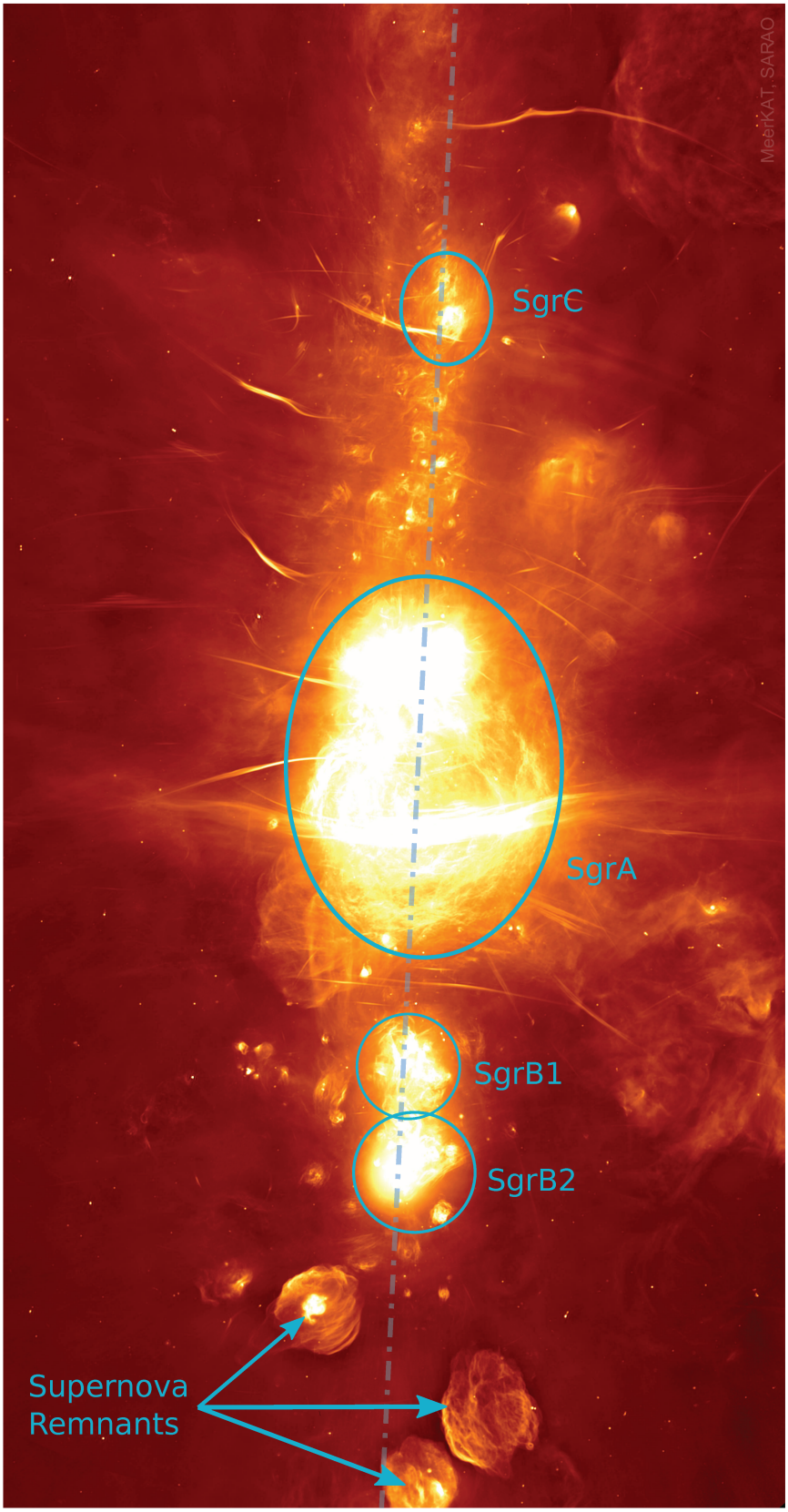

FIGURE 1.2: An image in radio of the CMZ remarking the most outstanding structures. Source: MeerKAT/SARAO.

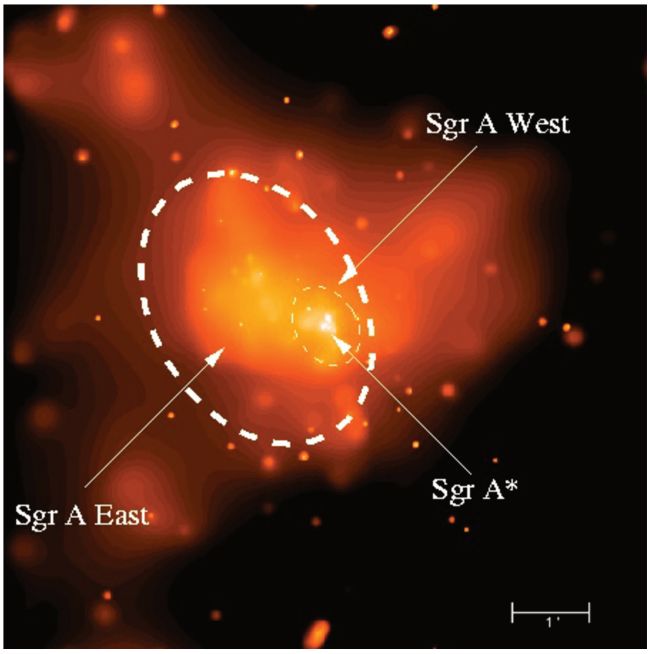

FIGURE 1.3: Image of the complex SgrA obtained by Chandra X-ray observatory. Source: NASA/G.Garmire (PSU)/F.Baganoff (MIT).

1.1.2 SgrA: The central cloud

The SgrA complex extends over the central 10 parsecs of our Galaxy. An image of SgrA taken by the Chandra space telescope is shown in Figure 1.3. Two big substructures can be identified, labelled as SgrA East and SgrA West (Ekers et al., 1983). The largest one, SgrA East, is a non-thermal source extending over an area of 7×9 pc with a shell structure, likely originating in a supernova explosion (Fryer et al., 2006).

The substructure known as SgrA West, whose emission is dominated by dust and ionized gas (Lacy et al., 1980; Lo and Claussen, 1983), occupies the central 2 pc of the Galaxy and hosts the nuclear stellar cluster. It is also called the central mini-spiral due to its filamentary shape, composed of several clumpy and ionized streamers whirling around the central object (Paumard, Maillard, and Morris, 2004; Zhao et al., 2009; Tsuboi et al., 2017). The mini-spiral is surrounded by a structure called the Circumnuclear Ring (CNR), a clumpy torus made of dust and neutral gas that encircles the central parsec (Becklin, Gatley, and Werner, 1982). The dense streamers and clumps that form the mini-spiral are thought to be the product of the inflow of the CNR towards the gravitational potential of the central object. In addition to the ionized gas, warm molecular hydrogen ($T_e \approx 2000$ K) has been detected in the central parsec (Ciurlo et al., 2016), whose origin is likely to be due to the presence of dusty clumps (Ciurlo et al., 2019). Finally, a hot plasma ($k_B T \approx 1.3$ keV) has been detected in X-ray (Baganoff et al., 2003) filling the volume inside the CNR. Two images of the mini spiral and the nuclear stellar cluster respectively are displayed in Figure 1.4 corresponding to the same field of view.

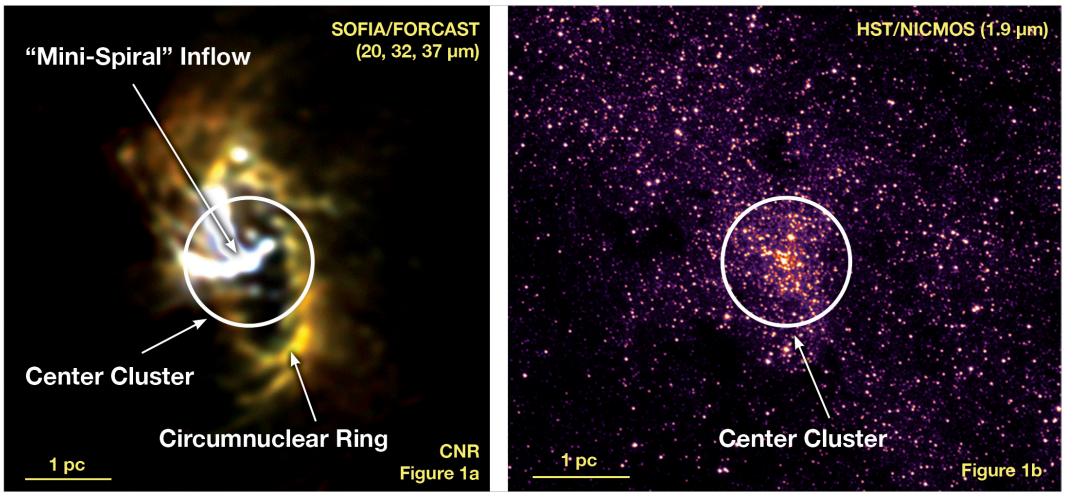

FIGURE 1.4: Left: Image in false color made with three FORCAST filters in the Mid Infrared (19.7μm, 31.5μm, 37.1μm). Right: Image of HST (1.9μm) of the same field of view, where the nuclear stellar cluster is revealed. Source: Figure 1a: NASA/DLR/USRA/DSI/FORCAST Team/Lau et al. (2013); Figure 1b: NASA/HST/STScI/AURA.

1.1.3 The Nuclear stellar cluster

The first infrared observations of the central parsec (Rieke and Low, 1973; Becklin and Neugebauer, 1975) revealed a population dominated by evolved stars (mainly red supergiants and AGB stars) in a dense nuclear stellar cluster. However, more recent observations (Genzel et al., 2000, 2003b; Paumard et al., 2006; Lu et al., 2009; Bartko et al., 2009; Yelda et al., 2014) have reported the presence of two disks rotating in opposite directions (clockwise and counterclockwise respectively) of young and massive stars, most of them being massive O-type supergiants and Wolf-Rayet stars (Martins et al., 2007; Bartko et al., 2010; Sanchez-Bermudez et al., 2014). A recent work (Ciurlo et al., 2019) also revealed that the central parsec is filled with clumps of dust and molecular gas.

Two objects from the Nuclear stellar cluster are involved in this thesis: the cluster IRS 16, used as a reference, and the supergiant star IRS 7 whose structure is deeply studied.

The IRS 16 complex

The infrared source labelled as 16 in Becklin and Neugebauer (1975) was found to be an extended source, matching with the location of the central radio source previously reported by Balick and Brown (1974). Several years later its K band spectrum was published by Hall, Kleinmann, and Scoville (1982), revealing the presence of strong and broad He emission lines without significant absorption lines, in contrast to the CO bands of IRS7, a late type star described in the next section. Further observations at that time led to an identification of IRS 16 as the dynamical nucleus of the Galaxy enclosing the central object (Storey and Allen, 1983) and identifying three components: two HII ionized regions due to the presence of hot stars ($T_{\rm eff} \approx 20000 - 30000$ K) and a cluster of late type stars in the center. The hypothesis of IRS16 hosting the central cusp of the Galaxy was finally rejected by Allen and Sanders (1986) with a new 2.2 μm new image providing the highest resolution at that time (1-2 arcseconds). They found that the observed brightness of SgrA* in K band is too low to

reproduce an expected energy diffusion cusp that IRS16 does reproduce. A few years later, Tamblyn and Rieke (1993) arrived at the same result by constructing stellar population models and concluded that IRS16 is a product of stellar evolution due to a star formation event.

Najarro et al. (1997) showed that the helium emission of the complex IRS 16 is due to the presence of evolved blue supergiants close to the Wolf-Rayet evolutionary stage. With the increase of angular resolution, further observations (Paumard et al., 2006, and references therein) have resolved this complex into a cluster of at least ten stars. All of them present physical characteristics of post main sequence OB stars, becoming luminous blue variable candidates (Paumard et al., 2001).

These stars are the closest bright sources to the actual galactic center, providing an excellent reference system for astrometry. They are easy to identify in the field of view (Figure 1.6). In this thesis work, two stars of the cluster (IRS 16NW, IRS 16C) are used for that purpose. As the work involves an interferometric study, they are use as a phase reference to measure the separation between the central source and the star S2, presented in Chapter 3.

1.1.4 IRS 7: The brightest infrared source of the central parsec of the Galaxy

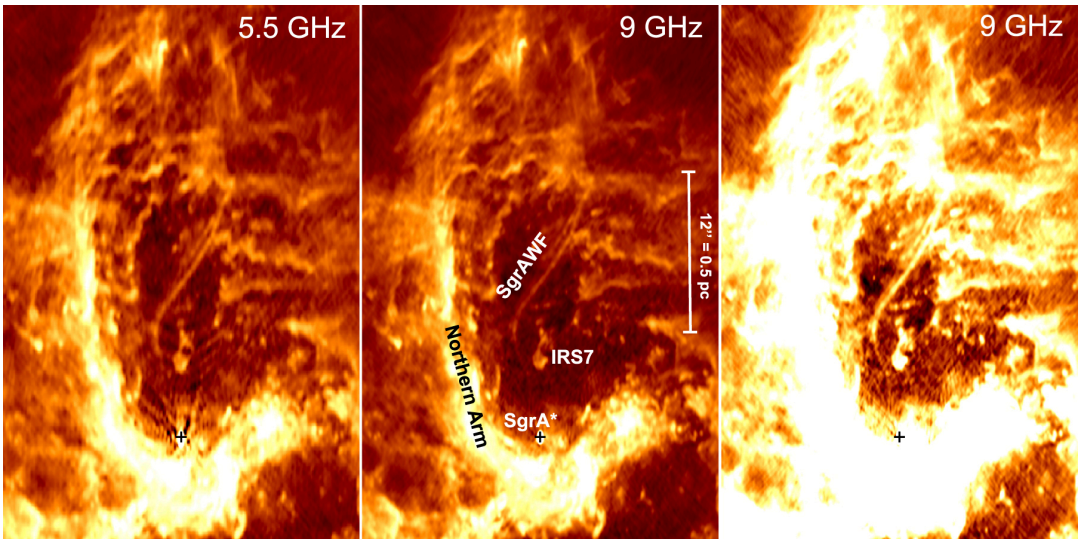

FIGURE 1.5: Radio images of the Sgr A West H_{II} region. IRS 7 is the first source located directly at the north of SgrA*. The cometary tail can be seen extended towards the north of the image. Source: Morris, Zhao, and Goss (2017).

IRS 7 has been one of the first identified sources of the central parsec of the Galactic Center, observed for the first time by Becklin and Neugebauer (1968) with a spatial resolution of $2.5''$ at $\lambda = 2.2\,\mu$m. It was confirmed as a stellar source by Becklin and Neugebauer (1975) being reported as the brightest object in $2.2\,\mu$m found in the central 2 parsecs with an absolute magnitude of $M = -8$. A year later, Neugebauer et al. (1976) gave it the name IRS 7 (Infra-Red Source 7) and classified the source as a late type super giant star, due to the strength of CO absorption. This was confirmed independently by Lebofsky, Rieke, and Tokunaga (1982) with high resolution K band spectroscopy ($R \sim 1000 - 2000$ at $\lambda = 1.9 - 2.5\,\mu$m) revealing the CO molecular band of IRS 7, and ranking the star among the three most luminous stars of the Galaxy

known at that time. Five years later, the first estimate of the extinction in K band in the direction of IRS 7 ($A_K = 3.1 \pm 0.2$) is obtained by Sellgren et al. (1987) also through K band spectroscopy.

Observations in radio with the Very Large Array (VLA) by Yusef-Zadeh and Morris (1991) showed a cometary tail extending $5''$ whose origin is IRS 7 and pointing to the opposite direction from Sgr A*. The mid-infrared (MIR) [N_{II}] emission (12.8 μm) of the tail is reported simultaneously by Serabyn, Lacy, and Achtermann (1991). Both works conclude that the origin of this cometary tail is the warm dust generated and expelled by the outer environment of the star, which is being dragged by the strong interstellar winds due to the presence of the central object. Morris, Zhao, and Goss (2017) provide the most recent image of the region in radio emission where the cometary tail can be clearly identified (Figure 1.5), although that work is not focused in IRS 7.

Regarding the structure of the star, the work of Paumard et al. (2014) presents data from 40 years and determines the fundamental parameters of the star as well as an estimate of its age (6.5-10 Myr), in agreement with the recent star formation event corresponding to IRS 16. This work reveals that the star presents variability in H and K band during these 40 years with variations from peak to peak of up to one magnitude in H band. The most recent work about this star, Tsuboi et al. (2020), estimates the mass loss of the star for the first time at 10^{-4} $M_\odot$/yr, in agreement with the expected mass loss of a typical red supergiant star.

The interest on studying IRS 7 relies not only in the general properties of the mass loss processes triggered by an individual RSG, but also in the presence of a Betelgeuse-like star in a dense and rich environment such as the central parsec of the Galaxy. It is indeed a truly unique scenario where the influence of the wind of several massive stars and even a SMBH over the outer layers of a low gravity star and circumstellar environment can be studied.

Is the atmosphere of IRS 7 similar to Betelgeuse-like stars? Does it show different properties due to the presence of the external winds corresponding to the massive stars in the environment? Does the diameter of the star change during this sharp brightness variations? Is it possible to link the variability with punctual mass loss processes that would enrich the nuclear interstellar medium? These are the aims of the work I allocated the second half of my thesis to, whose details can be found in Chapter 4.

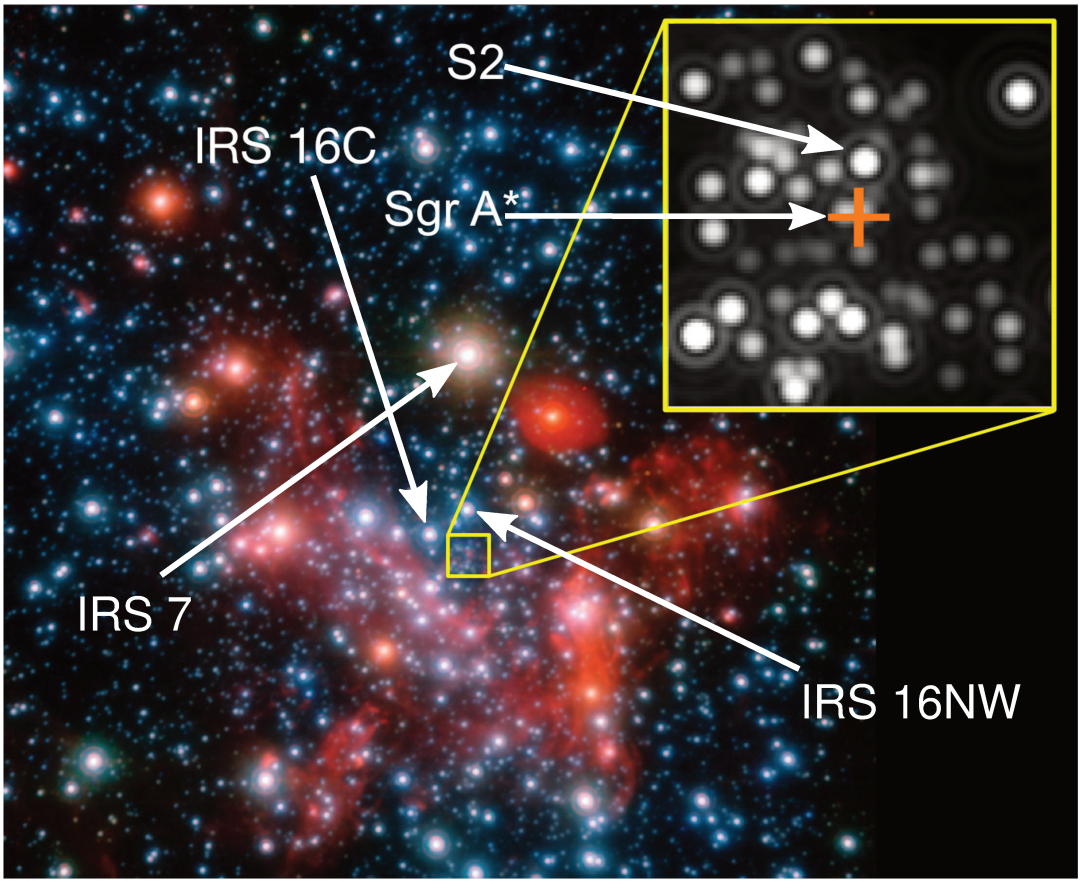

FIGURE 1.6: Central parsec of the galaxy and cluster of S stars. Source: ESO/MPE/S. Gillessen et al.

1.1.5 The central S cluster

The work of Eckart et al. (1995) revealed another component of the nuclear stellar cluster located in the central arcsecond which hosts to this date, the closest known stars to the central object. These B-type main sequence stars are typically faint ($m_K \leq 17$) and are distributed isotropically (Ghez et al., 2005). An image of the central parsec with a zoom on the S cluster (obtained with NACO) is displayed in Figure 1.6, with the position of other stellar sources described in this chapter.

A graph with the successful orbit tracking of 20 stars from Gillessen et al. (2009) is also shown in Figure 1.7. The stars of these cluster are known for their highly eccentric orbits whose orbital periods around the central object range from decades to centuries (with two of them being almost 1800 years). One of these stars, S2 (S0-2 depending on the nomenclature) completes an orbit around the central object in just 16 years being one of the brightest star of the S cluster in K band with $m_K = 14$ (Gillessen et al., 2009). The short period of its orbit and the brightness of this star provide to this date the most feasible approach to the gravitational potential of the central source.

In addition to the stars, (Gillessen et al., 2012) has revealed the presence of at least one dense gas cloud (G2) with a mass at the same order of magnitude as the Earth, in a highly eccentric orbit of 137 years. In the same way as the stars of the cluster, its astrometry might be useful to study the central object (Plewa et al., 2017).

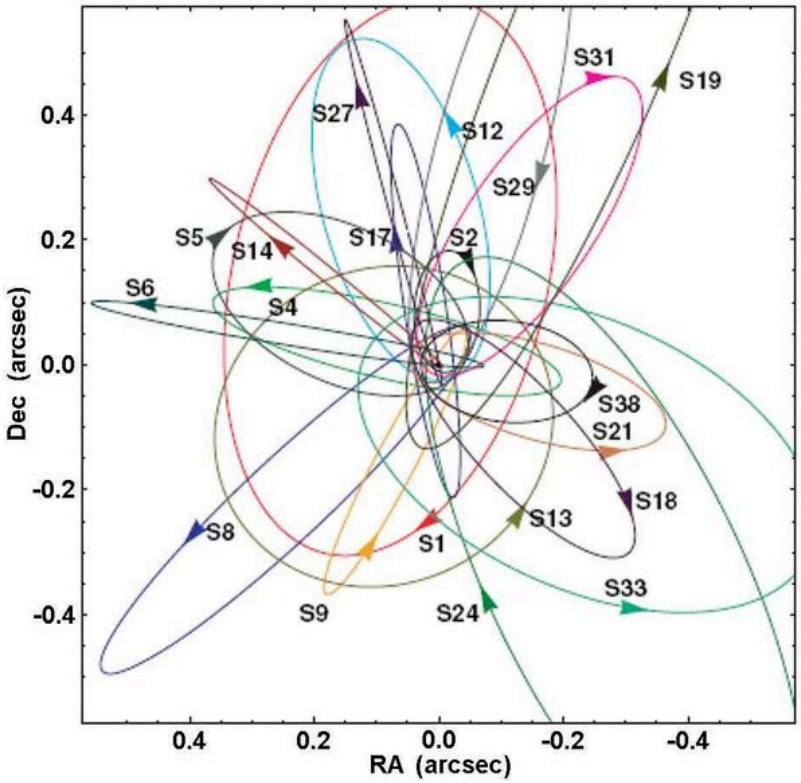

FIGURE 1.7: Orbits of the closest 20 stars to the central source. Source: Gillessen et al. (2009).

1.1.6 SgrA*: The central object

The first detection of the central object was reported by Balick and Brown (1974), revealing an unresolved central radio source whose position is compatible at 1 pc within the center of the galactic nucleus. A year later, Lo et al. (1975) detected a compact radio source whose position is compatible with the same object, and suggested its variability in radio. Such variability was later confirmed by Brown and Lo (1982), which links the study of the central source to the nucleus of other quasars and radio galaxies. The first estimate of its size was obtained by Lo et al. (1985), calculating a top limit of 20 AU and calling it SgrA*.

The central source is, by far, the closest supermassive black hole candidate, 100 times closer than the second one, in the nucleus of M31. With a luminosity of $\langle L_{\mathrm{SgrA*}} \rangle \approx 10^{-9} L_{\mathrm{Edd}}$ it is also the Galactic Nucleus with the lowest bolometric luminosity known, very far from its Eddington limit[1] which makes it a low-luminosity AGN (Genzel, Eisenhauer, and Gillessen, 2010). The fact that the interstellar environment reveals traces of higher activity in the past (Ponti et al., 2013) makes SgrA* the keystone to study galactic formation and evolution in the Milky Way, as it can be related with studies of other farther AGNs observed.

[1] This limit is defined for a source of light as the luminosity needed for the radiation pressure to overcome gravity.

Since their first detection in 1995, the S stars have served as test particles to probe the potential well around the central object, providing ever tighter constraints on the mass and distance of the central object. Several works have been published by the use of this technique, highly depending on technical observing capabilities: Schödel et al. (2002), Ghez et al. (2003), Eisenhauer et al. (2003, 2005), Ghez et al. (2005, 2008), Gillessen et al. (2009), and Boehle et al. (2016). Although not all the measurements are compatible with each other, all the results on the orbit tracking of the closest stars agree in a central mass compatible with $M \approx 4 \times 10^6 M_\odot$ at a distance of $R \approx 8$ kpc revealing the nature of SgrA* as a compact object beyond any reasonably doubt, likely a supermassive black hole.

The first estimations using the orbit of S2 (Ghez et al., 2003) yield $M = 4.1 \pm 0.6 \times 10^6\ M_\odot$ (assuming $R_0 = 8$ kpc). Eisenhauer et al. (2005), by using the orbits of the stars of the central 30 light days, obtained $M = (3.61 \pm 0.32) \times 10^6\ M_\odot$ and a measurement of $R_0 = 7.62 \pm 0.32$ kpc. The most recent estimation of the parameters of the central source (before the deployment of GRAVITY) is Gillessen et al. (2017), with $M = (4.28 \pm 0.21) \times 10^6\ M_\odot$ and a measurement of $R_0 = 8.32 \pm 0.14$ kpc using a sample of 17 S stars. This work also reveals a potential compatible with a point mass, with up to 1% of the mass attributable to an hypothetical extended object (not detected yet).

A Flaring source

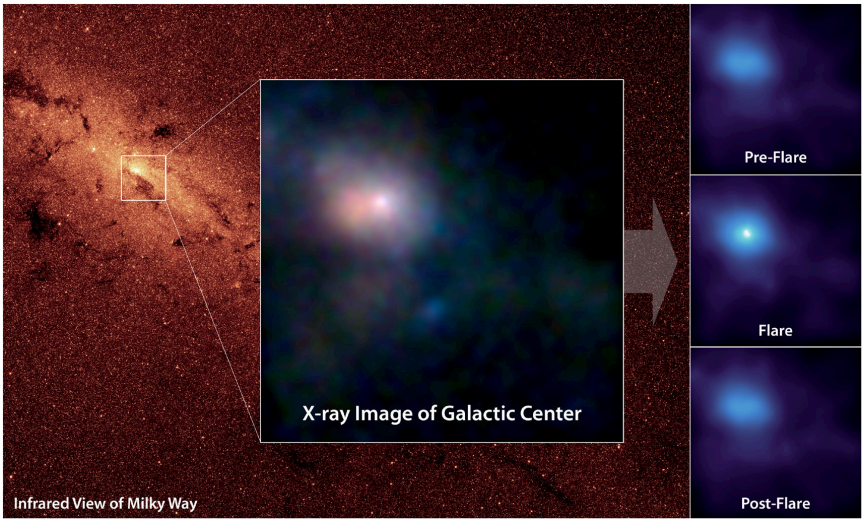

FIGURE 1.8: A flare detected in X-rays by the telescope NuSTAR. The background image was taken with the Spitzer telescope. Source: jpl.nasa.gov .

The central source, SgrA* is known to be truly faint in all wavelengths. It presents an apparently irregular variability in every wavelength domain, which could be interpreted as accretion processes in the environment of the super massive black hole (Genzel, Eisenhauer, and Gillessen, 2010, and references therein). Indeed, the detection of flares coming from SgrA* was firstly confirmed by Baganoff et al. (2001) in X-ray (Figure 1.8). The work of Genzel et al. (2003a) identified a quiescent state for SgrA* with rapid (a time span of less than three hours), apparently random flares in the near infrared domain, whose flux can reach more than triple of the quiescent state. Due to its variability, the origin of the infrared emission of these flares is predicted to be the environment of SgrA* at few milliarcseconds tracing hot gas from

the innermost accretion region (at several Schwarzschild radii). However, this flares had not yet been registered in radio.

The work of Markoff et al. (2001) discussed the origin of the strongest X-ray flare up to that date. They find that the flare is compatible with two scenarios: a jet model or shock acceleration, but they reject the possibility of this flare being the result of an increase of the accretion rate due to the low variability in radio. Five years later, Tagger and Melia (2006) proposes a model of the infrared and x-ray flares based on a Rossby wave instability inside the accretion disk (a model hereinafter called *RWI*), proving by magnetohydrodynamic simulations that a flare can last for several hours. The same year, Yusef-Zadeh et al. (2006) finds the flares in radio (VLA) and interprets the burst emission as an expanding outflow cooling down as it leaves the environment of SgrA*.

Another different scenario was proposed by Hamaus et al. (2009), called from now the *hotspot* model. Following the interpretation of Genzel et al. (2003b), this model proposes that the flare is generated by the heating of a dense clump of material rotating in the accretion disk of SgrA*. This model would be reflected in the periodicity of the flare and would be distinguishable with an optimal performance of the future (now present) instrument GRAVITY. A posterior work from Do et al. (2009) interpreted the near infrared flares as pure red noise (RN) as they did not detect periodicity.

Astrometric signal can be used to determined whether the origin of the flares is due to material ejection, a hot spot model or the product of red noise (Vincent et al., 2014, Figure 1.9). An interferometer with an accuracy comparable to tens of Schwarzschild radii (which in the case of SgrA*, it implies tens of μas) would give invaluable measurements approaching the immediate environment of a supermassive black hole.

A light curve built with 5 years of photometric data was published by Dodds-Eden et al. (2011). They confirmed at a longer timescale the initial findings of Genzel et al. (2003b) and defined the two state scenario observed in the light curve: SgrA* presents a continuous and variable quiescent emission (defined by a flux less than 5mJy) followed by random flares (flux higher than 5 mJy) sometimes as bright as the star S2. The maximum peak is observed at 27.5 mJy ($m_{\mathrm{K}} = 13.5$), which nearly reaches double of S2. The quiescent state is well explained by a log-normal distribution with a median flux of 1.1 mJy, but in the case of a flare the flux distribution flattens revealing a different nature.

Unfortunately, the flares cannot be predicted. Any study of them requires a consistent monitoring of SgrA* with the highest amount of observations possible. This is precisely one of the aims of the first part of the thesis work, which is discussed in Chapter 3. All the data of the GRAVITY consortium during the epochs 2017 and 2018 is presented and a new light curve is obtained with all the results.

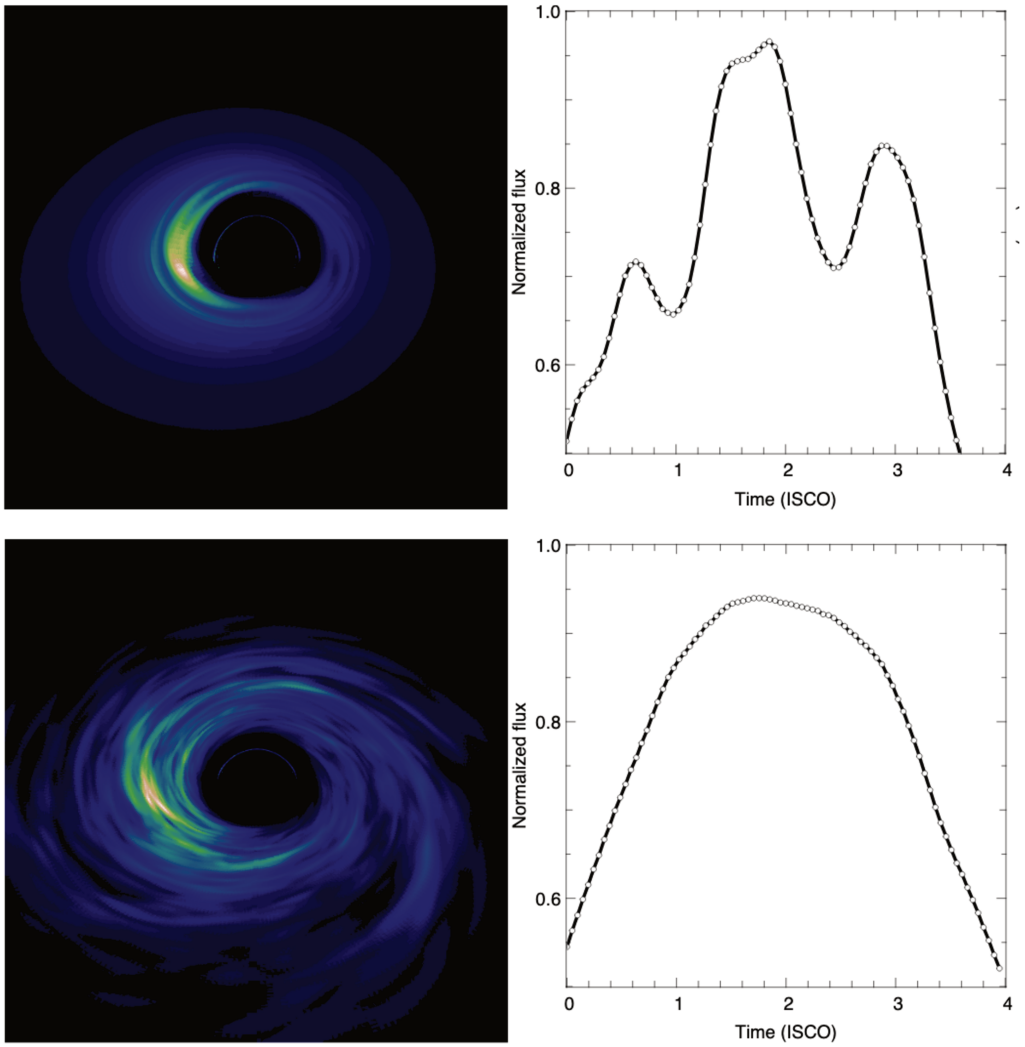

FIGURE 1.9: *Top*: an image resulting from a simulation of a RWI and the corresponding light curve. *Bottom*: an image resulting from a simulation of RN and the corresponding light curve. The x axes are given in units of the innermost stable circular orbit period (approximately 30 minutes for the properties of SgrA*). Source: Vincent et al. (2014).

1.1.7 Testing General Relativity

Since the formulation of the Law of Universal Gravitation by Newton (1687), the observed orbital motion of any celestial object was able to be expressed under first principles. It was not until 1859 that a discrepancy was found, by the observations of the director of Observatoire de Paris at that time, Urbain Le Verrier. His work was focused on the stability of the Solar System as a whole, considering the gravitational perturbations on the orbit of every planet based, of course, on Newtonian Physics.

The perihelion precession of the orbit of each planet, to which the rest of the bodies of the Solar System contribute, could be successfully described by ellipses in a flat geometry under Newtonian Mechanics except for two planets: Uranus and Mercury. The discrepancy of the orbit of Uranus was solved by assuming that an extra planet was causing such perturbations, which led to the discovery of the planet Neptune, first observed in 1846 under the instructions of Le Verrier. Due to his success with Uranus, Le Verrier proposed the same solution for Mercury (Le Verrier, 1859), accounting for an extra planet in the Solar System between the Sun and Mercury, but this planet was never observed. For half a century, the orbit of Mercury became the only discrepancy known relative to celestial mechanics which Newtonian Physics could not reproduce.

A consistent solution was not found until the General Theory of Relativity was formulated by Albert Einstein. Precisely, Einstein (1915) addresses the perihelion problem and obtains analytically a precession of 43" per century. The most recent observations at that time estimated the precession as 45 ± 5" per century. The solution to a 50 year problem was elegantly found by switching the flat geometry inherent to a Newtonian point of view by a new paradigm based on the curvature of the space-time. This is historically considered the first successful test of the General Theory of Relativity.

A second test was performed in 1919 by Sir Arthur Eddington to confirm or reject the deviation of light by a massive object (Eddington, 1919). For this purpose, a ray of light coming from a known location must be observed after trespassing the surroundings of certain object in the line of sight. As it depends on the characteristics of the gravitational field, the deflection is proportional to the mass of the object, but it is unfortunately too small for any object manipulable in any laboratory on Earth. For the deviation to be easily detected, the mass of the object must be of the order of magnitude of a stellar mass, making a solar eclipse the perfect scenario to study the deviation of light by gravity. During the solar eclipse of 29th May 1919 in West Africa, Eddington observed a star that should not be observable assuming hat light is not affected by the influence of gravity in a flat space-time, as its physical location was covered by the Sun. This work confirmed the existence of gravitational lenses, a phenomenon predicted by Einstein's theory.

The third test involves the brightest star of the sky (after our Sun), the binary Sirius (Holberg, 2010). The General Theory of Relativity predicts a spectral, non-Doppler redshift of a ray of light in the environment of a gravitational field as a consequence of the curvature of space-time, that can be interpreted as the loss of linear momentum of the light while moving out of a potential well, such as a massive particle would. Although this effect is present in the environment of a main sequence star, the shift is extremely low and therefore difficult to measure. However, if the object is highly dense this effect is much more noticeable, which makes the white dwarf Sirius B the ideal candidate for this experiment due to its proximity to the Sun. Also proposed by Eddington, the first measurement of this gravitational redshift was published by Adams (1925) obtaining 23 km s^{-1} by spectroscopic measurements of the binary star.

Although it is indeed a measurement of the gravitational redshift, the fact that central source is much brighter than the companion can contaminate the measurements if analyzed via spectroscopy. The target has been deeply studied during the following decades with a much better understanding of stellar structure and stellar evolution (Greenstein, Oke, and Shipman, 1971; Barstow et al., 2005; Joyce et al., 2018), obtaining measurements closer to 80 km s^{-1}.

The fourth classical test was proposed by Irwin Shapiro forty years later than Adams' results by using Mercury again, in Shapiro (1964). If Mechanics are described by the Theory of General Relativity, then the light does not travel in a straight line as a consequence of the curvature of space time due to the presence of certain mass. This phenomenon yields a time delay comparing to a case where Mechanics are described by Newtonian Physics, where the light travels in straight line. Such delay, proportional to the strength of the gravitational potential in the path of the ray of light, must be measurable by the reflection of radar emission (sent from Earth) on the surface of any object closer to the Sun, as Mercury itself. The Shapiro delay was confirmed four years later by Shapiro et al. (1968).

The last of the classical tests was the first one to be carried out in a laboratory. The work of Pound and Rebka (1959a), proposed a way to measure the gravitational redshift by studying γ-ray scattering over a solid surface at two different heights in a tower. The use of this technique overcame the difficulties of other tests based in atomic or molecular transitions, usually needing to compare the frequencies at two heights separated several kilometers. Their results confirmed the detection of the gravitational redshift in Pound and Rebka (1959b). This experiment paved the way for precision tests of General Relativity, such as Vessot et al. (1980), which measured the gravitational redshift in the frequency of a maser transition in a rocket and compared it with the same transition on Earth.

Strong gravitational field regime

The solution of the Einstein field equations for a gravitational field outside certain spherical mass M is given by the Schwarzschild metric, whose temporal component[2] is a function of M and the 3-dimensional distance r:

$$g_{00} = \pm \left(1 - \frac{2\Phi(M,r)}{c^2}\right) \ , \tag{1.1}$$

where $\Phi(M,r) = GM/r$ is the 3-dimensional gravitational potential, c is the speed of light in vacuum and G is the gravitational constant. The gravitational field is considered *weak* at $r = r_0$ if $\Phi(M,r_0) << c^2$, a scale applicable even for the most massive stars in their close surroundings. For a gravitational field to be considered *strong*, the value of $\Phi(M,r_0)$ has to be comparable with c^2. These gravitational fields can be found only in the close environments of extremely compact objects, such as neutron stars or black hole candidates, which are extremely difficult to detect and observe.

[2]Whether the sign is positive or negative depends on the convention used to write the metric, as long as it is the opposite sign to the one used to write the spatial components.

One of the first successful tests of General Relativity in strong regime was presented by Taylor and Weisberg (1982). In this work the authors determined the mass distribution and orbital parameters of the Hulse-Taylor pulsar, a neutron star binary discovered in 1974 (Hulse and Taylor, 1975). The orbital period decay reveal a loss of energy explained via gravitational radiation, another prediction of the General Theory of Relativity. For more than 30 years this was the best confirmation of the existence of gravitational radiation until the direct observation of an extra-galactic binary black hole merger by LIGO and VIRGO (Abbott et al., 2016), opening a new door to gravitational astrophysics. Concerning the galactic nuclei, a detection of the gravitational redshift was reported on an active galaxy through the measurement of the X-ray iron Kα line broadening (Tanaka et al., 1995). This phenomenon was observed afterwards in a wider sample of AGNs (Fabian et al., 2000).

General Relativity is not a theory easy to test due to the lack of highly compact massive bodies at stellar scale known in the Solar neighborhood. The existence (or not) of a scale at which General Relativity fails to reproduce Astrophysical phenomena still remains as one of the unanswered questions in Physics. Probing General Relativity in the strongest fields of the Universe pushes further our understanding of Nature and tests the limits of our actual knowledge.

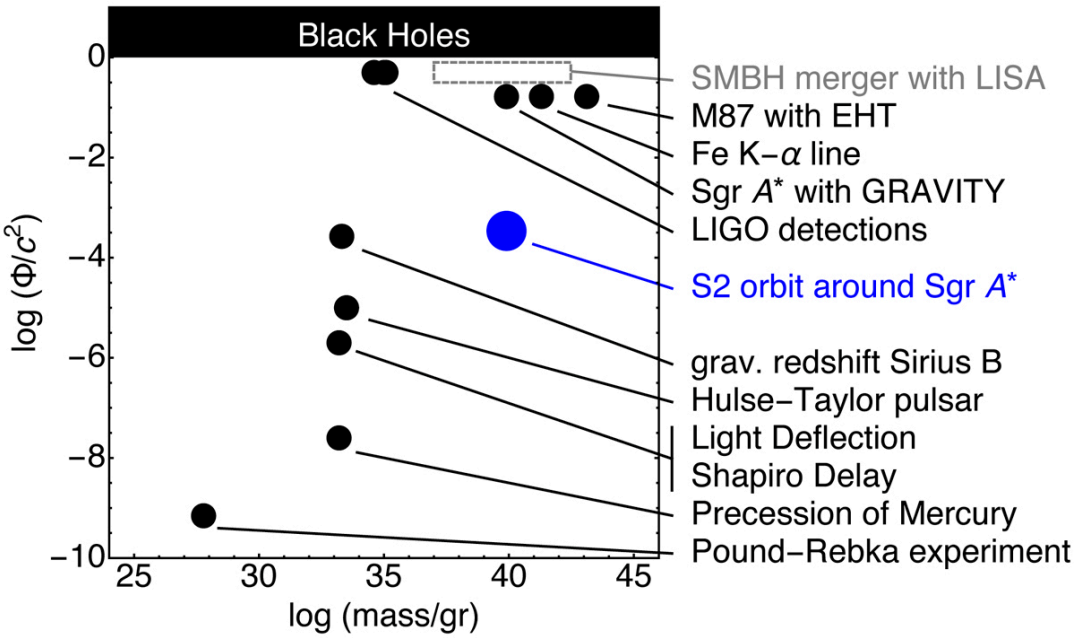

FIGURE 1.10: Potential-mass map displaying several tests of General Relativity. The test in grey colour correspond to future expected findings. In blue, the test where this thesis work has mainly contributed to. Source: Gravity Collaboration et al. (2020a).

A map gravitational potential-mass including all the tests described in this same chapter is presented in Figure 1.10. The upper right corner (from $M = 10^{35} - 10^{45}$ g) corresponds to the most challenging tests, approaching a region called the event horizon (where $\Phi = c^2$). This thesis work presents and discusses my contribution to the results obtained by the GRAVITY Consortium about the test marked in blue, relative to the orbit of the star S2 around the supermassive black hole candidate SgrA*.

1.2 The contribution of this thesis work

The collaboration I have been participating on corresponds to the first interferometric study of the Galactic Center in the infrared domain. The thesis work can be divided in two main parts, described in detail in Chapters 3 and 4:

- Astrometry of the star S2 and detection of flares of the supermassive black hole SgrA* before and after the pericenter passage: I have participated in the tuning, testing and improvement of a code developed by the team of the Observatoire de Paris to reach the maximum astrometric accuracy of the instrument GRAVITY while measuring the position of the star S2 on sky in its orbit around SgrA*. I have been part of the observing team for four observing runs (the final commissioning run in 2017 and three other runs during 2018). With a total of 2 years of data, I have measured the coordinates of the star S2 with unprecedented accuracy as well as detected three bright flares from the close environment of SgrA*. I have also considered and tested detection of extra sources in the field with the obtained data. My measurements have been combined with those of two other groups using independent codes to build the final GRAVITY measurements, which confirmed the detection of the gravitational redshift and the Schwarzschild precession for the first time in our galactic center. The results of this research have been part of four scientific papers inside the GRAVITY Collaboration, in the journal *Astronomy & Astrophysics* where I have been listed as coauthor within the alphabetically-ordered list.
- A study of the outer structure of the red supergiant star GCIRS 7: By using data obtained with GRAVITY in 2017 and taking advantage of the spectral resolution of the instrument I have applied a model consisting in a single thin shell to explain the different diameters observed in the molecular lines of the spectra of this star. By using allocated observing time of the team, I have prepared and carried out two observing runs with VLTI-GRAVITY in 2019 to complement the 2017 data and study the temporal evolution of the star. Thanks to the superb sensitivity of GRAVITY I have been able to measure the size of GCIRS 7 with an accuracy of 2%, resulting in the smallest angular diameter measured to date on a red supergiant. The observations are compatible with the expansion of an external molecular layer, for the first time seen in a red supergiant star which is known to present stellar pulsations. The outcome of this research has been presented in the *Galactic Center Workshop* 2019 (Yokohama, Japan). I have also produced a scientific paper submitted to the journal *Astronomy & Astrophysics* where I am the first author inside the GRAVITY Collaboration.

Chapter 2

The GRAVITY instrument

This section serves as a shallow introduction to the techniques and the instrument which the thesis is focused on, to provide a guide of several non trivial concepts used in further chapters of the thesis. The interferometric observables will be introduced. At the end, the reduction and calibration pipeline used is described in detail as well as the estimators of the interferometric observables.

2.1 An introduction to Optical interferometry

2.1.1 The Michelson stellar interferometer

Let us imagine two telescopes of the same aperture A located at positions $\mathbf{x_1}$, $\mathbf{x_2}$ respect to a common coordinate system, and therefore separated by a distance given by the vector $\mathbf{B} = \mathbf{x_2} - \mathbf{x_1}$ (called baseline vector). There is a single astronomical source located at a distance given by the vector $\mathbf{S}$ with respect to the origin of coordinates of the telescopes, that the user wants to observe with this pair of telescopes, whose pointing direction is given by the unit vector $\hat{\mathbf{s}} = \mathbf{S}/|\mathbf{S}|$. The influence of the atmosphere is not considered yet (see Section 2.1.4) and the beam of light is assumed to be monochromatic with wavelength λ. In the case of GRAVITY, the interferometer is designed to operate in coaxial beam combination, where the light collected by the telescopes interferes before being registered at the detector. Due to the inclination of the source in the sky, one of the telescopes always receives the light before the second one, resulting in a phase shift and a loss of coherence. For this reason there has to be delay lines of length d_1, d_2 before the beam combination which compensate this phase shift and guarantee coherence. The length of the delay lines depends on the distance of the telescopes, which is a fixed quantity, and the position of the source in the sky. Therefore, the delay lines must be moving elements. A picture of such interferometer is displayed in Figure 2.1 (Lawson, 2000).

The wave describing the beam of light E collected by the telescope $j = 1, 2$ is:

$$E_1 \propto e^{-ik(d_1 + \hat{\mathbf{s}}\cdot\mathbf{B})} e^{-i\omega t}$$
$$E_2 \propto e^{-ikd_2} e^{-i\omega t}$$

where $\omega = \frac{2\pi c}{\lambda}$ and $k = \frac{2\pi}{\lambda}$. For an interferometer in coaxial beam combination, both waves arrive at the beam combiner, where interference happens. The wave function resulting from the combination of two beams is $\mathbf{E} = E_1 + E_2$:

$$E \propto e^{-i\omega t} \left[e^{-ik(d_1 + \hat{\mathbf{s}}\cdot\mathbf{B})} + e^{-ikd_2} \right] . \tag{2.1}$$

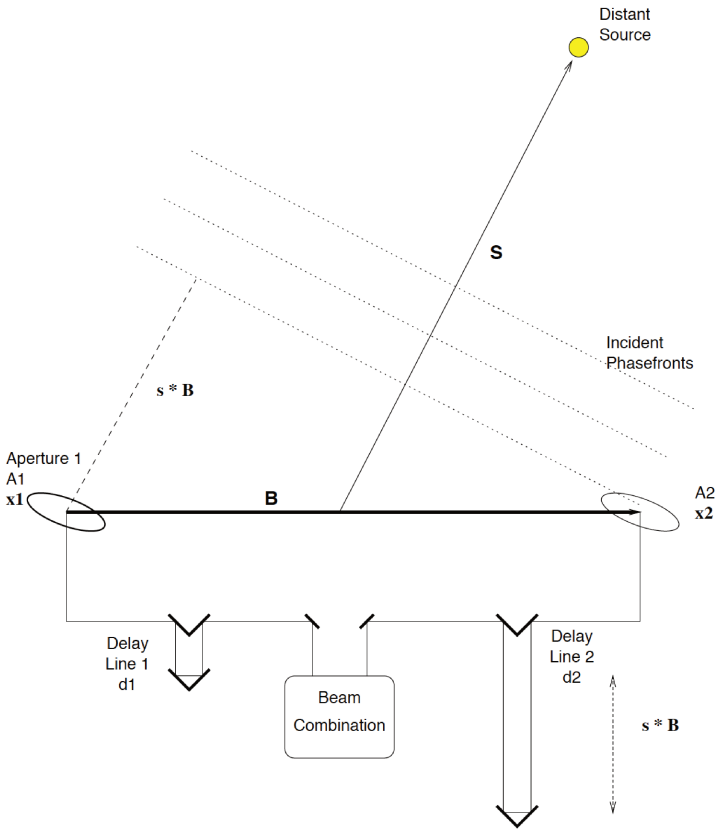

FIGURE 2.1: Sketch of an ideal interferometer in coaxial beam combination mode. Source: Lawson (2000).

The power recorded by the detector, where the output of the beam combiner is registered, reads $P \propto E_t^* E_t$ resulting in a sinusoidal patter of maxima and minima called fringes:

$$P(x) = P_1(t) + P_2(t) + 2\sqrt{P_1 P_2(t)}|V| \cos(kx + \phi_{12}) \ , \tag{2.2}$$

where $P_j(t)$ is the power received by each individual telescope ($j = 1, 2$ in this case). The quantity x is the optical path difference, with:

$$x = (\hat{\mathbf{s}} \cdot \mathbf{B} + d_1 - d_2) \ . \tag{2.3}$$

The term V, a complex quantity known as the visibility of the target, is the quantity we want to measure, as it accounts for the contrast losses due to the spatial distribution of the astronomical source (van Cittert, 1934; Zernike, 1938). The term $\phi_{12} = \phi_{12}^{\text{obj}} + \epsilon_{12}$ is the phase of the visibility of the object plus error terms due mainly to differential atmospheric piston. The term $|V|$ corresponds to its amplitude, which initially has been estimated by directly measuring on the interferogram the apparent contrast of the fringes relative to the total collected power (Michelson, 1920):

$$|V| = \frac{I_{\text{Max}} - I_{\text{min}}}{I_{\text{Max}} + I_{\text{min}}} \ , \tag{2.4}$$

but this method has shortcomings due to finite sampling, noise or photometric fluctuations. To estimate the modulus $|V|$ and the phase ϕ_{12} modern algorithms involve the use of four samples $ABCD$ (Colavita et al., 1999) recording the fringe at four different phase shifts (at $0, \pi/2, \pi, 3\pi/2$) building estimators for the visibility from them (see Section 2.1.5).

2.1.2 Astrometry based on metrology

In absence of chromatic dispersion, the position of the maximum of the interferogram is the one which minimizes the absolute value of the element inside the cosine from Equation 2.2:

$$|k\,(\hat{\mathbf{s}}_0 \cdot \mathbf{B} + d_1 - d_2) + \phi_{12}| = 0\ .$$

If the phase ϕ_{12} is zero, this defines a phase reference. By setting the phase to zero here, a phase center is defined. Then, as the distances d_i are known, the location of the maximum of the interferogram will be where $\hat{\mathbf{s}}_0 \cdot \mathbf{B} = d_2 - d_1$. Let us consider now a second source separated by a distance $\Delta\mathbf{s}$ from the phase center (defined by the first source), such as $\hat{\mathbf{s}}_1 = \hat{\mathbf{s}}_0 + \Delta\mathbf{s}$. In this case, the response of the interferogram reads:

$$P(x) = P(x)_0 + P(x)_1$$

or in other words, two interferograms whose maxima are separated a distance $\Delta\hat{s}$, that can be obtained by measuring the optical path difference:

$$\Delta_{\text{opd}} = \Delta\mathbf{s} \cdot \mathbf{B} = \hat{\mathbf{s}}_1 \cdot \mathbf{B} - \hat{\mathbf{s}}_0 \cdot \mathbf{B} = \hat{\mathbf{s}}_1 \cdot \mathbf{B} + d_1 - d_2\ . \tag{2.5}$$

Equation 2.5 implies that the position $\hat{\mathbf{s}}_1$ with respect to $\hat{\mathbf{s}}_0$ can be obtained by measuring the optical path difference between the maxima of the two interferograms. The accuracy at measuring the positioning of the source then relies on the precision at measuring the length of the optical paths and of the fringe positions. In first approximation, as δs (the astrometric accuracy) and δd (the accuracy on the optical path) are related via $\delta s = \delta d/B$, for a baseline of 100 m an astrometry can be determined with an accuracy of 10 μas if $\delta d = 5$ nm, which is feasible with a measurement system based on laser metrology.

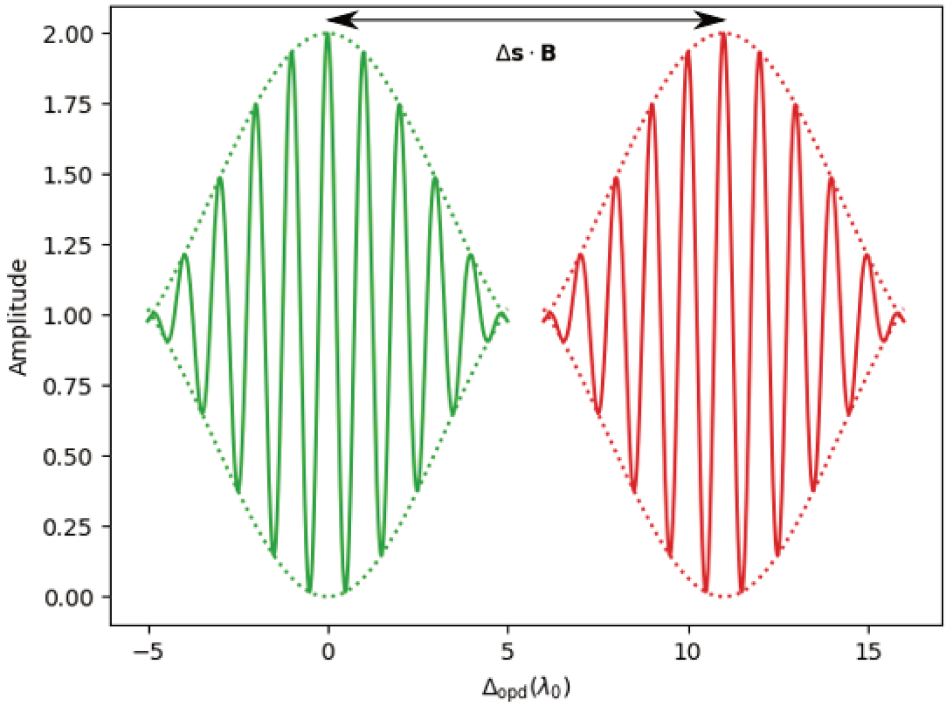

FIGURE 2.2: An interferogram with a finite bandwidth given by a point source in the phase center (green) and another point source at a projected distance Δ_s in the sky. Only one dimension is presented for simplicity.

For a more realistic case, the sources have to be considered polychromatic. In that case, the power recorded by the detector assuming a polychromatic source and a finite bandwidth $\Delta\lambda$ centered in the wavelength λ_0 yields:

$$P(x) \propto \{[1 + M(\Lambda_{\rm coh}, x) \cos[k_0 x(\lambda) + \phi_{12}(\lambda)]\} \tag{2.6}$$

where $k_0 = \frac{2\pi}{\lambda_0}$ and λ_0 is the wavelength reference for the spectral band (typically the center of the band). The function $M(\Lambda_{\rm coh}, x)$ is the fringe envelope, a function that in coaxial beam combination corresponds to the Fourier transform of the bandpass (which is typically a top hat function) expressed as a function of the coherence length $\Lambda_{\rm coh} = \lambda_0^2/\Delta\lambda$ (effect of temporal coherence). In the wide bandwidth case, the dispersion has to be taken into account in the optical path to define the zero of optical path difference:

$$\Delta_{\rm opd}(\lambda) = [\hat{\mathbf{s}} \cdot \mathbf{B} + d_1(\lambda) - d_2(\lambda)] \ . \tag{2.7}$$

In this case, the measurement of the distances becomes chromatic too and to determine the metrology the wavelength dispersion is modelled according to the optical design of the interferometer. The underlying idea of this method is presented in Figure 2.2. The sky separation projected on the baseline materializes as a distance between fringe packets.

2.1.3 Aperture synthesis

The description of an extended source can be understood as a spatial distribution of point sources in a given area of the sky. Calling F the source intensity as a function of the position $\hat{\mathbf{s}}$ and assuming that the radiation coming from several locations is incoherent, the output of the interferometer pointing at $\hat{\mathbf{s}}_0$ with a baseline $\mathbf{B}$ can be modified to account for this distribution as (Lawson, 2000):

$$P(\hat{\mathbf{s}}_0, \mathbf{B}, \delta) = \int d\Omega A(\Delta\mathbf{s}) F(\Delta\mathbf{s}) \left[1 + \cos\left(k\Delta\mathbf{s} \cdot \mathbf{B} + \delta\right)\right] \tag{2.8}$$

with $\Delta\mathbf{s} = \hat{\mathbf{s}} - \hat{\mathbf{s}}_0$. The term δ is a small added phase who accounts for any small shift added to the delay lines and $d\Omega$ is the solid angle unit. For simplicity the source is assumed to be monochromatic again. This equation can be expressed in the following way:

$$P(\hat{\mathbf{s}}_0, \mathbf{B}, \delta) = P_0(1 + \mathrm{Re}\{V e^{ik\delta}\}) \tag{2.9}$$

by defining (Lawson, 2000):

$$P_0 = \int d\Omega A(\Delta\mathbf{s}) F(\Delta\mathbf{s}) \tag{2.10}$$

and:

$$V(k, \mathbf{B}) = \frac{1}{P_0} \int d\Omega A(\Delta\mathbf{s}) F(\Delta\mathbf{s}) e^{-ik\Delta\mathbf{s}\cdot\mathbf{B}} \ . \tag{2.11}$$

By assuming that $\Delta\mathbf{s}$ is perpendicular to $\hat{\mathbf{s}}_0$ (which is true if the field of view is sufficiently small) the separation $\Delta\mathbf{s} \approx (\alpha, \delta)$ and the complex visibility can be expressed as a Fourier transform:

$$V(k, \mathbf{B}) = \frac{\int d\alpha d\delta A(\alpha, \delta) F(\alpha, \delta) e^{-2\pi i(\alpha u + \delta v)}}{\int d\alpha d\delta A(\alpha, \delta) F(\alpha, \delta)} \tag{2.12}$$

where $(u, v) = (B_x, B_y)/\lambda$ are nothing but the Fourier pair of the coordinates in the sky. They have dimensions of m^{-1} and are called spatial frequencies. This result is known as the Van Cittert-Zernike theorem (van Cittert, 1934; Zernike, 1938) and relates the complex visibility with the spatial distribution of the target. The angular separation of the first and second fringes projected in the sky yields:

$$\Delta s = \frac{\lambda}{|\mathbf{B}|} \tag{2.13}$$

which defines the resolving power of a stellar interferometer. The same target, observed by a single aperture with diameter D gives a spatial resolution of:

$$\theta = \frac{\lambda}{D} \tag{2.14}$$

If coherence is reached by a pair of telescopes separated by a distance $|\mathbf{B}|$, the equivalent spatial resolution is the one of a telescope of diameter $|\mathbf{B}|$. That is, the spatial resolution available in imaging mode by an interferometer built from two telescopes is the same that the one a single telescope of diameter equivalent to the separation of them has. A pair of telescopes can provide a better angular resolution by orders of magnitude while comparing to a single aperture observation. However, the main drawback is the loss of spatial coverage, therefore losing imaging capabilities.

The most powerful result of Equation 2.12 is the possibility to combine several apertures to improve the spatial coverage. Indeed, the larger the number of telescopes, the better the spatial coverage would be. Intuitively, it can be seen as an incomplete single dish telescope with a size equivalent to the largest baseline, with a measurement for each baseline. As the spatial frequencies depend intrinsically on the wavelength, this coverage can be also increased if the interferometer has a spectral response. Finally, the baseline coverage is complemented with the rotation of the Earth, which together with the baseline vector projects an ellipse on the sky whose shape depends on the position of the target in the sky and the location of the telescopes on Earth. This effect is called supersynthesis and can be used to wisely plan the observations to benefit from an improved spatial coverage.

2.1.4 The effect of the atmosphere

The main boundary condition while planning the deployment of any ground observatory is always the minimization of the atmospheric effects. In the case of optical and infrared astronomy, the atmosphere is always an external optical element that must be taken into account to perform any observation in order to remove any non desired effects over the data.

Modelling the behaviour of the atmosphere in detail is an extremely complex task. From the point of view of an optical system and assuming a small field of view, it can be approximated as a set of multiple layers that the light coming from an external source must pass through. The coherence length r_0 or Fried parameter (Fried, 1966) defines a diameter where the telescope and the atmosphere optical transfer functions have the same cut-off frequencies. It is closely related to the seeing point spread function as $\alpha_{\text{seeing}} \propto \lambda / r_0$. If the turbulence is strong, the value of r_0 decreases. As a function of wavelength it can be expressed as:

$$r_0 \propto \lambda^{6/5} \ .$$

The work of Taylor (1938) proposed that the turbulence caused by a layer can be seen as a frozen pattern transported by the wind if the turbulence velocity is much lower than the air stream velocity. In the simplified case of a single turbulent layer of speed v, the temporal variation of the turbulence can be characterized by the time scale:

$$\tau_0 = \frac{r_0}{v} \propto \lambda^{6/5} \ , \tag{2.15}$$

where v is the wind velocity, typically 10 m/s. A Fried parameter of $r_0 = 10$ cm yields $\tau_0 \approx 10$ ms. The fact that the atmosphere is a turbulent fluid always adds an additional stochastic phase to the interferogram resulting in a decrease of contrast that could cause the intensity of the fringes to be below the detection threshold.

The parameter τ_0, called coherence time, defines a time scale during which the phase varies by 1 rad^2 leading to a degradation of spatial coherence by $e^{-1/2}$ in the case of differential piston. By this formalism, if the observation is performed in a time interval shorter than τ_0 (short exposure) the atmosphere can be considered frozen. In practice, τ_0 is an average along the line of sight, as a more accurate modelling of the atmosphere involves the presence of a few turbulent layers with different speeds v.

This is the main reason why the available amount of observable sources is extremely limited in optical interferometry, as the integration time must be lower than τ_0 so the source must be extremely bright to be registered. There are, however, ways to overcome this issue by the use of adaptive elements such as fringe tracking (see Section 2.3.1).

2.1.5 Interferometric observables

The aim of any interferometry observation involves the measurement of the complex visibility and the use of Equation 2.12 to derive the spatial distribution of the object. For any visibility measurement to be meaningful, it must include information about the modulus and the phase, as it is a complex quantity. An interferometer made of two telescopes (or a single baseline) can measure the following observables:

- V^2 or the square of the modulus of the complex visibility. In modern interferometers it can be estimated by the use of four samples ABCD (Colavita, 1999):

$$V^2 = \frac{\pi^2}{2} \frac{\langle (X)^2 + (Y)^2 - B^{\mathrm{pn}} - B^{\mathrm{rn}} \rangle}{\langle N \rangle^2} \tag{2.16}$$

  where (A, B, C, D) is the intensity output of the interferogram in four separate bins by adding offsets to the measured phase ϕ_0 as $(\phi_0, \phi_0 + \pi/2, \phi_0 + \pi, \phi_0 + 3\pi/2)$, N is the total number of photons ($N = A + B + C + D$), B^{rn} is the bias due to the detector readout noise and B^{pn} the counting photon bias. The terms X, Y are $X = C - A$ and $Y = D - B$. Instead of applying a temporal modulation, GRAVITY measures the samples $ABCD$ directly by the use of integrated optics beam combiners (Gravity Collaboration et al., 2017).

- ϕ, or the observed phase. By the ABCD algorithm again (Colavita, 1999):

$$\phi = \arctan\left(\frac{Y}{X}\right) \tag{2.17}$$

  with X, Y described above. It is affected by a small vertical variation (called atmospheric piston) which is a consequence of the distance of the two telescopes, as the signal does not arrive at the same time to both pupils. By using only a pair of telescopes, any phase shift due to this effect cannot be distinguished neither from any internal phase error nor from an intrinsic phase of the source.

A new measurement of the phase, independent from atmospheric piston, can be obtained from the visibility phases if at least a third telescope is available. In that case, calling ϕ_{ij}^{obj} the visibility phase of the object measured by the baseline (i, j) and ϵ_i the atmospheric piston of the telescope i, for the triangle (i, j, k):

$$\phi_{ij} = \phi_{ij}^{\text{obj}} + \epsilon_i - \epsilon_j$$
$$\phi_{jk} = \phi_{jk}^{\text{obj}} + \epsilon_j - \epsilon_k$$
$$\phi_{ki} = \phi_{ki}^{\text{obj}} + \epsilon_k - \epsilon_i$$

The sum of the three visibility phases cancels the atmospheric piston while holding the object visibility phase information. This allows to define another observable:

- $T3_\phi$ as the closure phase of the triangle (ijk):

$$T3_\phi(ijk) = \phi_{ij}^{\text{obj}} + \phi_{jk}^{\text{obj}} + \phi_{ki}^{\text{obj}} \tag{2.18}$$

  This observable encloses all the phase information but it removes the atmospheric piston resulting in an unbiased and more stable phase measurement. For a number of telescopes N there are $(N-1)(N-2)/2$ independent triangles and $N(N-1)/2$ phases (one per baseline). If the observed source is spherically symmetric, this observable returns a value of zero. The closure phase can be seen as a sign of the presence of asymmetries in the object, giving essential information about its nature.

2.2 The VLTI interferometer

The observatory of Cerro Paranal in the North of Chile (Figure 2.3) is the European Southern Observatory (ESO) main observing site in the field of optical astronomy. Up to date, it has the most numerous set of telescopes belonging to ESO, being a unique facility where the most advanced instruments and techniques can be tested, commissioned and put into operation. It has a total of 10 telescopes from which 2 of them are used for survey observations (VST and VISTA). The remaining 8 are 2 quadruplets of telescopes that, when operated simultaneously, form the Very Large Telescope Interferometer (VLTI):

- The four Unit Telescopes (UT): with a 8.2m diameter single dish primary mirror, they are the largest telescopes of the observatory. Each of them hosts several instruments provided by different scientific collaborations associated with ESO. While operated individually, they are called Very Large Telescope (VLT). Their primary mirrors are assisted by active optics as well as by adaptive optics with a laser guide star if needed, depending on the instrument. In addition, they can operate simultaneously forming the most sensitive optical interferometer actually in use with a maximum baseline of 130m[1]. Due to their vast instrumentation and the high number of institutions participating, their use as an interferometer is limited to science cases requiring the highest sensitivity and faint targets (up to $m_{\mathrm{K}} = 19$), such as the Galactic Center, studies of AGNs, exoplanets or young stellar objects.
- The four Auxiliary telescopes (AT): a set of telescopes with a primary mirror of 1.8m. Unlike the UTs, they can be only operated in interferometric mode. The main advantage of the ATs is their mobility, as they can be placed in several configurations alongside the facility reaching a different interferometric coverage depending on the science target. The maximum baseline available for the ATs (200 m) is larger than the one of the UTs making this interferometer more appropriate for smaller targets (with a resolution of 2.2 mas in imaging mode against 3.5 mas for the UTs) as long as they are sufficiently bright (up to $m_{\mathrm{K}} = 16.5$). It is, however, less sensitive due to the smaller size of their primary mirrors.

While operating as an interferometer, the UTs are always assisted by adaptive optics thanks to the performance of MACAO (with wavefront sensing in the visible, Arsenault et al., 2004) and CIAO (with wavefront sensing in the infrared, Kendrew et al., 2012). Part of the collected light by the telescopes is sent to a curvature wavefront sensor, located in one of the Coudé focus of each UT telescope, who corrects the atmospheric aberration by acting over a deformable mirror in real time. This system is needed to perform interferometric observations due to the large size of the primary mirrors, which are more sensitive to the effects of the atmospheric turbulence than smaller telescopes. In the case of the ATs, the use of this interferometer was limited to nights where the quality of the sky was excellent. By the addition of NAOMI in 2018 (Woillez et al., 2019), these telescopes are also assisted by adaptive optics on each of the stations, significantly improving the amount of observing time.

[1] It is not, however, the optical interferometer with the largest baseline as this record is hold to this date by CHARA with 330m.

FIGURE 2.3: The four UTs and the four ATs. Source: eso.org.

The light is collected by the telescopes and sent into a room located below, with the shape of a 100m long tunnel. Here is where the four delay lines are placed (Figure 2.4). This element has two purposes:

- To send the light output of the telescopes to the interferometric laboratory, where the instruments are located.
- To compensate the optical path difference between the output of two different telescopes.

At the center of the tunnel there is a room called interferometric laboratory where all the instrumentation is located.

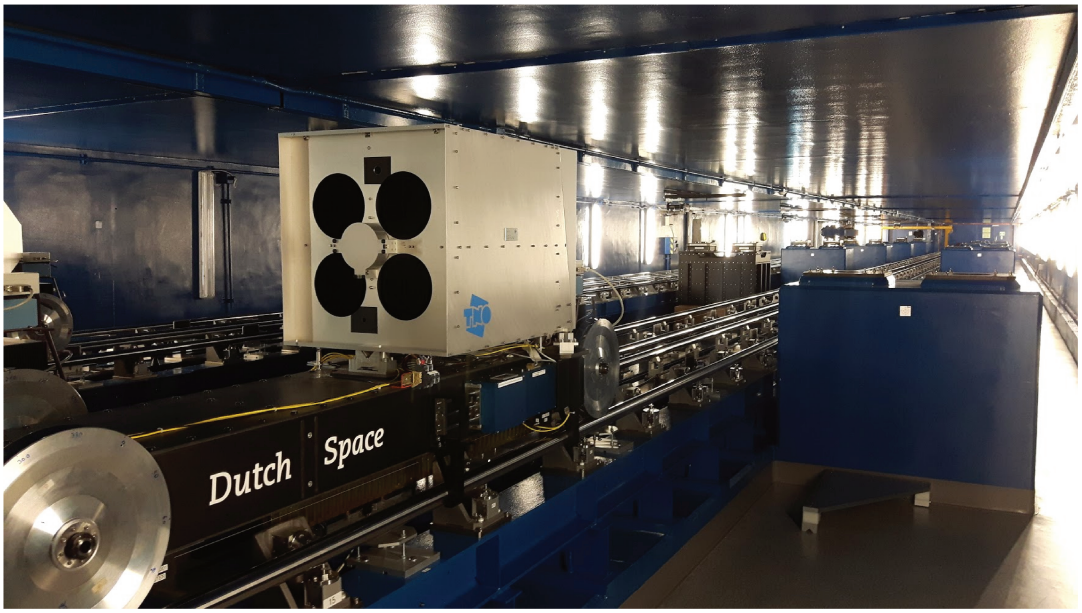

FIGURE 2.4: One of the four delay lines in the interferometric tunnel.

2.3 Overview of GRAVITY

GRAVITY is the first operative instrument of the so-called second generation instrumentation of the VLTI. It provides spectro-interferometry in K band in three different spectral resolutions. Its design was driven by the science case of the Galactic Center, boosting the performance of the VLTI system to reach out SgrA* and its environment. The project was accepted by ESO after concluding a feasibility study finished in 2007 (Eisenhauer et al., 2008). The commissioning phase started at the end of 2015 for the ATs and for the UTs in mid 2016. The first light of the instrument took place in October 2015 for the ATs and September 2016 for the UTs (Gravity Collaboration et al., 2017).

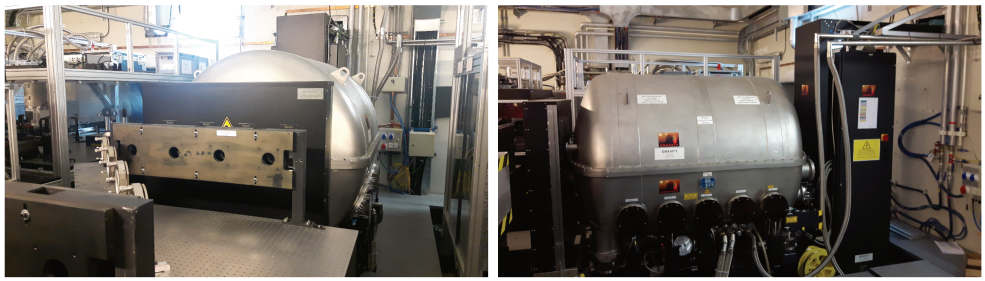

FIGURE 2.5: The GRAVITY cryostat. The beam combiners and the detector subsystems are located inside. The light enters directly from the delay lines (left).

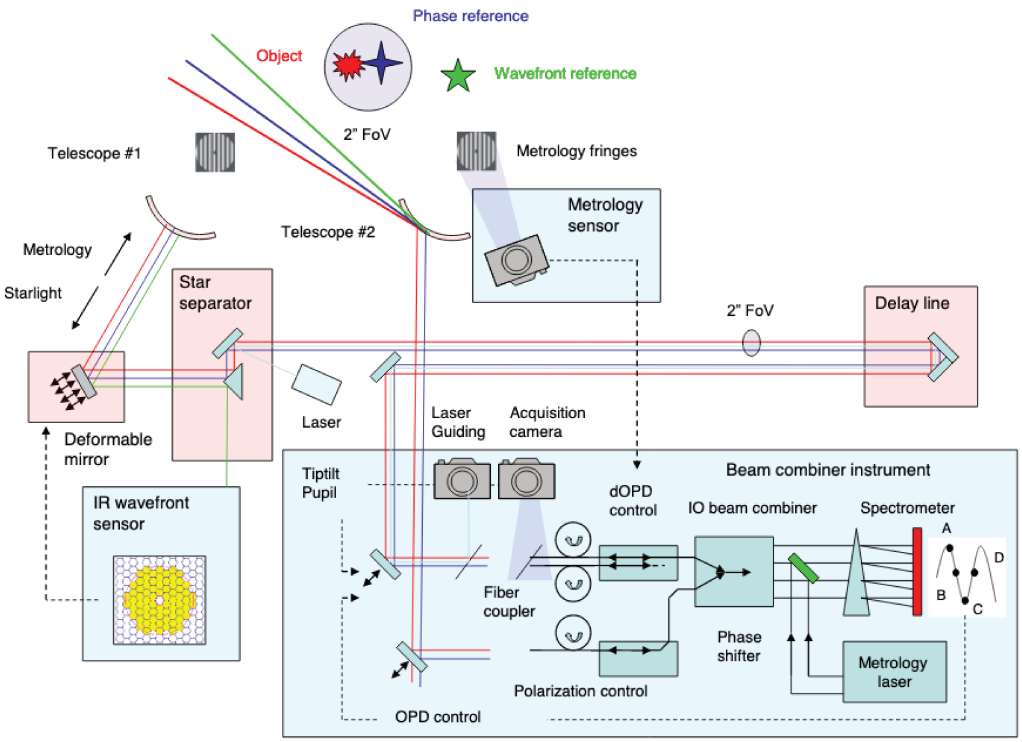

FIGURE 2.6: Diagram of GRAVITY subsystems. Source: Gravity Collaboration et al. (2017)

A sketch of the instrument can be seen in Figure 2.6, where only two telescopes (out of four), only one of the wavefront sensors (out of four, one per telescope) and only one beam combiner (out of two, one for science and the other one for the fringe tracker) are shown. The beam combiner instrument inside the cryostat is composed of the following subsystems:

- The fiber couplers: these four devices receive the beams from the four telescopes respectively and stabilize them to inject the light into fluoride glass single-mode fibers, designed by Le Verre Fluoré. Apart from the optics, it contains a system of motors to rotate the field and piezo actuators to stabilize the pupils, tip-tilt jitter and atmospheric piston (Pfuhl et al., 2014). The field rotation is also used to select objects in the field.
- The fiber control unit: the optical fiber subsystem collects the light from the fiber couplers and inject it into the beam combiners where interference happens. These fibers add a differential delay line, and are controlled by actuators which can vary the distance up to 6 mm with a relative accuracy up to 1 nm (given by the metrology) by stretching the fibers with the piezos. A second group of actuators twist the fibers acting as rotators used to control the fiber polarization. With these fibers it is possible to control the optical path difference between the science object and the phase reference, as well as to align the polarizations of all beams to maximize fringe contrast.
- The integrated optics (IO) beam combiners: these optical devices are an analog to an electrical integrated circuit. There is one per source input (FT and SC). It is here where interference happens and the interferograms are sampled (Jocou et al., 2014). It has four inputs from the fiber control unit (one per beam) and 24 outputs corresponding to four estimators at 0°, 90°, 180°, 270° phase shift (ABCD, following the scheme of Colavita, 1999) for each baseline. A picture of an integrated optics beam combiner is displayed in Figure 2.7 and the circuit used in GRAVITY is presented in the next Section, in Figure 2.9.
- The spectrometers: for each fiber input (FT and SC) there is a spectrometer receiving the output of the 24 channels of the respective IO beam combiner (Straubmeier et al., 2014). They split the light in the range $\Delta\lambda = 1.95 - 2.45\ \mu$m for the observation of the interferometric signals of one target (single field) or two targets, one of them bright being the fringe tracker source (dual field). The science spectrometer is optimized for long integration times (from a second to a minute) configured to provide three different spectral resolutions recording the spectral coverage in a different number of channels according to the needs of the observer:
  - LOW resolution: the number of spectral channels is 15 ($R = 22$). This mode maximizes the amount of light per channel and is optimal for source detection, or faint targets. The spectral information obtained, however, is poor.
  - MEDIUM resolution: the number of spectral channels is 250 ($R = 500$). This mode requires a moderately bright target and a science case who profits from spectral information.

– HIGH resolution: the number of spectral channels is 1740 ($R = 4500$). This mode maximizes the spectral information with the lowest amount of light per channel. It is the mode who gives the most spectral information but requires a target bright enough to give a significant signal to noise ratio per spectral channel.

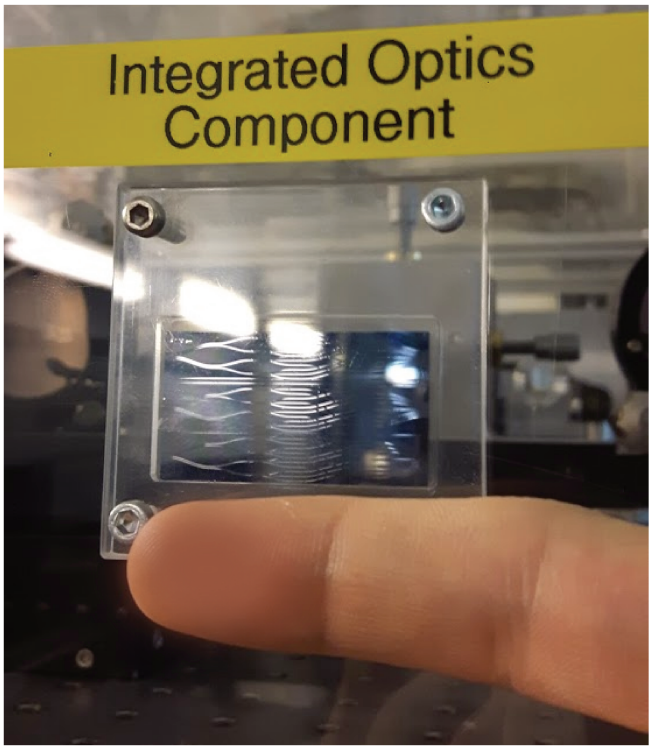

FIGURE 2.7: Picture of the real size of an IO component taken in the VLTI laboratory. The input of every telescope is collected here to obtain the light interference of every baseline.

The fringe tracker spectrometer, on the other side, has a single spectral resolution of $R \approx 22$ (LOW) and is optimized for fast recording (kHz) with 6 spectral pixels. A Wollaston prism is located at the output of the spectrometers providing two different observing modes:

– COMBINED mode: this mode does not make use of the Wollaston prism. The light obtained goes directly to the spectrometer after beam combining. It results in a data set for the science channel and another data set for the fringe tracker.

– SPLIT mode: the Wollaston prism splits the light in two equal beams resulting in two data sets (P1 and P2) per channel. This mode is designed to measure the Stokes parameters to characterize the polarization of the light. The system has also a rotating half-wave plate which is used for measuring the Stokes parameters which determine the polarization state of the light.

- The detectors: the science channel is equipped with a HAWAII2RG detector made of 2048×2048 pixels with a pixel size of 18 μm and a $\lambda_{\text{cutoff}} = 2.5$ μm (Finger et al., 2008). It presents a quantum efficiency of 80% at $\lambda = 2$ μm and a read noise of 3 e-rms by Fowler sampling. The fringe tracker detector is a Selex SAPHIRA near-infrared avalanche photo diode array (Finger et al., 2016) with 256×320 pixels in total and a pixel size of 24 μm. It registers the fringe tracker output in a twenty-four 32×3 pixel array, and it is designed for a fast readout (300 Hz-1 kHz). Its quantum efficiency is 70% at $\lambda = 2$ μm with a resulting effective read noise of less than 1 e-rms (Gravity Collaboration et al., 2017).

- The acquisition camera: another HAWAII2RG detector with the same specifications as the science channel registers four different outputs from the four telescopes simultaneously in a layout made of 2048×2048 pixels: the pupil tracker, the aberration sensor, the pupil imager and the field imager (Amorim et al., 2012). The pupil tracker displays four pupil images on the detector enabling the correction of the pupil motion in both lateral and longitudinal axes. The aberration sensor displays the output of a 9×9 Shack-Hartmann wavefront sensor which is able to measure the non-common path aberrations in the delay lines. This device is used to correct such aberrations together with adaptive optics for the UTs, as well as focus the telescopes for the ATs. The pupil imager displays the full pupil of each telescope and is used to check if the pupils are properly aligned during the observations. The field imager provides the field of view observed by each individual telescope, from which the fringe tracker target and the science target can be selected to be pointed and tracked by the respective fibers. It also displays the coordinates of each fiber measured by the metrology system, which allows to obtain the offset needed to correct by tip-tilt in the fiber coupler. The acquisition camera operates in H-band ($\Delta\lambda = 1.45 - 1.85$ μm).

- The metrology laser: the differential optical path between the two targets on sky (SC and FT) is determined by the metrology system (Lippa et al., 2016), by measuring the internal optical path difference inside the interferometer between the two sources. For this purpose a two-stage laser system ($\lambda = 1908$ nm) is implemented: a low-light level laser controlling the path inside the cryostat is propagated from the detector up to the fiber coupler where another brighter laser (1 W) propagates backwards from the fiber coupler up to the four telescopes. The metrology detectors are located on the secondary mirror spider arms of each telescope such as the whole optical trajectory is taken into account. The reason for this two step configuration is a compromise between distance and power: a single bright laser inside the cryostat would lead to non-linear effects and detector saturation, while a single low-light laser would lead to a very low SNR for the metrology system after the enormous dilution of the beams in the UT 8m pupils. The metrology system also provides the projected position in the sky of each fiber which is displayed in the acquisition camera.

2.3.1 Fringe tracking

Obtaining an infrared interferogram of certain astronomical source is a difficult task mainly due to the influence of the Earth's atmosphere. Any small fluctuation produces a phase shift which breaks the coherence of the light beams who are interfering. Without any adaptive technology, any observation under a very stable atmosphere would still be possible for a given interferometer, but it would limit the integration time to less than the atmospheric coherence time. The physical picture behind this phenomenon is simple: to obtain a measurement of the visibility contrast, the detector must be fast enough to freeze the interferometric fringes resulting from the two beams coming from the telescopes in the image. The more turbulent the atmosphere is, the faster the detector would have to be.

Concretely in the K band, the typical atmospheric coherence time is $\tau_0 < 100$ ms. All the information coming from that astronomical source would have to be collected in that time with an ultra fast detector. Considering also possible loss due to reflections as an interferometer is a complex optical circuit, the amount of collected photons during that interval is typically low (1%), unless the source is significantly bright or the diameter of the telescope primary mirrors is large. As a long integration is not available, in general the number of sources available to be observed by the use of optical interferometry is limited to hundreds.

One of the major contributions of GRAVITY to the instrumentation of VLTI is the fringe tracking subsystem (Lacour et al., 2019). Guided by the principle of adaptive optics (where a deformable mirror corrects the atmospheric turbulence according to the information sent by the wavefront sensor), an element is added to the optical path of the delay lines to overcome the phase shift injected by the atmosphere in real time. This is done by feeding two channels with an identical integrated optics beam combiner each. The first of them is called the science channel, which can integrate the desired time if fringe tracking is available. The second one is the fringe tracker channel, which operates in the lowest resolution available ($R = 22$) and at two available sampling rates: 300 Hz or 1kHz. The elements of the fringe tracking subsystem are the following:

- The fringe sensor: by taking the data output of the FT channel detector, the fringe sensor measures, for every baseline, the phase delay and the group delay (a detailed derivation of this quantities can be found in Lacour et al., 2019).
- The actuators: these elements form a two-stage system composed of a slow actuator in the VLTI delay lines and fast actuators in the fiber coupler. Their purpose is to control the optical path delay to guarantee the detection and tracking of the fringes according to the response on the detectors.
- The OPD controller: this element computes the necessary correction that will be sent to the actuators through a Kalman model, whose parameters are updated in a time span of seconds by exploring the OPD residuals and the response of the actuator. The purpose of the Kalman model is to reduce the vibrations on the optical path difference and predict turbulence during flux dropouts (Menu et al., 2012; Choquet et al., 2014).

The use of fringe tracking requires the presence of a bright target in the field to stabilize the fringes in the same way as adaptive optics requires a guide star. In the case of the UTs, the magnitude of this star must be $m_K < 10$, and for the ATs, $m_K < 7$ (Gravity Collaboration et al., 2017). Thanks to this technique and the use of adaptive optics, GRAVITY can integrate on the science channel[2], increasing the number of available targets up to a brightness limit of $m_K = 19$. Moreover, the possibility of obtaining the interferometry from two targets simultaneously with high sensitivity opens the way to astrometric measurements based on the instrument metrology reaching an unprecedented accuracy.

2.3.2 Observational modes

Depending of the science case, the instrument is configured to operate in the following modes:

- Single field: the fringe tracking fiber and the science fiber point to the same target, and then the light is split between FT and SC channels. This mode is appropriate if the science target is bright enough to track the fringes ($m_K < 7$ for the UTs or $m_K < 10$ for the ATs). The beam-splitter feeds the FT and the SC channels with 50% of the light respectively.
- Dual field: the fringe tracking fiber and the science fiber point to different targets in the same field of view ($2''$ for UTs and $6''$ for the ATs). This mode has to be selected if the science target is too faint to be used as fringe tracker. As the phases are recorded with respect to the FT source, this mode is required for astrometric measurements. Depending on the distance between FT and SC objects, the set-up can be:
  - Dual field *on-axis*[3]: used for separations lower than $0.27''$ for UTs or lower than $1.17''$ for ATs. The same beam-splitter as the single field mode is used, feeding each channel with 50% of the total amount of light.
  - Dual field *off-axis*: used for larger distances, higher than $0.27''$ for UTs or higher than $1.17''$ for ATs. In this case 100% of the light of each source is injected into each fibre.

[2]The maximum integration time does not directly depend now on the coherence time, but in the confusion of the (u, v) plane due to the rotation of the Earth.

[3]Only this mode is applicable for this thesis.

2.4 Estimation of interferometric observables

The reduction and calibration processes are fundamental to give any physical meaning to the measurements taken in the observatory. They involve the transformation of the electrical signal of the detector into physically measurable quantities of the target, as well as remove the instrumental and atmospheric biases. In this section the quantities used for the astrophysical analysis of the sources are formally described, from the detector to the final interferometric observable estimators.

In the case of GRAVITY, an observing block for a given science target is made of:

- Several science frames (SCI) which the astrophysical information is obtained from. These data frames must be corrected by all the atmospheric and instrumental effects that are present in the astrophysical signal.
- An interferometric calibrator (CAL frame), needed to debias the SCI observation from instrumental phase shifts and visibility losses. For this purpose an astrophysical target must be selected, to be observed at the same air mass as the science target to minimize errors due to anisoplanatism of turbulence and refraction effects of the atmosphere. They must be observed in the same instrumental configuration as the SCI frames, with the same DIT and number of exposures (NDIT). The calibrator, which is selected by the user, must be a very well known and stable object with a high and predictable visibility (close to one), to obtain the response of the interferometer. The calibration is applied as a multiplicative factor.
- At least a SKY frame for each observing sequence (CAL or SKY), typically interleaved between two SCI frames or two CAL frames. The purpose of these frames is nothing but remove the average bias of the sky on top of the target. These frames are obtained by applying a slight offset in an empty region of the sky. The processed SKY is directly substracted from the signal.

All of these data frames are recorded during the night. In addition, several extra frames are needed for a proper reduction of the data and its posterior calibration, obtained through a process who takes place after the end of the observations. They are the following:

- One DARK file associated with the observation, in the same instrumental configuration. They are obtained by recording the response of the detector without any source illuminating it. Its use is needed to remove, from the SCI frames, the bias due to the readout of the electronics of the detector. The correction is subtractive in a similar way as the SKY frames, being directly substracted from the signal of every frame. At the end of the night, there must be one DARK file for each configuration used. For example, if the dataset of the night includes two different Detector Integration Times (DIT), there will be two DARK files.

- A FLAT frame per telescope (4 in total). This correction guarantees that the response of the detector is clean of any perturbation due to individual defects in the optics, typically by observing a uniform field. By the way GRAVITY is designed with single-mode fibers this is not possible, and the flat field correction is performed by measuring the shape of the spectra by using an internal calibration source with each telescope individually. This correction is multiplicative, being applied by dividing the response of the instrument by the flat field. The flat is also used to calibrate the transmission of the instrument in each of the four inputs.
- The wavelength coverage for each spectral element stored in tables. There is a WAVE dataset for the fringe tracker data, and another one (WAVESC) for the science dataset.
- The raw pixel to visibility matrix (P2VM_RAW), which are the elements who translate input signals to visibility measurements. They are obtained by inverting the visibility to pixel matrix (V2PM), which is measured by using an internal light source. The V2PM depends on the photometric transmission of the integrated optics and the coherence terms, with one matrix per wavelength. For any observing night, there is one P2VM_RAW file per baseline (6 in total).

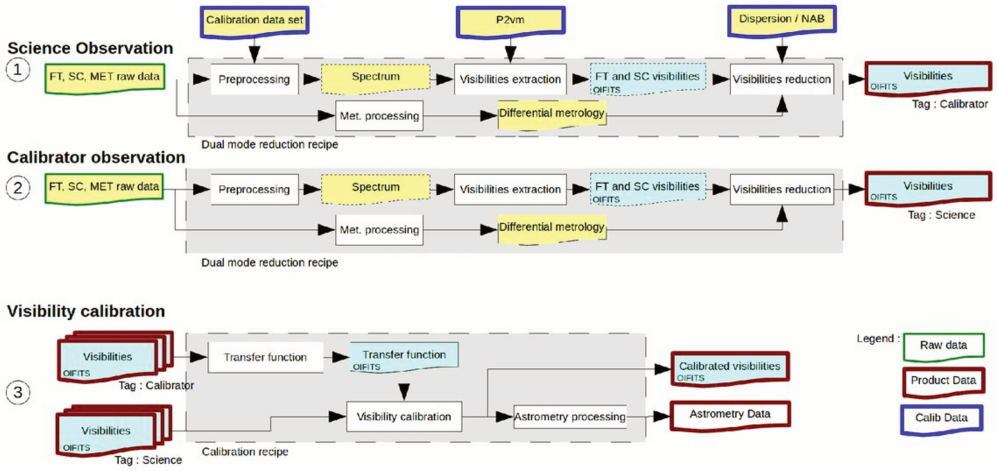

FIGURE 2.8: Diagram of the reduction and calibration pipeline. Source: Lapeyrere et al. (2014)

The whole reduction and calibration, for every frame used for this thesis work, is performed by using a pipeline written in C and developed by the GRAVITY collaboration, which is summarized in Figure 2.8 and its details can be found in Lapeyrere et al. (2014). The process from raw data to reduced visibilities is the following, performed both for the SCI files and the CAL files (steps 1 and 2 in 2.8):

(a) The first step builds the instrument response calibration. By using the DARK file corresponding to the 6 P2VM_RAW files, the WAVE and WAVESC files and the four FLATs the pipeline generates a map with the response of bad pixels (BAD_CALIB), the master calibration files (DARK_CALIB, FLAT_CALIB, WAVE_CALIB) and finally the reduced P2VMs corrected by the detector bias.

(b) In the second step the spectra of the instrument are extracted from the detector readout and calibrated in wavelength by the use of the files DARK_CALIB, FLAT_CALIB and WAVE_CALIB.

(c) The third step obtains the values of the visibilities and telescope fluxes by the use of the reduced P2VMs and the extracted spectra of the instrument. Once they are computed, the visibilities are reduced by phase referencing involving the metrology.

After these steps, the dataset is ready for calibration, which is finally obtained by the following process, corresponding to the step 3 in Figure 2.8:

(a) A transfer function is built for the phases and for the amplitudes of the visibilities respectively by the use of the CAL visibilities and the known diameter of the calibrator. It is also interpolated to the time of the SCI frame to calibrate.

(b) The reduced visibilities of the science frames are finally calibrated by dividing by the transfer function for the observables related to the amplitude of the visibility, or subtracting them from the phases for the observables related to the phase.

In case of any observation done by using the Wollaston prism (SPLIT mode), the two channels are reduced and calibrated independently. The final output of the whole pipeline returns all the visibility observables completely calibrated.

In the following sections, the whole process from the detection to the visibility calibration is described in detail. Due to the fact that the HIGH resolution mode is not used in this thesis (and it involves indeed a different approach), the following equations are only applicable for the LOW and MED resolutions. If SPLIT mode is chosen, the observables are estimated for both polarization outputs individually[4].

A full description of the pipeline can be found in Lapeyrere et al. (2014) or in the GRAVITY Pipeline User Manual (v 1.4.0). The quantities and indices used in this section are summarized in Tables 2.1 and 2.2.

[4]The study of polarized visibilities is not addressed in this thesis.

TABLE 2.1: List of quantities used in this section.

Quantity	Meaning
Y	Spectrum extracted from the detector readout
E	Incident electric field
S	Total flux registered by a detector
T	Transfer function term from the optical system
C	Instrumental coherence term
V	Natural coherence term (visibility)
R	Real part of the complex coherent flux
I	Imaginary part of the complex coherent flux
F	Flux recorded by each telescope

TABLE 2.2: List of indices used in this section.

Index	Meaning	Values
f	Frame, a single integration DIT	From 1 to NDIT
o	Output region of the detector	From 0 to 3 (ABCD)
i	The spatial direction of the pixel map	Pixel map size x
j	The spectral direction of the pixel map	Pixel map size y
l	The wavelength channel	From 0 to 15 in LOW From 0 to 250 in MED
t	The telescope index	From 1 to 4
b	The baseline index	From 1 to 6
n	The beam index	From 1 to 4
m	A beam index different than n	From 1 to 4
k	The output pixel index	From 1 to 24 ($6 \times o$)
λ	The wavelength of the channel	From 1.95 to 2.45 μm
τ	The time interval in a single integration	From 0 to DIT

A diagram of the beam combiners is displayed in Figure 2.9. In the nomenclature of Table 2.2, the four inputs n correspond to each telescope t. The 24 pixel outputs k are subdivided in four regions o corresponding to the samples ABCD. Each set of four regions corresponds to a baseline b labelled with the index of the two inputs (n, m) corresponding to two telescopes t.

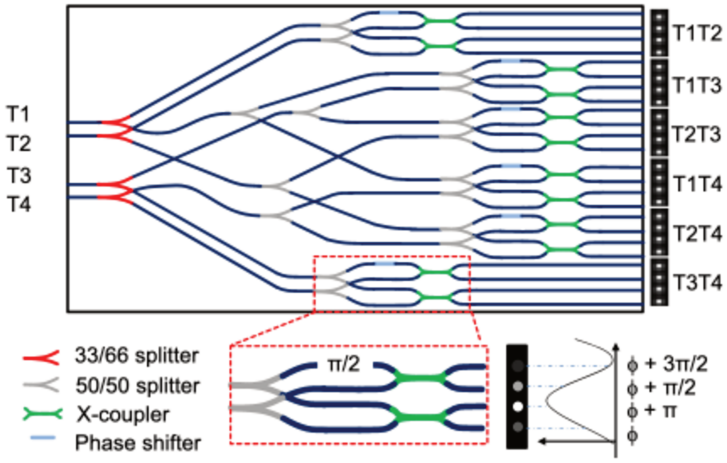

FIGURE 2.9: Diagram of the integrated optics beam combiners. Source: Gravity Collaboration et al. (2017).

2.4.1 Spectrum extraction

The readout of the detector must be calibrated in order to extract astrophysical information from the observed source. This implies a translation from the detector readout to counts, cleaned from bias sources. The first of these sources is the detector bias, measured by the readout of a column of pixels non illuminated. A single scalar bias value is used for the entire frame (for each frame), consisting in the mean over all the pixel of the bias lines (between the channels where the spectra are measured). The second one has already been mentioned in the text, the sky background bias. It is measured in the SKY frames obtained between the SCI sequences. The spectrum in intensity (counts) of the frame f in the output o for each detector (FT or SC) is obtained by the following expression:

$$\begin{aligned} Y_{foj} &= g \sum_i \left(X_{fij} - S_{ij}\right) p_{oij} \\ \sigma(Y)_{foj} &= \sqrt{g \sum_i \left(X_{fij} - K_{ij}\right) p_{oij}^2 + g^2 \sum_i \sigma^2(K)_{ij} p_{oij}^2} \,, \end{aligned} \tag{2.19}$$

where g is the gain (in counts per ADU):

- the term X_{fij} is the direct measurement of the pixel map (in ADU),
- the term S_{ij} is the mean image measured on the SKY calibration file (in ADU),
- the term p_{oij} is a normalized Gaussian profile (with a FWHM of 1.5 pixels) for the region o.

The term K_{ij} depends on the channel (SC or FT) and is used to estimate the variance on the spectrum:

- in the SC channel, K_{ij} and $\sigma(K)_{ij}^2$ are the mean level and the variance measured over the DARK_CALIB file respectively.
- in the FT channel, $K_{ij} = S_{ij}$ and $\sigma(K)_{ij}^2 = \sigma(S)_{ij}^2$, the mean image and the variance measured over the SKY frame (recorded during a SCI sequence)

respectively. The reason why the SKY is used instead of the DARK is the short exposure time of the FT channel, where the background emission of the sky around the target is negligible.

To ensure all the spectral samples j of the region o refer to the same effective wavelength, a spectral wavelength calibration must be performed. The wavelength tables, which are different for each output region o of the detectors, are stored in the files WAVE_CALIB and WAVESC_CALIB (FT and SC respectively). Depending on the spectral resolution chosen (LOW, MED or HIGH), a number of channels λ_l will be defined, but this wavelength cannot be directly used because the transmission of each channel may be different. For each region o, the target wavelength λ_l is located somewhere between two spectral samples jol and $jol+1$. In the SC channel, a common wavelength is then defined by:

$$\lambda'_{ol} = \lambda_{oj_{ol}} + \frac{(\lambda_l - \lambda_{oj_{ol}})(\lambda_{oj_{ol}+1} - \lambda_{oj_{ol}})}{(\lambda_{oj_{ol}+1} - \lambda_{oj_{ol}}) + (\lambda_{oj_{ol}+1} - \lambda_l)\frac{L_{oj_{ol}+1}}{L_{oj_{ol}}}} \ , \tag{2.20}$$

where the quantity L_{oj} is the flat recorded on the internal light source and stored in the file FLAT_CALIB. The flat correction guarantees that any spectral channel with a bad pixel is set to zero. The fluxes must be corrected by this offset, and that is done by defining the following quantity:

$$a_{ol} = \frac{\lambda_{oj+1} - \lambda'_{ol}}{\lambda_{oj+1} - \lambda_{oj}} \ . \tag{2.21}$$

Finally, the spectrum of the frame f in the region o and the wavelength channel l is then linearly interpolated as:

$$\begin{aligned} Y_{fol} &= a_{ol} Y_{foj_{ol}} + (1 - a_{ol}) Y_{foj_{ol}+1} \\ \sigma(Y)_{fol} &= \sqrt{a_{ol}^2 \sigma^2(Y)_{foj_{ol}} + (1 - a_{ol})^2 \sigma^2(Y)_{foj_{ol}+1}} \end{aligned} \tag{2.22}$$

2.4.2 P2VMs

By denoting E the incident electric field and S the output electric field, an optical system can be generally described by its transfer function T such as $S_k = \sum_n T_{kn} E_n$, n being the input channels and k being the output channels. In the case of the integrated optics beam combiners, where interference takes place, there are 4 input channels $n = 1, 2, 3, 4$ (one per telescope) and 24 output channels $k = 1, ..., 24$ (the four ABCD shifts to estimate the observables per baseline, see Figure 2.9). The flux registered by the pixel k at wavelength λ averaged over the interval $\tau = (0, \mathrm{DIT})$ is modelled as (Lacour et al., 2019):

$$q_k^\lambda = \left\langle \left| S_k^{\lambda\tau} \right|^2 \right\rangle_{\mathrm{DIT}} = \left\langle \left| \sum_n T_{kn}^\lambda E_n^{\lambda\tau} \right|^2 \right\rangle_{\mathrm{DIT}} \ . \tag{2.23}$$

As the way GRAVITY is designed there is a measurement q_k^λ for each wavelength channel λ. Hereinafter, the index τ is omitted for simplicity and the mean values

$\langle|E_n|^2\rangle$ are referred to integration over DIT. The quantities E and T are complex, which allows to decompose Equation 2.23 in the following:

$$\left\langle \left|S_k^\lambda\right|^2 \right\rangle = \mathrm{Re}\left[\sum_n |T_{kn}^\lambda|^2 \langle|E_n^\lambda|^2\rangle + 2\sum_n \sum_{m>n} \langle T_{km}^\lambda T_{km}^{\lambda *} E_n^\lambda E_m^{*\lambda}\rangle\right] , \tag{2.24}$$

where the index $*$ denotes the complex conjugated. The second term accounts for the loss of coherence inside the beam combiner, which have two components:

- An instrumental loss of coherence from now called C_{knm} that takes place inside the optical path of the beam combiner. It must be calibrated for each detector k in each baseline n, m.
- The intrinsic source spatial coherence term, from now called V_{nm} due to the spatial brightness distribution of the astrophysical target, which is the quantity we want to measure for each baseline n, m.

By approximating the second term as:

$$\langle T_{km}^\lambda T_{km}^{\lambda *} E_n^\lambda E_m^{\lambda *}\rangle = |T_{km}^\lambda T_{km}^{\lambda *}| C_{knm}^\lambda \sqrt{\langle|E_n^\lambda|^2\rangle \langle|E_m^\lambda|^2\rangle} V_{nm}^\lambda , \tag{2.25}$$

Equation 2.24 can be written as a matrix product as:

$$\begin{pmatrix} \left\langle \left|S_1^\lambda\right|^2 \right\rangle \\ \vdots \\ \vdots \\ \vdots \\ \left\langle \left|S_k^\lambda\right|^2 \right\rangle \end{pmatrix} = \mathrm{Re}\left[\mathrm{V2PM} \cdot \begin{pmatrix} \langle|E_1^\lambda|^2\rangle \\ \vdots \\ \langle|E_n^\lambda|^2\rangle \\ \sqrt{\langle|E_1^\lambda|^2\rangle \langle|E_2^\lambda|^2\rangle} V_{12}^\lambda \\ \vdots \\ \sqrt{\langle|E_n^\lambda|^2\rangle \langle|E_m^\lambda|^2\rangle} V_{nm}^\lambda \end{pmatrix} \right] . \tag{2.26}$$

Every component E and V are enclosed in the column vector at the right, which has $n + n(n-1)/2$ elements (n telescopes plus their baselines). The matrix V2PM, called *visibility to pixel* matrix (Tatulli et al., 2007) encloses all the dependence on the components T and C, accounting for all the instrumental effects related to the transfer function of the optical system. This matrix is not squared, with k rows and $n + n(n-1)/2$ columns.

The calibration of the V2PM matrix is needed to extract any astrophysical information for the observations and is done during daytime by illuminating the inputs with an internal source of GRAVITY located inside the cryostat (non resolved, guaranteeing $V_{nm} = 1$ $(\forall n \neq m \in 1, 2, 3, 4)$). Firstly, the individual transmissions T_{km} corresponding to every beam are calibrated by illuminating the inputs n individually closing the rest of the shutters. Secondly, the instrumental coherence terms C_{knm} are obtained by illuminating the inputs opening the shutters by pairs (and closing the rest). Finally, the instrumental closure phases are measured by illuminating all the inputs simultaneously.

The measurement of the coherent fluxes requires the inversion of the V2PM matrix, but unfortunately it is not squared. For this purpose, the pseudo-inverse matrix, called *pixel to visibility* matrix (P2VM) is obtained by splitting the V2PM into real and imaginary parts, and then performing a singular value decomposition (Lapeyrere et al., 2014). After inverting the V2PM matrix, the P2VM provides the measurements of the complex coherent fluxes per baseline and the individual telescope fluxes:

$$\begin{aligned}(F_{ftl}, R_{fbl}, I_{fbl}) &= \mathrm{P2VM}^{o}_{btl} \times Y_{fol} \\ [\sigma^2(F)_{ftl}, \sigma^2(R)_{fbl}, \sigma^2(I)_{fbl}] &= (\mathrm{P2VM}^{o}_{btl})^2 \times \sigma^2(Y)_{fol} \ ,\end{aligned} \tag{2.27}$$

where the indices are again the ones presented in Table 2.2. For the estimation of the variances, the propagation is done by assuming no correlation between the inputs Y_{fol}.

From the product of the P2VM and the spectra the following relations are derived:

$$\begin{aligned}R_{fbl} &= Y_{f0l} - Y_{f2l} \ , \\ I_{fbl} &= Y_{f1l} - Y_{f3l} \ .\end{aligned} \tag{2.28}$$

Which correspond to the real and the imaginary part of the (non-normalized) coherent flux of the baseline b $\Gamma_{fbl} = R_{fbl} + iI_{fbl}$, obtained by using the regions o of each baseline b from the spectrum Y_{fol}. In addition, for each baseline output the following equation is satisfied for the telescope fluxes F_{ftl}:

$$F_{ft_1l} + F_{f2t_2l} = Y_{f0l} + Y_{f1l} + Y_{f2l} + Y_{f3l} \ , \tag{2.29}$$

which constitutes a system of 6 linear equations (from which 2 are redundant) with a unique solution for the 4 variables F_{ftl}. Following the ABCD method of Colavita (1999), Equations 2.28 and 2.29 identify with $R = A - C$, $I = B - D$ and $F_1 + F_2 = A + B + C + D$.

The flux F obtained for each frame provides the first observable, which corresponds to an estimate of the photometric spectra of the source.

- The flux of each individual telescope, in counts:

$$F_{tl} = \sum_f F_{ftl} \tag{2.30}$$

2.4.3 Phase referencing

In dual field, SC and FT fibers are placed on different targets. The phase has to be calibrated under a reference system given by a phase reference. By defining as f_{FT} the frames recorded in the FT during a SC exposure of the frame f, the phase reference in SC is given by the following formula:

$$\phi^{\mathrm{ref}}_{fbl} = \arctan\left(\frac{\sum_{f_{FT}} I_{f_{FT}bl}}{\sum_{f_{FT}} R_{f_{FT}bl}}\right) + \frac{2\pi}{\lambda_l}(u_{fb}dE + v_{fb}dN) + \Delta^{\mathrm{opd}}_{fbl} \ , \tag{2.31}$$

where u_{fb}, v_{fb} are the spatial frequency coordinates sampled by the baseline b and dE, dN are the offsets of the fibers from FT to SC (the sky coordinates). The term $\Delta^{\text{opd}}_{fbl}$ is the optical path difference introduced by the differential delay line, which is obtained by the metrology based on the position of the fibers and a light dispersion model. Equation 2.31 provides the phase reference for astrometric measurements based on metrology.

2.4.4 Interferometric observables

To normalize the coherent flux collected by the SC channel, for the baseline b defined by two telescopes t_1, t_2 a flux product is constructed as:

$$FF_{fbl} = F_{ft_1l} \times F_{f2t_2l} \ . \tag{2.32}$$

For the closure phases, the average bispectrum of the triplet of baselines b_{xyz} ($x \neq y \neq z$ going from 1 to 6 each) is computed as:

$$B_{b_{xyz}l} = \sum_f \left(R_{fxl} + iI_{fxl}\right)\left(R_{fyl} + iI_{fyl}\right)\left(R_{fzl} - iI_{fzl}\right) \ . \tag{2.33}$$

In addition, to obtain the interferometric observables relative to the complex visibility, the complex coherent flux has to be rotated with the phase reference:

$$\begin{aligned} R'_{fbl} &= R_{fbl}\cos\left(\phi^{\text{ref}}_{fbl}\right) - I_{fbl}\sin\left(\phi^{\text{ref}}_{fbl}\right) \ , \\ I'_{fbl} &= R_{fbl}\sin\left(\phi^{\text{ref}}_{fbl}\right) + I_{fbl}\cos\left(\phi^{\text{ref}}_{fbl}\right) \ . \end{aligned} \tag{2.34}$$

Then the final estimators for the interferometric observables obtained by the GRAVITY pipeline and used in this thesis work, for the wavelength channel l, the baseline b and the triplet b_{xyz} , are the following:

- The modulus of the visibility function[5]:

$$(|V|)_{bl} = \frac{\sqrt{\left(\sum_f R'_{fbl}\right)^2 + \left(\sum_f I'_{fbl}\right)^2}}{\sum_f \sqrt{FF_{fbl} v_{fbl}}} \ . \tag{2.35}$$

- The phase:

$$(\phi)_{bl} = \arctan\left(\frac{\sum_f I'_{fbl}}{\sum_f R'_{fbl}}\right) \ . \tag{2.36}$$

- The visibility squared[6], which is debiased from noise variance:

$$(V^2)_{bl} = \frac{\sum_f R^2_{fbl} + \sum_f I^2_{fbl} - \sum_f \sigma^2(R)_{fbl} - \sum_f \sigma^2(I)_{fbl}}{\sum_f FF_{fbl} v_{fbl}} \ . \tag{2.37}$$

[5] In *single field* mode, the values $R' = R, I' = I$. That is, there is no phase reference rotation.

[6] Note that this estimator does not use the rotated coherent flux. It is the same in practice as it does not enclose any phase information.

- The closure phase:

$$(T3_\phi)_{b_{xyz}l} = \arctan\left[\frac{\mathrm{Im}\left(B_{b_{xyz}l}\right)}{\mathrm{Re}\left(B_{b_{xyz}l}\right)}\right] , \tag{2.38}$$

where v_{fbl} is a factor used to compensate the loss of contrast due to phase jittering, and is computed by using the FT frames during that SC exposure. The final uncertainties on the interferometric observables are computed by bootstrapping over the frames. If the number of frames (NDIT) is larger than 100, the pipeline splits the dataset in smaller segments and boostraps over them individually, changing the estimation of the uncertainties. On the other side, if the NDIT is lower than 5 frames, the dataset is complemented with mock frames adding a random theoretical noise (using the theoretical variance). None of these cases apply in this thesis work, as NDIT=30 for both science cases.

2.4.5 Calibration

In order to calibrate the SCI frames, a Transfer Function (TF) is built. For every observation c of a calibrator (CAL file), a transfer function is obtained for each baseline b and each spectral channel l as:

$$\begin{aligned} \mathrm{TFA}_{blc} &= \frac{(|V|)_{blc}\,(\pi\theta B_b/\lambda_l)}{J_1(\pi\theta B_b/\lambda_l)} , \\ \mathrm{TF}\phi_{blc} &= (\phi)_{blc} , \\ \mathrm{TF}(T3_\phi)_{blc} &= (T3_\phi)_{b_{xyz}lc} , \end{aligned} \tag{2.39}$$

where the term J_1 is the Bessel function of the first kind, B_b being the spatial frequencies sampled by the baseline b and θ the diameter of the calibrator, which is known. The equation for TFA corresponds to dividing the visibility amplitude of the calibrator by the expected visibility amplitude of a uniform disk[7] of diameter θ. The calibrator must be wisely chosen to be a source sufficiently small for the interferometer not to be able to resolve it at all (typically with a diameter lower than 0.5 mas) as the uncertainty on the diameter of the calibrator has little or no influence on the measurement on the transfer function.

[7] A detailed explanation of this model can be found in Chapter 4, Section 4.4.2.

To obtain an estimation at the time where the SCI measurement was taken, a weighted average of all the calibrator TFs is considered:

$$\begin{aligned} \mathrm{TFA}_{bl} &= \frac{\sum_c W_{bc}\mathrm{TFA}_{blc}}{\sum_c W_{bc}} \ , \\ \mathrm{TF}\phi_{bl} &= \arg\left[\sum_c W_{bc}\exp\left(i\mathrm{TF}\phi_{blc}\right)\right] \ , \\ \mathrm{TF}(T3_\phi)_{bl} &= \arg\left[\sum_c W_{bc}\exp\left(i\mathrm{TF}(T3_\phi)_{blc}\right)\right] \ , \end{aligned} \tag{2.40}$$

where the weights W_{bc} are chosen to obtain an estimation of the TF at the time τ where the frame SCI was taken:

$$W_{bc} = \frac{\exp\left[-2(\tau-\tau_c)^2/D^2\right]}{\mathrm{med}_l(\sigma^2_{blc})} \ . \tag{2.41}$$

Here, med_l corresponds to the median of the variances σ^2_{blc} of the respective estimator over the channels l, τ_c is the time where the calibrator observation was taken and D is a free parameter quantifying the expected stability of the instrument and the atmosphere responses. It is arbitrarily set at 2 hours such that the pipeline wisely averages the calibrations if they are separated within the distance $t - t_c$, interpolates them if they are separated about this interval and rejects them if they are far from this interval, guaranteeing that the calibrator always correspond to the appropriate SCI frame.

Finally, the calibrated observables are obtained as:

$$\begin{aligned} (|V|)^C_{bl} &= \frac{(|V|)_{bl}}{TFA_{bl}} \ , \\ (\phi)^C_{bl} &= \arg\left\{\exp\left\{i\left[(\phi)_{bl} - \mathrm{TF}\phi_{bl}\right]\right\}\right\} \ , \\ \left(V^2\right)^C_{bl} &= \frac{(V^2)_{bl}}{(TFA_{bl})^2} \ , \\ (T3_\phi)^C_{bl} &= \arg\left\{\exp\left\{i\left[(\phi)_{bl} - \mathrm{TF}(T3_\phi)_{bl}\right]\right\}\right\} \ , \end{aligned} \tag{2.42}$$

where their error bars are obtained by error propagation.

Chapter 3

The Central 100 astronomical units

While the central stellar cluster has been studied for decades, the spatial resolution reached with direct imaging with 8-10m class telescopes is insufficient to explore the surroundings of the central object up to physical distances comparable to our Solar System. The improvement of new techniques in infrared interferometry has opened the way to the innermost region, where phenomena predicted by General Relativity in strong regime can be finally tested.

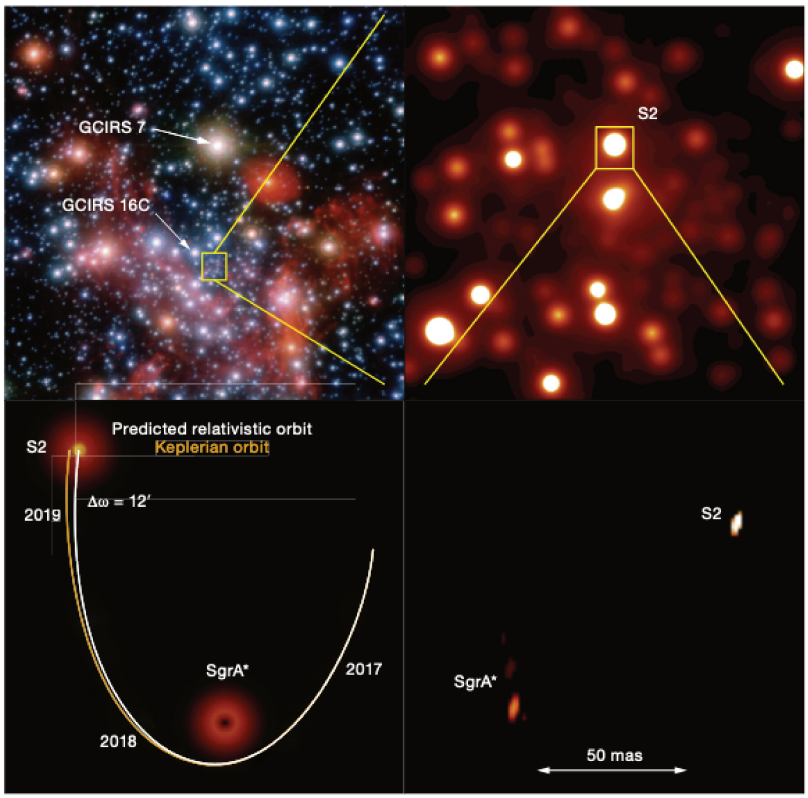

FIGURE 3.1: *Top left*: the central 20" of the Galactic Centre as seen by VLT/NACO. *Top right*: zoom at the central arcsecond also with VLT/NACO. *Bottom right*: reconstructed image of the pair S2-SgrA* corresponding to the first detection of SgrA* by GRAVITY in 2016. Both sources were recorded in the same field of view. *Bottom left*: expected difference between purely Keplerian and relativistic orbits of S2. Source: (Gravity Collaboration, 2017)

3.1 Observational properties of S2 and SgrA*

In the context of the central S cluster, the case of the star S2 is one of the few where a full orbit tracking is feasible in a reasonable time scale. This star, whose spectrum was classified as B0-B2.5 (Martins et al., 2008) is one of the brightest of the S cluster in K band with $m_K = 14$. By studying 10 years of astrometric imaging data, Schödel et al. (2002) estimated the period of its highly eccentric Keplerian orbit as $P = 15.2$ years for the first time, revealing a pericenter distance of $d_{\text{peri}} = 17$ light hours (122.6 astronomical units, approximately 4 times the mean distance Neptune-Sun). Its short pericenter distance provides a truly unique scenario to observe, for the first time, certain relativistic effects under a strong gravitational field regime such as the gravitational redshift or the relativistic precession.

S2 is not, however, the star with the closest pericenter distance as confirmed later by Meyer et al. (2012) with the detection of S0-102 ($m_K \sim 17$). However, S2 is three magnitudes brighter and its orbit has been deeply studied in the last decade, making it the perfect candidate to study the nature of SgrA*. Indeed, Gillessen et al. (2017) prove that an orbit fit by using S2 alone is robust enough to constrain the mass and distance to SgrA*. Their work provides the last orbital fit of S2 before the use of infrared interferometry, fitting 25 consecutive years of data in total by using adaptive optics assisted imaging and spectroscopy with VLT. The latest data obtained before the arrival of GRAVITY are fully compatible with a Keplerian, non-relativistic model (Gillessen et al., 2017) whose orbital parameters are listed in Table 3.1. This orbit is represented in Figure 3.2.

Before the next pericenter passage which took place in 2018, the results of Gillessen et al. (2017) could be considered the limit of what a single aperture approach can bring to the study of the orbits of the Galactic Center and the supermassive black hole lying on its core. However, through optical interferometry, the accuracy on the orbit fitting can increase substantially.

TABLE 3.1: Orbital parameters of S2 from Gillessen et al. (2017).

Parameter	Value
a (")	0.1255 ± 0.0009
e	0.8839 ± 0.0019
$i(^\circ)$	134.18 ± 0.40
$\Omega(^\circ)$	226.94 ± 0.60
ω (")	65.51 ± 0.57
t_P (years)	2002.33 ± 0.01
T (years)	16.00 ± 0.02

3.1.1 The pericenter passage

By the conservation of angular momentum, the pericenter is the point of the orbit where the radial velocity of the orbit is maximal. The pair S2-SgrA* can be seen as a binary system with an orbit of 16 years where the mass of the central source is about 10^5 times higher (Gillessen et al., 2017). The instantaneous orbital speed of the star in the pericenter is $v \approx 7650$ kms^{-1}, which is nearly 2.5% of the celerity of light. Indeed, the gravitational influence of SgrA* transforms the star S2 into a relativistic body near the closest approach, making the central 100 astronomical units of the Galaxy one of the best laboratories in sky to test and verify the theory of General Relativity in a strong regime.

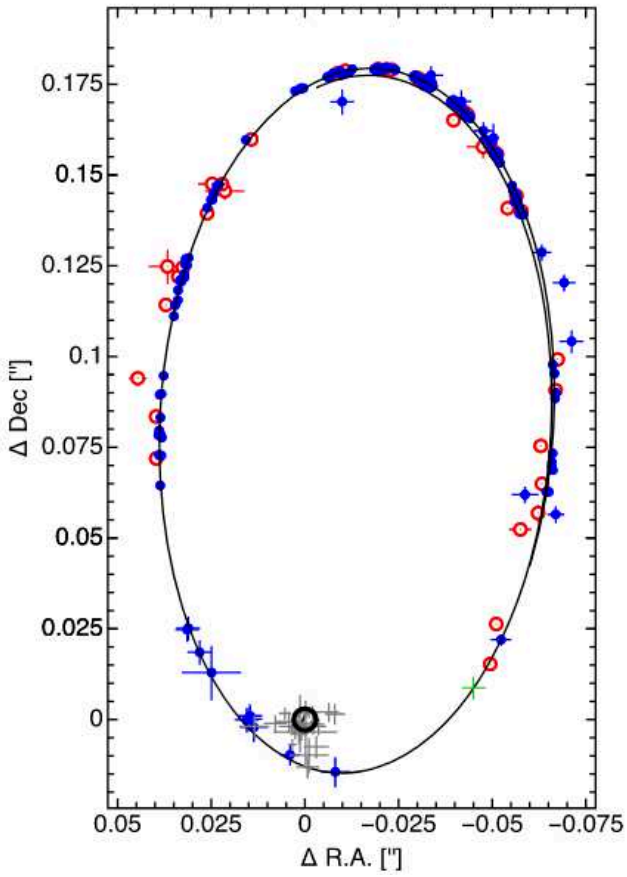

FIGURE 3.2: *Black line:* S2 Keplerian orbit fit by Gillessen et al. (2017). The orbit is not closed due to a residual drift motion of the mass in the reference frame. *Blue dots:* VLT data used in the orbit fit. *Grey crosses:* positions where a flare has been recorded (VLT data). *Red circles*: S2 data by Boehle et al. (2016) corrected by the reference frame shift. *Green cross*: estimated location of S2 at the beginning of the thesis work. Source: Gillessen et al. (2017).

Near the pericenter, the two sources are so close to each other that they are confused at single-dish resolution. This implies that both sources are simultaneously in the field-of-view of the fibre of GRAVITY, which brings a unique opportunity to study their relative astrometry by classical interferometric binary fitting. It is indeed at the pericenter approach where the two targets are easier to observe by the use of fiber assisted interferometry such as the way GRAVITY is designed for. As the transmission of the fiber decreases with distance to the center of the field of view, it is always better to have the second source not too far, making the response of the four fibers the same and increasing the accuracy on the positioning. It can happen, however, that both sources could be confused depending on the spatial coverage of the interferometer. The latest pericenter passage took place in May 2018. Precisely, the data obtained in 2017 and 2018 (before and after the peri passage) add some new samples to the curve in a poorly explored region of the orbit (Figure 3.2).

3.1.2 Observing SgrA* in K band

Although the central source is known to be truly faint at all wavelengths, it presents an apparently irregular variability in every wavelength domain, which could be interpreted as accretion processes in the environment of a plausible super massive black hole (Genzel, Eisenhauer, and Gillessen, 2010, and references therein). The first detection of the variable emission from SgrA* was reported by Baganoff et al. (2001) in X-rays, identifying them as flares. Their detection in the near infrared was reported by Genzel et al. (2003a) by using adaptive optics assisted imaging with VLT/NACO (Figure 3.3). The physical connection between X-ray and infrared flares is still under study (Dodds-Eden et al., 2009; Mossoux et al., 2016; Boyce et al., 2019). The study of these flares and the physical processes underlying behind them opens a new path to understand the nature of SgrA* by itself.

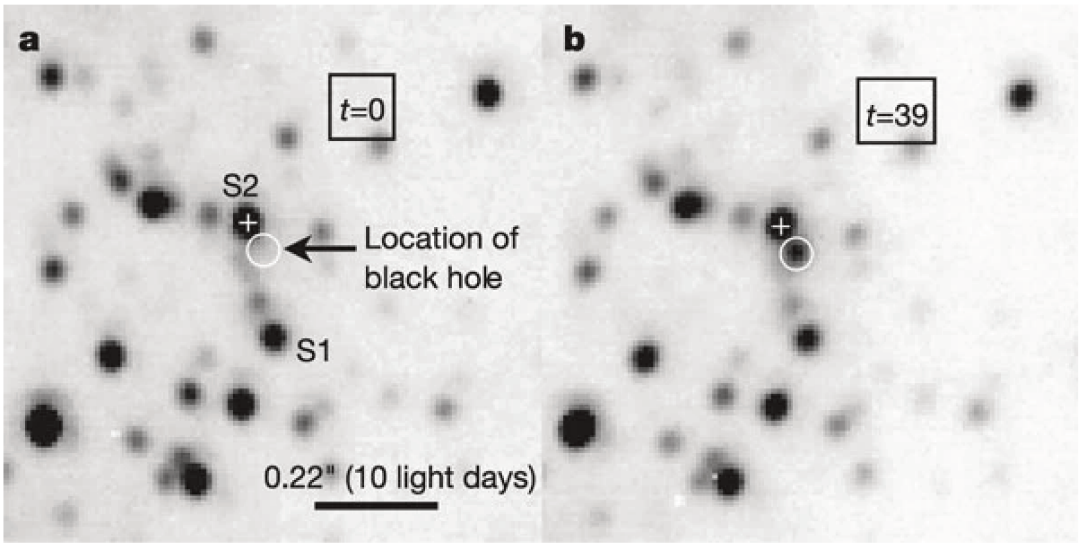

FIGURE 3.3: Two images of the Galactic Center obtained in May 2003. At t=0 there is no H band emission at the location of SgrA*. At t=39 minutes, the emission is nearly as bright as S2, coincident with SgrA* location at the very limited resolution of the image. This is a flare. Source: Genzel et al. (2003a).

Looking back to Figure 3.2 one can see the distribution of grey points around the origin of coordinates, consistent with the location of the radio source SgrA* within 10 mas. These points correspond to detections of K band emission observed with VLT/NACO corresponding to flares. The field of view seen by the science fiber of GRAVITY is 60 mas for the UTs and the highest astrometric accuracy the instrument is able to reach is 10 μas (Gravity Collaboration et al., 2017), which is lower than the expected angular size of 50 μas for the supermassive black hole shadow in the core of SgrA* (Vincent et al., 2016, Figures 2 and 3). By astrometry based on metrology, under optimal conditions GRAVITY is able to track the motion of the sources originating the flares.

3.2 Data

The data set considered for this thesis work comprises every single SgrA* and S2 data frame taken by GRAVITY during the epochs 2017 and 2018, with enough data to measure the relativistic effects at the pericenter. They correspond to the ESO IDs of 099.B-0162(A,B,C, D and E) for 2017 and the programs 0100.B-0731(A) and 0101.B-0576(A,B,C,D,E,F,G and H) for 2018. From all the observing runs, I have been actively part of the observer team during the runs of November 2017, April 2018, July 2018 and August 2018. For all the observations in this chapter, the baseline coverage involves the four UTs, whose spatial distribution is presented in Figure 3.4.

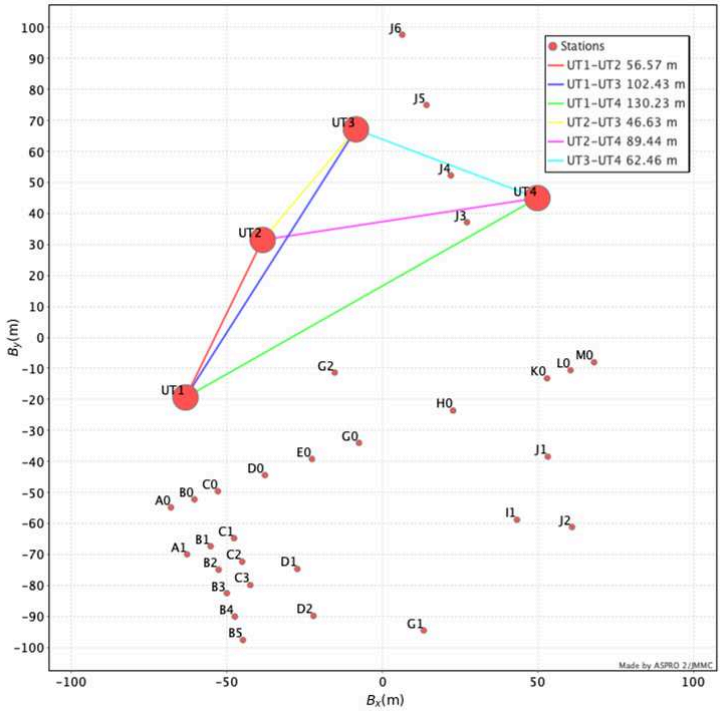

FIGURE 3.4: UT configuration of VLTI. The small red dots correspond to the available stations for the ATs, which are not used in this chapter. Source: JMMC/Aspro.

The dual field mode is selected for these observations, the fringe tracker source being used as a phase reference (Section 2.4.3). The requisites for fringe tracking in dual field (described in Section 2.3.1) are fulfilled due to the numerous bright stars in the field of view, from which IRS16C ($m_K = 9.83$, Blum, Sellgren, and Depoy, 1996) and IRS16NW ($m_K = 10.03$, Blum, Sellgren, and Depoy, 1996) are selected as fringe tracking stars. As the total amount of light is limited the observations are recorded at the LOW resolution mode, with the bandwidth sampled in 13 points. The bandwidth involved is $\Delta\lambda = 2.1 - 2.45\,\mu$m (the first channels of GRAVITY at $2 - 2.1\,\mu$m present in general a worse response and are contaminated by the back-scattering from the metrology laser). The observations make use of the Wollaston prism (SPLIT mode) as the polarimetric information gives information about the nature of the light coming from SgrA*[1].

[1]However, the polarimetric information is not considered in this thesis work. The two datasets are treated as independent measurements.

3.2.1 Observations

The GRAVITY instrument is designed and developed to take full advantage of the configuration of the Galactic Center. The observing process is delicate as the aim is to maximize the interferometric accuracy to reach the innermost regions. Several calibrations are needed for this purpose, as well as certain corrections on site. The nature of the high variability of SgrA* in the near infrared, with apparently random flaring events lasting no longer than three hours, makes crucial the presence of a team of astronomers in the VLTI room making quick decisions as the observing plan can totally change in case of occurrence of a flare. The full observing sequence is the following:

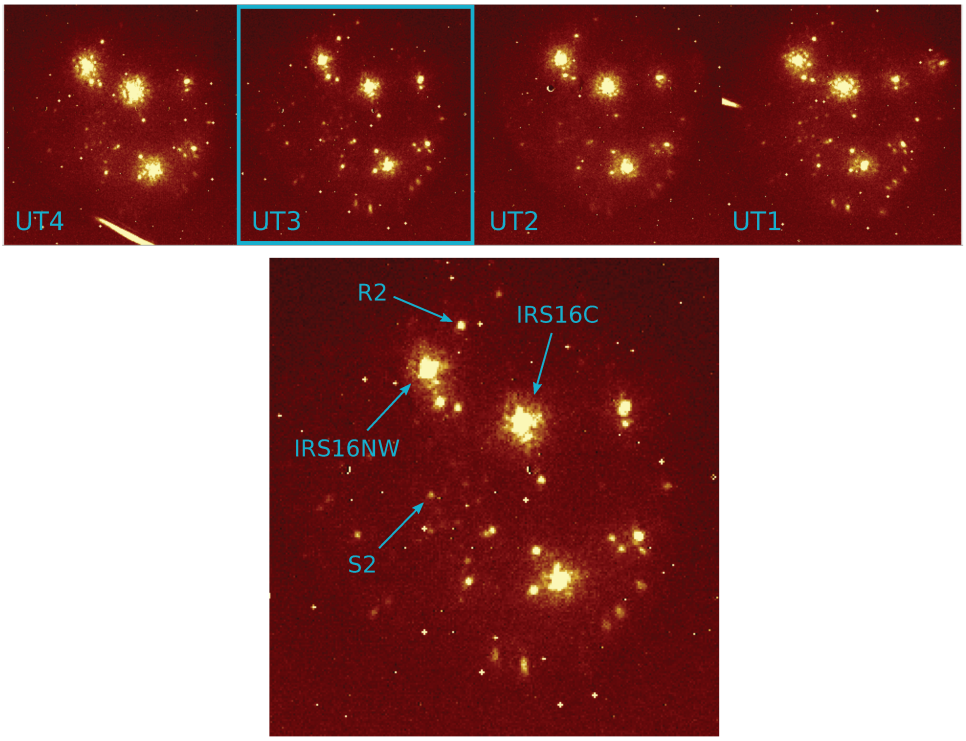

FIGURE 3.5: Example of the readout of the acquisition camera from a Galactic Center single data frame (one DIT). The relevant stars in this chapter are identified.

1. We point the four telescopes to the Galactic Center at the beginning of the observations by selecting any target in the central 2 arcseconds. The field of view observed by the acquisition camera is similar to the one presented in Figure 3.5. It is important to identify in the field the targets IRS16C and IRS16NW as they will be used for fringe tracking and phase referencing. Once they are identified, the field is centered between IRS16C and IRS16NW.

2. When the four telescopes are pointing to the Galactic Center, we need to select a target for wavefront sensing. This step is needed to maximize the Strehl ratio of the system, as the flux injected into the fibers used for interferometry is proportional to it, ultimately helping to find and stabilize the interferometric fringes. For that purpose the CIAO infrared wavefront sensor (Kendrew et al., 2012) is used in off-axis configuration. The loop is guaranteed to be closed if the seeing (at 500 nm) is better than 1.1" with a coherence time (at 500 nm) higher than 1.5 ms, the airmass is lower than 2, and if the target has $m_K \leq 10$

being located at least 4" away from the scientific target. In these conditions, the optimal target for wavefront sensing is GCIRS 7[2] (the brightest star in K band, see Chapter 4). The star is pointed in the field of view of CIAO and the correction is done individually on each telescope with the help of the MACAO deformable mirror. For the rest of the night, the telescopes will be tracking the same field, and the optical fibers of the instrument, with a smaller field of view, will be used to inject light on the instrument from the source of interest.

3. After applying adaptive optics the main optical aberrations due to the Earth atmosphere are corrected. The next step is the pupil alignment of the four beams to avoid vignetting. For this purpose GRAVITY takes advantage of IRIS (Gitton et al., 2004), located in the VLTI laboratory before the GRAVITY cryostat. This tilt sensor corrects the drift of the four beams coming from the telescopes simultaneously and requires to align individually each of the four pupils any time the telescopes points a new target. Despite the fact that the field of view of the individual telescopes is slightly larger, the resulting field of view after IRIS pupil alignment is 2" for the UTs (and 6" for the ATs).

4. The pupils are now aligned and the instrument is ready to integrate. The four aligned pupils and the field of view seen by the each telescope are recorded in the acquisition camera of GRAVITY, where they can be monitored in real time. Two targets have to be selected to feed the fringe tracker and the science fiber respectively, To achieve this, the 2" field-of-view is imaged on a fixed roof prism that splits the field in two halves and sends each half to one of the fiber couplers. The field is rotated to align the median line between the two sources on the edge of the roof and the fibers are moved to reach the separation between the two targets.

5. The targets are now feeding the fibers, but before starting any science integration, fringe tracking must be operational. This process is critical as long exposure integrations cannot reach optical coherence without it. The integration process can start when at least four of the six baselines[3] find and track the fringes (the reader may find a detailed description of the procedure in Lacour et al., 2019). The science frames (SCI) are obtained by exposures always taking five minutes with a number of subexposures NDIT = 30 of DIT = 10 s each. To remove the background sky emission, at least one sky frame (SKY) has to be taken for each science sequence, obtained by recording the same exposure time (NDIT = 30 of DIT = 10 s) in an empty region nearby, by applying a slight offset to the science fiber.

6. As the differential optical path delay projected in the sky between two separated targets has a non common instrumental component (Lippa et al., 2016), the first sequence of the night is devoted to determine the zero point of the metrology in order to cancel this component and be able to measure phases of visibilities. This is done by selecting a pair of bright stars in the field, in our case IRS16NW and IRS16C, and recording two sequences SCI-SKY-SCI by swapping the targets: we place first the fringe tracking fiber on IRS16NW and the science fiber on IRS16C, we record a sequence, we swap the fibers (fringe tracking fiber on IRS16C and the science fiber on IRS16NW) and we record another sequence. The correction is applied during the reduction process, where

[2]This is intentional: CIAO has been optimized to use GCIRS 7 for wavefront sensing.
[3]This guarantees that every telescope beam benefits from fringe tracking.

the subtraction of both optical path delays cancel all the common terms and allows to calibrate the zero point of the metrology. We make the assumption that this calibration is totally internal and remains the same independently of the targets observed. In order to improve its accuracy, this process has to be repeated at least once during the night, ideally after a long time span (half of the allocated time).

7. For the rest of the night and until this last calibration sequence is repeated, the fringe tracking fiber will remain unchanged on IRS16C. The science fiber now is placed on the calibrator star R2 (Figure 3.5) and a sequence is recorded as SKY-CAL (a sky offset is applied obtaining a new sky frame, then going back to R2, a calibrator exposure is recorded on it just before moving to S2). The purpose of this observation is to calibrate the phase center (and the visibilities of S2) as $\phi_0 = \phi_{S2} - \phi_{R2}$ (the details can be found in Section 2.4.5).

8. The science fiber is now placed on S2 and a sequence SCI-SKY-SCI is recorded. Right after, a blind offset is applied to the science fiber to the expected position of SgrA* by using the coordinates derived in Gillessen et al. (2017), and five exposures of SgrA* are then recorded (5 SCI). After them, a SKY frame is taken again by offsetting the SC fiber.

A sketch of the sequence since the fringes are found and tracked is shown in Figure 3.6. Steps 7 and 8 are usually repeated twice more with a total of 15 SgrA*, 3 SKY and 3 S2 frames. When finished, we start again from Step 6 until the night comes to an end. The steps presented in this section correspond to the standard sequence for observing SgrA* during the epochs of 2017 and 2018. However, the sequence can be modified depending on certain conditions such as:

- The weather forecast: A single complete sequence (S2 + 5 SgrA*) takes around 30 minutes. Depending on the number of frames previously recorded and their quality, it might be more convenient to focus on obtaining more frames of certain objects (specially SgrA*) before the weather gets worse and the observations become impossible.

- Flares: Any exceptionally bright state from SgrA* can be quickly identified in the data as the phase modulation becomes intense (see Section 3.4.5), even in raw data. As these events are transient and unpredictable, it is worthwhile to record the maximum amount of them, and therefore it might be needed to change the schedule in real time for this purpose. This is the reason why there is always one member of the team checking and validating the data output immediately after recording a frame.

- Polarimetry: In order to study the polarization state of the incoming light, an internal rotating half-wave plate located inside the beam combiner instrument can be configured to measure specific Stokes parameters. Several sequences have been recorded for this purpose during 2018, but their analysis is out of the scope of this thesis.

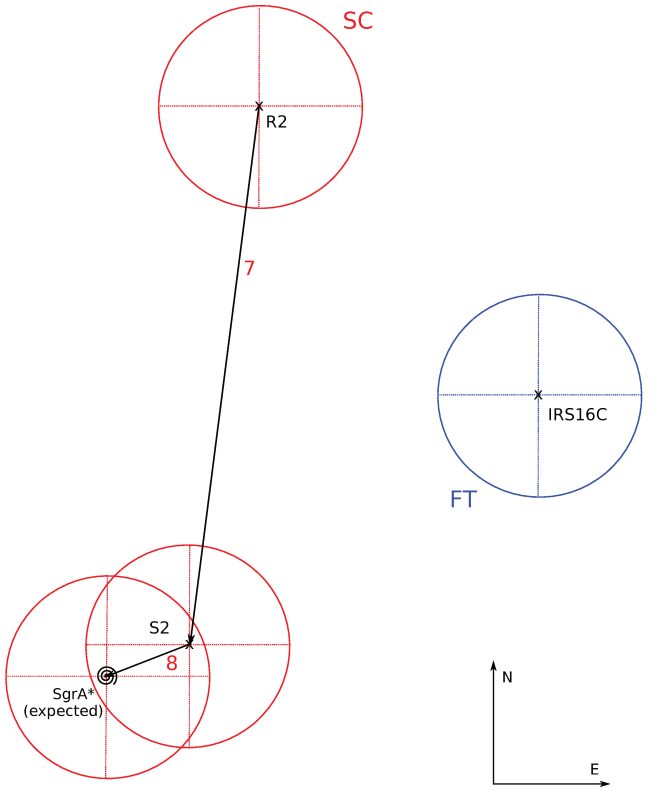

FIGURE 3.6: Sketch corresponding to Steps 7 and 8, from IRS16C to SgrA*. The distances are not at scale: the field of view of the fibers is two orders of magnitude smaller than the distance SC-FT.

3.2.2 Data reduction and visibility calibration

The total number of expositions on SgrA* considered for this chapter is 634 resulting in a total of 1268 measurements due to the SPLIT mode (one measurement per polarization P1 and P2 for each frame).

The computation of the calibrated visibilities from the data has been done by the use of the GRAVITY data reduction and calibration pipeline (Lapeyrere et al., 2014) whose details are introduced in Section 2.4. Each observing run involved in this chapter has the following set of auxiliary data frames:

- A DARK frame, with a NDIT of 79 and a DIT of 10 s.
- Four FLAT frames, one per telescope with a NDIT of 25 and a DIT of 300 ms.
- Two WAVE files (WAVE, WAVESC) with a NDIT of 512 and a DIT of 300 ms.
- Six P2VM files, one per baseline with a NDIT of 256 and a DIT of 300 ms.

A single SKY frame has been used to remove the background light from each sequence made of 1+5 SCI frames (a frame centered in S2 plus 5 frames centered in SgrA*) and it has been taken after the end of the sequence, with the same DIT, NDIT configurations as the SCI frames (DIT=10 s, NDIT=30). The calibrator used is the star R2 whose frames are taken in a sequence SKY-CAL recorded right before the S2 frames, also with the same DIT and NDIT (DIT=10 s, NDIT=30). All the frames of this work have been recorded in SPLIT mode and LOW resolution.

3.3 Model fitting

The GRAVITY outputs are the observables corresponding to the interferogram generated by the simultaneous observation of the target source with two telescopes (for each telescope pair). In other words, it samples the spatial frequency plane with visibility measurements in the Fourier space, corresponding to an unknown intensity distribution depending on the characteristics of the target. To solve the inverse problem of obtaining the on-sky light distribution of the astrophysical system starting from first principles, we use a model fitting approach. This procedure assumes certain intensity distribution as a prior to obtain a geometrical description of the sources present in the field of view of the instrument.

3.3.1 The field of view

Because of the way GRAVITY is designed (see Chapter 2), the interference happens in the field of view observed by the optical fibers who feed the science or fringe tracker beam combiner, respectively. The whole field observed by the telescopes is displayed in the acquisition camera (see Figure 3.5), where the target is selected manually by the observer to be pointed by the fibers. Following the observation schedule (Section 3.2.1), the position of the fiber is moved from the FT target to R2 and then to S2. After recording a frame on S2, a *blind* offset is applied by using the predicted separation between S2 and the central source according to Gillessen et al. (2017), and several frames centered on SgrA* are recorded. However, the real position of SgrA* with respect to the center of the fiber (and by extension to the phase center) is essentially unknown, not necessarily being exactly at the center. To illustrate this, a sketch of the field of view seen by the science fiber can be seen in Figure 3.7, assuming that there are only two bright sources in the field (SgrA* and S2).

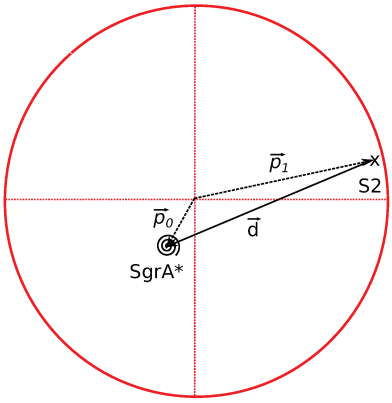

FIGURE 3.7: Sketch of the field of view seen by the science optical fiber (SC). The injection profile is Gaussian with a full width at half maximum of 60 mas.

In order to obtain an accurate astrometry of S2 and to understand the nature of SgrA*, the quantities of interest are:

- The separation S2-SgrA*. In Figure 3.7, $\mathbf{p_0} = (\alpha_0, \delta_0)$ and $\mathbf{p_1} = (\alpha_1, \delta_1)$. The separation between sources corresponds to $\mathbf{d} = (\mathrm{dx}, \mathrm{dy})$.
- The flux of SgrA*. This information is provided by the flux ratios.

Each optical fiber has a Gaussian profile with a full width at half maximum of 60 mas in the sky. As there are four telescopes, four is the number of optical fibers available. The centering of the fibers is done by pointing at S2, and then an offset is applied to arrive at the position of SgrA*. This implies that the centering of the four fibers might be different within a few mas[4]. This is specially important when S2 is far from SgrA* as seen in the field of view of the fibers, which implies that the star is recorded at at the outskirts of the fiber (Figure 3.7), where the gradient of the Gaussian profile is large. As a consequence, the response of every fiber might be different due to field aberration.

3.3.2 The Binary source model

Due to the characteristics of the inner 100 au and the features of GRAVITY, two sources are expected in the field of view corresponding to S2 and SgrA*. While the light observed from S2 is purely stellar, the emission from SgrA* when the source is not strongly flaring is assumed to be steady and close to the event horizon. The first approach involves two intensity distributions each given by a uniform disk of diameter d_i:

$$D_{d_i} = \begin{cases} 1 & \text{if } \sqrt{\alpha^2+\delta^2} \leq d_i/2 \\ \\ 0 & \text{otherwise,} \end{cases} \tag{3.1}$$

where α and δ are the sky coordinates with respect to the phase center, which is given by using the star R2 as a reference. In this picture, two sources with diameters d_0 and d_1 located at (α_0, δ_0) and (α_1, δ_1) respectively, I_0 and I_1 being the total intensities of each source and each target being described by the disk distribution D_{d_i}, the complex visibility of the system is, according to the van Cittert-Zernike theorem (van Cittert, 1934; Zernike, 1938):

$$V^{\mathrm{b}}(\lambda) = \frac{\int_\alpha \int_\delta \left[I_0 D_{d_0}(\alpha-\alpha_0, \delta-\delta_0) + I_1 D_{d_1}(\alpha-\alpha_1, \delta-\delta_1)\right] e^{[-2\pi i(u\alpha+v\delta)]} \mathrm{d}\alpha \mathrm{d}\delta}{\int_\alpha \int_\delta \left[I_0 D_{d_0}(\alpha-\alpha_0, \delta-\delta_0) + I_1 D_{d_1}(\alpha-\alpha_1, \delta-\delta_1)\right] \mathrm{d}\alpha \mathrm{d}\delta} \tag{3.2}$$

By defining $f_i(\lambda)$ as the relative flux of the source i over the total flux:

$$f_i(\lambda) = \frac{\int_\alpha \int_\delta I_i D_{d_i}(\alpha, \delta) \mathrm{d}\alpha \mathrm{d}\delta}{\int_\alpha \int_\delta \left[I_0 D_{d_0}(\alpha, \delta) + I_1 D_{d_1}(\alpha, \delta)\right] \mathrm{d}\alpha \mathrm{d}\delta} \,, \tag{3.3}$$

and considering V_{d_i} as the complex visibilities of a single disk[5] of diameter d_i, $J_1(x)$ being the Bessel function of the first kind:

$$V_d(\lambda) = \frac{2J_1(\pi\sqrt{u^2+v^2}d)}{\pi\sqrt{u^2+v^2}d} \,. \tag{3.4}$$

[4] This is solved in 2018: the instrument control software has been significantly improved and the metrology is now used to control the location of the four fibers in the sky.

[5] A further detail can be seen in Section 4.4.2, in the next chapter.

To simplify the explanations, let us consider that the source 0 is located exactly at the phase center. In such case, the expression 3.2 can be written as:

$$V^{\mathrm{b}}(\lambda) = f_0 V_{d_0}(u,v) + f_1 V_{d_1}(u,v) \exp\left[-2\pi i(u\alpha_1 + v\delta_1)\right] . \tag{3.5}$$

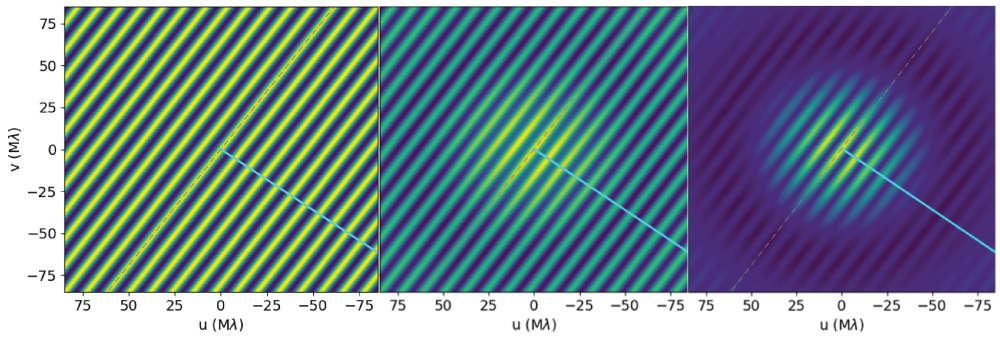

FIGURE 3.8: Interferograms corresponding to three different cases of Equation 3.5 with a central source and a second body around it. The flux ratio is fixed as the same for both and the position of the targets is the same in the three cases. The cyan line runs along the separation between the two sources always being perpendicular to the direction of the fringes. *Left*: two point sources. *Center*: a resolved uniform disk central source with a point-like second source orbiting around it. *Right*: two resolved uniform disks.

If the sensitivity of the interferometer during the exposure is enough to reveal the second source in the field of view, its presence will always introduce a modulation in the complex visibility, which determines the orientation of the pair. Figure 3.8 illustrates this feature, where the characteristic modulation of a binary system is present.

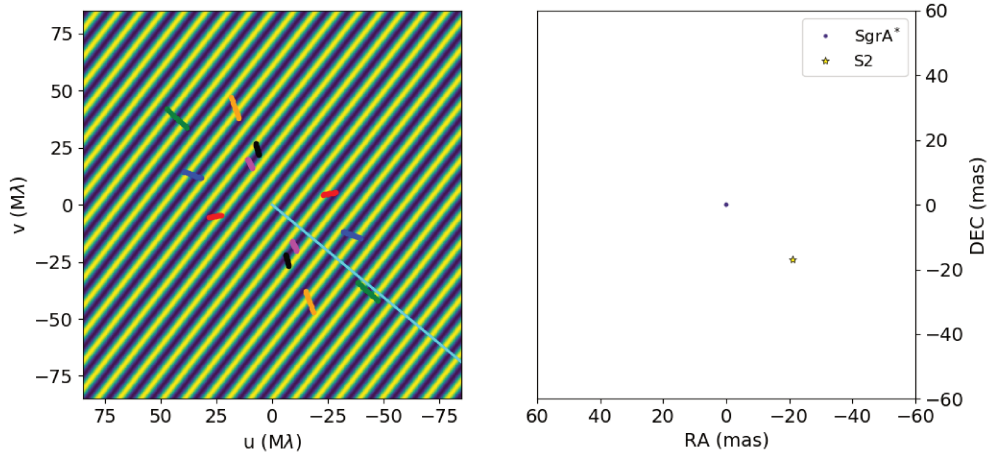

FIGURE 3.9: *Left:* interferogram given by Equation 3.5 corresponding to two point sources, with the VLTI coverage corresponding to the four UTs. Each colour traces one baseline considering the bandwidth of GRAVITY. *Right*: sketch of the model corresponding to that interferogram.

Unfortunately, the whole interferogram is not accessible, as the spatial frequency sampling is limited by the baseline configuration. An example is given in Figure 3.9, where the observables can be measured only for the regions of the spatial frequencies covered by the baselines. Due to the spectral bandwidth, at a given time each pair of telescopes sample a small radial line in the *uv plane* instead of a single point. Depending on the orientation of the binary and the baseline coverage involved, it might be not possible to determine unambiguously the physical parameters of the model (coordinates of each target or relative fluxes). Indeed, if the baseline configuration is perpendicular to the orbit vector, the model yields a maximum constant value of the visibility and null phase. Such configuration can easily lead to degeneracies as a same complex visibility could be reached by a different system such as a single disk with certain background light, as the phase information vanishes. This is the reason why at least two independent orientations are needed to be able to characterize a binary.

One could be tempted to fit each spectral channel individually by a different visibility curve, but this is wrong due to the fact that (u, v) depend directly on the wavelength and the study involves a finite bandwidth. Indeed, the interferometer measures a single value of the visibility per wavelength channel, taken as the average of the visibilities over the interval $(\lambda, \lambda + \mathrm{d}\lambda)$ (the width of the channel). Due to the fact that a change of λ leads to a radial displacement in the *uv plane*, the result is a radial smear leading to a visibility contrast attenuation, that could lead to wrong conclusions if not taken into account. The higher the spectral resolution, the lower is the smear effect, because of a better recording of the whole variation of the visibility over the interval. Unfortunately, due to the faintness of the targets, the intensity must be privileged over the spectral resolution, and the LOW resolution mode has been used to observe S2 and SgrA*.

This phenomenon is called bandwidth smearing and it is particularly remarkable when the second source is far from the center. Indeed, the exponential term of the Fourier transform intrinsically depends on the wavelength through the spatial frequencies (u, v). To correct this effect, it is needed to work with integrated quantities. In fact, to be more realistic, the input of GRAVITY is not a total intensity I. Indeed each pixel collects the specific intensity integrated over the bandwidth, and the interferogram expressed in specific intensity is nothing but:

$$I_\lambda = I_\lambda^0 \left[1 + \mathrm{Re}\left(V_\lambda e^{-i\frac{2\pi}{\lambda}s}\right)\right] \ , \tag{3.6}$$

where s is the optical path difference, V_λ is the specific complex visibility per wavelength unit and I_λ^0 a normalization parameter. The interferogram integrated over the bandwidth yields:

$$\langle I\rangle_{\Delta\lambda} = I^0 \left(1 + \left(\langle V\rangle_{\Delta\lambda}\right)\right) \ , \tag{3.7}$$

I^0 being:

$$I^0 = I_\lambda^0 \Delta\lambda$$

and $\langle V\rangle_{\Delta\lambda}$ being:

$$\langle V\rangle_{\Delta\lambda} = \frac{1}{\Delta\lambda}\mathrm{Re}\left[\int_{\Delta\lambda} V_\lambda e^{-i\frac{2\pi}{\lambda}s}\mathrm{d}\lambda\right] \ , (\lambda \in \Delta\lambda) \ .$$

If the optical path difference is fixed to $s = 0$ the integration over the bandwidth is equivalent to:

$$(I_\lambda, V_\lambda) \longrightarrow (\langle I\rangle_{\Delta\lambda}, \langle V\rangle_{\Delta\lambda}) \ ,$$

and then the normalized visibility integrated over bandwidth at $x = 0$ with I_λ as a function of wavelength can be obtained as:

$$\langle V\rangle^{\mathrm{N}}_{\Delta\lambda} = \frac{\int_{\Delta\lambda} V_\lambda \mathrm{d}\lambda}{\int_{\Delta\lambda} I_\lambda \mathrm{d}\lambda} \ . \tag{3.8}$$

While considering the effect of the bandwidth integration, a band pass around λ_0 (in our case a door function) must be introduced to take into account the spectral response of the fiber. Calling $B(\lambda)$ that band pass and wrapping up Equations 3.2, 3.4 and 3.8, the binary visibility yields:

$$\langle V^{\mathrm{b}}(u,v)\rangle_{\Delta\lambda} = \frac{\int_\lambda B(\lambda)\left\{I^{(0)}_\lambda \frac{2J_1(x_0)}{x_0} + I^{(1)}_\lambda \frac{2J_1(x_1)}{x_1} e^{-2\pi i(u\alpha_1+v\delta_1)} \frac{\int_\alpha\int_\delta D_{d_1}(\alpha,\delta)\mathrm{d}\alpha\mathrm{d}\delta}{\int_\alpha\int_\delta D_{d_0}(\alpha,\delta)\mathrm{d}\alpha\mathrm{d}\delta}\right\}\mathrm{d}\lambda}{\int_\lambda B(\lambda)\left\{I^{(0)}_\lambda + I^{(1)}_\lambda \frac{\int_\alpha\int_\delta D_{d_1}(\alpha,\delta)\mathrm{d}\alpha\mathrm{d}\delta}{\int_\alpha\int_\delta D_{d_0}(\alpha,\delta)\mathrm{d}\alpha\mathrm{d}\delta}\right\}\mathrm{d}\lambda} \ , \tag{3.9}$$

where x_i has been defined as $x_i = \pi\sqrt{u^2+v^2}d_i$, which intrinsically depends on λ through the spatial frequencies (u, v). In order to assign an intensity profile, it is well known that the star S2 emits as a black body in the Rayleigh-Jeans regime (at $T \approx$ 25000 K, Martins et al., 2008), which makes a power law the natural choice to describe its profile as its blackbody spectrum is already known. In addition, although SgrA* emits a mixture of thermal and non-thermal radiation (Yuan, Quataert, and Narayan, 2003), its profile in the GRAVITY band can be also well approximated by a power law, but with a different spectral index. Therefore, the intensity profile is defined for both sources as:

$$I^{(i)}_\lambda = I_i\left(\frac{\lambda_0}{\lambda}\right)^{k_i} \ , \tag{3.10}$$

where k_i will be treated as parameters to fit (discussed in the next section). The central source is of course SgrA* labelled with $i = 0$ and the star S2 with $i = 1$. As an absolute flux is not accessible via interferometry alone, it is convenient to define the flux ratios r_i as:

$$r_i = \frac{I_i}{I_{\mathrm{ref}}}\int_\alpha\int_\delta D_{d_i}(\alpha,\delta)\mathrm{d}\alpha\mathrm{d}\delta \ . \tag{3.11}$$

where I_{ref} is a arbitrary normalization constant that is fixed by choosing a reference for the fluxes. A priori the flux of SgrA* is highly variable with plenty of uncertainties

(Vincent et al., 2019, and references therein) as opposed to the stability of the flux of S2 which is already known (Martins et al., 2008). An interesting point about this parameter for the central source (r_0) is that it gives information about its brightness and therefore about the flares.

Writing Equation 3.9 in terms of Equations 3.11 and 3.10:

$$\langle V^{\mathrm{b}}(u,v)\rangle_{\Delta\lambda} = \frac{\int_\lambda B(\lambda)\left[r_0\left(\frac{\lambda_0}{\lambda}\right)^{k_0}\frac{2J_1(x_0)}{x_0} + r_1\left(\frac{\lambda_0}{\lambda}\right)^{k_1}\frac{2J_1(x_1)}{x_1}e^{-2\pi i(u\alpha_1+v\delta_1)}\right]\mathrm{d}\lambda}{\int_\lambda B(\lambda)\left[r_0\left(\frac{\lambda_0}{\lambda}\right)^{k_0} + r_1\left(\frac{\lambda_0}{\lambda}\right)^{k_1}\right]\mathrm{d}\lambda}. \tag{3.12}$$

In addition of the two sources, a diffuse background is considered accounting for all the remaining sources that could be present in the field of view. This background can be described by a uniform disk whose diameter extends towards infinite. As Equation 3.4 becomes 0 when $d \to \infty$, the background will not contribute for the numerator of the complex visibility. However, it has to be considered in the denominator as it contributes to the total flux with a quantity r_{bg} in the same way as Equation 3.11:

$$r_{\mathrm{bg}} = \frac{I_{\mathrm{bg}}}{I_{\mathrm{ref}}} \tag{3.13}$$

where I_{bg} is the intensity of the background[6]. As such background must be wavelength dependent[7], its spectrum has been modelled by a power law in a similar way than the other two sources with an index k_{bg}:

$$\langle V^{\mathrm{b}}(u,v)\rangle_{\Delta\lambda} = \frac{\int_\lambda B(\lambda)\left[r_0\left(\frac{\lambda_0}{\lambda}\right)^{k_0}\frac{2J_1(x_0)}{x_0} + r_1\left(\frac{\lambda_0}{\lambda}\right)^{k_1}\frac{2J_1(x_1)}{x_1}e^{-2\pi i(u\alpha_1+v\delta_1)}\right]\mathrm{d}\lambda}{\int_\lambda B(\lambda)\left[r_0\left(\frac{\lambda_0}{\lambda}\right)^{k_0} + r_1\left(\frac{\lambda_0}{\lambda}\right)^{k_1} + r_{\mathrm{bg}}\left(\frac{\lambda_0}{\lambda}\right)^{k_{\mathrm{bg}}}\right]\mathrm{d}\lambda}. \tag{3.14}$$

This is the visibility corresponding to a binary with the two sources resolved and one of them purely central. In the next section some considerations will be taken to adapt this model to the constraints of GRAVITY.

[6] Once the flux reference is fixed, the value of I_{ref} is the same for all the observables.

[7] Although it is possible to approach it as wavelength independent, this would mean three sources with spectral indices k_0, k_1 and $k_{\mathrm{bg}} = 0$, inherently implying a background much redder than the other two sources. This is not accurate as the background is likely to be produced by other fainter stars of the same kind as S2.

A binary observed by GRAVITY

To simplify the nomenclature, the parameter r_0 will be called now r_* and r_1 will be called now r_{S2}. According to the first observations with GRAVITY (Gravity Collaboration et al., 2017) the star S2 alone is an unresolved source by VLTI as the mean squared visibility is $V^2 = 0.96 \pm 0.07$ (indistinguishable from 1). Therefore, by observing with VLTI, the star S2 can be modelled as a point source. As Equation 3.4 tends towards 1 when $d \to 0$, the complex visibility is simplified removing the parameter d_1:

$$\langle V^{\mathrm{b}}(u,v)\rangle_{\Delta\lambda} = \frac{\int_\lambda B(\lambda)\left[r_*\left(\frac{\lambda_0}{\lambda}\right)^{k_0}\frac{2J_1(x_0)}{x_0} + r_{S2}\left(\frac{\lambda_0}{\lambda}\right)^{k_1} e^{[-2\pi i(u\alpha_1+v\delta_1)]}\right]\mathrm{d}\lambda}{\int_\lambda B(\lambda)\left[r_*\left(\frac{\lambda_0}{\lambda}\right)^{k_0} + r_{S2}\left(\frac{\lambda_0}{\lambda}\right)^{k_1} + r_{\mathrm{bg}}\left(\frac{\lambda_0}{\lambda}\right)^{k_{\mathrm{bg}}}\right]\mathrm{d}\lambda} \,. \quad (3.15)$$

The size of the beam that enters in the science fiber is 60 mas, while the separation of the pair S2-SgrA* for March 2017, the date where the observations start, can be estimated from Gillessen et al. (2017) to be 50 mas in RA. This implies that the target would be at the edge of the field of view, where each fiber is more sensitive to small differences relative to centering. To take into account these differences, an individual response per telescope is considered for the flux ratio r_{S2}. Therefore, following again Equation 3.11 and calling $(1, 2, 3, 4)$ the individual telescopes, there are four flux ratios r_j such as:

$$r_j = (r_{S2})_j = \left(\frac{I_{S2}}{I_{\mathrm{ref}}}\right)_j \quad (3.16)$$

which are nothing but the flux ratio of S2, as seen by the telescope $j = (1, 2, 3, 4)$. They can be also written as $r_j = r_{S2}t_j$ where t_j encloses the instrumental effects of each individual telescope. By fixing at least one of the j flux ratios to 1, the value of I_{ref} is determined: it is the value of the flux of S2 as it is measured by the telescope j. The rest of the quantities will be referred to that value.

The location of SgrA* has been measured with an accuracy of 170 μas with respect to the reference frame of the maser stars in the Galactic Center (Plewa et al., 2015). In the best scenario, GRAVITY would be able to determine the position of a source with respect to a phase reference with an accuracy of 10 μas. For this reason, although the central source is expected to be at the center of the field of view, it is convenient to consider a pair of coordinates (α_0, δ_0) with respect to the phase center to obtain a position for the central source. In this framework, the physical separation on sky of S2 with respect to SgrA* can be obtained by considering an offset dx and dy (Figure 3.7).

The final expression for the quantity $\langle V_{\rm bin}(u,v)\rangle_{\Delta\lambda}$ generalized for two targets located at (α_0,δ_0) and $(\alpha_0+\mathrm{d}x,\delta_0+\mathrm{d}y)$ related to the phase center and considering a pair of telescopes (j,k), yields $\langle V^{\rm b}_{jk}(u,v)\rangle_{\Delta\lambda}=\mathcal{N}_{jk}(u,v)/\mathcal{D}_{jk}$ with:

$$\mathcal{N}_{jk}(u,v)=r_*\int_\lambda B(\lambda)\left(\frac{\lambda_0}{\lambda}\right)^{k_0}\frac{2J_1(x_0)}{x_0}e^{-2\pi i(u\alpha_0+v\delta_0)}\mathrm{d}\lambda + \sqrt{r_j r_k}\int_\lambda B(\lambda)\left(\frac{\lambda_0}{\lambda}\right)^{k_1}e^{-2\pi i[u(\alpha_0+\mathrm{d}x)+v(\delta_0+\mathrm{d}y)]}\mathrm{d}\lambda \quad (3.17)$$

and:

$$\mathcal{D}_{jk}=\sqrt{r_*\int_\lambda B(\lambda)\left(\frac{\lambda_0}{\lambda}\right)^{k_0}\mathrm{d}\lambda+r_j\int_\lambda B(\lambda)\left(\frac{\lambda_0}{\lambda}\right)^{k_1}\mathrm{d}\lambda+r_{\rm bg}\int_\lambda B(\lambda)\left(\frac{\lambda_0}{\lambda}\right)^{k_{\rm bg}}\mathrm{d}\lambda} \times\sqrt{r_*\int_\lambda B(\lambda)\left(\frac{\lambda_0}{\lambda}\right)^{k_0}\mathrm{d}\lambda+r_k\int_\lambda B(\lambda)\left(\frac{\lambda_0}{\lambda}\right)^{k_1}\mathrm{d}\lambda+r_{\rm bg}\int_\lambda B(\lambda)\left(\frac{\lambda_0}{\lambda}\right)^{k_{\rm bg}}\mathrm{d}\lambda}\,. \quad (3.18)$$

With the wavelength reference taken as $\lambda_0=2.2\,\mu$m (near the center of the whole bandwidth) and a band pass $B(\lambda)$ taken as a Dirac on every wavelength channel, this is the central model which all the data analysis is based on. The model follows naturally the observing schedule obtaining the separation of the two sources by fitting the offset $(\mathrm{d}x,\mathrm{d}y)$ as well as estimating the flux of the central source.

3.3.3 Parameter estimation

The orbit of S2 has been previously studied for 25 years with the last update before GRAVITY published in Gillessen et al. (2017), with spectroscopy and adaptive optics assisted imaging. There is, indeed, an available model able to describe the orbit of S2 via keplerian orbit fitting. On the other side, the work which this thesis has contributed to involves for the first time an interferometric approach with the aim of maximizing the accuracy of the positioning of S2 with respect to SgrA*. Thanks to the astrometry based on metrology provided by GRAVITY, it is possible to reach an accuracy of a few ten μas (see Section 2.1.2).

With the diameter of the central source, the coordinates of both sources with respect to the phase center, the ratio between the flux of SgrA* and S2 seen by each telescope, the flux ratio of the background with respect to S2 and the spectral indices of both sources and the background, the binary model described in Equations 3.17 and 3.18 has in total 13 free parameters:

$$\{d_0,\ \alpha_0,\ \delta_0,\ \mathrm{dx},\ \mathrm{dy},\ r_*,\ r_1,\ r_2,\ r_3,\ r_4,\ r_{bg},\ k_0,\ k_1,\ k_{\mathrm{bg}}\}$$

Under certain assumptions, some parameters might be fixed to known values. Indeed:

- The star S2 is well studied and it is known to be a very stable point like source, unresolved with VLTI (Gravity Collaboration et al., 2017). It emits as a black body in the Rayleigh-Jeans regime, and therefore its color index can be fixed with a value of $k_1 = 4$.
- The background light is modelled as another black body. As its origin might come from other stars in the area, the spectral index is assumed to be equal to the one of S2. Therefore, the spectral index of the background is fixed also as $k_{\mathrm{bg}} = k_1 = 4$.
- To give any meaning to the flux ratios, at least one of the r_j has to be fixed, which acts as the reference flux. In this case, I have chosen $r_1 = 1$ and therefore I_{ref} is equal to the flux of S2 as seen by the telescope 1. All the flux ratios will be referred to that one.

While trying to find the solution for this model, two problems appear if a direct calculation via least squares fit is attempted. The first one is the high number of dimensions of the parameter space, which would be extremely expensive computationally speaking. The second one is the probable existence of multiple local minima. A different numerical approach is needed, which is presented and described below.

Markov Chain Monte Carlo

The culmination of 25 years of study of the orbit of S2 gave a very robust estimation of the position of that star with respect to the Galactic Center (Gillessen et al., 2017). For this reason the underlying idea of the fitting algorithm is the exploration of the surroundings of a certain first guess in the parameter space given by the expected position of the star S2 in the field of view. The algorithm implemented for this work to build the posterior probability distribution makes use of the python library *emcee* (Foreman-Mackey et al., 2013). Called the *stretch move* (Goodman and Weare, 2010), it makes use of elements called *walkers*: random discrete samples X_k such as the proposal distribution for any walker k depends on the current status of the other walkers and their evolution is simultaneous. This method is particularly efficient to explore the parameter space in all directions being barely sensitive to local minima.

The inputs of the method are a prior distribution for each parameter (an a priori probability distribution set by the user) plus a way to compute the likelihood of the data, given a certain parameter set. The output of the code is the distribution of the individual parameter sets which has the correct probability density.

From the Bayes theorem (Bayes, 1763), the posterior probability of certain parameter set Θ being true given a set of observations D is (Foreman-Mackey et al., 2013; Sharma, 2017):

$$p(\Theta, \alpha|D) \propto p(D|\Theta, \alpha) \times p(\Theta, \alpha) \tag{3.19}$$

with a marginalization equation as:

$$p(\Theta|D) = \int_{\alpha} p(\Theta, \alpha|D) d\alpha \tag{3.20}$$

where α represents the nuisance parameters (as the standard deviations from the mean values). Equation 3.19 can be explained as the product of the likelihood of the model $p(D|\Theta, \alpha)$ multiplied by certain prior $p(\Theta, \alpha)$. The likelihood function is chosen as:

$$\log[p(D|\Theta, \alpha)] = -\frac{1}{2} \sum_i \left[\frac{(\Theta_i - \langle\Theta\rangle)^2}{\alpha_i^2} + \log(2\pi\alpha_i^2) \right] \tag{3.21}$$

The expectation value of any parameter Θ in this approximation can be obtained as the average of the values obtained on each step i (Trotta, 2008):

$$\langle\Theta\rangle = \int p(\Theta|D)\Theta d\Theta \approx \frac{1}{M} \sum_i^{M-1} \Theta_i \ . \tag{3.22}$$

And the marginalized constraints on Θ are approximated by the histograms of the samples projected in the parameter subspace generated by Θ (Foreman-Mackey et al., 2013). The prior has to be carefully chosen by the observer taking into account initial information (informative prior) or certain degree of ignorance (uninformative prior). In this case, we have selected a weakly informative prior consisting in a uniform distribution around the expected position of S2 according to the orbital fit work of Gillessen et al. (2017).

For each frame is considered:

- For SgrA*:
  - A first guess for the diameter as $d_0 = 1$ mas, within an interval $(0, 10)$ mas.
  - A first guess for the flux ratio as $r_* = 0.1$, within an interval $(0, 100)$.
  - A first guess for the spectral index $k_0 = -2$. The interval explored is (-4,3). Such choices are justified as the index of the SgrA* spectrum depends on the intensity of the flux, being highly variable. Previous observations reveal an index of $\alpha \in (-1, 1)$ at high flux levels (higher than 5 mJy) while it is inconclusive at low levels as photometric observations show $\alpha = 0$ but spectroscopic observations yield $\alpha \in (-3, -1)$ (Genzel, Eisenhauer, and Gillessen, 2010, Figure 32).
  - SgrA* is expected to be in the center of the field of view. Therefore as a first guess $(\alpha_0, \delta_0) = (0, 0)$. The chosen interval is $(-20, 20)$ mas in both coordinates.
- For S2:
  - A first guess for the remaining flux ratios also as $r_j = 1$ under the assumption that they may be similar to each other. The interval selected is $(0, 100)$.
  - A first guess for the coordinates $(\mathrm{dx}, \mathrm{dy}) = (X_1(t), Y_1(t))$ where $X_1(t), Y_1(t)$ is the expected separation (in mas) of S2 with respect to SgrA* at the time t, according to the prediction from the orbit obtained in Gillessen et al. (2017). The selected intervals to explore are $(X_1(t) \pm 100, Y_1(t) \pm 100)$ mas, which guarantees that the whole field of view can be explored.
- For the background, an arbitrary first guess value of $r_{\mathrm{bg}} = 0.1$ is used, in an interval $(0, 10)$.

The complex visibility of the initial guess is built evaluating Equations 3.17 and 3.18 with these values and the ones of the fixed parameters (described in Section 3.3.3).

3.3.4 Approaching the pericenter passage

Up to 2017, the fibers are not well centered by a difference of about several mas on sky. This is due to a large extent to an anamorphic distortion of the field of view, which varies on the minute timescale due to the moving delay lines. A technical update called active fiber centering was implemented before the beginning of the observations in 2018. In this case, the SC fiber is recentered automatically by the measurement of the on-sky separation between FT and SC of the metrology signal, while the centering of the FT fiber is performed due to a permanently optimizing flux injection.

The observing runs carried out in 2018 involve a tracking of approximately one week per month from March to August (both included), and they benefit from active fiber centering. These runs were critical as the pericenter passage took place at the end of April 2018. In addition, in 2017 the position of S2 with respect to SgrA* is located at the edge of the field of view of the fibers, but this is not the case for 2018. As the distance S2-SgrA* is much shorter, the fibers observe both targets near the center of the field of view where the response of the four science fibers is the same (Figure 3.7),

now with the certainty that the four fibers point at the same place. A simplification of the parameter space is considered in 2018:

- The fits can be now performed by using only two flux ratios instead of five. For 2018, all the parameters $(r_1, r_2, r_3, r_4) = (1, 1, 1, 1)$. This implies to assume that all the fibers observe exactly the same field of view, which is justified due to an improved centering and due to the proximity between sources. The value of $I_{\rm ref}$ corresponds to the flux of S2 as seen by the system. The remaining flux ratios are r_* and $r_{\rm bg}$ which give a direct measurement of the intensity of SgrA* and the background respectively. Due to the fact that S2 is a well known source, this approximation allows to directly estimate the flux of SgrA*.
- Due to the fact that now all the fibers see the sources in the same surface being pointing at the same location of the sky (given by the offset), the model can be simplified assuming for SgrA* a source purely central and therefore $(\alpha_0, \delta_0) = (0, 0)$. The separation of S2 is still given by $(\mathrm{dx}, \mathrm{dy})$. The closure phases have been used for this epoch, which are only sensitive to the separation, and not to the individual positioning.

The final parameter space for the binary model for 2017 and 2018 respectively is summarized in Table 3.2. Thanks to the approach to the pericenter and active fiber centering, the model has been substantially simplified for 2018 with a total number of parameters of 5. With both targets near the center of the fibers where the collected flux is maximum, this dataset is now ready to explore the existence of any circular motions in the case of a bright flare, as sensitivity is expected to improve significantly.

Table 3.2: Parameter space considered for the binary fit.

	2017	2018
Fixed parameters		
From the central source	$d_0 = 0$	$d_0 = 0, (\alpha_0,\, \delta_0) = (0, 0)$
From S2 and background	$(k_1,\, k_{\rm bg}) = (4, 4)$	$(k_1,\, k_{\rm bg}) = (4, 4)$
Flux ratios	$r_1 = 1$	$(r_1,\, r_2,\, r_3,\, r_4) = (1, 1, 1, 1)$
Free parameters		
From the central source	$(\alpha_0,\, \delta_0)$, k_0	k_0
From the star S2	(dx, dy)	(dx, dy)
Flux ratios	r_*, $(r_2,\, r_3,\, r_4)$, r_{bg}	r_*, r_{bg}
Total free parameters	10	5

3.4 Model diagnostics

A previous study on the outcome of the model is needed before providing any results, to ensure their reliability. In this section the convergence and the choice of hyperparameters and observables is discussed. At the end of the section, the results of the first fits are shown and their quality is discussed.

3.4.1 Choice of observables

To obtain an adequate estimation of the source distribution on sky, the observables to fit should include a visibility amplitude estimator and a phase estimator. This implies the use of at least two interferometric observables (with information about the modulus and the phase of the visibility) with an input of 6 baselines. Although the pipeline of GRAVITY evaluates each estimator separately (see Section 2.4.4), they are not independent as they use the same input light. In an attempt to consider the correlations of each estimator involved in the analysis, their error bars have been weighted by a different value depending of the nature of the observable. For this work two different configurations have been used:

- $|V|, V^2$ and ϕ, used for 2017. As $|V|, V^2$ are correlated measurements, their errors have been weighted by $\sqrt{2}$.
- V^2 and $T3_\phi$, used for 2018. The error bars on the closure phase have been weighted by $\sqrt{4/3}$ due to the fact that each triplet is not independent from each other.

The closure phase provides a phase measurement unbiased from differential piston being sensitive to the target separation, and not to the phase reference (see Section 2.1.5). Although in principle its use must be prioritized instead of the visibility phase, this quantity was not used in 2017 as the correlations among the interferometer output were not fully implemented until the start of 2018. In an attempt to account for all the uncertainties corresponding to extra sources not taken into account by the model, the error bars on each parameters after the fit have been rescaled by the value of the reduced χ^2 as:

$$\sigma_R^{(x_i)} = \sigma^{(x_i)} \times \sqrt{\chi_r^2} \tag{3.23}$$

where $\sigma^{(x_i)}$ corresponds to the error bar of the parameter (x_i).

3.4.2 Convergence and choice of hyperparameters

To ensure confidence and meaning on the obtained values for each parameter, the convergence behaviour must be addressed before. For this purpose an option of the code gives the possibility to store the value of each step evaluation for each parameter of the sample. Then the normalized convergence of the parameter $\theta^{(i)}$ in the step t can be defined as:

$$NC(\theta^{(i)})_t = \frac{\theta_t^{(i)}}{\theta_*^{(i)}} \tag{3.24}$$

where $\theta_*^{(i)}$ is the value obtained in the last step. Such profile returns the distribution of each parameter after a MCMC sampling step by step. It is useful not only to verify the confidence in the final distribution of the parameters but also to study the minimum number of steps needed (in order to minimize computing time avoiding unnecessary steps) as well as to check if certain parameters must be redefined or fixed because of a poor sampling.

The other parameter of interest is the acceptance fraction. It is defined for each walker as the ratio of samples accepted over the total number of samples drawn (for that walker). This parameter is the key to understand if the drawn samples are representative. A value close to 0 would mean that none of the samples is accepted which implies that the actual samples drawn are far from the target density. On the other side, a value near 1 would mean that nearly all the random walks are accepted which is a signature of samples not representative of the target distribution. The optimal value oscillates between 0.2 and 0.5.

A first test was made treating the central source as a uniform disk with diameter $d_0 > 0$ in an attempt to verify if the emission of SgrA* is resolved by GRAVITY. A total number of 11 parameters were tested by measuring convergence (Equation 3.24) and the acceptance fraction, by using 2000 steps and 100 walkers. The results of the convergence test are presented in Figure 3.10.

The acceptance fraction obtained is optimal, with a value around $a_f = 0.39 \pm 0.02$. About the individual parameters, all of them converge properly before 1500 steps except the diameter d_0 and the color index of the central source k_0. About the spectral index k_0, unfortunately is a magnitude difficult to measure and fluctuating too much to be taken into account for the study. Therefore, although a value is given for every fit performed, it is not considered in this work.

Regarding the diameter of the central source, if the the central source would be resolved, this parameter would have converged quickly to a consistent value. It is finally discarded as a parameter, as it is taken as $d_0 = 0$. The central source is then described by a Dirac function.

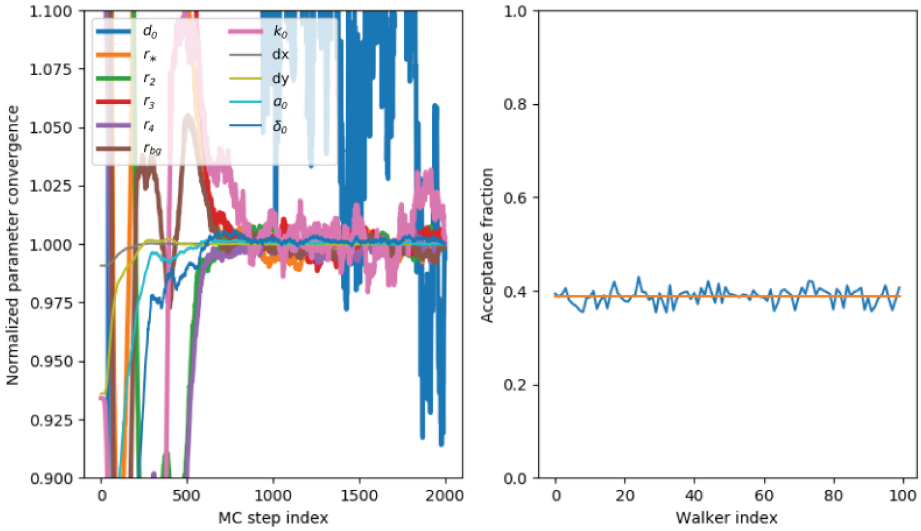

FIGURE 3.10: Analysis of convergence for a 2017 frame. The number of steps was fixed to 2000 and the number of walkers to 100.

The chosen hyperparameters for the model are the following:

- The number of steps for the walkers: According to Figure 3.10, a random distribution of the parameters is not reached until the step 1000. The code has an option called *burn-in*, accounting for a number of steps (the first steps) that will not be used to obtain the final distribution. For this case, a good sampling would be reached by the use of 2000 steps with a burn-in of 1000. After performing several tests (without fitting d_0), an adequate sampling has been reached for the rest of the fits in 2017 with 2000 steps and a burn-in of 500.
- The number of walkers for the stretch move: This parameter remains untouched as the choice of 100 walkers guarantees a good convergence and a reasonable acceptance fraction.

Each performed fit (from each frame) stores information about all the MC steps taken to build the final probability density function. The convergence diagnostics are used to evaluate the quality of each fit, and the one presented in Figure 3.10 corresponds to a single frame from 2017.

3.4.3 Fitting 2017 data

An example of a successful fit with good quality is presented in this section. It follows the standard fitting routine chosen for 2017 (fitting $|V|$, V^2 and ϕ with number of steps 1500, 100 walkers). The convergence plot of the fit is displayed in Figure 3.11. The spectral index of the central source does still not converge properly even after dropping d_0 as a parameter. Although it is fitted in every data frame, the spectral index of SgrA* is not reliable and it will not be used for the rest of the study. The acceptance fraction lies in the optimal interval ($0.2 < a < 0.5$) and therefore the model is performing properly, without the risk of accept or reject too many walker steps.

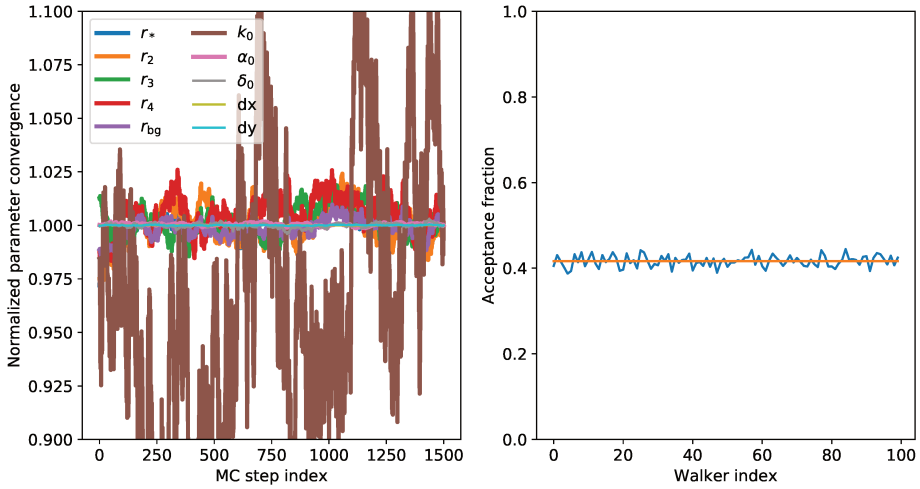

FIGURE 3.11: Convergence and walker acceptance fraction for a fit corresponding to a single data frame in 11-07-2017.

The result of the model fit corresponding to Figure 3.11 can be seen in Figure 3.12 where the three observables fitted, $|V|$, V^2 and ϕ are shown alongside with the uv coverage over the binary model resulting from that fit. The dirty map with the position of the fibers in the sky is also shown. The binarity signature is strong (oscillations in V^2 and drastic variations of the phase) which implies that both sources have been detected.

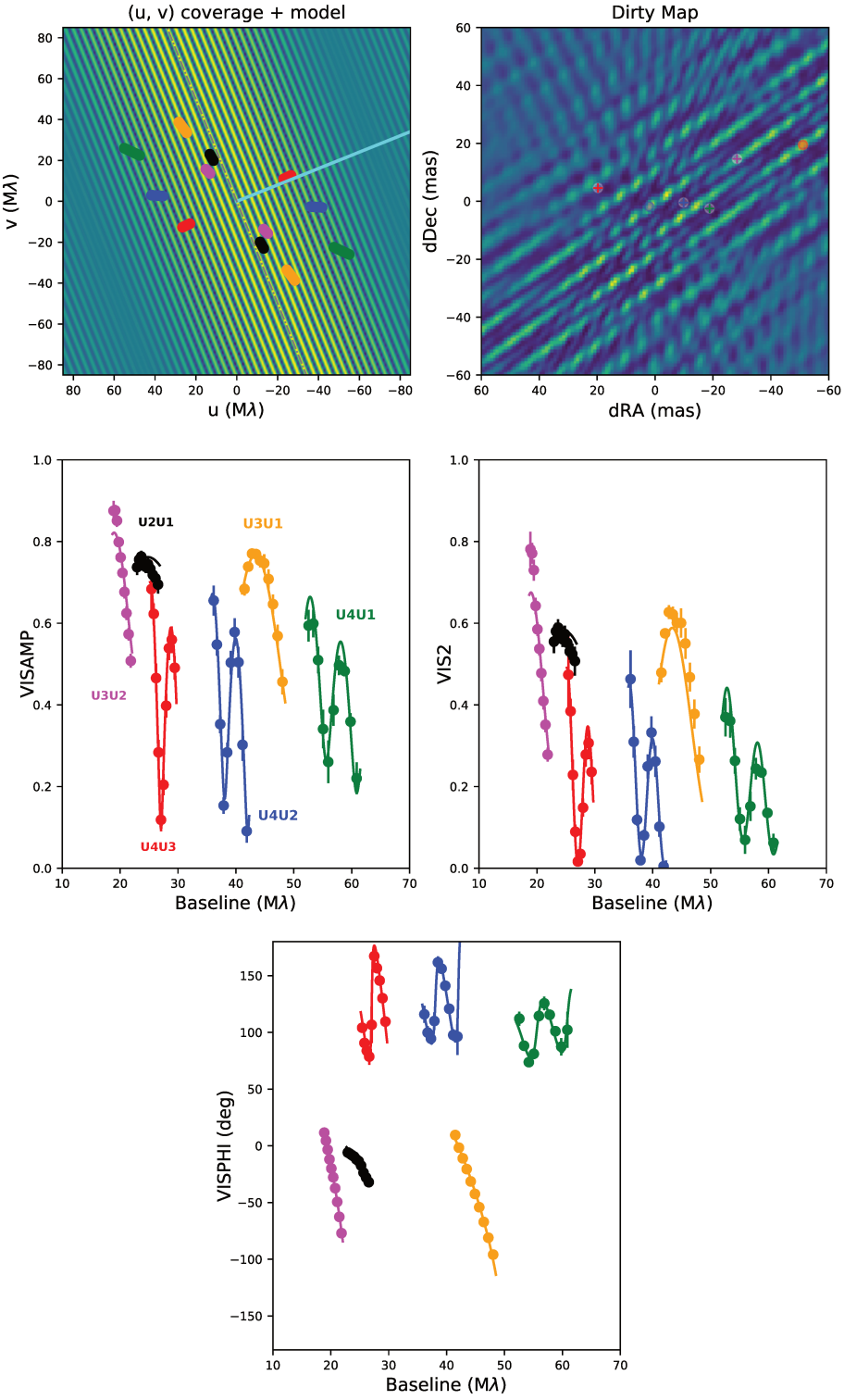

FIGURE 3.12: Example of a successful fit of the same data frame (Figure 3.11) corresponding to 11-07-2017. The blue line in the uv coverage traces the separation vector of the pair S2-SgrA* and each color corresponds to a baseline. The crosses in the dirty map correspond to the centers of the four fibers, the blue circle is the obtained location of SgrA* and the red circle the obtained location of S2.

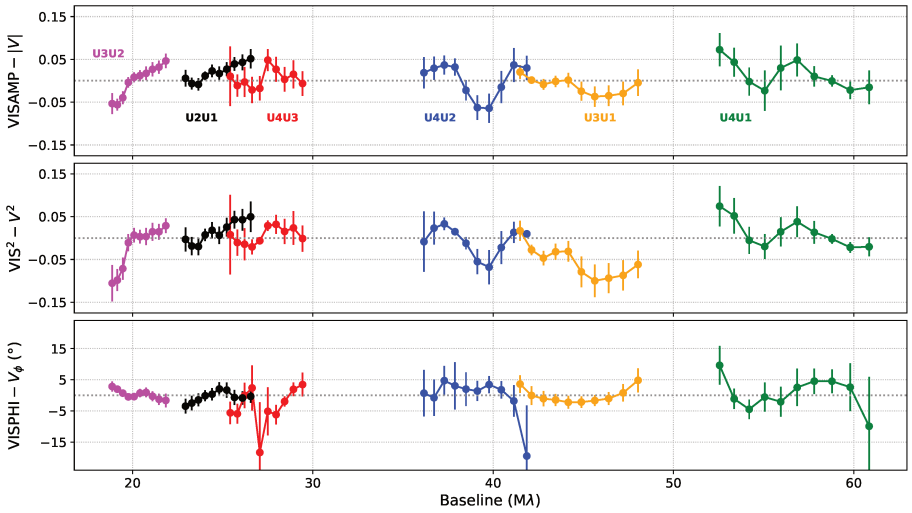

FIGURE 3.13: Residuals of the previous fit. The visibility phase is expressed in degrees.

Taking a look at the interferogram corresponding to the posterior model (upper left, Figure 3.12) it is straightforward to see the importance of the baseline coverage depending on the position of the two sources. The baseline perpendicular to the binary vector (U2U1) does not any present modulation signatures. Generally speaking, it is here where the model could present difficulties to fit the observables as there might be extra sources in the field (see Section 3.7). If the interferometer strictly sees two sources plus a background, the visibility measurements should trace a flat curve for those baselines.

In this case, the model detects two sources, and therefore it is expected that the central source has a higher flux ratio than the background. The total $\chi^2_r = 1.60$. The use of χ^2_r as a parameter to classify the quality of a fit is not prioritized in this work. However, as described in Section 3.4.1, their value is considered to rescale the error bars on each parameter.

The residuals of the fit are displayed in Figure 3.13 for the three observables, expressed by:

$$R(q) = Y - \bar{Y}(q) \tag{3.25}$$

where Y corresponds to the observations for each wavelength and baseline and $\bar{Y}(q)$ is the quantity predicted by the model at the spatial frequency q. The errorbars on the figure correspond to the uncertainties in the measurements (Figure 3.12). Overall, the residuals reveal a very good fit, although there are several channels deviating from the predicted value.

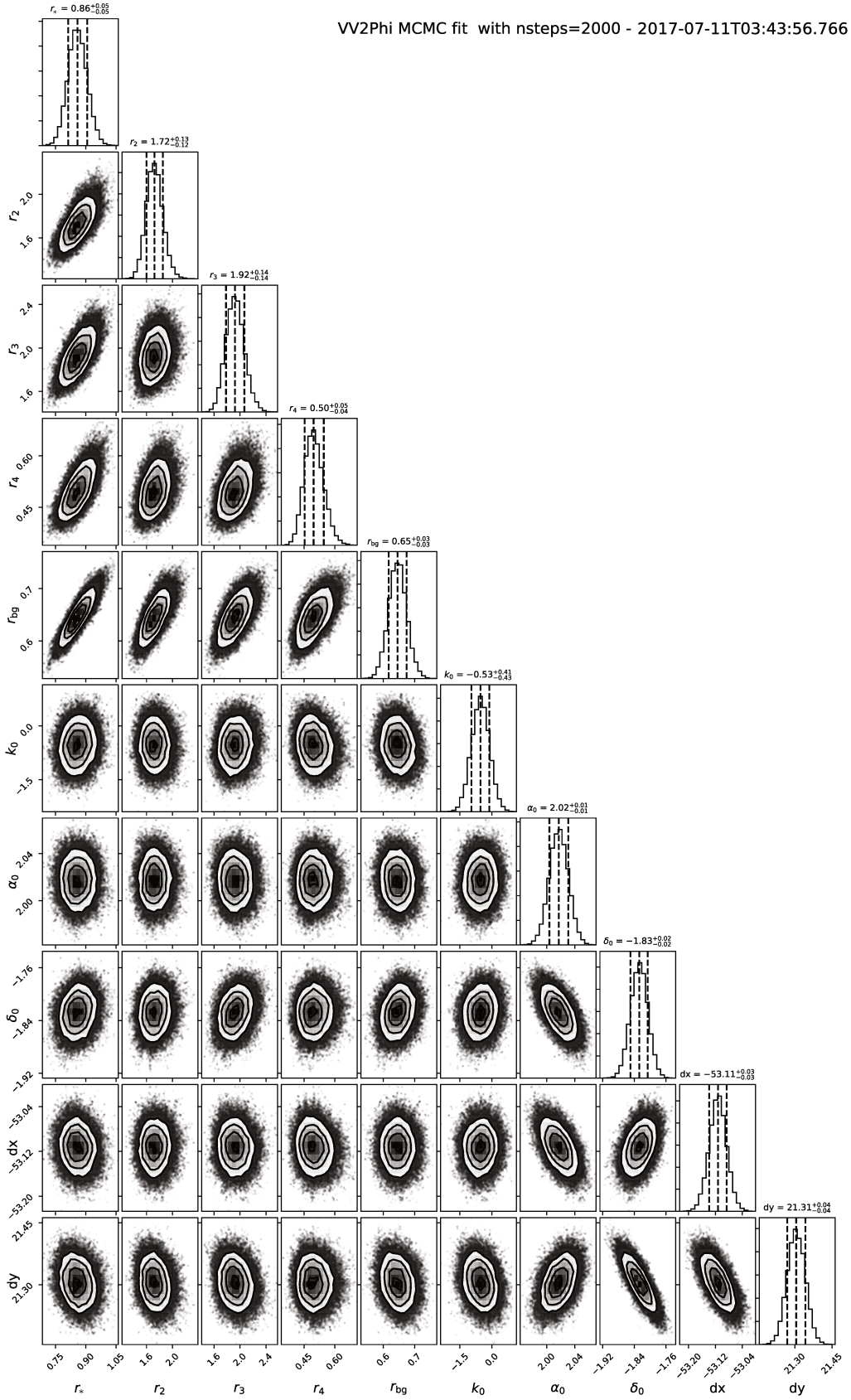

FIGURE 3.14: Corner plot displaying the 2D projection of the posterior probability distribution on over each pair or parameters fitted for the fit shown in Figure 3.12.

By using the python package *corner* (Foreman-Mackey, 2016), a graph is displayed presenting the 2D projection of the posterior probability distribution for each pair of parameters. It is presented in Figure 3.14. The values of each parameter are shown in the same figure together with their uncertainties (direct, non rescaled yet by χ^2_r). In 2017, the corner plot presents a slight correlation between parameters of the same nature:

- There is a correlation between all the flux ratios. This is expected as all of them are obtained with respect to a common reference, and therefore they share the same uncertainties.
- The correlation between α_0 and δ_0 is the interferometric lobe (the shape of the Point Spread Function). It is the same case for dx and dy.
- The correlation between dx and α_0 is due to a degeneracy: α_0 is the X coordinate of SgrA* with respect to the phase center and dx is the position of S2 with respect to SgrA*. It is the same for δ_0 and dy.
- The correlations between α_0 and dy is due to the combination of the interferometric lobe and the correlation between δ_0 with dy. It is the same for δ_0 and dx.
- The rest of the correlations are zero revealing a normal distribution.

TABLE 3.3: Model fit corresponding to 2017-07-11T03:43:56.766

Parameter	Fit ($\chi^2_r = 1.60$)
Flux ratio of the central source	$r_* = 0.86 \pm 0.06$
Flux ratios of S2	$r_2 = 1.72 \pm 0.16$
	$r_3 = 1.92 \pm 0.18$
	$r_4 = 0.50 \pm 0.06$
Flux ratio of the background	$r_{\rm bg} = 0.65 \pm 0.04$
Spectral index of the central source	$k_0 = -0.53 \pm 0.53$
RA of SgrA* from the phase center (mas)	$\alpha_0 = 2.017 \pm 0.017$
DEC of SgrA* from the phase center (mas)	$\delta_0 = -1.828 \pm 0.028$
RA of S2 from central source (mas)	dx $= -53.11 \pm 0.033$
DEC of S2 from the central source (mas)	dy $= 21.305 \pm 0.046$

The uncertainties on the coordinates obtained imply an astrometric accuracy of 46 μas. The results of the complete dataset and their interpretation are shown in Section 3.5.1, where the data analysis is explained in detail. Concerning the flux, the measurements of the flux of S2 given by the four telescopes present strong differences as a consequence of the large distance between the sources and the fact that the four fiber centers are positioned in different regions of the sky. Indeed, the light coming from the targets might be injected in different sections of the optical fiber where the transmission is lower than in the center. This tendency is present in all the 2017 data frames and vanishes in 2018 with active fiber centering.

3.4.4 Fitting 2018 data

This epoch is critical for the study of SgrA*, as it is the one of the whole orbit where the two targets are easier to be observed, because of their proximity. In addition, it is the location of the orbit where the gravitational potential is higher and therefore where S2 reaches the maximum orbital velocity. In general, the quality of the fits in 2018 have substantially improved while comparing them to the ones in 2017. This result is expected as the distance between sources is shorter and fiber active centering is implemented. As a counterpart, it is expected that the size of the fringes will increase as the two targets are now closer to each other. As the wavelength coverage is the same, this implies that the visibility curves will present smoother variations, in contrast to 2017 where the visibility phases or squared visibilities could easily present two minima.

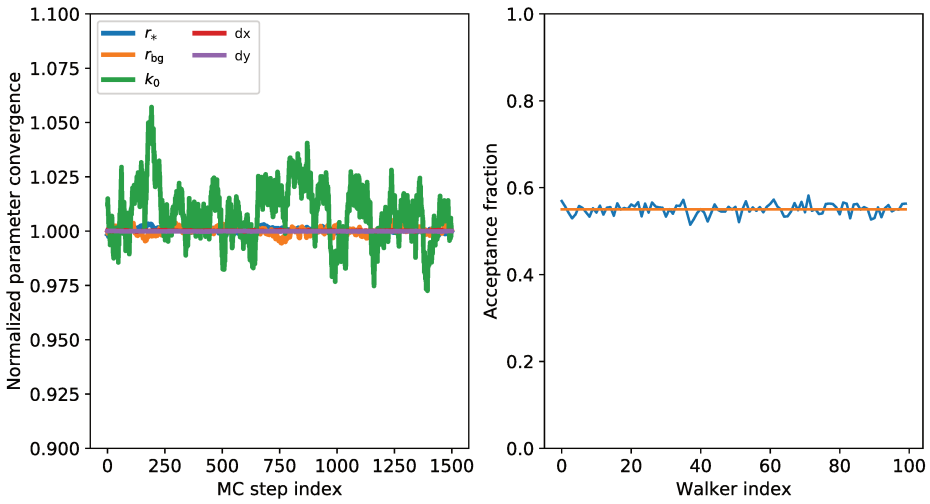

FIGURE 3.15: Convergence and walker acceptance fraction for a fit corresponding to a single data frame in 05-05-2018.

In a similar way than in 2017, an example of a successful fit with good quality for 2018 is presented in this section. It follows the standard fitting routine chosen for 2018 (fitting V^2 and $T3_\phi$ with number of steps 1500[8], 100 walkers, burn-in 500). The convergence and the acceptance fraction of the fit are displayed in Figure 3.15. The acceptance fraction is slightly over the optimal interval ($0.2 < a < 0.5$) with $a = 0.55$ but is still reasonable. This means that around 55% of the walkers steps are accepted. The convergence is quickly reached, except for the spectral index k_0 which is still not reliable.

[8] After several tests, we found out that this number was enough to guarantee an adequate sampling.

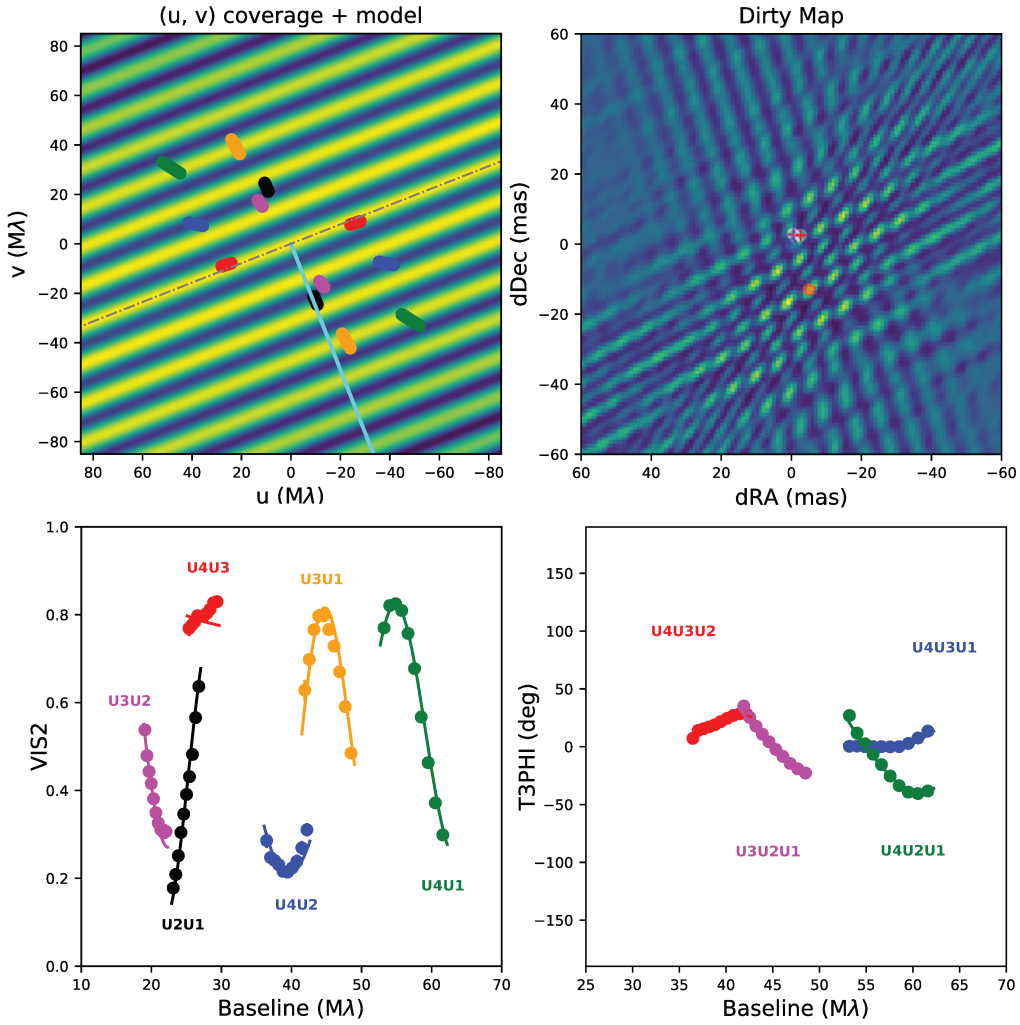

FIGURE 3.16: Example of a successful fit of a single data frame corresponding to 05-05-2018. The cyan line in the uv coverage traces the separation vector of the pair S2-SgrA* and each other color corresponds to a baseline or a triplet respectively. The crosses in the dirty map correspond to the centers of the four fibers, the blue circle is the obtained location of SgrA* and the red circle the obtained location of S2.

The posterior model is shown in Figure 3.16. The frame presented in this section corresponds to another bright state of SgrA* right after the pericenter passage. It is straightforward to see how the fiber alignment has improved since 2017 (in the dirty map, upper right). The background is low (around 10%) as the squared visibility reaches a maximum value over 0.8. As expected, the closure phase does not present strong variations if we compare, for example, with the visibility phase registered in Figure 3.12.

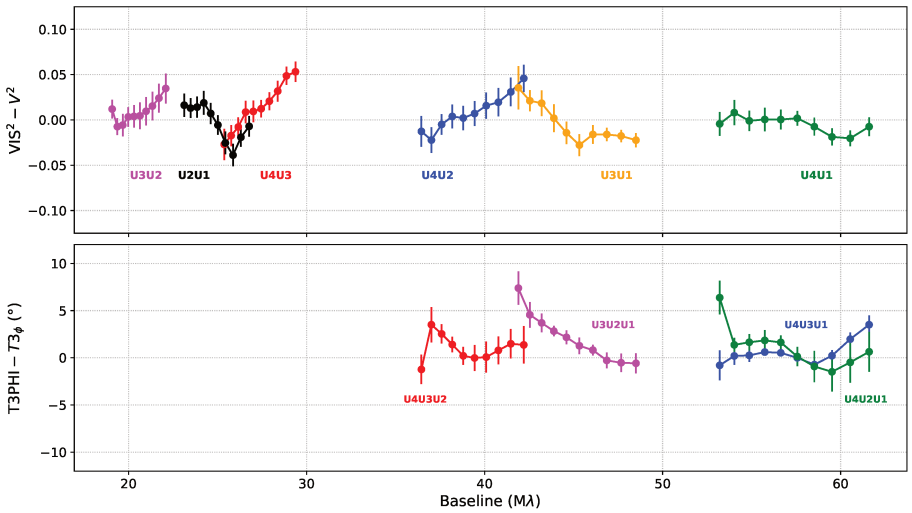

FIGURE 3.17: Residuals of the previous fit. The closure phase is expressed in degrees.

The residuals of the fit are displayed in Figure 3.17 for the two observables fitted in the same manner as the fit from 2017. The value of $\chi^2_r = 3.33$, which is slightly high (for this case) due mainly to the contribution of bad fits of the squared visibility for the U4U3 baseline (red), which is perpendicular to the binary vector. The rest of the baselines and triplets present reasonable fits.

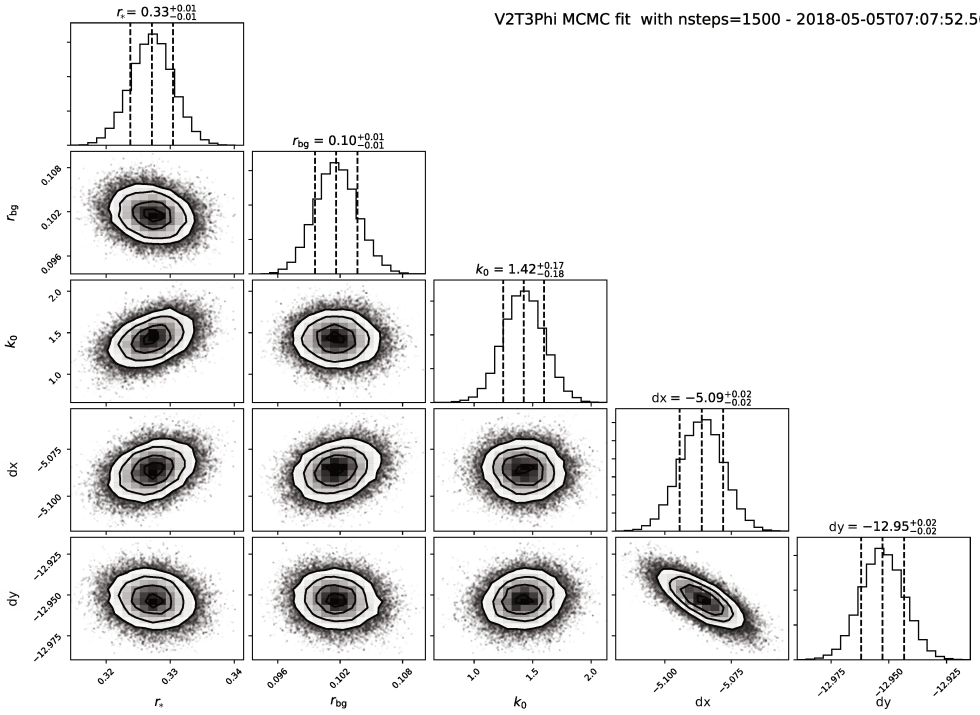

FIGURE 3.18: Corner plot displaying the 2D projection of the posterior probability distribution on over each pair or parameters fitted for a good quality fit from a data frame in 05-05-2018.

The corner plot corresponding to this specific fit is shown in Figure 3.18. The correlation between dx and dy appears again, a trend that is also observed in the corner plot corresponding to the fit in 2017 (Figure 3.14). This correlation corresponds to the shape of the point spread function of the interferometer and is related to the *uv* sampling. In the case of the two flux ratios used in the fit, strictly speaking they are still correlated due to the total flux used as a reference. However, thanks to a much better fiber pointing their individual uncertainties are much lower so they appear uncorrelated. The rest of the parameters can be considered uncorrelated revealing a Gaussian distribution.

The resulting parameters of this fit are presented in Table 3.4, where the obtained error bars (Figure 3.18) have been rescaled by $\chi^2_r = 3.33$ following Equation 3.23. The background is relatively low and the central source is clearly detected over the background.

TABLE 3.4: Model fit corresponding to 2018-05-05T07:07:52.569

Parameter	Fit ($\chi^2_r = 3.33$)
Flux ratio of the central source	$r_* = 0.33 \pm 0.01$
Flux ratio of the background	$r_{\rm bg} = 0.10 \pm 0.01$
Spectral index of the central source	$k_0 = 1.42 \pm 0.32$
RA of S2 from the central source (mas)	dx $= -5.086 \pm 0.015$
DEC of S2 from the central source (mas)	dy $= -12.953 \pm 0.017$

3.4.5 Bright and quiescent SgrA*

The accuracy of the binary model at measuring the astrometry of the star S2 relies in the feasibility of detecting two sources simultaneously[9]. As the emission of S2 is steady, the success of the model depends mainly in the capability of the interferometer to find SgrA*, an issue that depends strongly on the brightness of this source. The features of the flaring emission of SgrA* in the near infrared have been classified in Dodds-Eden et al. (2011) as quiescent or bright depending on the flux of the source (a flaring state is said to happen if the flux is higher than 5 mJy and quiescent emission if its lower). In this work three cases are used depending on the interferometric output, the two first corresponding to the quiescent state in literature:

- Quiescent-faint SgrA*: The phase signal is nearly flat, being zero or close to zero. The visibility modulus is typically high ($V^2 > 0.5$). It corresponds to a state where SgrA* is barely detected, sometimes lower than the background emission. These fits do not present generally an optimal fitting quality due to the fact that SgrA* is not or barely detected.
- Quiescent-moderate SgrA*: The phase signal present certain curvature with variations of more than 10°. The visibility modulus presents an evident curvature but its values are not too low ($V^2 > 0.2$). It corresponds to a case comparable to faint SgrA* but showing a clear phase signal, proving that the central source is detected over the background emission but it is still faint comparing with S2 ($r_* \leq 0.3$). It is the most frequent case for both 2017 and 2018 datasets, their fitting quality being much better in 2018 than in 2017 due to fiber active centering.
- Flare: The phase signal present strong variations of more than 50°. The visibility modulus presents strong modulations ($\Delta V^2 \gtrsim 0.5$ from maximum to minimum). It corresponds to a state where SgrA* is certainly detected and its brightness ($r_* \gtrsim 0.3$) can be even comparable to S2. They typically correspond to flaring states of SgrA* presenting the highest accuracy due to the fact that the contribution of the background is low ($r_{\rm bg} < 0.2$) and the model finds two distinct sources. These states are random and not too frequent, but they provide the best measurements and the most relevant information about the nature of SgrA*.

To illustrate this sorting criterion, an example for each of the three cases is shown in Figure 3.19 during a flare registered in April 2018. They correspond to a time sequence of a quiescent-faint state, a flare state, and a quiescent-moderate state. The total time span of these sample (not necessarily the whole flare) is 45 minutes. The residuals of the fits are shown in Figure 3.20 following the same scheme than in Figures 3.13 and 3.17. The quality factor Q shown in the figures is explained in the next section.

In general, the fit of the squared visibilities is better for the bright and quiescent-moderate states. The fit of the closure phases, however, becomes more complicated in the bright states.

[9] Assuming, of course, that both sources are located inside the field of view, as it is during 2017 and 2018, but not in future epochs.

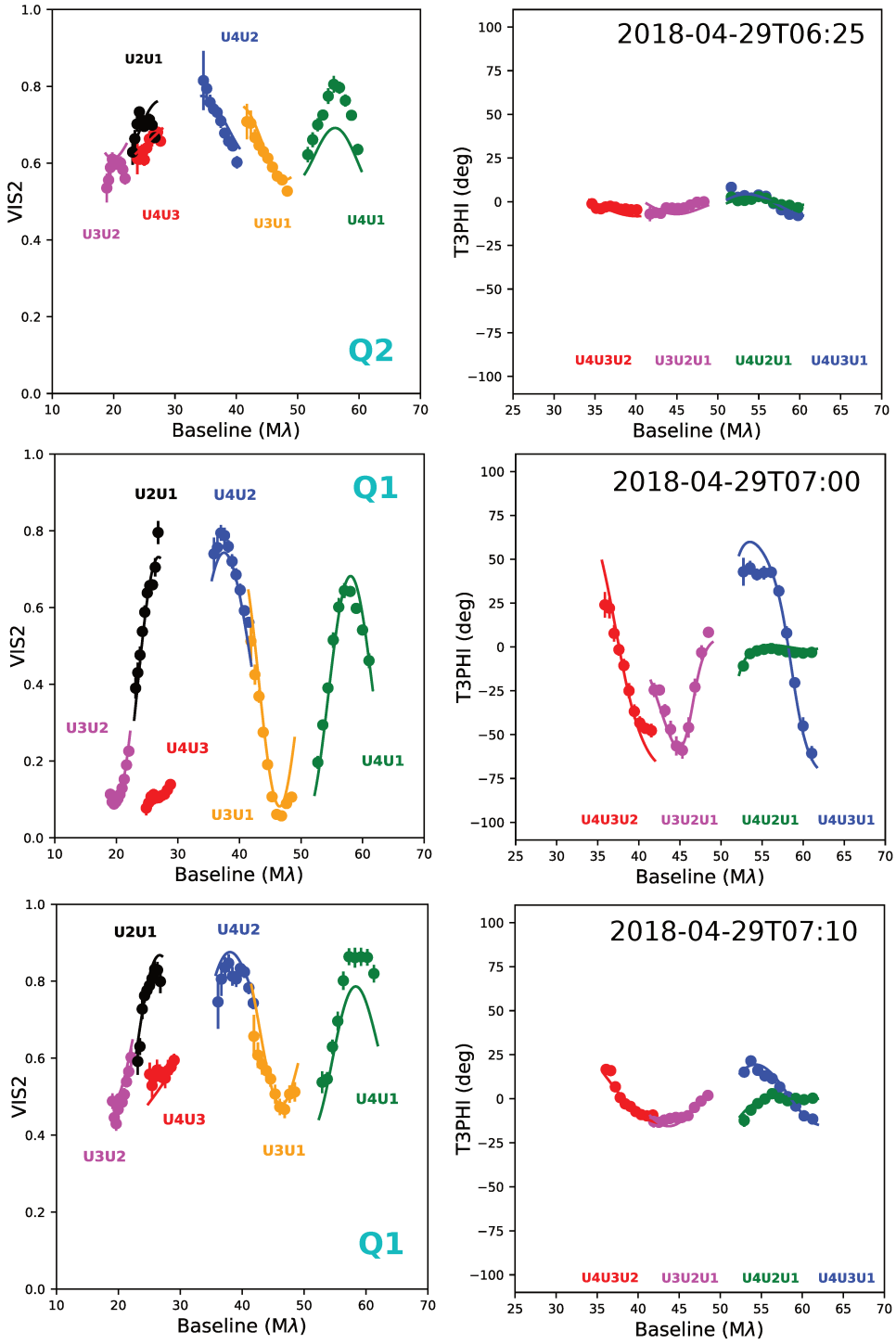

FIGURE 3.19: Three different states of SgrA* observed during a model fit in a single night, corresponding to 29-04-2018: quiescent-faint state, bright state, quiescent-moderate state respectively.

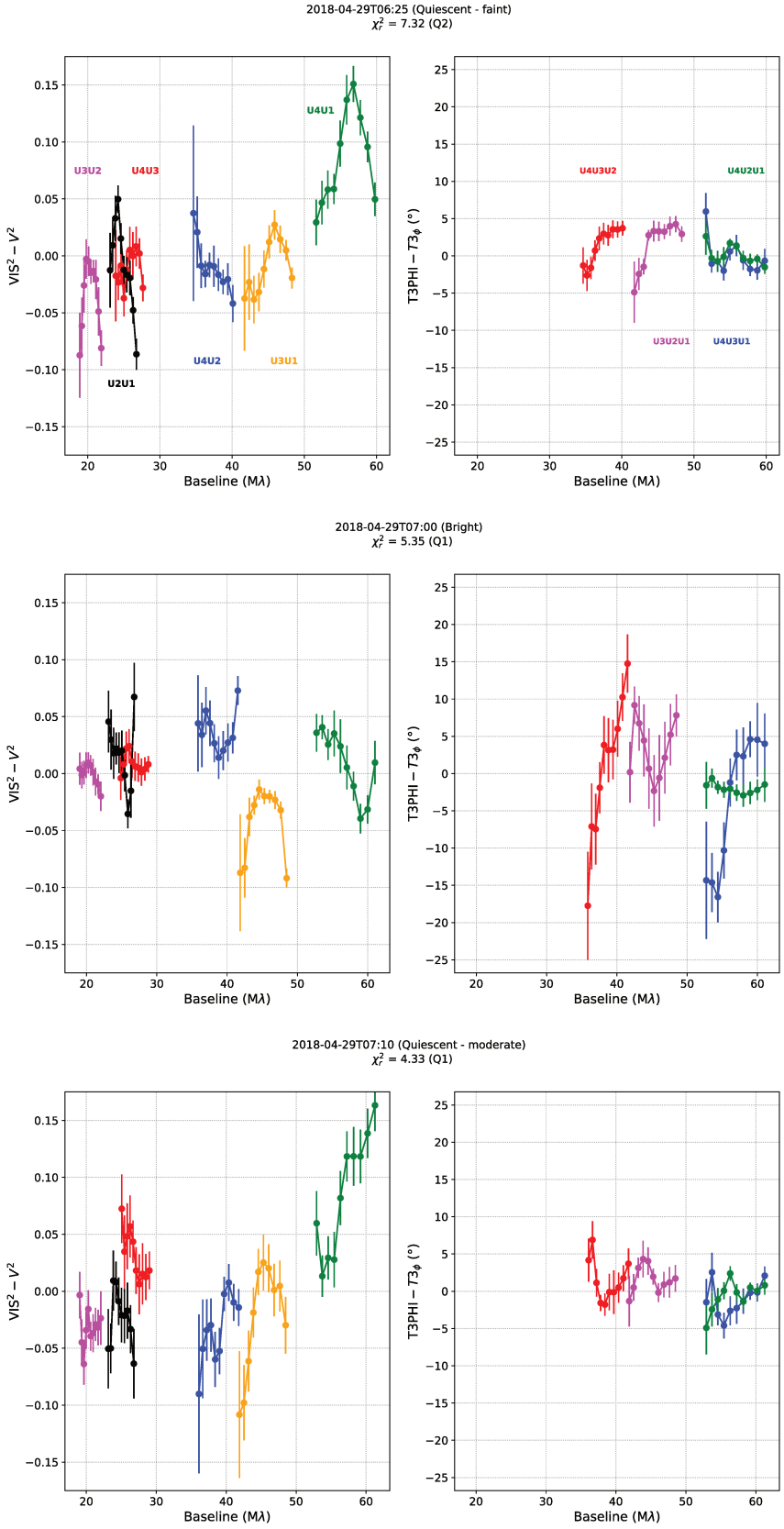

FIGURE 3.20: Residuals of the previous fits.

3.4.6 Assessing the quality of the fits

Multiple effects can make difficult to obtain an adequate fit to each data frame. They can be external factors such as the atmosphere, which can reduce the collected light by the instrument or add external noise to the data, instrumental effects such as pointing problems, difficulties to find and track fringes or a wrong fiber centering, natural effects as the dimming of the central source while the integration is taking place or even the fact that the chosen model is perhaps too simple to describe what the interferometer is observing in the field of view. Most of these effects are impossible to overcome, becoming reflected in the data products.

In order to classify the quality of the resulting fits, a criterion is established and a quality flag of 1, 2 or 3 is assigned to each data fit, given by visually checking every frame. This factor is completely qualitative and it has not been used other than for discriminating those fits with problems and selecting the ones who reproduce better our data. In an attempt to reduce the human bias, the quality factors have been given to each data frame not taking into account any final values of the parameters. The criterion is defined as:

- Quality 1: the posterior model follows the trend of the data in at least 5 baselines. All the fibers observe both targets in their field of view. This case is typically guaranteed during a flare, but it is not so common for frames where SgrA* is faint. During 2018 and thanks to the technical improvements, most of the cases with a quiescent-moderate SgrA* present optimal features and they have been classified as 1 too. Two examples can be seen in Figure 3.19 and 3.20 (labelled with Q1) or Figures 3.12 and 3.16.
- Quality 2: the posterior model is not excellent but it has the expected shape (the binarity is observed in case of quiescent SgrA* or visibilities are flat in case of faint SgrA*) and the fiber centering is optimal (all the fibers observe both targets). This qualifier has been given to data frames where typically at least four baselines are well fitted. Sometimes certain baselines have problems to fit a model as they are aligned towards a direction of the interferogram which does not present any phase variation. This case is common in those data frames presenting a quiescent SgrA*. An example is shown in Figure 3.19 and 3.20 (labelled with Q2).
- Quality 3: Either some fibers do not fully see the pair S2-SgrA* or the model fails to reproduce the data, or the data frame presents calibration problems. These frames are always discarded for the study.

The two polarizations in the data frames recorded in SPLIT mode have been treated separately as two independent data sets. For estimation of the astrometry of S2, the frames with a quality factor 1 and 2 are used. An example of a binary fit for a whole night (28th July 2018) is presented in Figure 3.21, with 23 data frames in total. The results of the flux ratios and coordinates of S2 are shown, each point corresponding to an individual binary fit. The bright state of SgrA* clearly contributes to a much better accuracy and quality of the fits. While giving a best estimate per night, the weighted average has been considered independently of the given quality factor.

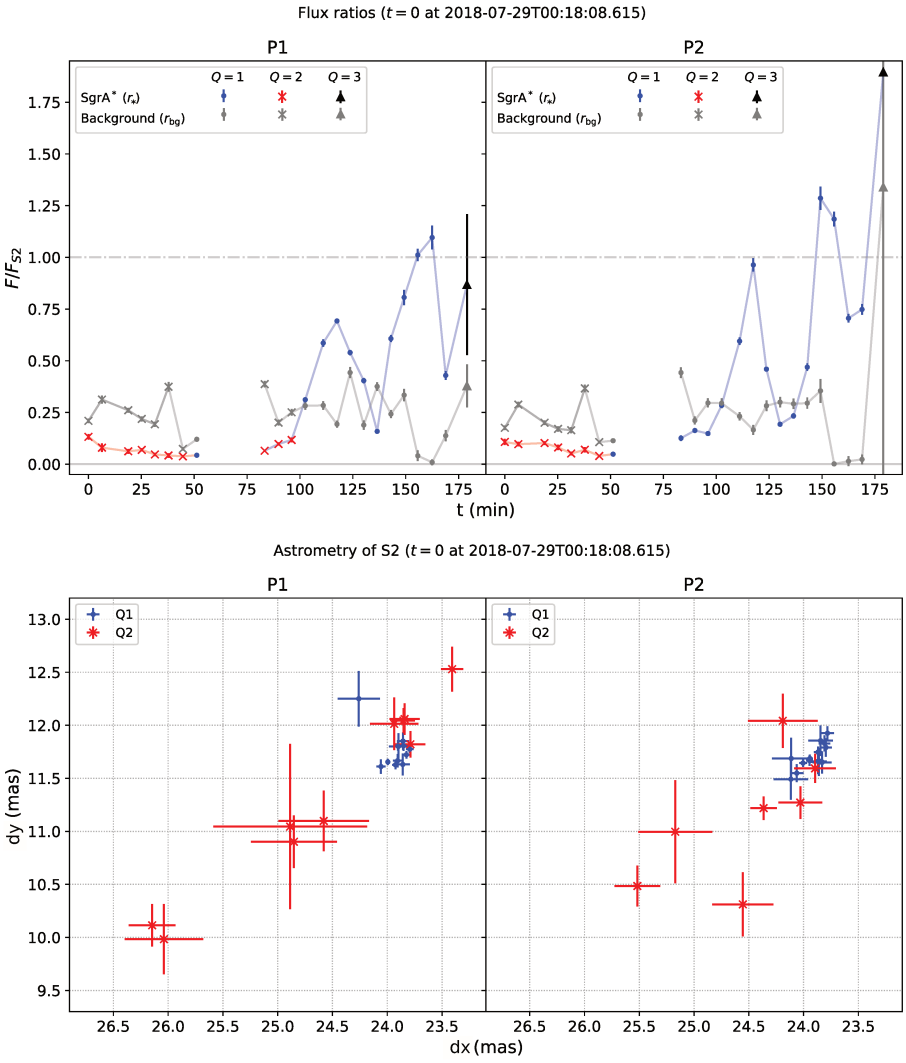

FIGURE 3.21: Example of a binary fit for all the frames on a specific night (28th July 2018), where a strong flare took place. Both polarizations are presented with the results for the flux ratios and astrometry of S2. The data points are classified by quality. The gap in the upper graph corresponds to a time interval where a calibration sequence in R2 has been taken, following the observing sequence described in Section 3.2.1.

3.5 Analysis of the binary model results

Due to the individual characteristics of each epoch, this section presents the results of 2017 and 2018 individually, where the significance, behaviour of the parameters through individual nights and quality of the fits are presented, discussed and compared with previous studies.

3.5.1 2017: First results before the pericenter passage

Astrometry of S2

The criterion of exclusively using the fits with quality 1 may be too restrictive as certain nights do not have or have too few fits with optimal quality. In an attempt to provide at least one measurement per night, the astrometry of S2 is done considering the fits with a quality 1 and 2.

By assuming the center of mass to coincide with SgrA* as seen by GRAVITY, the code returns the position of S2 relative to SgrA* in the parameters $(\mathrm{dx}, \mathrm{dy})$. A single estimate per night (n) can be obtained as a weighted average of the result:

$$dX^{(\mathrm{n})} = \frac{\sum_i^{(\mathrm{n})} \mathrm{dx}_i \sigma_{\mathrm{dx}_i}^{-2}}{\sum_i^{(\mathrm{n})} \sigma_{\mathrm{dx}_i}^{-2}} \; ; \; dY^{(\mathrm{n})} = \frac{\sum_i^{(\mathrm{n})} \mathrm{dy}_i \sigma_{\mathrm{dy}_i}^{-2}}{\sum_i^{(\mathrm{n})} \sigma_{\mathrm{dx}_i}^{-2}} \tag{3.26}$$

and its error bar is given by the standard deviation from the weighted mean:

$$\sigma_{dX}^{(\mathrm{n})} = \sqrt{\frac{\sum_i^{(\mathrm{n})} \sigma_{\mathrm{dx}_i}^{-2} (\mathrm{dx}_i - dX^{(\mathrm{n})})^2}{\frac{M-1}{M} \sum_i^{(\mathrm{n})} \sigma_{\mathrm{dx}_i}^{-2}}} \; ; \; \sigma_{dY}^{(\mathrm{n})} = \sqrt{\frac{\sum_i^{(\mathrm{n})} \sigma_{\mathrm{dy}_i}^{-2} (\mathrm{dy}_i - dY^{(\mathrm{n})})^2}{\frac{M-1}{M} \sum_i^{(\mathrm{n})} \sigma_{\mathrm{dy}_i}^{-2}}} \tag{3.27}$$

where M is the total number of non zero weights (which in this case is the same as the total number of points). An estimate of the position of the source per night is obtained for each dataset individually (P1 and P2), and then the ultimate estimate per night is obtained by the average of both datasets on each night.

In this epoch, the separation S2-SgrA* (more than 55 mas at the first runs of 2017) reaches the limit of the field of view of the fibers, which have a Gaussian shape with a FWHM of 60 mas. As a result, the sources feed the fibers in two different surfaces resulting in an effect of field aberration over the astrometry of S2, where a phase shift can occur yielding wrong measurements. This effect is being studied by the consortium and it is commented at the end of Gravity Collaboration et al. (2020a).

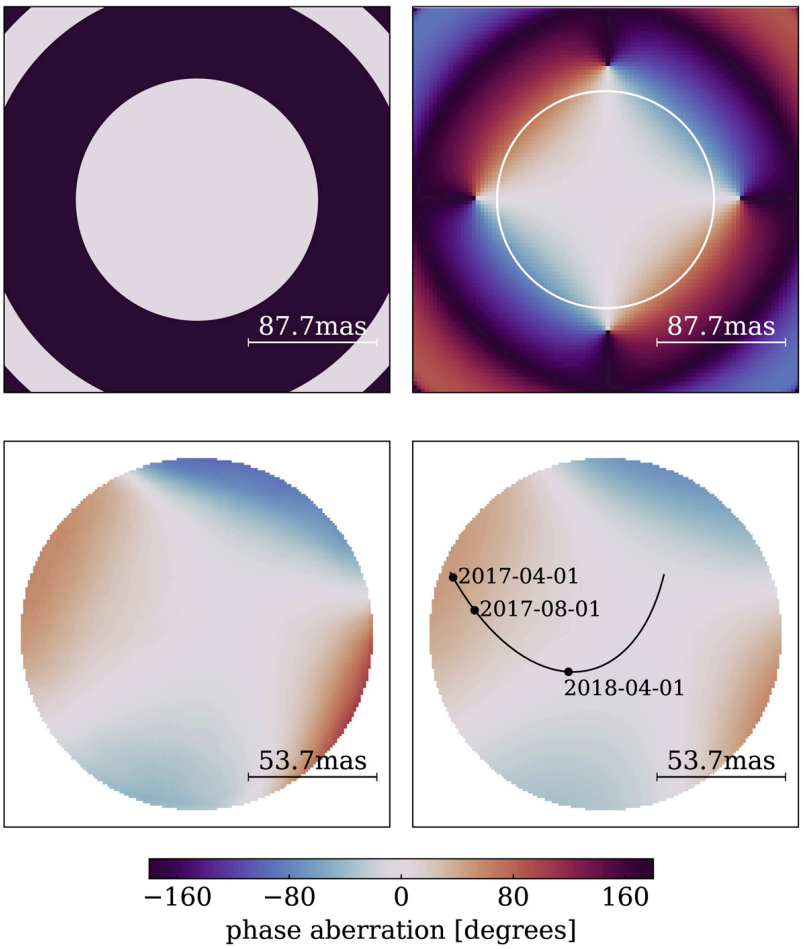

FIGURE 3.22: Phase maps corresponding to the aberration field study performed by the GRAVITY team. *Upper left*: phase map corresponding to a perfect Airy pattern. *Upper right*: simulation with static astigmatism over the full pupil (root mean square of 180 nm). The white circumference encloses the area considered for the phase maps. *Lower left*: a phase map example. *Lower right*: the same example after applying a gaussian kernel, which accounts for atmospheric smoothing. The black line shows the prediction of the position of S2 over the pupil. Source: Gravity Collaboration et al. (2020a)

In that work, the field aberration study has been performed by simulating phase maps. An example of them is shown in Figure 3.22. By implementing these phase maps into the fitting routine and comparing with the non-corrected results, the team has found that the correction by aberration can be approximated by adding a time-dependent offset to the astrometry of 2017 data such as:

$$\begin{aligned} \delta X &= 0.44 \times (t - 2018) - 0.10 \\ \delta Y &= -0.86 \times (t - 2018) + 0.28 \ , \end{aligned} \tag{3.28}$$

where t is the observing time of the corresponding night, in decimal years. This correction is large in early 2017 where S2 was the furthest away, and become smaller near the end of 2017. In my work, the correction by field aberration has been done by applying this a-posteriori offset to the obtained results.

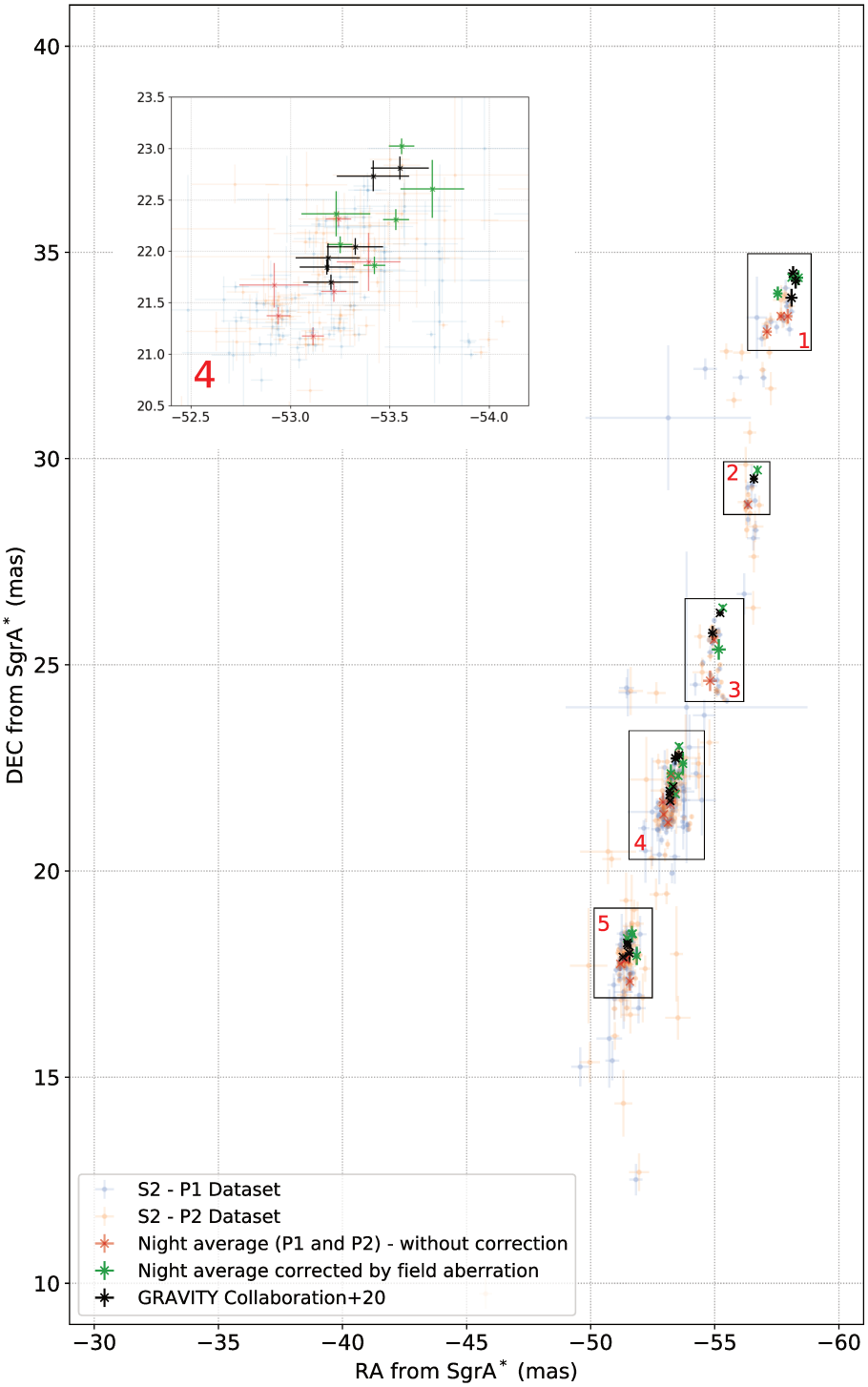

FIGURE 3.23: Coordinates of S2 with respect to SgrA* obtained for 2017 with the best estimate per night, the correction by field aberration and the results obtained by the consortium published in Gravity Collaboration et al. (2020a). The zoom corresponds to the region labelled as 4. The rest of the zooms of the highlighted regions are displayed in Figure 3.24.

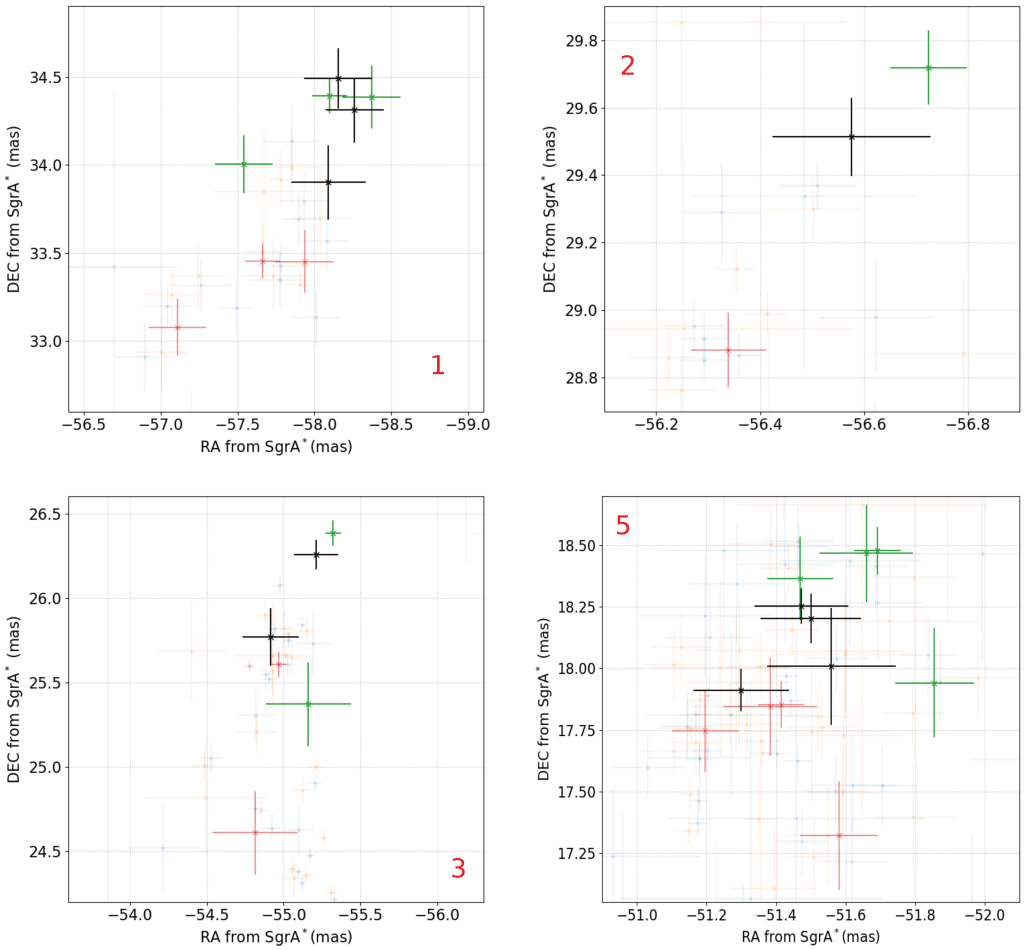

FIGURE 3.24: Zooms over every observing run during 2018. The number tags correspond to the areas highlighted in Figure 3.23.

The final results are presented in Figure 3.23, where the night average and the corrected average are shown together with the results of the whole consortium (Gravity Collaboration et al., 2020a). The results obtained in this thesis are part of the consortium data which produced the GRAVITY Collaboration publications about the Galactic Center: apart of my contribution, the data analysis was performed by two other independent teams with independent fitting code. Indeed, the data points in the S2 orbit fitting publications correspond to an average among the results of the three different teams, which explains the possible small offsets between my data and the consortium data in the plots. For a better readability, a zoom on every observing run is presented in Figure 3.24. The astrometry obtained in this work and the results of the team are compatible point by point at 1σ or less.

3.5.2 2018: The pericenter passage

Astrometry of S2

The four fibers are now placed in the same location of the sky, given as a blind offset after fiber active centering. In addition, the sources are located much closer to each other than in 2017. In the same way, a best estimate per night for the orbit of S2 is obtained by using a weighted average (Equation 3.26 and Equation 3.27 for the error bars), where all the fits with qualities 1 and 2 are considered. In the same way than for 2017, the separation vector of S2 is given directly by $(\mathrm{dx}, \mathrm{dy})$. Again, as the SPLIT frames have two data sets, the final position per night has been taken as the average of both data sets P1 and P2.

The results for 2018 are presented in Figure 3.25 where the average points of the whole GRAVITY Consortium used in Gravity Collaboration et al. (2020a) are also shown. Unlike 2017, the field aberration does not affect 2018 data as both sources are seen at the center of the fibers (Figure 3.22), and therefore no offset has to be applied. For a better readability, a zoom is shown on every observing run, which can be seen in Figure 3.26. The points are clearly compatible with the overall consortium measurements. It is in this run where the most accurate positioning of S2 of the whole dataset has been obtained with an astrometric accuracy of just 24 μas in right ascension, and 33 μas in declination. This accuracy goal confirms the initial hypothesis about the convenience on the simplification of the model, reducing the number of variables related to the flux ratios from four to one and obtaining the separation directly through the fitting of the closure phase.

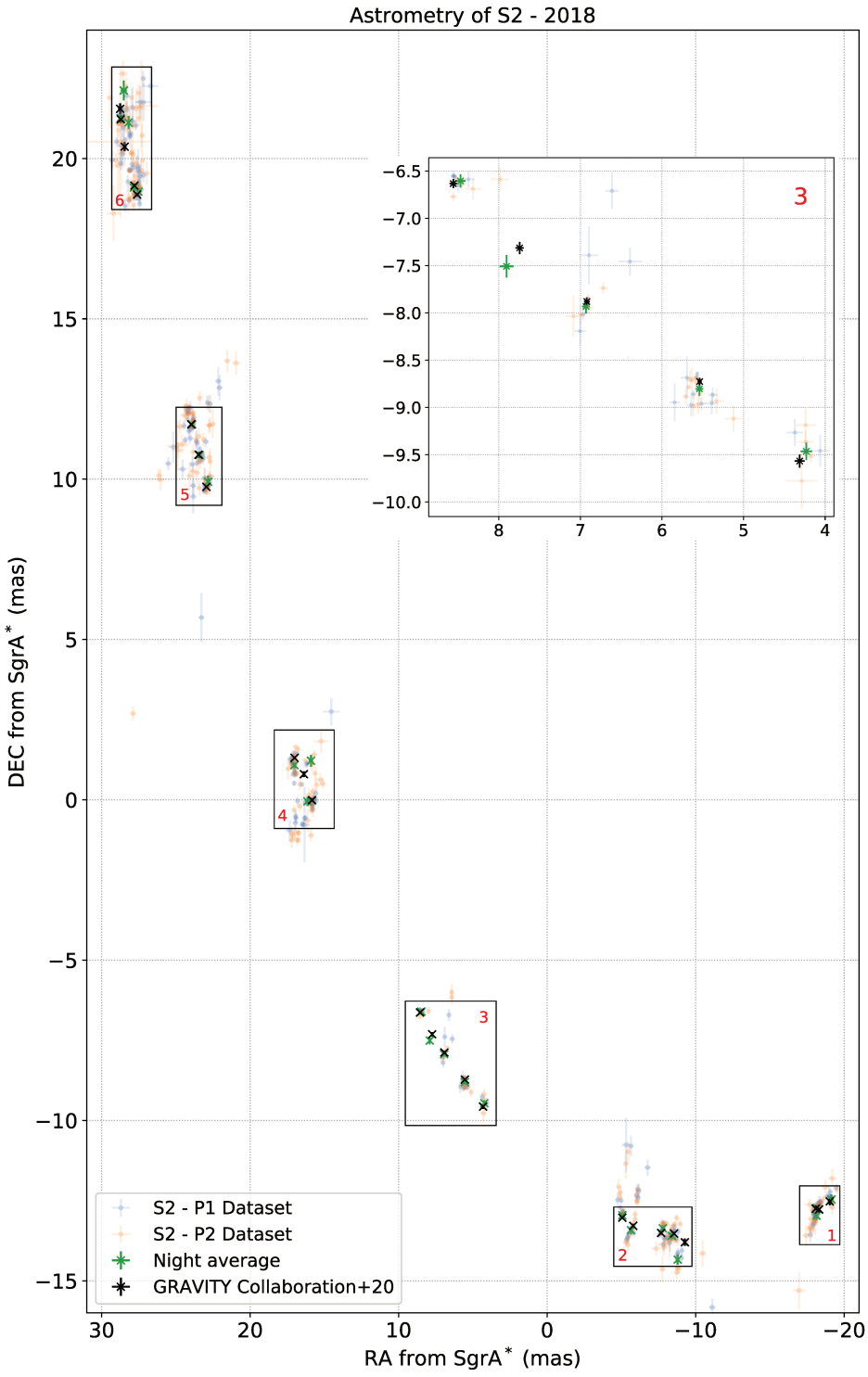

FIGURE 3.25: Coordinates of S2 for each night of the 2018 epoch and the best estimate per night. The prediction of the orbit by the use of the parameters derived in Gravity Collaboration et al. (2020a) is also shown. The zoom corresponds to the region labelled as 3. The zooms over the rest of the highlighted areas are displayed in Figure 3.26.

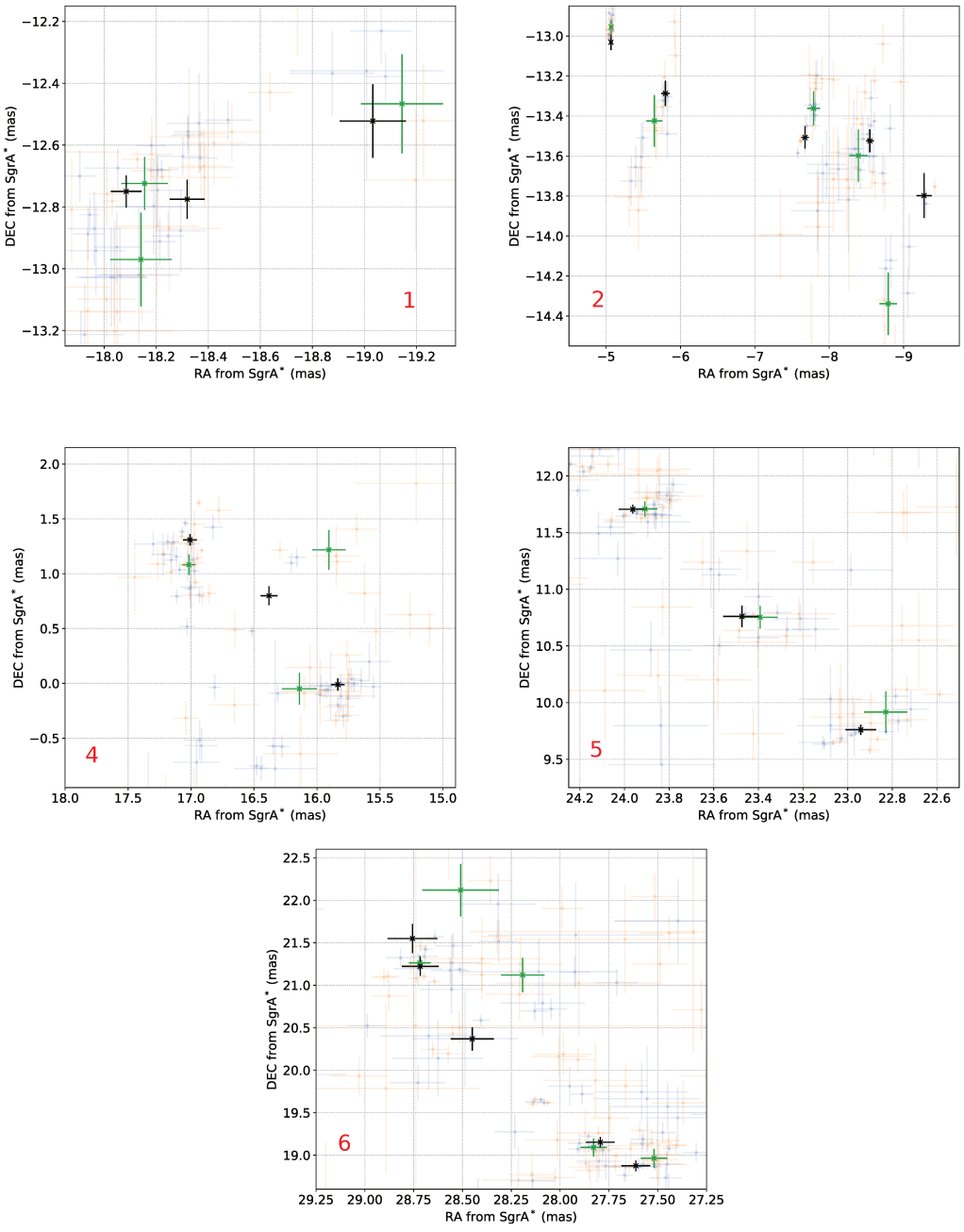

FIGURE 3.26: Zooms over every observing run during 2018. The number tags correspond to the areas highlighted in Figure 3.25.

The absolute flux of SgrA*

The flux ratios in 2018 are obtained by using only two indices instead of four, and the results of the fits classified with quality 1 and quality 2 (see Section 3.4.6) are presented in Figure 3.27. For a better readability, the gaps in the abscissa axis have been removed resulting in a graph where the temporal distance between two consecutive points is not linear. However, the datasets store the temporal information, and therefore specific flaring events can be identified individually. In an attempt to estimate the flux of SgrA* to be able to compare with literature, following our work in Gravity Collaboration et al. (2020b) the flux of S2 is taken as $F_{S2} = 15.8$ mJy and is assumed constant in time (Habibi et al., 2017). The figure shows the estimate of the absolute flux of SgrA* in mJy.

The light curve of SgrA* in 2018 confirms the results of Dodds-Eden et al. (2011), who by the analysis of previous light curves in the near infrared demonstrated the presence of a quiescent state with a clear flux density followed by occasional flares, which are defined as states where the flux of the central source exceeds 5 mJy. The background has been modelled as a blackbody similar to S2, and infinite size. As it is incoherent by definition, its origin can be natural (residual sky emission) or instrumental (stray light leading to a loss of coherence). The average background value is under 0.2, comparable to the average quiescent emission of SgrA*.

Two bright peaks show a higher flux than S2 itself. The first is a single peak being the brightest data frame of 2018 with $r_* = 1.1 \pm 0.14$, corresponding to the night of 2018-07-22 (frames 148-162). The second one is a very promising data set with two peaks ($r_* = 0.72 \pm 0.08$ and $r_* = 1.08 \pm 0.12$) corresponding to the night of 2018-07-28 (frames 171-190). It has been previously displayed in Figure 3.21. Other three peaks present a flux higher than the half of the flux of S2: one corresponding to the night of 2018-04-28 (frames 49-57) with a peak at $r_* = 0.65 \pm 0.11$, a second one during the night of 2018-08-22 (frames 205-216) with a peak at $r_* = 0.64 \pm 0.11$ and the last one during the night of 2018-07-30 (frames 226-232) with a peak at $r_* = 0.77 \pm 0.17$. There is another remarkable peak, slightly fainter with $r_* = 0.45 \pm 0.03$ during the night of 2018-05-27 right after the pericenter passage (frames 87-95).

The longest of the recorded flares corresponds to the double peak of 2018-07-28 with 65 minutes in total. It is also the most intense with a peak of 20.31 ± 0.95 mJy ($r_* = 1.28 \pm 0.06$) in P2 and 12.74 ± 0.95 mJy ($r_* = 0.81 \pm 0.06$) in P1. The large errorbars of the average on the peaks is due to the fact that the emission of the flare is polarized and therefore the differences between P1 and P2 are significant, especially in the peaks. This is reflected in other flares such as 2018-04-28 or 2018-07-22, where one of the polarization states stands out over the other. The polarization state is not analyzed in the present thesis, the reader may refer to Gravity Collaboration et al. (2018a) and Gravity Collaboration et al. (2020b).

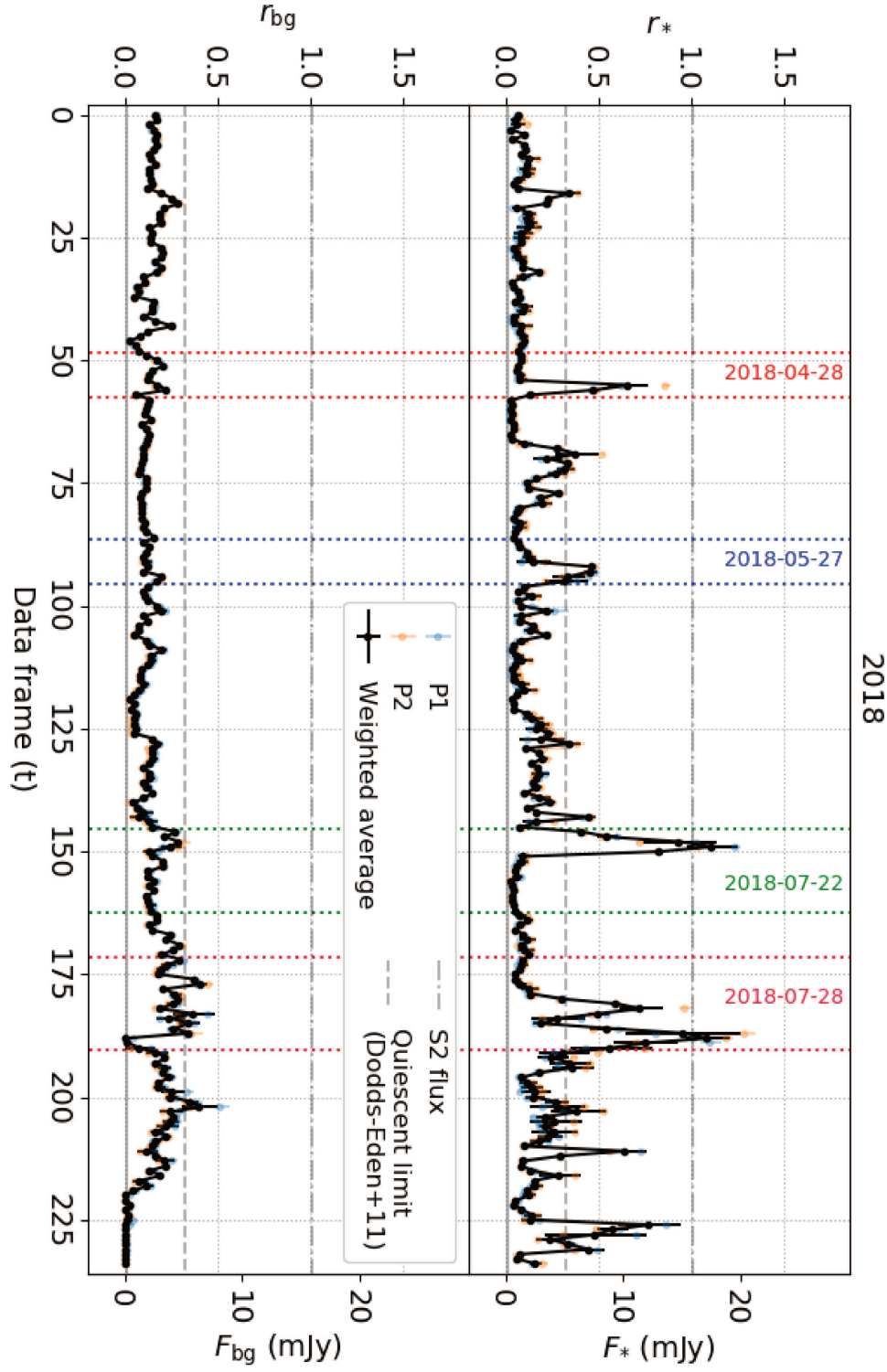

FIGURE 3.27: Flux ratio obtained for SgrA* and the background with respect to S2 in 2018. The colored dots correspond to the two polarization datasets and the black is the weighted average of them.

3.6 Contributions that directly make use of this work

In this section I will mention and describe the scientific works that have been published by the use of the astrometry and fluxes presented in this chapter.

3.6.1 The pericenter passage and the gravitational redshift

The results of this thesis work have been part of a larger study involving three independent teams inside the GRAVITY Collaboration (MPE Garching, LESIA and University of Cologne) obtaining the separation of the star S2 from the central source (the LESIA contribution being the astrometry of S2 obtained in this work and presented in Figures 3.23 and 3.25). For each night, a weighted average of the results of the three teams has been used to determine a final orbit for GRAVITY, from which the orbital parameters of the star have been estimated.

The GRAVITY results are added to the sample already published in Gillessen et al. (2017). A total of 26 years of data resulted in the first scientific paper of the Galactic Center team of the GRAVITY Collaboration (Gravity Collaboration et al., 2018b). The study involves the simultaneous observation of S2 with GRAVITY and SINFONI, which provides the third coordinate of the orbit by providing high resolution spectroscopy. Thanks to the accuracy achieved by GRAVITY and the spectral information of SINFONI, the gravitational redshift has been observed for the first time in a strong gravitational field during the pericenter passage of S2, successfully validating another test of General Relativity (see Section 1.1.7).

The total observed redshift from S2 can be expressed as the sum of two terms, as the contribution of the Keplerian orbit $z_{\rm K}$ alone and the one who includes General Relativity effects $z_{\rm GR}$:

$$z = z_{\rm K} + f(z_{\rm GR} - z_{\rm K}) \tag{3.29}$$

where $f = 0$ if physics are purely Newtonian and $f = 1$ for pure General Relativity. Our team has measured $f = 0.9 \pm 0.09$ at the surroundings of the periastron, rejecting Newtonian physics at 10σ. The residuals obtained by considering $f = 1$ with respect to $f = 0$ (where the positions of the orbit of this thesis work has contributed to) as well as the radial velocity measurements taken by SINFONI are displayed in Figure 3.28.

The observation of this effect is intrinsically relativistic: it corresponds to a loss of energy of the photons as they have to overcome a strong gravitational potential such as the one of SgrA*, resulting into a longer wavelength compared to. This work is considered the first major breakthrough result from the GRAVITY Collaboration, accomplishing the first successful test of General Relativity directly measured on a star in the Galactic Center. A similar result excluding Newton at 5σ was obtained a year later by the group of UCLA in Do et al. (2019) also by orbit fitting of S0-2 (S2 in our nomenclature).

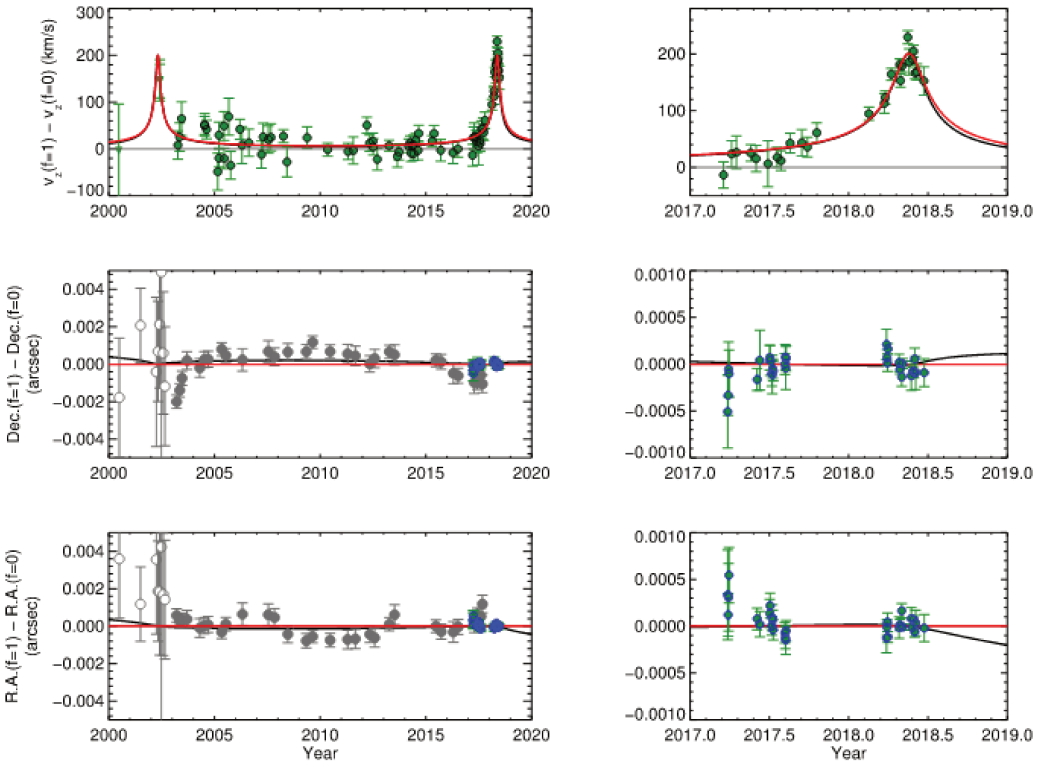

FIGURE 3.28: Top: Radial velocity residuals measured by NIRC2, NACO, and SINFONI. The model in red corresponds to $f = 1$ (GR) and the model in gray $f = 0$ (Keplerian). Center and Bottom: Coordinates of S2 measured by NACO and SHARP (grey) and GRAVITY (blue). The black line displays the GR model plus the contribution of the Schwarzschild precession. The plots at the right are the zooms of the left ones where SINFONI and GRAVITY (including the contribution of my work) have been involved. Source: Gravity Collaboration et al. (2018b)

3.6.2 Orbital motions around SgrA*

Each GRAVITY data frame has an integration time of NDIT=30 (DIT=10s), with a total of five minutes. By default, the fitting routine is implemented by exploring the parameter space using the whole integration time as the signal to noise ratio is maximal. However, the strongest flaring events of SgrA* have two main characteristics (high flux ratios and very short timescales) that do not necessarily require to integrate the whole exposure to obtain a reasonable signal to noise ratio.

The aim of such approach is the hypothesis testing of the hotspot model (see Section 1.1.6 or Vincent et al., 2014). If the signal to noise ratio is enough, GRAVITY is able to reach an accuracy enough to track any orbital motion in the environments of SgrA* (Gravity Collaboration et al., 2017), which will be reflected in a wander of the separation of S2-SgrA* during the timescale of the flare. The feasibility of this procedure is much higher in 2018 than in 2017 for a simple reason: when S2 is near the pericenter, both targets are seen by the same region of the fiber so the response of the instrument to both targets is nearly the same. It is not a surprise than in Figures 3.23 and 3.25 the spread of the positioning of S2 is minimum at the pericenter, while they are substantially higher in the rest of the orbit. The fact that in 2017 active fiber centering was not implemented in GRAVITY makes also this year less accurate when trying to observe tiny deviations of the separation vector S2-SgrA*. For all these reasons, the search for orbital motions is performed only in 2018.

According to the results for the flux of SgrA* presented in Figure 3.27, there has been at least four exceptionally bright flares in 2018. By re-reducing the data, the team has used individual subexposures in which a binary fit (Section 3.3.2) has been launched. A total of three flares (2018-05-27, 2018-07-22, 2018-07-28) present an offset compatible with orbital motions. By the use of two codes developed by two groups of the consortium (GYOTO by LESIA and NERO by MPE), the group performed several orbital fits resulting in the first attempt of estimating the inclination an rotation of the Galactic Center black hole. The results are compatible with a hotspot located at just 7 R_g from the center, reaching a linear velocity of 0.3c. Assuming spin zero, the orbit presents an inclination of $i = 160°$ for the three flares, similar to the inclination of the clockwise stellar disk ($i = 129°$ Buchholz, Schödel, and Eckart, 2009), or the orbit of the G2 cloud ($i = 123°$ Plewa et al., 2017). The last flare (28 July) has been studied by using the half wave plate (see section 3.2.1) and found polarization loops by studying the Stokes parameters. The results have been published in Gravity Collaboration et al. (2018a).

Overall, the orbital motions and the polarization rotation found provide strong evidence for the hotspot model to be the origin of the observed flares (against the Rossby instabilities or jet models). They also reinforce the evidence that Sgr* is a supermassive black hole where the first measurements of the inclination of the accretion disk are attempted.

The study of the nature of the flares is currently a truly active field of research inside the consortium, with another published work about their modelling (Gravity Collaboration et al., 2020a). More observations would help in the future to increase the amount flares where to attempt the tracing of orbital motions. A good sampling of flares would be useful to constrain other fundamental parameters of the black hole such as the spin, to obtain information about the space time in its environments.

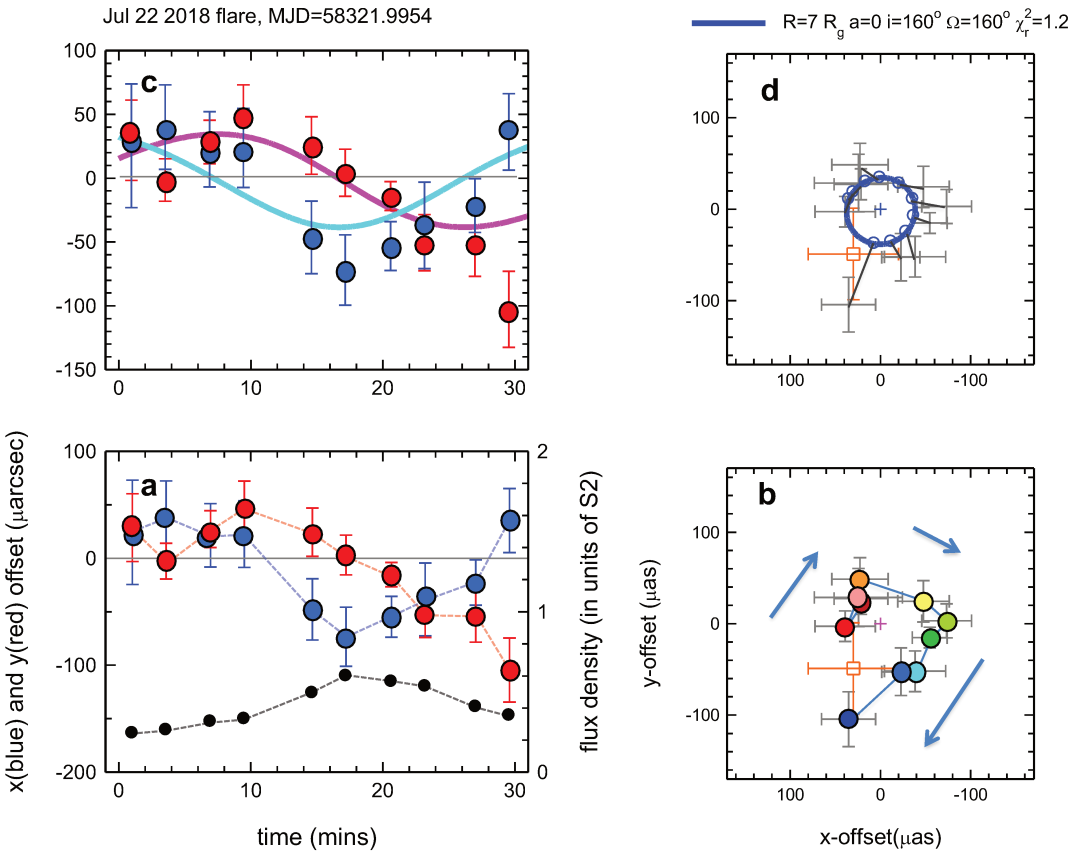

FIGURE 3.29: Orbital motions observed in one of the flares, July 22. The blue and the red dots correspond to the x and y coordinates of the offset, respectively. The fit is compatible with an orbit of $i = 160°$ and a radius of just 7 R_g assuming spin zero. Source: Gravity Collaboration et al. (2018a).

3.6.3 The Schwarzschild precession

The Schwarzschild precession is another effect on the orbit predicted by General Relativity: there is an expected precession for an orbit of a body due to the curvature of space time in the environments of another massive body, which gets substantially more perceptible if the gravitational potential is strong. This effect is similar to the precession of Mercury around the Sun (Section 1.1.7), and the work presented in this section corresponds to the first measurement on an extra solar body, in this case a dwarf star as S2 around a supermassive black hole, SgrA*.

According to Figure 3.28, this effect could be distinguished from 2019 by GRAVITY becoming more notorious with time. The team has successfully claimed the first detection of the Schwarzschild precession in the orbit of S2 (Gravity Collaboration et al., 2020a) by complementing the archival NACO, SINFONI data and GRAVITY 2017 and 2018 epochs with another epoch in 2019 consisting in six extra observing runs. The results continue to be fully consistent with GR (Figure 3.30).

Although I have not been directly participated in any observation of S2 in 2019, the astrometry of S2 in 2019 have been obtained using the same fitting routine in which development I have been involved during 2017 and 2018. The paper uses also the data of these two epochs obtained during my thesis work, to perform an orbit fitting where the Schwarzschild precession has been confirmed. At the very end of my thesis, this is the last update of the orbit of S2 from the GRAVITY Collaboration.

Another of the results of the paper is the update of the value of the distance to the Galactic Center and the mass of the central object, as $R_0 = 8246.7 \pm 9.3$ pc and $M_0 = 4.261 \pm 0.012(10^6) M_\odot$. An estimate of the extended mass of SgrA* is obtained as 0.1% of the total mass. The paper also provides a correction by aberration that has been used to update the results of 2017 in this thesis. Together with Gravity Collaboration et al. (2018b,a), Amorim et al. (2019), and Gravity Collaboration et al. (2019), this work provides a fifth successful test of General Relativity in three years, all of them obtained with the contribution of LESIA where this thesis has been part of.

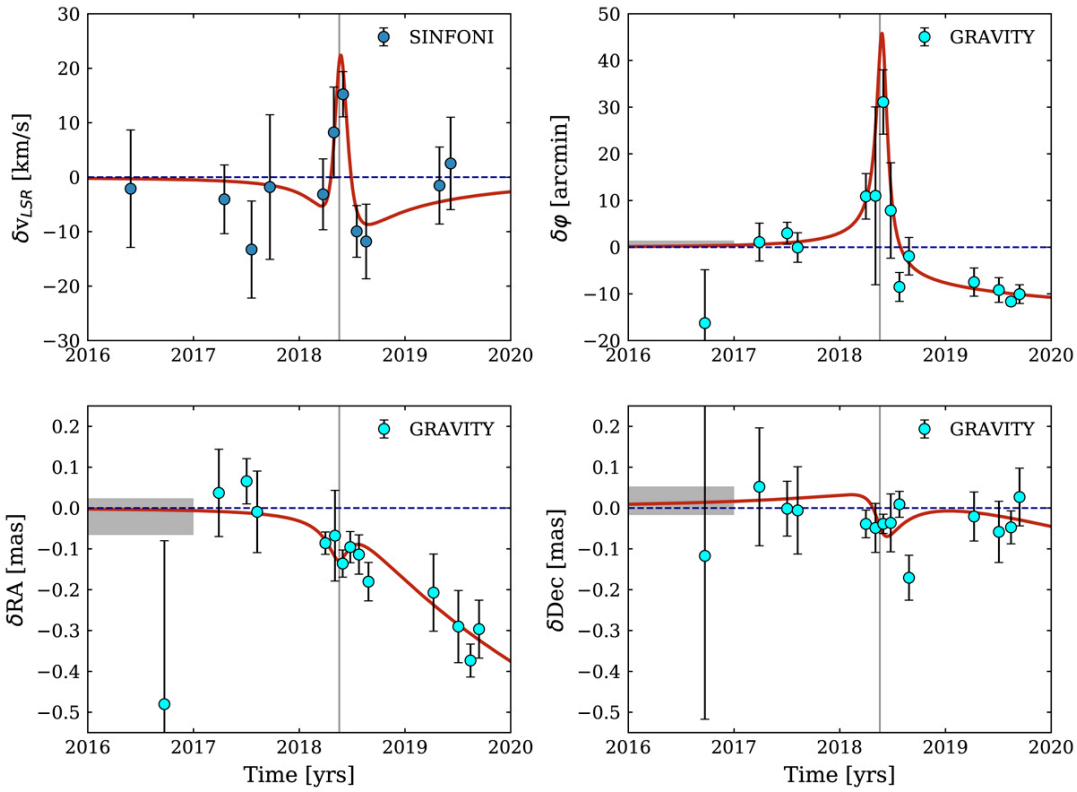

FIGURE 3.30: Posterior analysis of the orbital fit. *Top left*: radial velocity residuals with measurements of SINFONI, the best fit of the model in red with $f_{\rm SP} = 1.1$ assuming General Relativity, compared to the dashed line with $f_{\rm SP} = 0$ (Newtonian plus gravitational redshift, Roemer effect and transverse Doppler effect of special relativity). *Top right*: residuals of the Schwarzschild precession obtained with the measurements of GRAVITY. *Bottom*: residuals on the coordinates with the measurements of GRAVITY. The grey rectangles to averages of the NACO data. Source: Gravity Collaboration et al. (2020a).

3.6.4 The flux of SgrA*

With the results of the fluxes obtained during the three GRAVITY epochs (from which my work corresponds to the contribution of LESIA during 2017 and 2018), a light curve of SgrA* has been built by the Consortium and published in (Gravity Collaboration et al., 2020c). It summarizes the binary fits of the measurements performed during all the runs of the consortium in 2017, 2018 and 2019. This thesis work has contributed concretely to the light curve of 2018.

As it has been described in Section 3.5.2, the paper officially confirms the two state scenario introduced by (Dodds-Eden et al., 2011): a quiescent state with a well defined median flux density followed by random flares. The light curve is presented in Figure 3.31, where 2019 shows flares systematically brighter than 2018. The paper explores the influence of the pericenter passage of S2 and the cloud G2 (Gillessen et al., 2012) on the accretion flows that generate the flares and concludes that there is no evidence that it could affect the quiescent emission, but the possibility of affecting the flaring events is not ruled out.

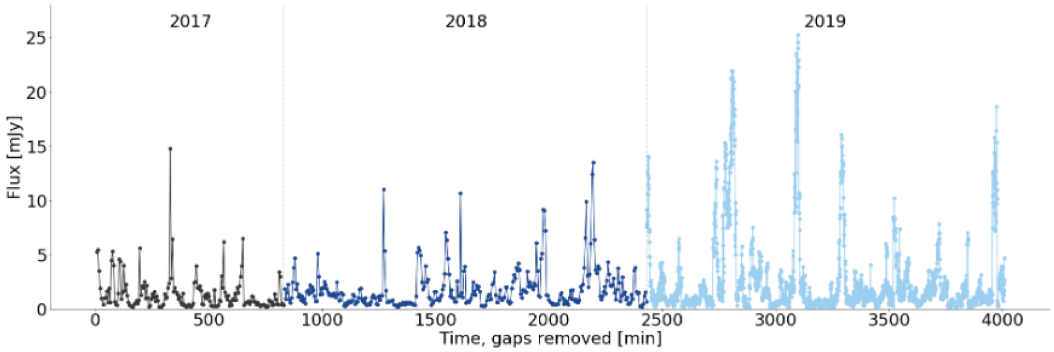

FIGURE 3.31: Light curve of all the corresponding binary fits performed during 2017 and 2018 by the GRAVITY Collaboration. The fits during 2019 had to be performed by using unary models such as the one described at the end of Section 3.3.2 as S2 has left the field of view of the fibers. Source: Gravity Collaboration et al. (2020c)

3.7 Perspectives: towards a detection of an extra source

One of the reasons why the binary model fit is not completely successful for all the frames in all the baselines might be the underestimation of the number of detected sources in the field of view of the fibers. Before the arrival of GRAVITY, no bright source was consistently detected inside the orbit of S2 around SgrA* (Gravity Collaboration et al., 2017). However, as any star closer to the central source might have an orbit shorter than 16 years, the possibility of any extra source appearing in the field of view of certain data frames must not be a priori ruled out. In addition, dense clouds of gas have been found in elliptical orbits around SgrA* such as G2 (Gillessen et al., 2012, 2013) or G1 (Witzel et al., 2017) and more objects of this nature may be present in our data. Indeed, any trace of material ejected during the pericenter passages of these objects could also form minor dense clumps which would enrich the accretion disk of SgrA*, which could potentially be detected as an extra source in the field.

One question that comes up is the possibility of the star S2 to be a binary system in its orbit around SgrA*. In that case, the companion star would appear as a third source (S2, its companion and SgrA*). This question has been addressed during the first observations taken by GRAVITY (Gravity Collaboration et al., 2017) but no significant closure phase variations have been found for S2 in the first interferograms taken by the instrument. This implies that, if such a companion exists, it is probably too faint to be seen by GRAVITY. A similar conclusion was found by spectroscopic measurements in Chu et al. (2018), ruling out the possibility of a companion for S2 with $K < 18$. In addition, they found that the effect of a companion for S2 does not affect significantly the detection of the gravitational redshift on the orbit of S2. Therefore, any third source potentially found within our current observations would not be a companion star of S2, but another kind of body such as a non-bound binary, a gas cloud or a dense clump.

The detection of an extra source inside the orbit of S2 that could potentially be tracked in the same way would imply a study of a gravitational potential stronger than the one which S2 is subjected, paving the way for implementing new tests in General Relativity. Such source would have an impact on the separation of S2 and SgrA* too as the binary model could be biased by it.

3.7.1 The triple model

The binary model relies on the assumption that there are only two bright sources. To take into account the stray light and the rest of the (faint) sources present in the field of view, a background is considered. Sometimes the central source is faint due to lack of activity and only one bright source plus a background is revealed. If the central source is flaring then its brightness overcomes the background and two sources are identified (plus a lower background). While fitting the binary model, the computer is forced to find these two sources and hide all the incoherent light under the variables background flux and background index. By giving a significance factor such as χ^2, it returns the accuracy of the model.

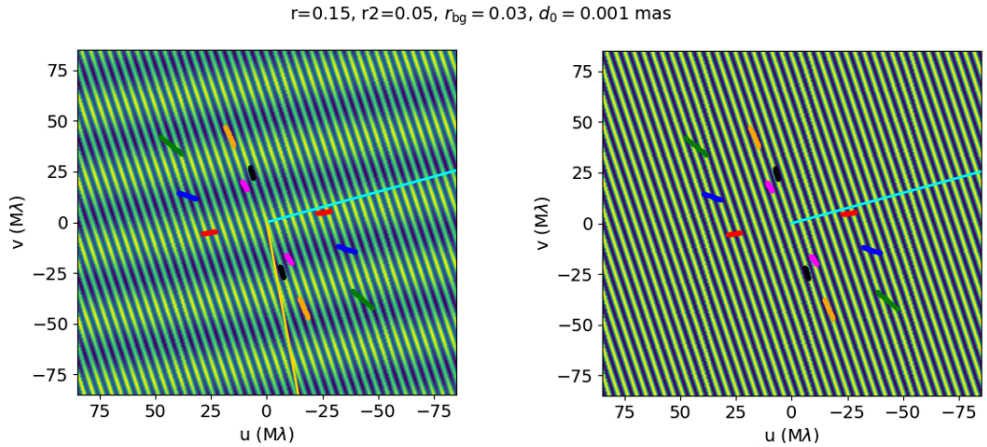

FIGURE 3.32: *Left*: simulation of an interferogram corresponding to three sources in the field of view. *Right*: simulation of an interferogram corresponding to two sources. The yellow line traces the direction of the vector third source - central source and the cyan line traces the the direction of the vector S2 - central source.

But we have seen in Section 3.3 that depending on the orientation of the two stars some baselines might not be able to distinguish the binary. If the baseline is parallel to the binary vector and the fit does not explain the expected outcome of a binary system, it could be a hint that the interferometer is seeing an extra source. According to Gravity Collaboration et al. (2017) it is very unlikely to find a star brighter than $m_K = 17.1$ inside the orbit of S2. However, it is worth looking as any star closer to SgrA* would bias the S2 measurements. If detected, this star could be perhaps even a better candidate than S2 as a probe to test General Relativity. An example of an interferogram with SgrA* and two stars in the field can be seen in Figure 3.32. The expected flux corresponds to $m_K = 17.2$ and it must be in principle close to the maximum possible for such star.

In addition to the binary model, a generalization has been considered adding a third source to Equations 3.17 and 3.18. This new model is applied only on those cases where the binary fit is inconsistent for certain baselines. In this case, the model becomes, with $\langle V^{\rm tri}(u,v)\rangle_{\Delta\lambda} = \mathcal{N}^{\rm tri}(u,v)/\mathcal{D}^{\rm tri}$:

$$\begin{aligned}\mathcal{N}^{\rm tri}(u,v) = r_* \int_\lambda B(\lambda)\left(\frac{\lambda_0}{\lambda}\right)^{k_0} \frac{2J_1(x_0)}{x_0} e^{-2\pi i(u\alpha_0+v\delta_0)}{\rm d}\lambda \\ + r_1 \int_\lambda B(\lambda)\left(\frac{\lambda_0}{\lambda}\right)^{k_1} e^{-2\pi i[u\alpha_0+{\rm d}x+v(\delta_0+{\rm d}y)]}{\rm d}\lambda \\ + r_2 \int_\lambda B(\lambda)\left(\frac{\lambda_0}{\lambda}\right)^{k_2} e^{-2\pi i[u(\alpha_0+{\rm d}x_2)+v(\delta_0+{\rm d}y_2)]}{\rm d}\lambda \quad (3.30)\end{aligned}$$

and:

$$\mathcal{D}^{\rm tri} = \int_\lambda B(\lambda)\left[r_*\left(\frac{\lambda_0}{\lambda}\right)^{k_0} + r_1\left(\frac{\lambda_0}{\lambda}\right)^{k_1} + r_2\left(\frac{\lambda_0}{\lambda}\right)^{k_2} + r_{\rm bg}\left(\frac{\lambda_0}{\lambda}\right)^{k_{\rm bg}}\right]{\rm d}\lambda\ , \quad (3.31)$$

where k_2 corresponds to the spectral index of the third source and dx_2, dy_2 are the separation between the third source and SgrA*. It is straightforward to see that if $r_2 \to 0$ the model returns to the binary case. As in principle the maximum size expected for this source is stellar, this third source is assumed to be a point source in the similar way as S2.

Due to their better quality, this method is only tested in 2018 data. The following parameters must be considered in addition to the ones of the binary model (Section 3.3.2):

- As fixed parameters: in principle, the spectral index $k_2 = 4$ as the target I am trying to find is stellar. In case of a meaningful detection, this parameter can be set free.
- As free parameters there is a total of 8 including:
  - Another offset $(\mathrm{dx}_2, \mathrm{dy}_2)$.
  - An extra flux ratio r_2. It provides an estimation of the flux ratio of the third source with respect to S2 by fixing $r_1 = 1$ in the same way as the binary model in 2018.

The closure phase is used and $(\alpha_0, \delta_0) = (0, 0)$. The first guess of the complex visibility is built in the same way that in the binary fit, evaluating Equations 3.30 and 3.31 with the values and the rest of the parameters already fixed in the the binary case (described in Section 3.3.3). To build the prior (an uniform distribution, by the same procedure that in the binary case), the first guess and the parameter bounds considered are the following, in addition to the ones described in Section 3.3.4:

- We are looking for a faint star that is expected to be in the field of view and could probe the potential well closer to SgrA*. This requires a first guess for the flux ratio to be detectable, comparable to the average emission of SgrA*. The model uses as a first guess $r_2 = 0.15$ within the interval $(0, 100)$.
- Regarding to the location of this third source, the choice of the first guess is $(\mathrm{dx}_2, \mathrm{dy}_2) = (1, 1)$ exploring the interval $(-10, 10)$ mas. This position is completely arbitrary and it can be changed in case of a promising data frame according to the information given by the phase. The explored interval is wide enough to take into account any plausible third source, but small enough not to compromise the location of S2.

Nevertheless, the detection of the third source is not the central point of the study. In an attempt to strongly constrain the orbit of S2 and extract the effects of SgrA* from it, the procedure has been focused on the binary fits. It is convenient to consider the binary fitting at first order, and if any deviation from a binary visibility suggests the presence of a third source, then fit three bodies using this model. In any case, if any binary and triple fitting show the same significance, the third source detection is discarded for simplicity.

3.7.2 Attempt to detect the third source

The triple model described in Section 3.7 has been tested only in data frames where the binary fit presents a quality factor 1 or 2 (as it is explained in Section 3.4.6). In principle, the ideal third source detection would be easier near the closest approach of S2 to SgrA* (where the flux feeding the fibers is maximum).

To be considered physical, a significant third source detection would necessarily imply no difference on the coordinates of any of the other targets either in a binary or triple fit. In addition, it must be present in a position compatible between the two datasets P1 and P2 corresponding to the frames recorded by using the Wollaston prism.

Among all the data frames, the most promising night for the search for the third source has been the night of 22nd July 2018, involving one of the most luminous flares recorded since the first light of GRAVITY, and only two months after the pericenter passage (who took place on May of the same year). In addition to the usual binary fit, a triple fit has been performed for all the data frames obtained during that night. Then, from all these fits, the ones with an optimal quality (classified as 1) have been selected. The detected position of S2 in the binary fits and the detected position of S2 and the third source in the triple fits are displayed together in Figure 3.7.2 for both datasets P1 and P2 corresponding to the two polarizations.

Overall, the detection of a third source is not convincing for the following reasons:

- The third source does not present coordinates compatible between the fits corresponding to both datasets P1 and P2. Despite having perhaps certain differences (such as higher flux in one polarization compared to the other one), for the source to be natural, its light must come from the same spatial origin.
- The spread of the coordinates of S2 increases significantly when the software is asked to detect three sources in the field. If the third source would be natural, the positioning of S2 would not be affected by it.
- Apparently the positions of the third source during the night (orange in the figure) present certain linear trend, which is parallel to another linear trend appearing in the positions of S2 (red in the figure). These trends are likely compatible with the PSF of the interferometer in the location of both S2 and SgrA*. Instead of finding a natural source, the code is overfitting a third point source where there is already two sources.

This result confirms what it was proposed in the paper of the first light of GRAVITY (Gravity Collaboration et al., 2017) about the presence of extra sources (there are no new extra sources inside the orbit of S2 with $m_K < 17.1$). At the moment where the signal to noise ratio is the highest from all the data obtained during the two years since GRAVITY started operating, still no extra sources apart from S2 and SgrA* have been observed at less than 60 mas from SgrA* in the sky (the radius of the field of view collected by the optical fibers). It might be feasible to revisit the source detection when S2 leaves the field of view of the fibers of GRAVITY while pointing at SgrA*. In this case, any trace of binarity signature in a frame recorded during a flaring state of SgrA* would be a hint of the presence of any extra star in the field.

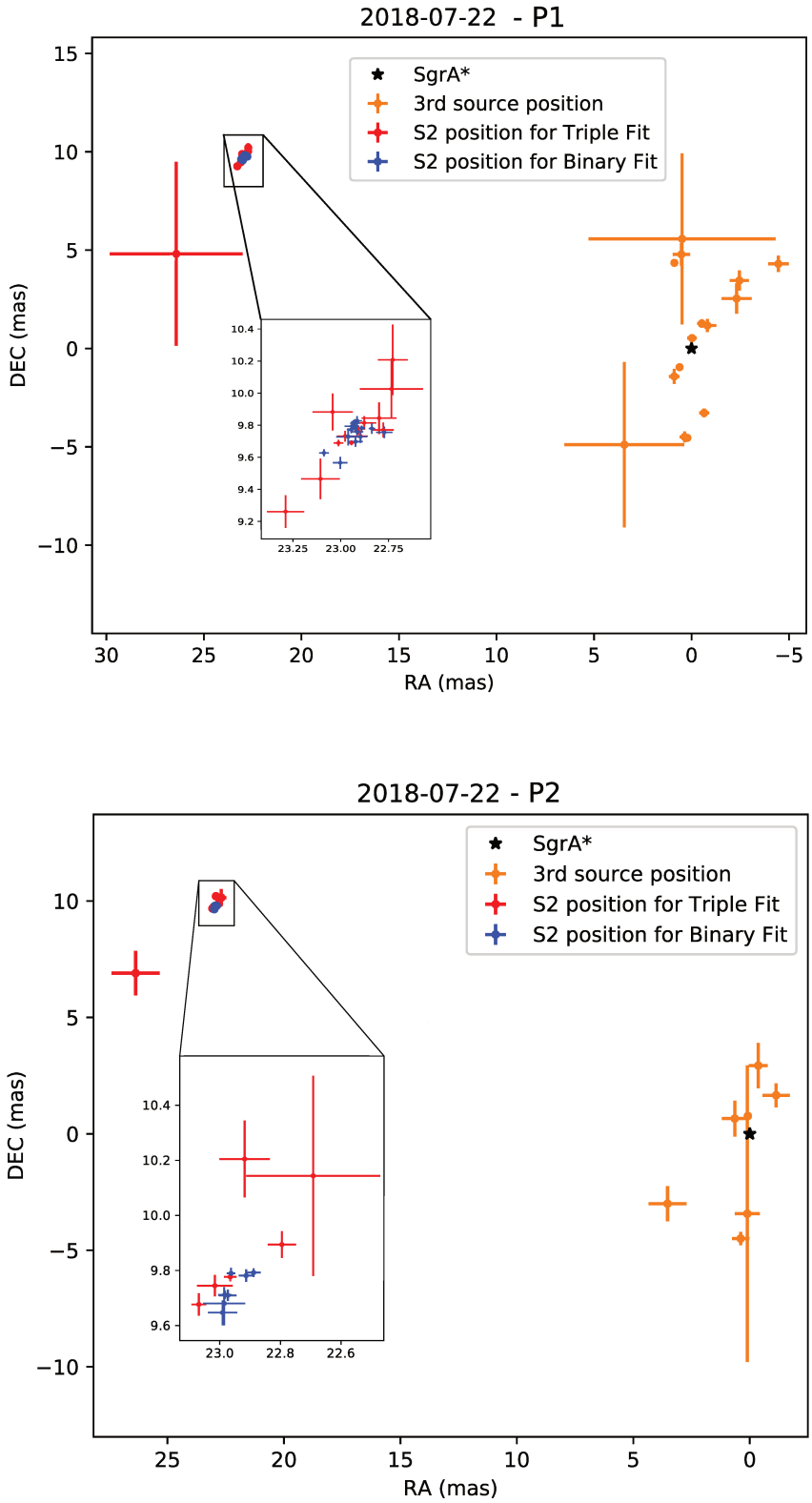

FIGURE 3.33: Results for the coordinates of several binary and triple fits performed in a date where a flare has been observed, in both polarizations. The red and the orange dots correspond to the same fits using a triple model, while the blue dots correspond to a binary fit. A zoom is displayed at the location of S2 (with respect to SgrA*) to reveal the spread on the coordinates.

Chapter 4

The close environment of GCIRS 7

4.1 A brief introduction on Red Supergiants

Let there be a giant molecular cloud in gravitational collapse. As long as matter is compressed, the temperature on the system rises due to increasing pressure. When the temperature inside of its core is high enough to ignite hydrogen nuclear fusion reactions, a star is born. This instant is used as reference point of its age and is called Zero Age Main Sequence (ZAMS) where they reach what is called the Main Sequence stage (Figure 4.1). The life cycle and the physical properties of this star are mainly determined by their mass in that instant.

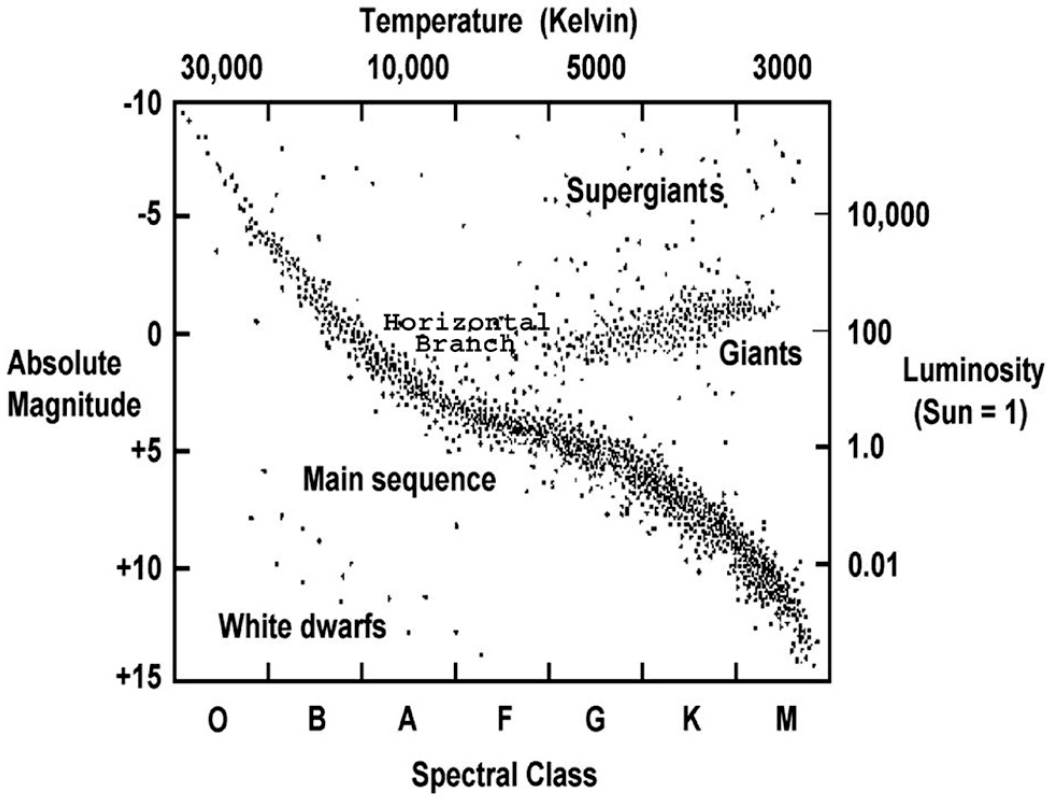

FIGURE 4.1: Example of a Hertzsprung-Russell diagram given a stellar population. The Red Super Giant stars are located in the upper right corner. Source: https://chandra.harvard.edu

Stars with an initial mass of few solar masses or less ($< 10\,M_\odot$) are known to be the most numerous and most stable. They spend the majority of their lives (up to a tenth of billion years) in the Main Sequence phase, with a radiative core and convective outer layers. During this stable phase they keep burning hydrogen in their cores until they consume all of it. In this state they reach the temperature and pressure conditions to start burning hydrogen outside the core. As a consequence they expand by several stellar radii and their effective temperature decreases reaching a stage called Red Giant phase.

If the initial mass of the star is more than $8M_\odot$ but less than $30M_\odot$ (Levesque, 2017), the physical conditions of pressure and temperature make the hydrogen fusion much more efficient during the Main Sequence phase, being therefore much shorter (5-20 million years). The star then expands and cools down to reach the Red Supergiant phase (RSG) where it will spend most of its lifespan.

Structure and physical properties

The typical size of a RSG goes from several hundreds to over a thousand $R_\odot$. Their maximum luminosity is only constrained by the Eddington limit[1], which for a star of $25M_\odot$ is $L_{\max} = 8.25 \times 10^5 L_\odot$. The effective temperature of their photosphere is between 3200 and 4300 K, significantly lower than Main Sequence stars' (Levesque et al., 2005).

These evolved stars present interiors composed of spherically concentric thick layers where they are capable to burn elements heavier than hydrogen up to iron[2], a limit that stars with lower mass cannot reach. Indeed, the nuclear fusion processes in their cores make them the main contributors to the chemical evolution of the interstellar environment, specially after the supernovas they experience at the end of their existence. These violent explosions occur when the mass of the iron formed in its core exceeds the Chandrasekhar mass ($1.4\,M_\odot$) and the star collapses gravitationally. The resulting pressure expels violently all the outer layers of the star, reaching the physical conditions to generate chemical elements heavier than iron via nuclear fusion.

The outer structure of RSGs is radiative and their surface gravity is substantially lower compared to Main Sequence stars. As a consequence of this, the ejection of material is favoured presenting large mass loss rates ($\dot{M} = 10^{-4} - 10^{-6} M_\odot \mathrm{yr}^{-1}$) that can play a major role during their evolution, specially among the most massive stars ($M > 15\,\mathrm{M}_\odot$). Unfortunately the physical mechanism the mass loss is driven by is not yet fully understood (Smith, 2014), which leads to a high uncertainty on stellar evolution models. Up to date, there is not a single theory able to derive the mass loss processes under first principles. There are several empirical approaches, starting by de Jager, Nieuwenhuijzen, and van der Hucht (1988) who, using a sample of 271 stars, fitted the mass loss rate as a function of the luminosity and effective temperature. The most recent prescription, recently published by Beasor et al. (2020) is based on the study of stellar clusters. The mass loss rate is derived as a function of the physical properties of the dust, assumed to be located in spherical shells enshrouding RSGs.

The study of the circumstellar environment of RSGs becomes, indeed, the key to understand the mass loss process. The low temperatures of the photosphere and the

[1] A star that would reach the Eddington luminosity during its evolution would immediately start ejecting material through a strong stellar wind, which would prevent it from reaching a luminosity above the Eddington limit.

[2] The binding energy per nucleon makes ^{56}Fe the most stable atom.

stellar envelope make possible the formation of certain molecules (as carbon monoxide or water) in their close environments. This is confirmed by the presence of deep lines in the infrared spectra corresponding to those molecular bands (Spinrad and Wing, 1969). Certain RSGs present a diverse and complex molecular circumstellar environment and high mass loss rates ($10^{-4} M_{\odot}/\mathrm{yr}$) as VY CMa (Mauron and Josselin, 2011; Kamiński, 2019). Others, with a much lower mass loss rate as Betelgeuse (α Ori, $10^{-6} M_{\odot}/\mathrm{yr}$), seem to present molecular underabundance (Teyssier et al., 2012).

Long observing programs have revealed that RSGs present certain variability in their light curves (Kiss, Szabó, and Bedding, 2006; Yang and Jiang, 2012), seeming to be periodic or semi periodic with a primary period ($\sim$ 400 days) and a long secondary period ($\sim$ 2000 days). The first period is explained by radial amplitude pulsations related in principle to a change of size of the photosphere, as events such as bright flares are unlikely to happen or be periodic. The long period has been suggested to be explained by the formation of large convection cells on the surface (Stothers, 2010), sometimes as large as half of the diameter of the star, as it was observed in the first image of Betelgeuse by Haubois et al. (2009) or in Antares by Montargès et al. (2017).

With the help of interferometry, the spatial distribution of the dust shells became accessible (Monnier et al., 2004), and inner molecular gas shells were found (Perrin et al., 2004, 2005, 2007), being responsible for the absorption observed in certain molecular bands of the near infrared spectra. This scenario has been observed in more recent studies as in Montargès et al. (2014) and even upgraded for several outer molecular layers over the atmosphere (Hadjara et al., 2019). The innermost layers are usually located[3] at less than $2R_*$, considering R_* the radius of the photosphere of the star, presenting temperatures around 2000 K. Such layers are expected to be responsible of the production of the observed dust at higher radii as a result of the mass loss process which characterizes these immense and cool stars. The work of Arroyo-Torres et al. (2015) proved that their presence beyond the photosphere cannot be explained by convection or pulsation alone. Since the discovery of a 1 Gauss magnetic field on Betelgeuse (Aurière et al., 2010), Alfvén Waves have been invoked as a possible source of energy to levitate material in the atmosphere (Airapetian, Carpenter, and Ofman, 2010). Hence more research is needed to articulate a full theory to ultimately understand the mass loss processes in RSGs. Nevertheless, the study of these molecular layers requires spatially resolved targets (or at least partially resolved), an issue that strongly depends on the current technical limitations observing a type of stars that is not precisely frequent.

The work I have developed during my thesis aims at contributing to the sample of RSGs where at least one molecular shell has been found by studying the properties of a RSG located in the central parsec of the Galaxy, in order to help understanding the mass loss process.

[3]For RSG stars. Asymptotic Giant Branch stars, for example, have molecular shells much higher over the photosphere, at several R_*.

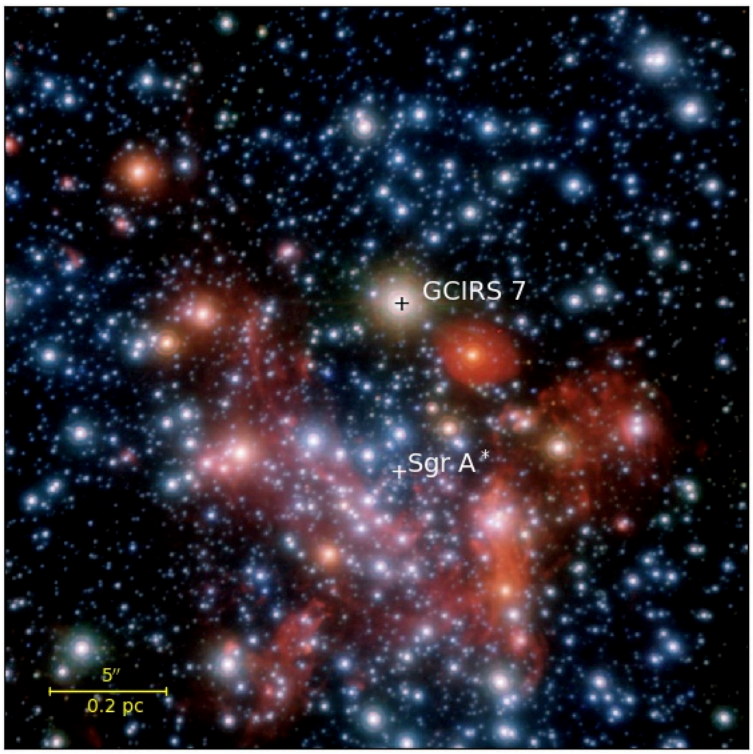

FIGURE 4.2: Central parsec of the Galaxy. Image obtained with NACO data (Source MPE: https://www.mpe.mpg.de/ir/GC)

4.2 The Red Super Giant star GCIRS 7

The first signatures of the variability of IRS 7 were reported by Blum, Sellgren, and Depoy (1996), who presented photometric measurements in J, H, and K bands proving the star has varied in brightness by 0.8, 0.5 and 0.3 magnitudes respectively in the last 10 years. They also classified the star as a M1-2 super giant, featuring the same physical properties as Betelgeuse, the closest and most studied RSG in the sky. With observations all over the decade, IRS 7 it is later classified as a Long Period Variable (LPV) by Ott, Eckart, and Genzel (1999).

The first interferometric observations of the star, called from now GCIRS 7 (Galactic Center Infra-Red Source 7) were published by Pott et al. (2008) with data collected by AMBER (NIR) and MIDI (MIR) at VLTI, studying the suitability of the star as a phase reference source for future interferometric studies of the Galactic Center. In the MIR they confirm the presence of silicate absorption, corresponding to the presence of warm dust ($T = 200$ K) extending far from the source with a strong interferometric signal (V<0.2). They obtained in K band the first estimate of the diameter of the photosphere as 2.6 mas, higher than the expected suggesting the presence of molecular shells and hot circumstellar dust.

Before this thesis, the latest analysis corresponding entirely to GCIRS 7 in the near infrared is the exhaustive work accomplished by Paumard et al. (2014), collecting all the archival data and complementing them with new spectroscopic (SINFONI) and interferometric observations in H band (PIONIER) and K band (AMBER). They built JHKL light curves with a total time span of 40 years (Figure 4.3), measured the effective temperature ($T_{\rm eff} = 3600 \pm 195$ K), determined the diameter of the source in H band for the first time ($\theta_{\rm H} = 1.076 \pm 0.093$ mas, or $R = 960 \pm 92\, R_\odot$ at

8.33 ± 0.35 kpc) and, by comparing with the K band measured diameter, they confirm the circumstellar contribution (up to 20%). With the collected data, they determine the age and initial mass of the star, resulting in 6.5-10 Myrs and $M_0 = 22.5 \pm 2.5\, M_\odot$ and determined a brightness variability consisting in a double period light curve of 470 days and 2800 days with an amplitude of 1.1 magnitude. Later, the first estimate of the mass loss of the star came by Tsuboi et al. (2020) with $\dot{m} = 10^{-4}\ M_\odot \mathrm{yr}^{-1}$. They report through ALMA observations a detection of an ionized shell at 4650 K enclosing the photosphere of IRS 7 located at $\sim 10^6\ R_\odot$ above it. The initial mass, the age of the star and the estimated mass loss suggest that this amount cannot have been constant since the birth of the star.

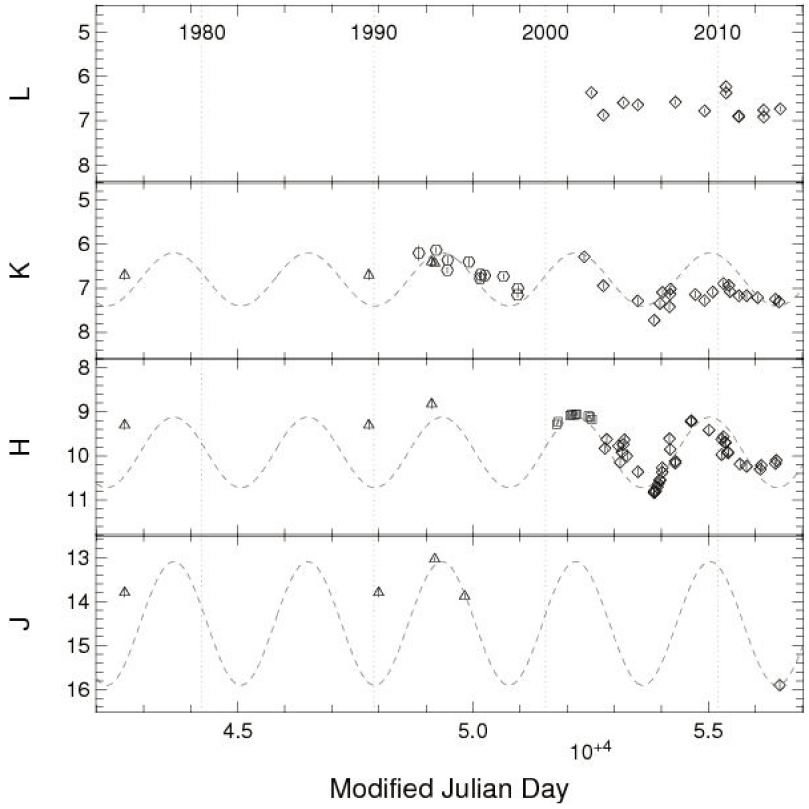

FIGURE 4.3: Archival light curves of GCIRS 7. Source: Paumard et al. (2014)

Observations taken with a difference of more than a year might reveal the phenomenology behind the light curve variations. The fact that the target can be moderately resolved by VLTI shows that it is not an appropriate interferometric calibrator to be used in Galactic Center studies. With the arrival of GRAVITY, the target is however a good candidate to be used as a fringe tracking star (and of course as adaptive optics natural guide star), to observe the stellar population[4] in dual field mode due to its brightness. One of the questions I considered while studying this target is the point whether the star's atmosphere and outer layers are distorted by the SMBH wind (as the cometary tail already observed) or on the contrary they present the shape of a shell like a typical RSG. This information can be extracted from the phase of the interferometer, revealing possible asymmetries.

[4]But not the central source, as the separation is higher than the diameter of the effective field of view transported by the VLTI for the UTs.

The spectral resolution of GRAVITY and its impressive sensitivity open the gate to determine the wavelength dependence of the visibility curves and characterize with better accuracy the size and shape of the photosphere, as well as the immediate circumstellar environment of GCIRS 7. Together with the already known variability of the target, a temporal evolution of its fundamental parameters can be determined choosing the adequate model.

4.3 Observations

The target is bright enough in K band to be observed with the AT telescopes (1.8m). Despite the fact that these auxiliary telescopes have less collecting surface and therefore they are less sensitive than the UTs, the variety of interferometric configurations available make them more suitable for certain bright targets, reaching in general a broader uv coverage. GCIRS 7 has been observed in two epochs, 2017 and 2019.

2017 data

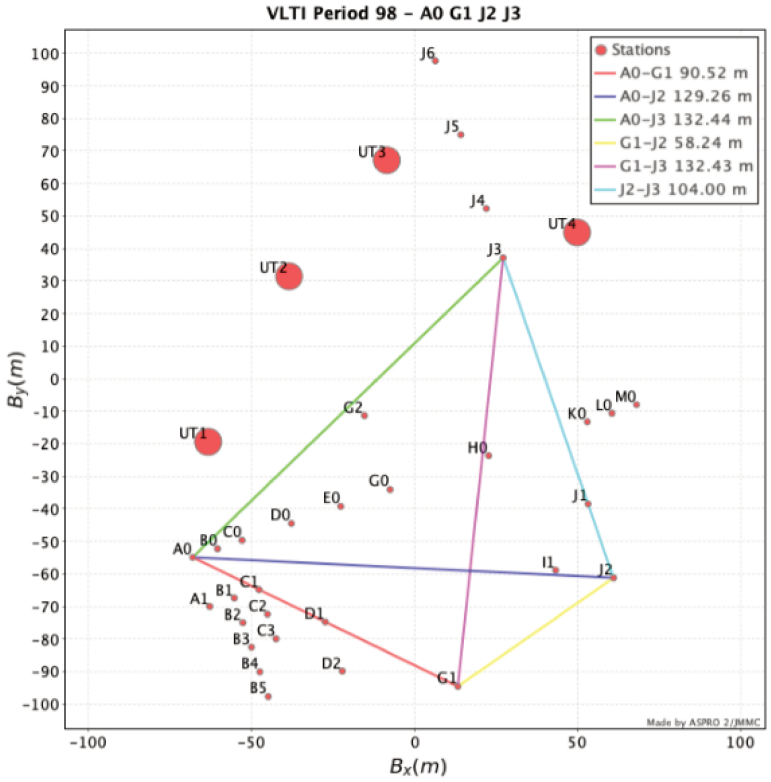

FIGURE 4.4: Telescope configuration for 2017 (LARGE). Source: JMMC/Aspro.

The data were collected before the start of the thesis work by other members of the GRAVITY collaboration in a stellar physics program, involving the study of surfaces and outer environments of giant stars (ID. 098.D-0250(B)). The run took place in the nights of 17 and 18 March of 2017 corresponding to GTO time. It made use of the four AT telescopes in the LARGE configuration (Figure 4.4) with a longest baseline of 132 m. This configuration prioritizes reaching high spatial frequencies (instead of a maximizing the sampling) being optimal for diameter measurements of particularly small targets.

Several stars were observed during this run, including five data frames from GCIRS 7 obtained at the end of the night (from 2017-03-18 09:06 UTC to 2017-03-18 09:55 UTC), in single field, MEDIUM resolution mode (210 spectral channels), COMBINED polarization (see Section 2.3 for a description of the modes). The strength of this study relies on the spectral resolution of the interferometer hence only the science channel is used in the thesis work[5].

The data have been taken in sequences SCI-SCI-SKY (SCI being the science frame and SKY a sky frame used in posterior reduction and calibration) with a total exposure time per frame of 300 seconds (NDIT=30 with DIT=10 s), followed by a sequence CAL-SKY (CAL being the interferometric calibrator frame, in this case the star HD160852) in the same configuration. The details on the calibration are explained in Section 4.3.1.

From this sample of five data frames, the first two of them are excessively noisy, non significant visibility samples with an average SNR$(V^2) < 3$ per spectral channel, and the third of them present inconclusive visibilities (some longer baselines present higher visibilities with a null phase). For these reasons I decided to take only the last two frames for this study. The total number of samples in the visibility curves is 1220 per frame, 2440 in total with an average signal-to-noise ratio of SNR$(V^2) = 18$ per spectral channel.

2019 data

According to the K band light curves derived by Paumard et al. (2014) (Figure 4.3), the predicted brightness in K band for 2017 would be near the peak of maximum brightness while an observation in 2019 would be near the valley (Figure 4.5). If this extrapolation is right, the magnitude difference between those cases could be $\Delta K \approx 1$.

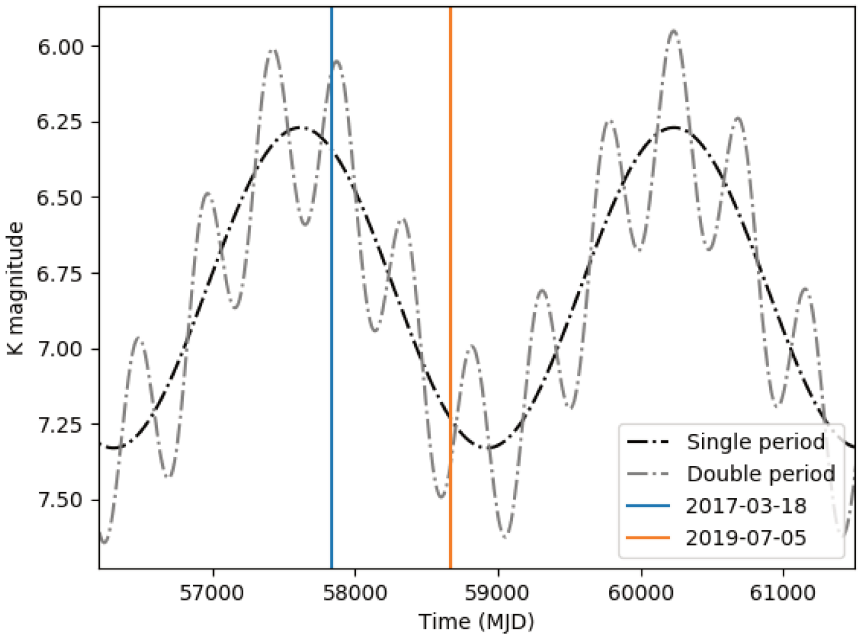

FIGURE 4.5: K magnitude prediction for 2019 using the curves derived in Paumard et al. (2014).

[5]The fringe tracker data is always recording in LOW resolution mode.

Such change of brightness could be due to a variation on the fundamental parameters of the star that an interferometer can observe. In order to determine whether or not the mechanisms responsible for this variability have changed in the recent years, I decided to extend the 2017 data that I was already analyzing by observing the target in 2019 for a deeper study. Therefore, I proposed including GCIRS 7 among the targets to be observed in the Galactic Center program of the GRAVITY Collaboration in 2019, as a part of the stellar population of the central parsec. We used part of the Guaranteed Time for Observations (GTO) we had already assigned for the AT telescopes for that purpose.

The planning and development of these runs and the data acquisition have been part of my thesis work, where I was in charge of the observations in Paranal for both of them with the help of the observatory staff and remote support from other members of the team in Europe. The first one took place in May (run ID: 0103.B-0032(E)) and the second one in July (run ID 0103.B-0032(F)).

The first run, during the nights of the 25^{th}, 27^{th} and 28^{th} of May 2019, was planned to observe GCIRS 7 and GCIRS 29N (a Wolf-Rayet star in the Galactic Center) using the star HIP88033 as an interferometric calibrator. Although I could have chosen the same interferometric calibrator than in 2017, the spectral class of this new one, a K0III star, makes it an optimal candidate to be used for both spectral and interferometric calibrator at the same time, without the need of any additional target (see Section 4.3.1). This decision was taken while preparing the 2019 run and could not be applied for 2017 as this last run was not planned to use the photometric spectral information. As a backup target we planned to observe the object HD163296, part of the exoplanet program of the GRAVITY Collaboration (ID 0103.C-0183(A)). The total assigned observing time was 1.3 nights always allocated in the second half of the night ($4 \times 0.65H2$). Unfortunately the weather conditions did not allow to find or track any fringe in GCIRS 7 during that run as the seeing was always over 1.5". As the conditions were impossible to observe the Galactic Center, I took a few data frames from the backup target (HD163296) in the first night. It was not possible to get any data from the rest of the nights due to bad weather.

The second run allowed me to take the necessary data from 2019. It took place during the nights of the 3^{rd}, 4^{th}, 5^{th} and 6^{th} of July 2019 with a total assigned observing time of 1.3 nights, always allocated in the first half of the night ($4 \times 0.65H1$). Again, I was the responsible of the data acquisition in Paranal, with the help of the observatory staff and remote support from Europe. As in 2017 it makes use of the four AT telescopes but with a slightly different telescope configuration, called ASTROMETRIC (Figure 4.6). It is an alternative of the LARGE configuration with a maximum baseline of 129.26 m with all the telescopes at the south of the delay line, which is needed to maximize astrometric measurements[6]. Although I have observed GCIRS 7 in single field mode, the reason why this configuration was chosen is the possibility to allocate some extra observing time to astrometric sequences of the central parsec stellar population.

Another difference with respect to 2017 is the use of the Wollaston prism (SPLIT polarization mode) obtaining at the end two data sets P1 and P2. However, the polarization is not studied in this thesis and the data sets are considered independently and averaged afterwards. The chosen spectral resolution has been MEDIUM

[6]This is due to the presence of asymmetries in the optical train, which translates into asymmetries in polarization, a problem for precision astrometry.

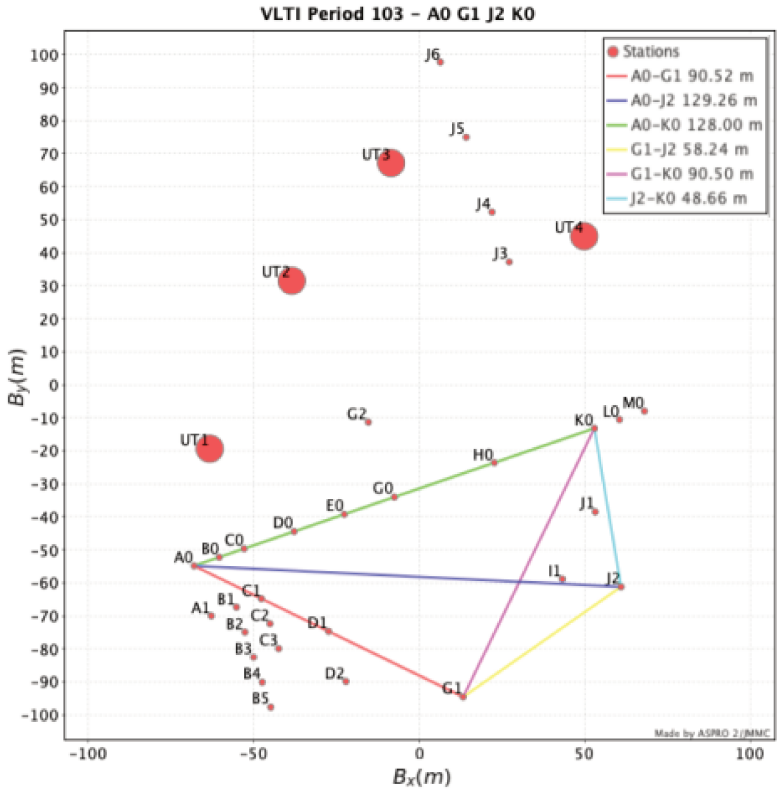

FIGURE 4.6: Telescope configuration for 2019 (ASTROMETRIC). Source: JMMC/Aspro.

as in 2017. After the implementation of NAOMI (Woillez et al., 2019) in 2018, the observations were assisted by adaptive optics also in the ATs, operating in the optical (450-900 nm) by using a visible natural guide star that is faint (R 14) and far away (about 15"). For this reason, the effect of the adaptive optics on the observations is very limited. The data have been taken in sequences SCI-SCI-SKY with a total exposure time per frame of 150 seconds (NDIT=30 with DIT=5s), followed by a sequence CAL-CAL-SKY recorded at the same exposure time and same number of integrations. The main targets for this run were GCIRS 7 and GCIRS 29N again. As calibrator I chose the same star as in the last run (May 2019), HIP88033.

I started observing the first night with some thin clouds and a seeing of 0.82". Fringes were found and we got some frames of GCIRS 7. We realized later that the calibrator presented a strong phase signal (probably signs of binarity) and I hence rejected it immediately as calibrator. As an alternative I chose the star HD153368 already used in AMBER observations. We kept recording frames during the night, until thick clouds made impossible to continue. A total of 3 sequences with 2 frames each were recorded, but the quality was not optimal due to the thin clouds in the atmosphere. At the end they were not used for this thesis work.

The second night was entirely focused on GCIRS 7 again. A more optimal calibrator[7] was chosen this time, the star HD161703 with spectral class K0III (see Section 4.3.1). The sky was clear during all the nighttime and the seeing was good, always between 0.5" and 0.9". The night came to its end with a total of 2 sequences with (4 data

[7]This calibrator was closer to the target, it was selected during the day when I have more time to plan the observations.

frames) in MEDIUM spectral resolution, from which 2 frames are used in this work corresponding to one of the two sequences (the other presented a strange visibility behaviour due to a problem in the calibration). We also tried to get a sequence observing GCIRS 7 also in HIGH spectral resolution mode (exposing 30 seconds with 10 integrations each), but the frames obtained were excessively noisy ($SNR(V^2) < 1$) and were finally not used for the thesis work.

The third night started with an attempt of an astrometric sequence over the central parsec stellar population with some technical problems related to the ESO pipeline. We decided at the end to focus again in GCIRS 7 and to try the astrometric sequence for the next night. We started recording in MEDIUM spectral resolution with an impressive seeing of 0.45", which kept increasing up to 0.95". After taking 3 sequences with 6 frames in total, I decided to record some data for other backup targets (ATMic, GJ65), for the proto-planetary disks and binary stars programs of the GRAVITY collaboration. This was the best night of all, from which I have used 5 frames (the first five) for this study, and rejected the last frame for visibility inconsistencies (higher visibilities for longer baselines despite having null phase). Unfortunately, the fourth night resulted in a weather loss due to high clouds so GCIRS 29N could not be observed. The uv coverage of the frames involved in this study is presented in Figure 4.7.

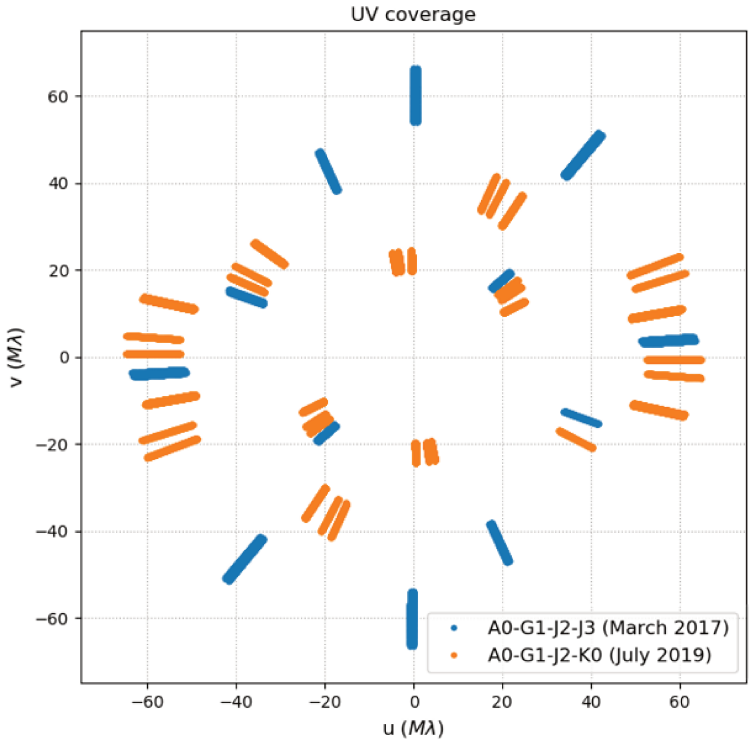

FIGURE 4.7: Total UV coverage for the data frames used for this thesis work. Each line, whose length is defined by the spectral coverage, corresponds to an observation.

4.3.1 Reduction and Calibration of the data

The data reduction and visibility calibration have been done by using the version 1.3.0 of the GRAVITY pipeline (Lapeyrere et al., 2014). An overview of the reduction process and the reduction files needed is described in Section 2.4.

TABLE 4.1: Observation log of the data frames used in this chapter. HD45124 (*) has been used for spectral calibration only (see Section 4.3.1). The atmospheric data has been obtained from Paranal ASM (Astronomical Site Monitoring).

Time (UT)	Target	Seeing (")	τ_0 (ms)
18-03-2017 (COMBINED mode)			
01:46:02	(*) HD45124 (CAL-SKY-CAL)	0.68-0.52	6.05
09:43:10	GCIRS 7 (SCI-SCI-SKY)	0.55-0.58	6.27
10:08:04	HD160852 (CAL-SKY)	0.71-0.64	4.48
05-07-2019 (SPLIT mode)			
04:49:38	GCIRS 7 (SCI-SCI-SKY)	0.69-0.53	4.49
05:08:29	HD161703 (CAL-CAL-SKY)	0.72-0.81	4.45
06-07-2019 (SPLIT mode)			
03:13:00	GCIRS 7 (SCI-SKY)	0.51-0.60	6.66
03:25:51	HD161703 (CAL-CAL-SKY)	0.60 -0.64	5.59
03:43:00	GCIRS 7 (SCI-SCI-SKY)	0.53-0.55	5.88
03:59:51	HD161703 (CAL-CAL-SKY)	0.72-0.88	3.68
04:17:12	GCIRS 7 (SCI-SCI-SKY)	0.91-0.75	3.55
04:33:39	HD161703 (CAL-CAL-SKY)	0.73-0.79	5.23

Data reduction

All the data frames used in this work and their corresponding observation modes are presented in Table 4.1. From all the data of the night, the frames used for the reduction of GCIRS 7 correspond to the following (all of them recorded in COMBINED, MEDIUM resolution modes using a DIT of 300 ms):

- A DARK frame, with a NDIT of 100.
- Four FLAT frames, one per telescope with a NDIT of 25.
- Two WAVE files (WAVE, WAVESC) with a NDIT of 512.
- Six P2VM files, one per baseline with a NDIT of 256.

In addition, one SKY frame has been used to remove the background light from the SCI frames, taken in the same sequence of the two SCI frames involved in the study, with the same configurations as the SCI frames (DIT=10 s, NDIT=30).

In the case of 2019, the calibration files are the same but in SPLIT, MEDIUM resolution modes. This time, all the frames are recorded in 30 sequences (NDIT=30) of 5 seconds each. From the total of 7 files used for this epoch, 4 SKY frames recorded in the same configuration and integration time are used.

Visibility calibration

In the same way as the data reduction, the calibration of the visibilities has been done by using the last version of the GRAVITY reduction and calibration pipeline (Lapeyrere et al., 2014). In 2017, the visibility calibrator used for the processing of GCIRS 7 is the star HD160852 ($\theta_{\rm LD} = 0.148 \pm 0.004$ mas, , Chelli et al., 2016) seen as a point source by the VLTI with $V^2 = 0.997 \pm 0.001$. It has been observed with the same integration time and exposures than the SCI frames (DIT = 10 s, NDIT = 30), and at the same airmass (Z=1.01).

In 2019, the chosen calibrator is the star HD161703 ($\theta_{\rm LD} = 0.38 \pm 0.01$ mas, , Chelli et al., 2016) with a visibility of $V^2 = 0.983 \pm 0.001$ and therefore not resolved for VLTI. It has been observed at the same configuration as the SCI frames (DIT = 5 s, NDIT = 30) as well as the same airmass as the corresponding frames of GCIRS 7 (Z=1.01).

Spectral calibration

To be fully successful, the model implemented to interpret the data must explain the interferometry and the spectroscopy at the same time, and no conclusion from the spectra can be obtained without a proper calibration. This step is needed to give a physical meaning to the continuum as well as to remove features introduced by external elements such as the Earth atmosphere from the recorded flux of GCIRS 7. The process begins with the observation of the spectral calibrator during the night, preferably as close as possible to the target (same air mass if possible) and with the comparison to a theoretical spectrum. For this work, I have chosen one of the supertemplates obtained from Cohen et al. (2003), corresponding to the star HD5319 with $A_V = 0$, a giant star classified as K0III (Houk and Swift, 1999). The calibration would be successful only if the calibrator observed during the night presents the same spectral features, and therefore the calibrator must have the same spectral class.

From the archive of 2017, only one K0III star was observed during the night (HD45124 with $m_{\rm K} = 4.95$, Cutri et al., 2003), recorded with DIT = 10 s, NDIT = 25 and a slightly higher airmass (Z=1.25) than the SCI sequence. This is not a problem as the use of this star in this study was limited to the spectral calibration and the study involves normalized spectra. In 2019, the same star (HD161703) and the same frames used for interferometric calibration (with the same airmass, DIT and NDIT) are also used to get the photometric spectral calibration.

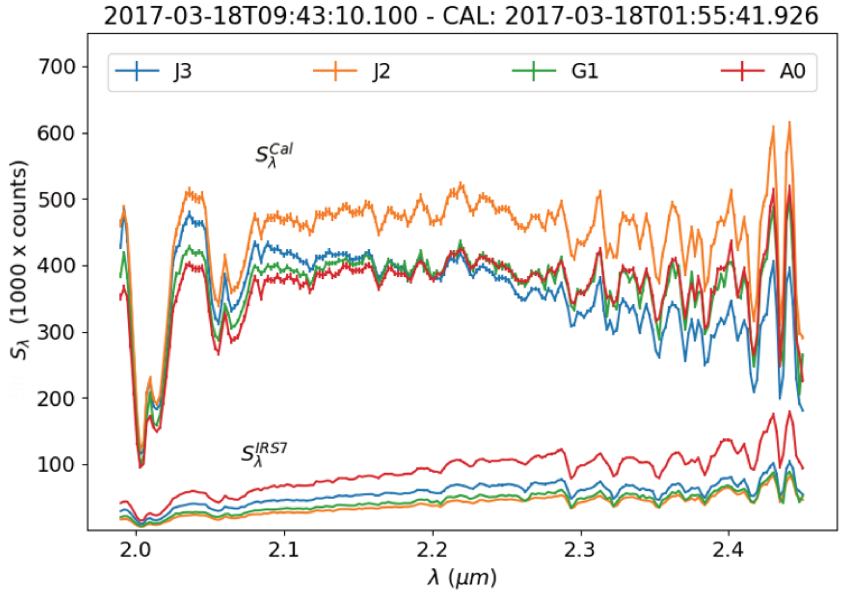

FIGURE 4.8: Signal recorded per telescope and spectral channel in a 2017 GCIRS 7 data frame (lower curves) and calibrator (upper curves).

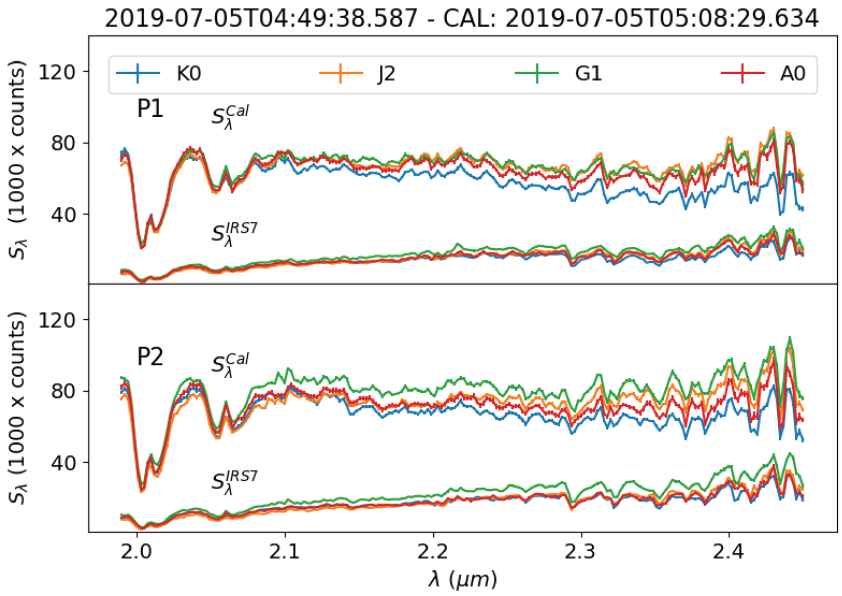

FIGURE 4.9: Signal recorded per telescope, spectral channel and polarization (P1 upper graph, P2 lower graph) in a 2019 GCIRS 7 data frame (lower curves of each graph) and calibrator (upper curves of each graph).

For each telescope, the calibrated spectra is given by the following flux density:

$$F_\lambda^{\mathrm{IRS7}} = \frac{S_\lambda^{\mathrm{IRS7}}}{S_\lambda^{\mathrm{cal}}} \times \frac{F_0^{\mathrm{ref}} \times \Delta\lambda \times 10^{-0.4 \times m_{\mathrm{K_S}}^{\mathrm{cal}}}}{\int_{\mathrm{K_S}} T(\lambda) F(\lambda)^{\mathrm{Cohen}} d\lambda} \times F(\lambda)^{\mathrm{Cohen}} \tag{4.1}$$

where:

- $S_\lambda^{\mathrm{IRS7}}$ is the recorded (non calibrated) signal of each GCIRS 7 frame (Figures 4.8 and 4.9).
- S_λ^{cal} is the recorded signal of the calibrator frame (Figures 4.8 and 4.9).
- $m_{\mathrm{K_S}}^{\mathrm{cal}}$ is the magnitude of the calibrator in the filter $\mathrm{K_S}$ of the 2MASS photometric system.
- $T(\lambda), F_0^{\mathrm{ref}}, \Delta\lambda$ are the transmission curve, the magnitude zero flux reference of the 2MASS $\mathrm{K_S}$ filter and its bandwidth, respectively, with $\Delta\lambda = 0.262$ μm and $F_0^{\mathrm{ref}} = (4.283 \pm 0.081) \times 10^{-14}$ $\mathrm{Wcm^{-2}\mu m^{-1}}$. The transmission curve is shown in Figure 4.10a.
- $F(\lambda)^{\mathrm{Cohen}}$ is the theoretical spectrum of the calibrator HD5319 in $\mathrm{Wcm^{-2}\mu m^{-1}}$. It is shown in Figure 4.10b.

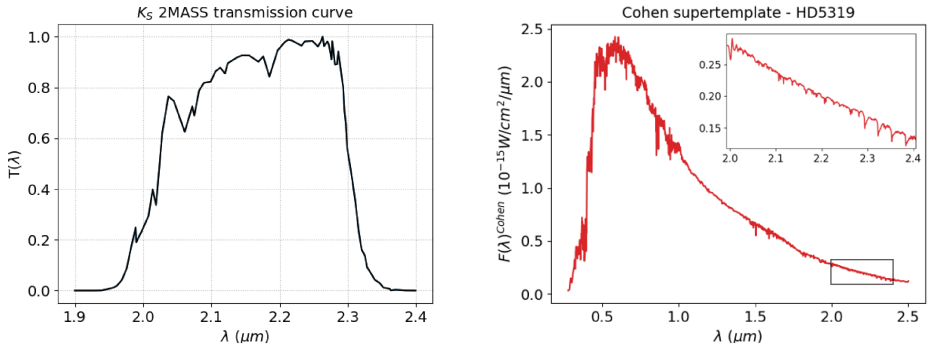

(A) Transmission curve of the 2MASS K_S filter (Skrutskie et al., 2006)

(B) Synthetic spectrum from Cohen et al. (2003).

FIGURE 4.10: Auxiliary curves used for the spectral calibration.

Calling $\sigma_\lambda^{\mathrm{IRS7}}$ and $\sigma_\lambda^{\mathrm{cal}}$ the uncertainties in the signal of the GCIRS 7 data frames and the calibrator frames respectively, the error bars of the calibrated flux have been obtained using error propagation:

$$\sigma_{F_\lambda}^c = \sqrt{\left(\frac{F_\lambda^{\mathrm{IRS7}}}{S_\lambda^{\mathrm{IRS7}}}\sigma_\lambda^{\mathrm{IRS7}}\right)^2 + \left(\frac{F_\lambda^{\mathrm{IRS7}}}{S_\lambda^{\mathrm{cal}}}\sigma_\lambda^{\mathrm{cal}}\right)^2} \tag{4.2}$$

where $F_\lambda^{\mathrm{IRS7}}$ comes from Equation 4.1. The calibrated spectra can be seen in Figure 4.11. While 2017 has been recorded without the Wollaston prism, 2019 is recorded in SPLIT mode and the calibration is done, in each case, applying Equation 4.1 to each polarization separately.

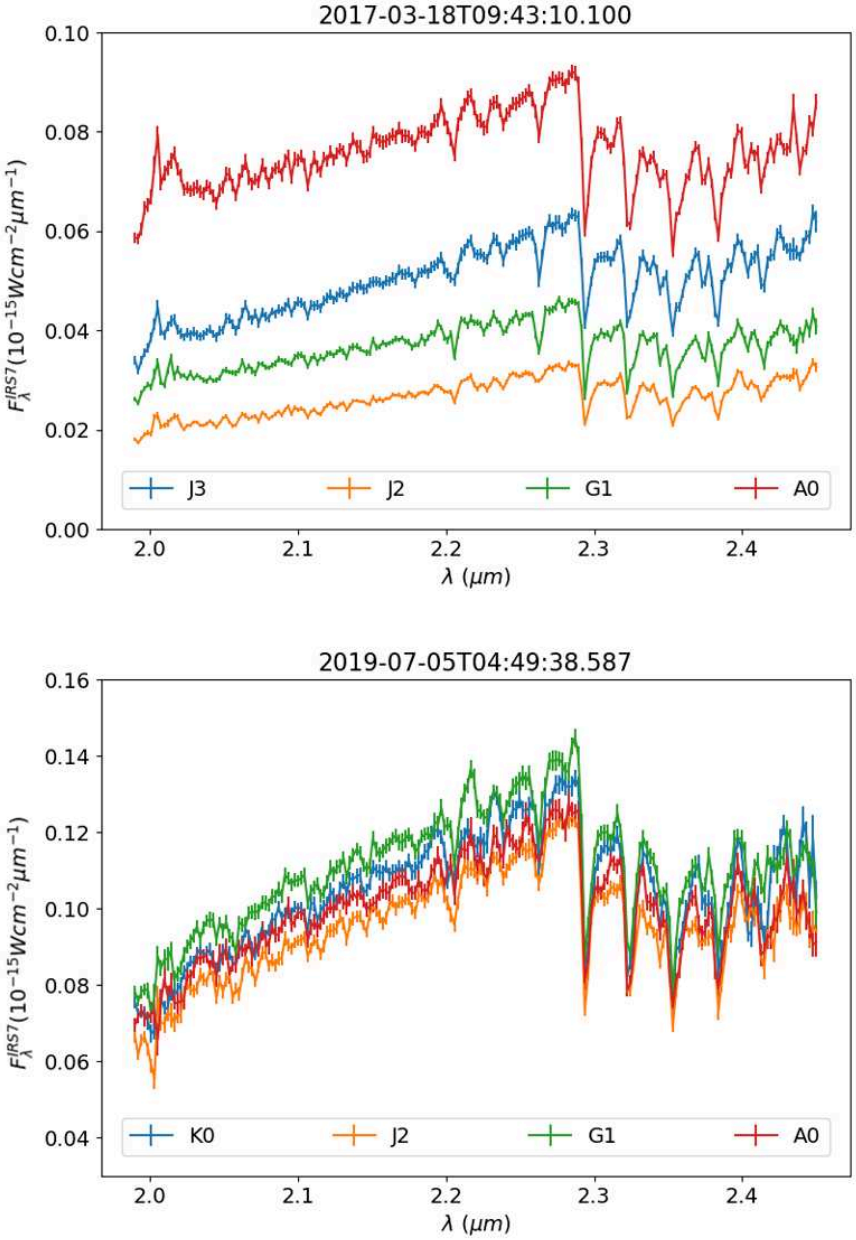

FIGURE 4.11: A calibrated frame for each epoch (Equation 4.1). The spectra of 2019, observed in SPLIT mode, is the average by channel between both polarizations P1 and P2, weighted by the square of their uncertainties.

The resulting spectra for 2019 are obtained as the average of the two polarizations weighted by the square of the uncertainties:

$$\left(F_\lambda^{\mathrm{IRS7}}\right)^{(2019)} = \frac{w_{\mathrm{P1}}\left(F_\lambda^{\mathrm{IRS7}}\right)^{(2019,\ \mathrm{P1})} + w_{\mathrm{P2}}\left(F_\lambda^{\mathrm{IRS7}}\right)^{(2019,\ \mathrm{P2})}}{w_{\mathrm{P1}} + w_{\mathrm{P2}}}$$

where $w_{\mathrm{P}i} = \left[(\sigma^c_{F_\lambda})^{(2019,\ \mathrm{P}i)}\right]^{-2}$ with $i = 1, 2$. The quantities $\left(F_\lambda^{\mathrm{IRS7}}\right)^{(2019,\ \mathrm{P}i)}$ are obtained independently using Equation 4.1. Their respective uncertainties have been obtained with the Equation 4.2.

The quotient $S_\lambda^{\mathrm{IRS7}}/S_\lambda^{\mathrm{cal}}$ removes the instrumental effects and the features introduced by the Earth's atmosphere, and multiplying by $F(\lambda)^{\mathrm{Cohen}}$ removes the spectral line features introduced by the calibrator, but only if the calibrator and the theoretical template share the same spectral class[8]. In the case of 2017, there was already data from a K0III star in the archive for that night. It is HD45124 with $m_{\mathrm{K_S}}^{\mathrm{cal}} = 4.952$ (Houk and Swift, 1999), observed at the beginning of the night. Unfortunately, it was not observed at the exact same air mass as GCIRS 7 ($Z_{\mathrm{cal}} = 1.2$ while $Z_{\mathrm{IRS7}} = 1$). This could potentially affect the molecular bands in water and for this reason, those wavelengths are not considered for this study. About 2019, I chose HD161703 with $m_{\mathrm{K_S}}^{\mathrm{cal}} = 5.582$ (Houk, 1982), which is also a K0III star (the same class as the supertemplate chosen), as well as an appropriate interferometric calibrator as it is not resolved by the interferometer. Hence, for 2019 the same star is used in both steps, interferometric calibration and spectroscopic calibration. As the transmission curve $T(\lambda)$ is not defined for $\lambda > 2.4$ μm, I did not use the GRAVITY channels for $\lambda > 2.4$ μm for the final study.

The spectra corresponding to the four telescopes after the calibration are not equal, but proportional to each other (Figure 4.11). This effect, which happens in every data frame and is more noticeable in 2017 than in 2019, is likely due to the fibre injection, an instrumental effect corrected during the commissioning phase of the instrument. Although a measurement of the absolute flux could possibly be done in 2019, the same measurement in 2017 would be completely inaccurate. As no conclusion could be taken from the absolute flux, it is finally not used for this work. Luckily it does not affect the slope of the spectrum, and a normalization of the spectrum is applied after the correction by interstellar extinction.

[8]The spectral class must be the most stable possible (an evolved or a variable star as a calibrator, for example, would not work).

4.4 Modelling the data

4.4.1 Interstellar extinction

In presence of dust, photons with optical wavelengths are absorbed by the dense interstellar medium and re-emitted with higher wavelengths. This effect is called interstellar extinction, and makes an astrophysical target appear redder than how it really is. As the contrast of the target is normalized by definition, the interstellar extinction does not affect the visibility curves, but it strongly affects the spectrum. Studying extinction towards a target can give insights about how this interstellar matter is behaving, or even its own nature.

It is no surprise that it is precisely towards the Galactic Center where we find the greater accumulation of interstellar matter in the Galactic plane. The region is mostly opaque at optical wavelengths ($A_V > 30$), and even in the infrared interstellar extinction can be important. Due to the nature and composition of the nuclear stellar cluster, it is known that presents an interstellar medium clumpy and heterogeneous (Ciurlo et al., 2016), which can vary from a line-of-sight to the next and along a given line-of-sight (Ciurlo et al., 2019). For this reason, I have decided to derive the extinction from the source itself for each epoch, to be able to extract conclusions from the spectra. The relative extinction between two spectral lines is measured in magnitudes and it can be defined as (Fritz et al., 2011):

$$A_{\lambda_2-\lambda_1} = -2.5 \log_{10} \left(\frac{F_{obs}(\lambda_2)/F_{obs}(\lambda_1)}{F_{exp}(\lambda_2)/F_{exp}(\lambda_1)} \right) \tag{4.3}$$

where the indices exp and obs refer to the expected and the observed flux densities, respectively. The absolute extinction could be obtained if the extinction in a certain wavelength is known. For that purpose it is common to derive extinction laws comparing two different spectral domains to estimate the expected reddening for a certain wavelength, given a particular region in the sky. For the thesis work, I took the extinction law obtained in Fritz et al. (2011), a power law specific for the Galactic Center:

$$A_\lambda = A_0 \times \left(\frac{\lambda}{\lambda_0} \right)^\alpha . \tag{4.4}$$

By using a radio continuum map (2 cm) with data from VLA, ISO-SWS spectra (mid infrared) and SINFONI spectra (near infrared), they have created maps in Brackett γ among other spectral lines. For K band (2-2.5 μm), the index 0 is therefore taken at the Brackett γ line ($\lambda = 2.166$ μm) and their best fit gives $A_0 = 2.62 \pm 0.11$ and $\alpha = -2.11 \pm 0.06$.

Unfortunately GCIRS 7 is an extremely bright source which saturates all the maps and therefore it has been removed from them, leaving a hole in its position (Figure 4.12). For this reason, the obtained value of A_0 is not applicable to the extinction observed towards GCIRS 7 as there should be some extra extinction due to some circumstellar contribution. To estimate its value it is possible to use the slope of the spectra measured with GRAVITY after the flux calibration (Figure 4.11).

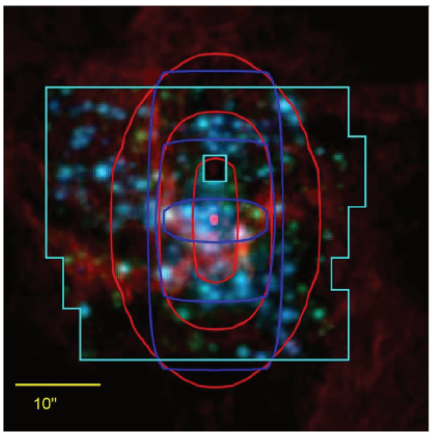

FIGURE 4.12: Field of view of the maps used to derive the extinction law towards the Galactic Center. Red is for radio continuum from VLA, blue and green are H band and K_S band from SINFONI, respectively. Unfortunately the hole corresponds to the position of GCIRS 7. Source: Fritz et al. (2011).

In order to avoid line contamination, the slope of the spectrum must be taken as the slope of the continuum. I chose to take $2.1 < \lambda < 2.2$ (in μm) as the continuum where to find the value of A_0 with $\lambda_0 = 2.166$ μm. Assuming the target as spherically symmetric and isotropic in the continuum with an expected flux from a perfect black body, the observed flux is:

$$F_\lambda = \Gamma B_\lambda(T) 10^{-0.4 A_\lambda} \tag{4.5}$$

$B_\lambda(T)$ being the Planck law, defined as:

$$B_\lambda(T) = \frac{2hc^2\lambda^{-5}}{\exp\left(hc/\lambda k_B T\right) - 1}. \tag{4.6}$$

The factor Γ encloses all the geometry and the instrumental effects on the target, and it vanishes taking, for a fixed T:

$$\frac{d(\log F_\lambda)}{d\lambda} = \frac{1}{F_\lambda}\frac{dF_\lambda}{d\lambda}. \tag{4.7}$$

Introducing Equation 4.4 in Equation 4.5 and taking Equation 4.7:

$$A_0 = \frac{-2.5}{\alpha \log(10)} \left(\frac{\lambda}{\lambda_0}\right)^{-\alpha} \left[\frac{\lambda}{F_\lambda}\frac{dF_\lambda}{d\lambda} - \frac{z}{\lambda T}\left(1 + \frac{1}{e^{(z/\lambda T)} - 1}\right) - 5\right] \tag{4.8}$$

where $z = hck_B^{-1}$. The value proposed for T is the effective temperature measured in Paumard et al. (2014) ($T_{\text{eff}} = 3600 \pm 195$ K). According to Figure 4.13 the extincted black body curve is not distinguishable from a straight line in the continuum region (comparing with the size of the error bars), which allows to simplify the calculations by taking the value of the slope of that straight line as the value of the derivative of the flux, taking the range $2.1 < \lambda < 2.2$ (in μm).

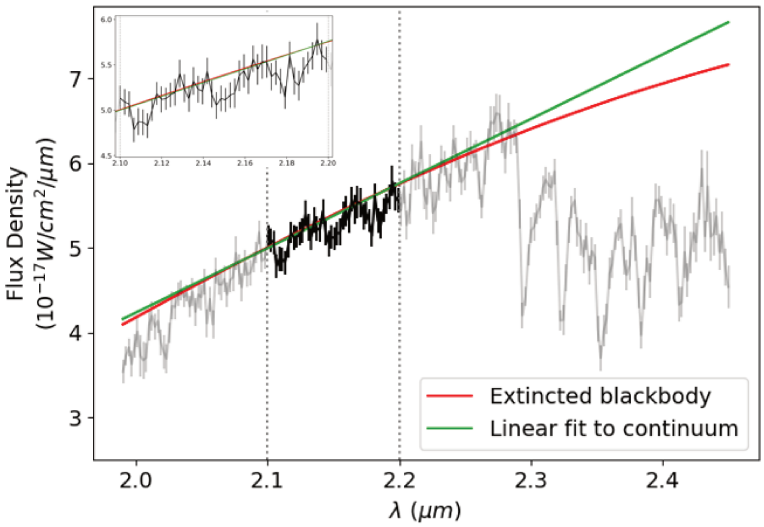

FIGURE 4.13: Approach to obtain the parameter A_0. The red line corresponds to an extincted black body multiplied by a constant (Equation 4.5). In the continuum region, the difference is small enough to simplify the calculations by fitting a straight line.

A single straight line fit is done for every spectrum in the sample (8 for 2017, 14 for 2019) returning a value of A_0 for each telescope by using Equation 4.8. The average result per epoch obtained is:

$$A_0(2017) = 3.29 \pm 0.28 \ ,$$
$$A_0(2019) = 3.27 \pm 0.12 \ .$$

The average of the two epochs (weighted by the square of their uncertainties) is $A_0 = 3.27 \pm 0.11$, as the extinction is the same at the two epochs. This value is higher than that obtained in Fritz et al. (2011) at 4σ ($A_0 = 2.62 \pm 0.11$), possibly confirming the initial hypothesis of the close circumstellar contribution. A further discussion can be found in Section 4.6.1.

The average of all the values of A_0 per epoch is used to normalize every spectrum separately. With the calibration and the correction by extinction, the only remaining step is to correct by the factor Γ:

$$F_\lambda^N \Gamma = \frac{F_\lambda^{\mathrm{IRS7}}}{B_\lambda(T) 10^{-0.4 A_\lambda}} \ . \tag{4.9}$$

This quantity is shown in Figure 4.14. By definition the value of the corrected flux in the continuum must be equal to one. The value of Γ, which is different per telescope, is then taken as the average of the quantity shown in Equation 4.9 in the continuum (the black points). For that purpose, the continuum sample has been extended towards $\lambda < 2.29$ μm as the value of Γ can be sensitive, avoiding the deepest spectral lines whose peak is observed at $2.2057, 2.2277, 2.2387, 2.2629$ μm, by rejecting the channels with $\lambda = 2.2 - 2.21$ μm, $2.22 - 2.24$ μm, and $2.26 - 2.27$ μm in its calculation.

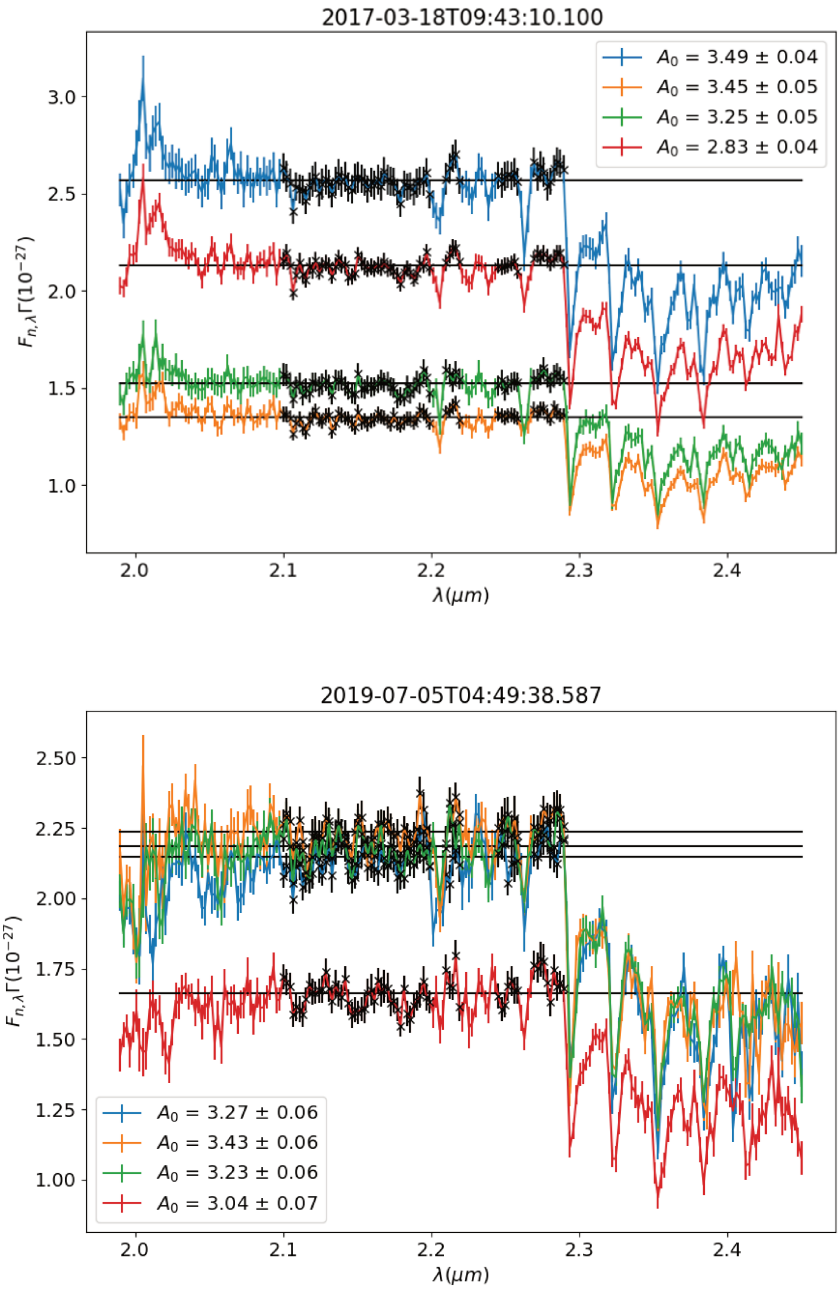

FIGURE 4.14: Result from Equation 4.9 for a data frame of each epoch. The black points are the ones used to estimate the value of Γ.

The final correction is, according to Equation 4.9:

$$\left(F_\lambda^N\right)_i = \frac{\left(F_\lambda^{\mathrm{IRS7}}\right)_i}{B_\lambda(T)10^{-0.4A_\lambda}\Gamma_i} \ , \tag{4.10}$$

where $\left(F_\lambda^{\mathrm{IRS7}}\right)_i$ is the calibrated flux (from Equation 4.1) for the channel λ and the telescope i. The error bars are obtained as follows:

$$(\sigma_{F_\lambda})_i = \frac{\left(\sigma_{F_\lambda}^c\right)_i}{B_\lambda(T)10^{-0.4A_\lambda}\Gamma_i} \ , \tag{4.11}$$

with $\left(\sigma_{F_\lambda}^c\right)_i$ obtained from Equation 4.2. As the four telescopes observe the target simultaneously, the fact that every Γ_i is different implies that every telescope presents a different response for a same spectrum, probably related to instrumental effects[9], such as differences due to local seeing effects and to the centering of the fibers. For each epoch a weighted average of the normalized spectra is obtained by using:

$$\left(F_\lambda^N\right)^{(\mathrm{year})} = \frac{\sum_i^m (\sigma_{F_\lambda})_i^{-2}\left(F_\lambda^N\right)_i}{\sum_i^m (\sigma_{F_\lambda})_i^{-2}} \ . \tag{4.12}$$

The number m is the total number of samples per year, which is $m = 8$ for 2017 (4 telescopes, 2 data frames) and $m = 28$ for 2019 (4 telescopes, 7 data frames). The error bar considered corresponds to the standard deviation from the weighted mean[10]:

$$\left(\sigma_\lambda^N\right)^{(\mathrm{year})} = \sqrt{\frac{\sum_i^m (\sigma_{F_\lambda})_i^{-2}\left[\left(F_\lambda^N\right)_i - \left(F_\lambda^N\right)^{(\mathrm{year})}\right]^2}{(m-1)\sum_i^m (\sigma_{F_\lambda})_i^{-2}}} \ . \tag{4.13}$$

The result can be shown in Figure 4.15. The two spectra share the same continuum, slightly differing in the regions where the presence of molecules is known, as $\lambda = 2.03$ μm (water) or beyond $\lambda = 2.29$ μm (CO and water, Perrin et al., 2004). Emission lines are not expected in the K band spectra of a RSG star, and knowing that water is involved in the region near $\lambda = 2.03$ μm, the discrepancy observed between both spectra is probably due to the effect of the Earth atmosphere. Furthermore, the first channels and the last channels of GRAVITY corresponding to the shortest and the largest wavelengths present in general a poorer response than the central channels. For these reasons, in addition to the limits imposed by the 2MASS K_S band filter transmission curve ($\lambda_{\max} = 2.4$ μm), I have decided to limit the study to the range $\lambda = [2.05, 2.40]$ μm.

[9] Luckily this does not affect the study of the different components of the spectrum as the work is done over normalized quantities. However, it is not possible to obtain an accurate measurement of the absolute flux to contribute to the archival light curves.

[10] This formula is valid if every weight is different from zero, which is the case.

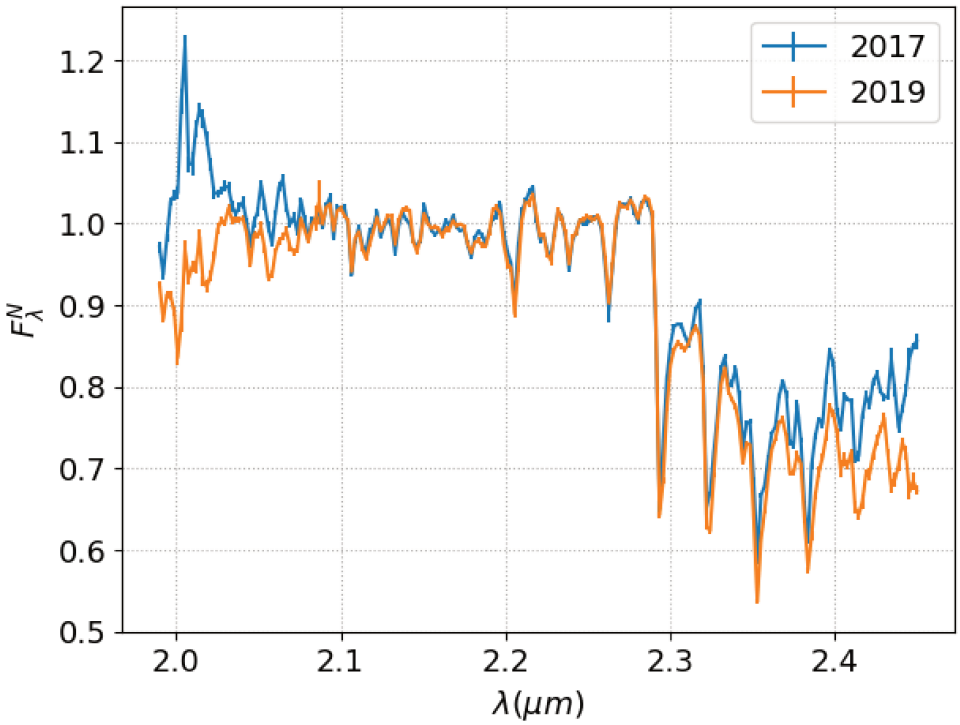

FIGURE 4.15: Normalized spectra per epoch.

4.4.2 The Uniform disk + background

The simplest of the geometrical models that can describe an axisymmetric extended source in the sky is the uniform disk. It constitutes the very first approach towards the structure of any unresolved target. Taking $\theta_{\rm UD} = 2\sqrt{\alpha^2 + \delta^2}$ with α and δ the angular distance to the phase center in the sky, the specific light intensity distribution of a uniform disk can be written as:

$$I_\lambda(\theta_{\rm UD}) = \begin{cases} I_0 & \text{if } r \leq \theta_{\rm UD}/2 \\ \\ 0 & \text{otherwise,} \end{cases} \tag{4.14}$$

where r is the radial distance from the center of the target in the sky's plane. The quantity $\theta_{\rm UD}$ is therefore called uniform disk diameter, with angular units. If interferometry is available for that target, this quantity can be measured using the van Cittert - Zernike theorem (van Cittert, 1934; Zernike, 1938), which applied to Equation 4.14 and adding a uniform background becomes:

$$V_{\rm UD}(q, a, \theta_{\rm UD}) = \frac{2aJ_1(\pi q \theta_{\rm UD})}{\pi q \theta_{\rm UD}} \ , \tag{4.15}$$

where J_1 is the Bessel function of the first kind, a is a parameter quantifying the fraction of coherent light from the star and $q = \sqrt{u^2 + v^2}$, where u and v are the Fourier pair of α, δ and correspond to the spatial frequencies sampled by the interferometer.

The visibility curves given by Equation 4.15 can be seen in Figures 4.16 and 4.17 for certain values of θ_{UD} and a, along with the maximum spatial frequency observed with the baseline configurations involved in the study. According to those figures, if the target is well described by an uniform disk[11], the first zero of the visibility amplitude is observable for this interferometer only if its diameter is $\theta_{\mathrm{UD}} \geq 3.83$ mas. If the target is smaller, it will not be completely resolved. In the most recent work about GCIRS 7, Paumard et al. (2014) obtain a size in K band for GCIRS 7 in the range $\theta = (1.5, 2)$ mas. This implies that the target would never be fully resolved with the actual VLTI baseline coverage. However, this is not an obstacle to extract spatial information from the visibility curves.

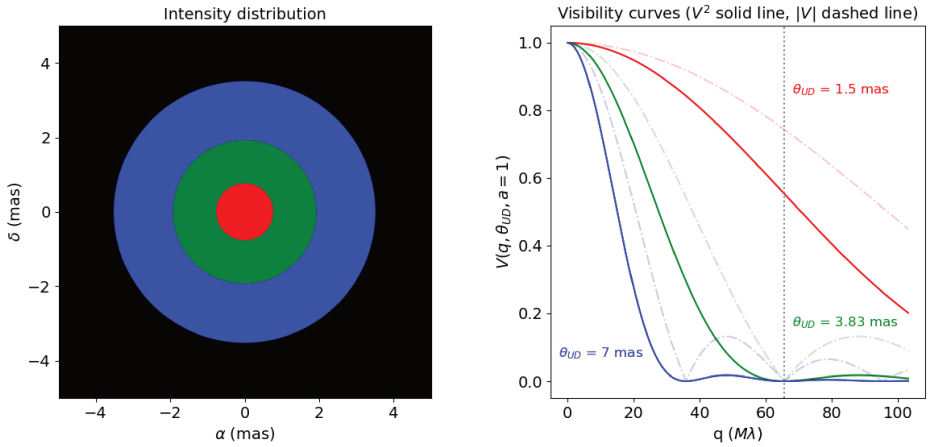

FIGURE 4.16: Intensity distribution and visibility curves for three uniform disks with different sizes (without background light). The pointed vertical line represents the maximum coverage VLTI is able to reach with the used configurations (Section 4.3).

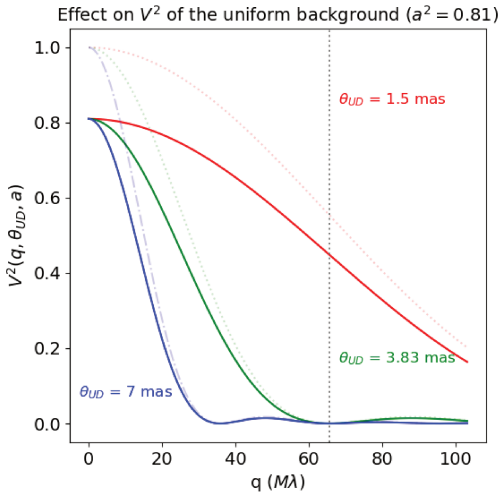

FIGURE 4.17: Squared visibility decrease due to an uniform background $a = 0.9$. The position of the zeroes does not change.

[11] A limb darkening model would be more realistic if the coverage was larger, but the fact that no visibility measurement is smaller than 0.4 will not make any significant difference with the uniform disk model.

As $u = \frac{B_x}{\lambda}$ and $v = \frac{B_y}{\lambda}$, for each wavelength channel involved there is a number of spatial frequency samples equivalent to the total number of baselines (6 in our case). These samples define a visibility curve that can be treated independently per spectral channel (Section 4.5.1). At the end, after a correction by incoherent background a $\theta_{\mathrm{UD}}(\lambda)$ profile is derived. Such profile would be nothing but the sizes of a set of uniform disks observed by the interferometer as a function of λ (in a similar manner as Figure 4.16 but considering a disk for every spectral channel) providing a first approach to the spectral dependency of the geometry of the object. Any significant deviation from a central value would hint the presence of a physical structure that would require a more complex model to be explained.

4.4.3 The thin layer model

To interpret a dependency of the uniform disk diameter on wavelength, a more complex model is needed. In this thesis work, I have studied and implemented a two component model: a photosphere responsible for the continuum light surrounded by a layer of negligible thickness responsible of the deep absorption lines. This model, called MOLsphere and firstly proposed for red supergiants by Tsuji (2000), has been successfully implemented for the first time by Perrin et al. (2004) in a sample of Mira stars and by Perrin et al. (2005) in a RSG star. It has also been proven successful for fully resolved stars like Betelgeuse (Perrin et al., 2007; Montargès et al., 2014), constituting a first step to study the circumstellar environment of a given evolved star. Thanks to the spectral resolution of GRAVITY, I have been able to apply this model to produce the first characterization of the photosphere and the circumstellar environment around GCIRS 7, which is to this date the evolved star with the smallest apparent size and the farthest one where a structure has been characterized.

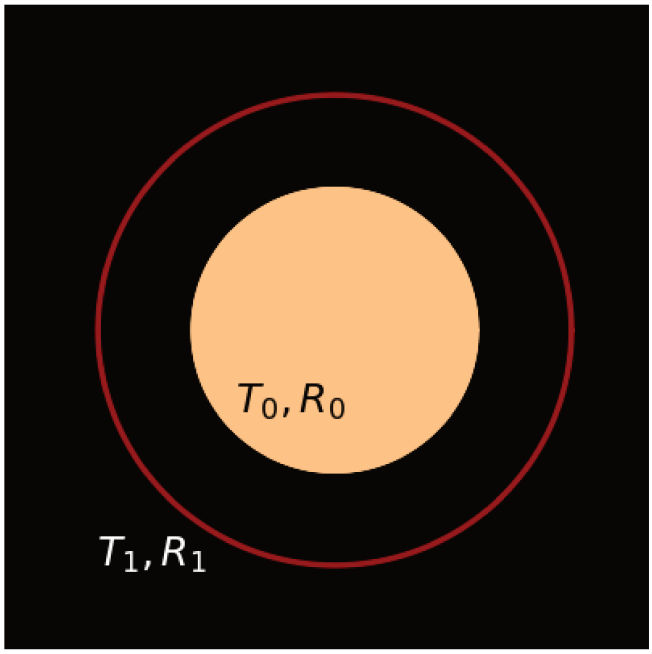

FIGURE 4.18: Pictorial description of the thin layer model. The space between the photosphere and the layer is assumed to be empty.

The specific light intensity distribution of the whole target is defined as:

$$I_\lambda(r, T_k, R_k, \tau_\lambda) = \begin{cases} B_\lambda(T_0) \exp\left(-\tau_\lambda \Big/ \sqrt{1-(r/R_1)^2}\right) \\ +B_\lambda(T_1)\left[1-\exp\left(-\tau_\lambda \Big/ \sqrt{1-(r/R_1)^2}\right)\right] & \text{if } 0 \le r \le R_0 \\ B_\lambda(T_1)\left[1-\exp\left(-2\tau_\lambda \Big/ \sqrt{1-(r/R_1)^2}\right)\right] & \text{if } R_0 < r \le R_1 \\ 0 & \text{otherwise,} \end{cases} \tag{4.16}$$

where $k = 0, 1$. The photosphere and the shell are each defined by a radius R and a temperature T such as $T_0 > T_1$ and $R_1 > R_0$. The optical depths τ depend on the wavelength and are associated to the thin layer only, which has negligible thickness. The function $B_\lambda(T_k) = B(\lambda, T_k)$ is the Planck function and r is the angular distance between the center and the limb of the star.

If the optical depth is zero, the model returns Equation 4.14 with $I_0 = B(\lambda, T_0)$ and $\theta_{\mathrm{UD}} = 2R_0$, which is a uniform disk with the parameters of the photosphere. If the optical depth is so high that the shell is optically thick ($\tau \to \infty$) the model also converges to Equation 4.14 but in this case $I_0 = B(\lambda, T_1)$ and $\theta_{\mathrm{UD}} = 2R_1$.

As it is assumed that the layer cannot be hotter than the photosphere and the spectrum has been already normalized, it is convenient to divide Equation 4.16 by $B(\lambda, T_0)$, with a result displayed in Figure 4.19. This quantity presents an attenuation limit which is reached for high values of τ, and its value depends uniquely on the ratio of temperatures for a given wavelength. Indeed, if $\tau \to \infty$ the value of $I_\lambda(r, T_k, R_k, \tau_\lambda)/B(\lambda, T_0) = B_\lambda(T_1) \Big/ B_\lambda(T_0)$.

Let us call $\Omega_\lambda(T_0, T_1) = B_\lambda(T_1) \Big/ B_\lambda(T_0)$ this limit of brightness attenuation due to the presence of the shell, which is nothing but the ratio between the two black body emissions and obviously, $\Omega_\lambda(T_0, T_1) \le 1\ \forall\lambda$. Given a spectral line, an intensity profile lower than $\Omega_\lambda(T_*, T_{\mathrm{L}})$ would be the signature that the medium is too dense (Figure 4.19) and the assumption of negligible thickness would not be adequate. This is the main limitation of the model, and it can be a problem explaining deep absorption lines. The center to limb variation can be expressed as a function of this parameter Ω_λ:

$$\frac{I_\lambda(r,T_k,R_k,\tau_\lambda)}{I_\lambda(0,T_k,R_k,\tau_\lambda)} = \begin{cases} \dfrac{1+\left[\frac{1-\Omega_\lambda(T_0,T_1)}{\Omega_\lambda(T_0,T_1)}\right] f(r,R_1)^{-\tau_\lambda}}{1+\left[\frac{1-\Omega_\lambda(T_0,T_1)}{\Omega_\lambda(T_0,T_1)}\right] e^{-\tau_\lambda}} & (0 \leq r \leq R_0) \\ \dfrac{1-f(r,R_1)^{-2\tau_\lambda}}{1+\left[\frac{1-\Omega_\lambda(T_0,T_1)}{\Omega_\lambda(T_0,T_1)}\right] e^{-\tau_\lambda}} & (R_0 < r \leq R_1) \\ 0 & r > R_1 \ , \end{cases} \tag{4.17}$$

where $f(r,R_1) = \exp\left(1 \Big/ \sqrt{1-(r/R_1)^2}\right)$. It is straightforward to see that if $\tau = 0$, $I_\lambda(r)/I_\lambda(0) = 1$ for $r \leq R_0$ and 0 otherwise. For $\tau \to \infty$, $I_\lambda(r)/I_\lambda(0) = 1$ for $r \leq R_1$ and 0 otherwise. The thin layer model therefore represents a balance between these two cases: for continuum lines the expected optical depths would be near zero corresponding to the first case, while for strong absorption lines the expected output is the second case (Figures 4.19 and 4.20). From now, let us call $*, L$ the indices for the photosphere and layer previously called $0, 1$.

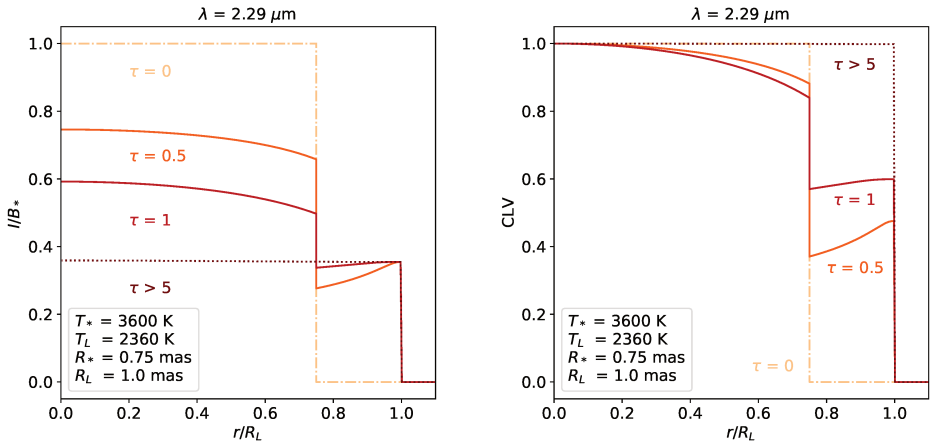

FIGURE 4.19: *Left*: Equation 4.16 normalized by a black body with $T = T_*$. The maximum attenuation factor is 1.53 for that temperature pair. *Right*: center to limb variation as a function of τ_λ fixing the rest of the model parameters (Equation 4.17).

As seen in the Figure 4.20, the sole variation of τ could explain an apparent change of size of the target observed in two different spectral channels. The shell is also responsible of the limb darkening effect on the photosphere. While the uniform disk model is purely phenomenological, the single thin layer constitutes a physical approach to the environment of the star, being able to explain a set of different apparent disk sizes by the presence of a single object.

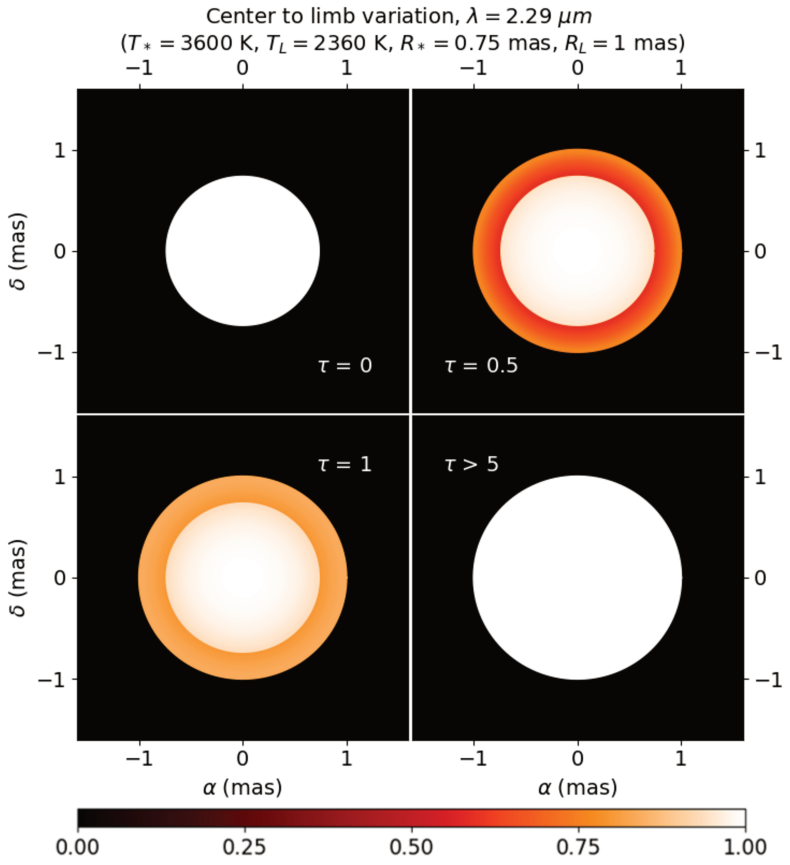

FIGURE 4.20: 2D Center to limb variation as seen by the observer for several values of τ_λ (Equation 4.17). The model tends to reproduce a uniform disk with the size of the layer if τ increases.

As for our model $I_\lambda = 0$ for $r > R_\mathrm{L}$, the observed flux density at the wavelength λ would be the following:

$$F_\lambda(T_*, T_\mathrm{L}, R_*, R_\mathrm{L}, \tau_\lambda) = 2\pi \int_0^{R_\mathrm{L}} I_\lambda(r, T_*, T_\mathrm{L}, R_*, R_\mathrm{L}, \tau_\lambda) r dr \ . \tag{4.18}$$

This quantity corresponds to the observed spectrum (after calibration). The fact that $T_* > T_\mathrm{L}$ and the conservation of energy implies that the maximum flux would be that given by the photosphere alone (Figure 4.19) as the layer is responsible of the absorption lines. The flux would be maximum if the transparency is full. As it is more convenient to work with normalized quantities, we can define the normalized flux density using the photosphere as a reference:

$$F^N_\lambda(T_*, T_\mathrm{L}, R_*, R_\mathrm{L}, \tau_\lambda) = F_\lambda(T_*, T_\mathrm{L}, R_*, R_\mathrm{L}, \tau_\lambda) \Big/ F_\lambda(T_*, T_\mathrm{L}, R_*, R_\mathrm{L}, \tau_\lambda = 0) \ , \tag{4.19}$$

which is the same quantity as the observed flux after normalization (Equation 4.10).

Introducing Equation 4.16 in Equation 4.18 and combining them in Equation 4.19, we get an expression for the normalized flux:

$$F_\lambda^N(T_*, T_\mathrm{L}, R_*, R_\mathrm{L}, \tau_\lambda) = \frac{2\Omega_\lambda(T_*, T_\mathrm{L})}{R_*^2}\left[\frac{R_\mathrm{L}^2}{2} + \frac{1-\Omega_\lambda(T_*, T_\mathrm{L})}{\Omega_\lambda(T_*, T_\mathrm{L})}\int_0^{R_*} f(r, R_\mathrm{L})^{-\tau_\lambda} r dr - \int_{R_*}^{R_\mathrm{L}} f(r, R_\mathrm{L})^{-2\tau_\lambda} r dr\right] . \quad (4.20)$$

The normalized flux density equation presents three terms. The first one corresponds to the emission of a black body of the size of the layer normalized by the photosphere. The second term correspond to the limb darkened emission[12] of the inner photosphere. The third term corresponds to the self-absorption of the layer as it is substracted from the total. For $\tau_\lambda = 0$ the first and the third terms cancel each other and the total flux is $F_\lambda^N = 1$. For $\tau_\lambda \to \infty$ the first term is the only one which does not vanish returning a uniform disk with the size of the layer, who acts now as the new photosphere.

The interferometer observables can be modelled using the van Cittert - Zernike theorem (van Cittert, 1934; Zernike, 1938) which, assuming azimuthal symmetry, becomes the Hankel transform of the intensity function divided by the observed flux density:

$$V_\mathrm{mol}(q, T_*, T_\mathrm{L}, R_*, R_\mathrm{L}, \tau_\lambda) = \frac{2\pi\int_0^{R_\mathrm{L}} I_\lambda(r, T_*, T_\mathrm{L}, R_*, R_\mathrm{L}, \tau_\lambda)\exp(2\pi q r)dr}{F_\lambda(T_*, T_\mathrm{L}, R_*, R_\mathrm{L}, \tau_\lambda)} . \quad (4.21)$$

These visibility curves depend intrinsically on λ via τ_λ. Their value can be computed by solving four integrals:

$$V_\mathrm{mol}(q, T_*, T_\mathrm{L}, R_*, R_\mathrm{L}, \tau_\lambda) = \frac{\int_0^{R_*} I_\lambda(\mathrm{in})\exp(2\pi q r)dr + \int_{R_*}^{R_\mathrm{L}} I_\lambda(\mathrm{out})\exp(2\pi q r)dr}{\int_0^{R_*} I_\lambda(\mathrm{in}) r dr + \int_{R_*}^{R_\mathrm{L}} I_\lambda(\mathrm{out}) r dr} , \quad (4.22)$$

where

$$I_\lambda(\mathrm{in}) = I_\lambda(0 \le r \le R_*, T_*, T_\mathrm{L}, R_*, R_\mathrm{L}, \tau_\lambda)$$

and

$$I_\lambda(\mathrm{out}) = I_\lambda(R_* < r \le R_\mathrm{L}, T_*, T_\mathrm{L}, R_*, R_\mathrm{L}, \tau_\lambda)$$

as $I_\lambda(r, T_*, T_\mathrm{L}, R_*, R_\mathrm{L}, \tau_\lambda)$ is defined in Equation 4.16. An example can be seen in Figure 4.21, generated by considering a set of four wavelengths with the values $\lambda = 2.26, 2.30, 2.34, 2.38\ \mu$m, with the same fundamental parameters and optical depths of the Figures 4.19 and 4.20. If the optical depth is null or too big, the model returns the visibility curve of a uniform disk (Figure 4.16), which is exactly the same as described in Figures 4.19 but in the Fourier space.

[12] The limb of the photosphere is darkened by the shell.

A contrast function can be defined to show the effect of the absorption lines on the visibility samples, as the visibility counterpart to the normalized spectrum. This quantity is nothing but the average of the band to continuum visibility ratio over a sample of visibilities:

$$C_{V2}(\lambda) = \left\langle \frac{V_c^2(q_i, T_* = T_{\rm eff}, T_{\rm L}, R_* = \theta^*_{\rm UD}/2, R_{\rm L}, \tau_\lambda)}{V_c^2(q_i, T_* = T_{\rm eff}, T_{\rm L}, R_* = \theta^*_{\rm UD}/2, R_{\rm L}, \tau_\lambda = 0)} \right\rangle_i . \tag{4.23}$$

It is a powerful tool to visualize the accuracy of the model relative to the visibilities. Taking the appropriate subset of baselines, C_{V2} is displayed as a function of λ combining both spectral and spatial information in a same picture.

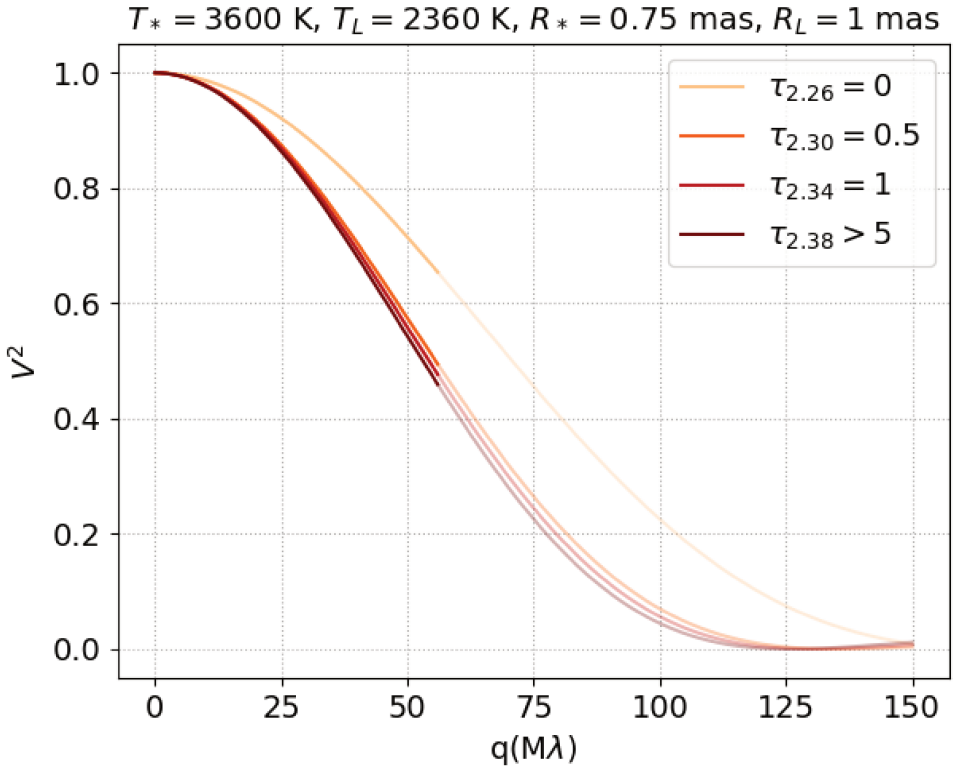

FIGURE 4.21: Visibility squared for a hypothetical shell model (Equation 4.21). The fainter curves correspond to spatial frequencies unavailable for VLTI.

4.5 The components of GCIRS 7 observed by GRAVITY

The full data set, calibrated and corrected by interstellar extinction is shown in Figure 4.22. The lack of significant phase signal (compatible with a random distribution of mean zero degrees and a standard deviation of less than 5 degrees) reveals that the target can be considered point-symmetric in the two epochs. Therefore, for the whole study, I made use only of the calibrated spectra and the visibility squared samples to fit the models.

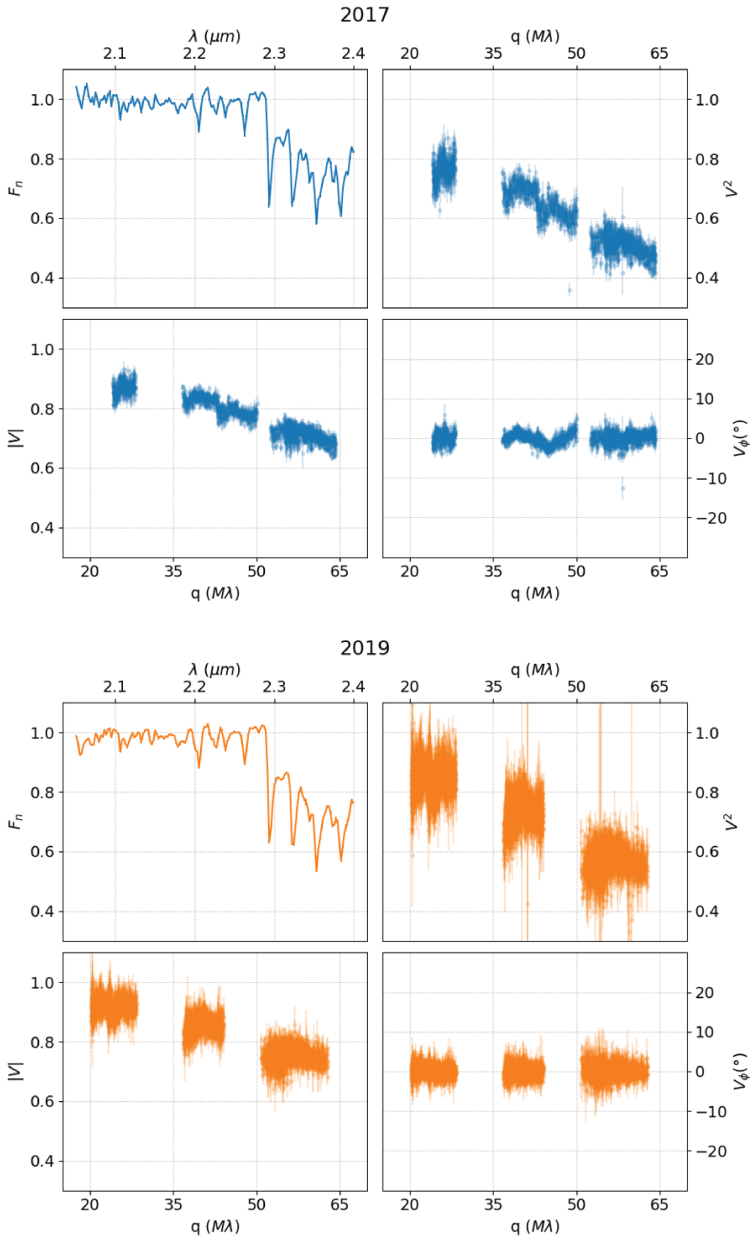

FIGURE 4.22: 2017 data set, involving 2 data frames and 2019 data set, involving 7 data frames. The data shown in 2019 corresponds to the average of P1 and P2.

4.5.1 The resolved incoherent background and the photosphere

If the interferometer has spectral coverage, its output can be interpreted as a visibility curve for each spectral channel i, sampled with N baselines. A wavelength dependent background $a(\lambda)$ can be obtained fitting a uniform disk for each of those curves with a Levenberg-Marquardt least squares fit, taking the squared visibility from Equation 4.15 and minimizing:

$$\chi_i^2 = \sum_{j=0}^{N} \left(\frac{V_{\rm UD}^2(q_j, a_i, \theta_{UD,i}) - V_i^2(q_j)}{\sigma_{V_i^2}(q_j)} \right)^2 , \tag{4.24}$$

where $V_{\rm UD}^2 = |V_{\rm UD}|^2$ (defined in Equation 4.15), V_i^2 are the squared visibilities sampled and measured by the interferometer and $\sigma_{V_i^2}$ the uncertainties on the measurements. For every wavelength channel in the data frame and for each polarization state, a fit involving two parameters $(a, \theta_{\rm UD})$ and six samples (one measurement per baseline) is performed. In 2017 there are in total 2 data frames in COMBINED polarization, making a total of N=12 samples per wavelength channel and therefore 10 degrees of freedom per fit. In 2019, there are 7 frames in SPLIT polarization, making a total of 2 data sets (P1 and P2) of N=42 samples per wavelength channel each, and therefore 40 degrees of freedom per fit. The results of the parameters have been averaged among polarizations afterwards, using the weighted average formula (in a similar manner as Equation 4.12). The profiles $a(\lambda)$ are shown in Figure 4.23 with the minimum χ_r^2 reached for each fit. Overall the result is satisfactory as 81% of the spectral channels involved in the study ($\Delta\lambda = 2.05 - 2.40$ μm) return a minimum $\chi_r^2 < 3$ for 2017, while this rate increases to 96% for 2019 (both for P1 and P2 individually).

Although $\theta_{\rm UD}(\lambda)$ could be obtained directly from this fit, part of its contribution is absorbed in the quantity a_i as $\theta_{\rm UD}(\lambda)$ and $a(\lambda)$ are degenerate. As by definition the background must be incoherent, to remove it properly and to obtain a realistic measurement of the uniform disk diameter an average value a_c can be removed from V_i^2 choosing the appropriate continuum to minimize the signal loss. The chosen continuum is again $\lambda_c = [2.1 - 2.2]$ μm and the average values of a_c obtained are:

- 2017: $\bar{a_c} = 0.93 \pm 0.01$.
- 2019: $\bar{a_c} = 0.97 \pm 0.01$.

Consequently, 7% of the light collected by the fibers of GRAVITY coming from the circumstellar background in 2017 is spatially incoherent, while this percentage drops to 3% in 2019. Putting these average values of a into perspective, it seems that the background level has changed between the two epochs. In the work of Paumard et al. (2014) they obtain a coherent stellar flux of $a = 0.76$ using AMBER (UT telescopes, 8.2m), much lower than GRAVITY (AT telescopes, 1.82m). The difference observed is not necessarily attributed to the only influence of circumstellar dust, as instrumental effects such as the size of the effective field of view or the angular resolution of the telescopes can be involved in its value. Indeed, the increase of coherence in 2019 compared to 2017 could be explained by the reduction of the field of view while using adaptive optics, after the implementation of NAOMI. The effect of the background in the visibility modelling can be seen in Figure 4.24, as well as the diameter limits obtained in Paumard et al. (2014).

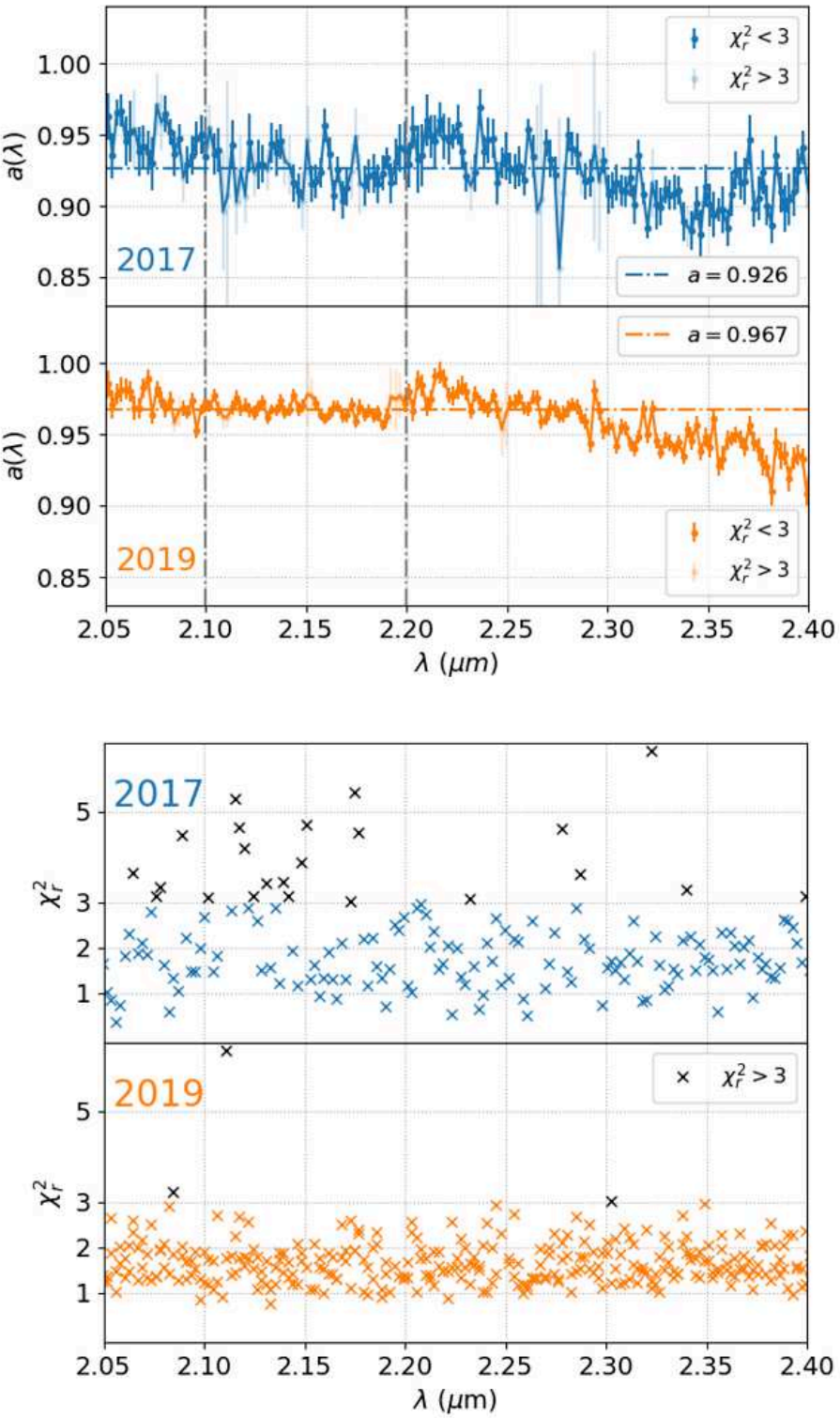

FIGURE 4.23: *Top:* background per wavelength channel according to Equation 4.24. The average value in the continuum is shown for each epoch. *Bottom:* resulting χ_r^2 for each epoch minimizing Equation 4.24 per spectral channel. Each point corresponds to a visibility curve fit.

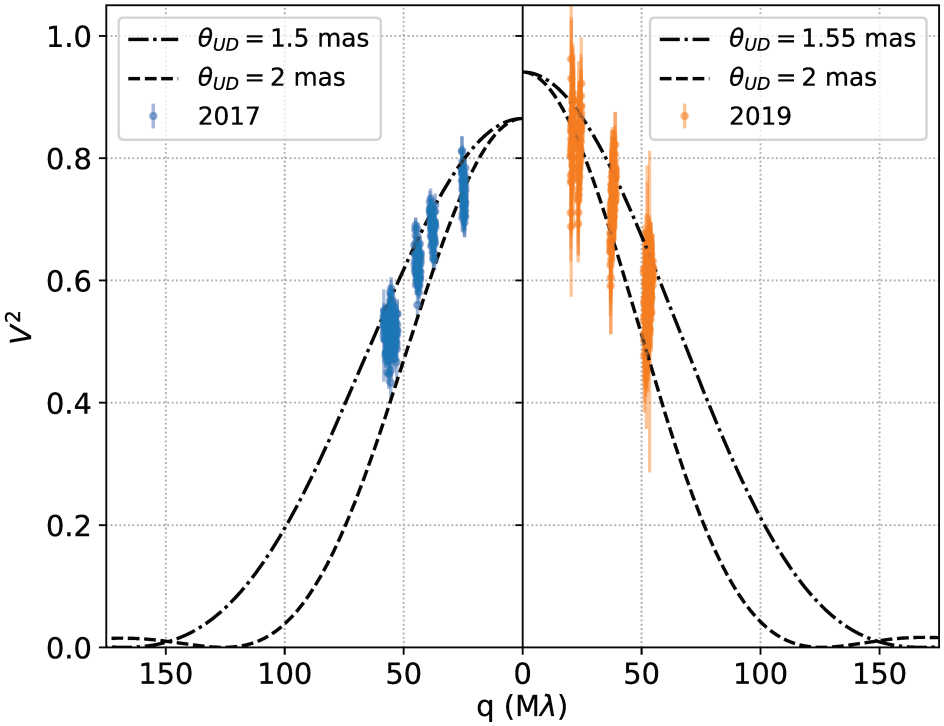

FIGURE 4.24: V^2 data. The visibility curves corresponding to the diameter limits obtained by Paumard et al. (2014) are presented with the average background levels shown in Figure 4.23.

The contribution of the incoherent background can be removed from the visibilities by:

$$V_{c,i}^2 = V_i^2 / \bar{a_c}^2 \ , \tag{4.25}$$

and therefore a diameter-wavelength profile $\theta_{\rm UD}(\lambda)$ can be finally obtained by fitting:

$$\chi_i^2 = \sum_{j=0}^{N} \left(\frac{V_{\rm UD}^2(q_j, a=1, \theta_{UD,i}) - V_{c,i}^2(q_j)}{\sigma_{V_{c,i}^2}(q_j)} \right)^2 \ , \tag{4.26}$$

with $\sigma_{V_{c,i}^2}(q_j) = \sigma_{V_i^2}(q_j)/a_c^2$. This profile would give a first approach to the spatial distribution of the chemical components present in the outer layers of the atmosphere of the star. The results are shown in the Figures 4.25 and 4.26. Any significant deviation from the average diameter for any spectral channel would constitute a strong evidence of the existence of certain structure impossible to detect only via spectroscopy.

In the second fit routine, after correcting by background, 152 out of the 159 spectral channels involved present $\chi_r^2 < 3$ (96%) in 2017 and in the two polarizations of 2019[13]. Unfortunately for 2017 the diameter peak corresponding to the first CO overtone line is not successfully fitted ($\chi_r^2 > 3$), as it is for 2019. In absence of strong spectral lines, the average UD diameter corresponding to the continuum (again 2.1-2.2 μm) is:

- 2017: $\theta_{\rm UD}^* = 1.548 \pm 0.050$ mas.
- 2019: $\theta_{\rm UD}^* = 1.550 \pm 0.050$ mas.

However, this method has two limitations: by fitting channel by channel, one does not measure the slope of the model very well, which make the two parameters being degenerate, and by fitting all the data sets at once, one does not probe the instrument stability. An alternative approach has been proposed when the paper (Rodríguez-Coira et al. 2020, Appendix A) has been discussed with the co-authors of the consortium: instead of splitting the data by wavelength all the channels at once are fitted, but SCI frame by SCI frame (and still polarization by polarization in 2019). This way, the slope of the visibility curve is clearly visible in each fit, breaking the degeneracy between the two parameters and being able to measure a scatter between the various data sets. This scatter is due to the stability of the instrument and of the atmosphere and dominates the uncertainty. This second method gives:

- 2017: $\theta_{\rm UD}^* = 1.547 \pm 0.030$ mas.
- 2019: $\theta_{\rm UD}^* = 1.549 \pm 0.030$ mas.

[13]The spectral channels with a wrong fit are not the same from data set to data set, but their quantity is surprisingly conserved.

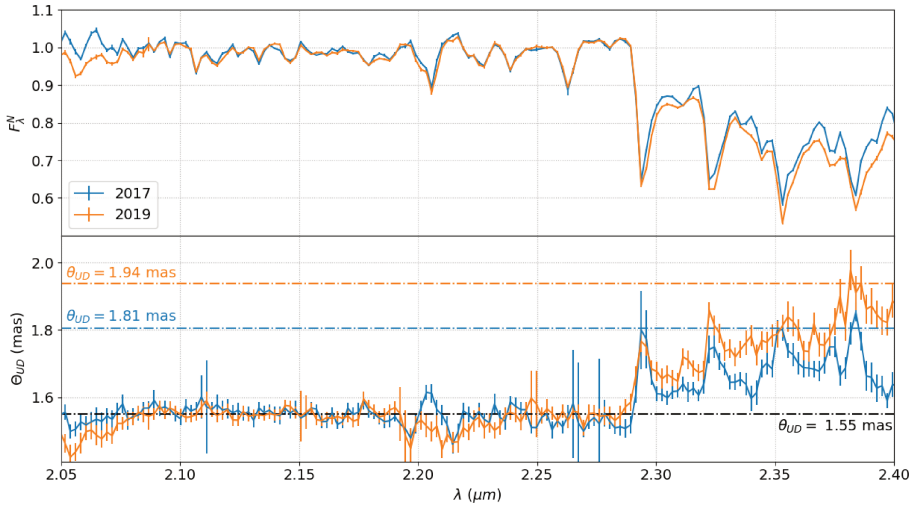

FIGURE 4.25: Calibrated spectra and Uniform disk per channel fit obtained by minimizing Equation 4.26.

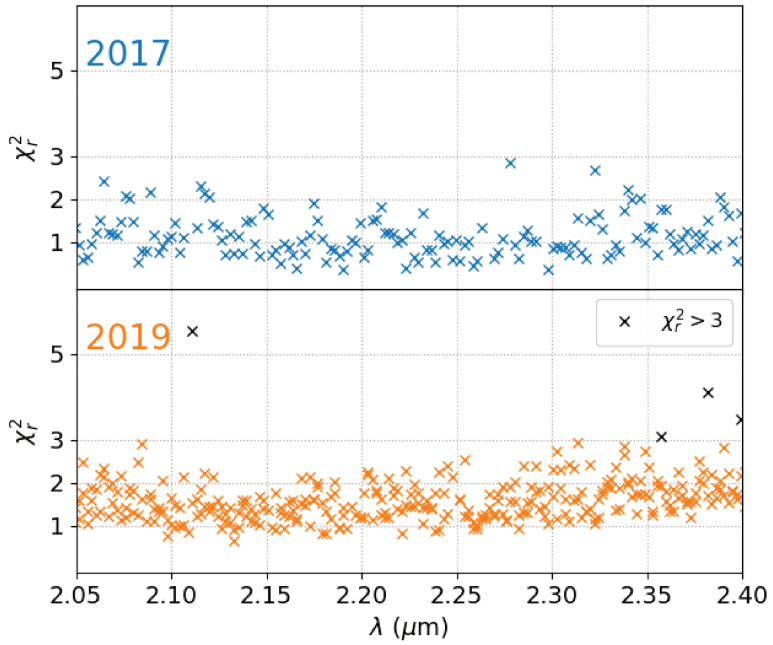

FIGURE 4.26: Resulting χ_r^2 for each epoch minimizing Equation 4.26 per spectral channel. Again, each point corresponds to one visibility curve fit but this time the visibility curves have been corrected by background. For 2019 the two polarizations are shown (two points per spectral channel), fitting their visibility curves independently.

It is worth noting that this uncertainty on the uniform disk diameter (30 μas) is itself quite an achievement, of the same order as the astrometric measurements performed by GRAVITY (Gravity Collaboration et al., 2020a).

I have adopted a same diameter of $\theta^*_{\rm UD} = 1.55 \pm 0.03$ mas as the average of them, proving that it is the same at the two epochs. This result is in principle surprising due to the K band variability of the target according to archival data (Paumard et al., 2014). A further discussion can be found in Section 4.6.2.

There is a significant increase in the apparent uniform disk diameter corresponding to the wavelengths higher than 2.29 μm, with the diameter peaks matching the overtone molecular lines of CO. The presence of a shell surrounding the photosphere where the CO molecule is located would explain this diameter increase, an expected outcome in the context of the structure of a typical RSG (Perrin et al., 2004, 2005; Montargès et al., 2014). A lower limit on the diameter of the shell can be obtained by measuring the maximum uniform-disk size in the CO bands:

- 2017: $\theta^L_{\rm UD} \geq 1.805 \pm 0.017$ mas $= (1.166 \pm 0.027)\ \theta^*_{\rm UD}$.
- 2019: $\theta^L_{\rm UD} \geq 1.939 \pm 0.019$ mas $= (1.251 \pm 0.026)\ \theta^*_{\rm UD}$.

To measure these minimum diameters I have chosen the central peak of the fourth CO head band and the two values at its sides, then averaged their diameter values. A quick comparison with other RSGs yields a ratio shell-photosphere of 1.28 for μ Cep (Perrin et al., 2004), or 1.25 for α Ori (Montargès et al., 2014). A more complex model (several layers) implemented by Hadjara et al. (2019) founds a larger ratio of 1.76 for the outer layer for α Sco. This result for GCIRS7 would be compatible with all of them.

The UD diameters in the CO molecular bands in 2019 are slightly higher than the ones for 2017. This could be a hint that the size of this hypothetical layer could have increased, although it is not strong evidence, as this apparent change of size could be due to the variation of other parameters such as temperature or density. Hence the need for a more complex model to describe the circumstellar environment of the target, as the thin layer model described in Section 4.4.3.

The corrected fitted visibility curves (Equation 4.25) corresponding to the minimum uniform disk size of the hypothetical shell (measured at $\lambda = 2.381 - 2.386$ μm) and the continuum (measured at $\lambda = 2.1 - 2.2$ μm) are shown in Figure 4.27 with the respective visibility samples corresponding to those wavelength channels. These data sets cannot be properly explained with a single model consisting in a unique uniform disk. Although the target is partially resolved, the impressive sensitivity of GRAVITY allows to guess the presence of an extended structure and even study its temporal evolution.

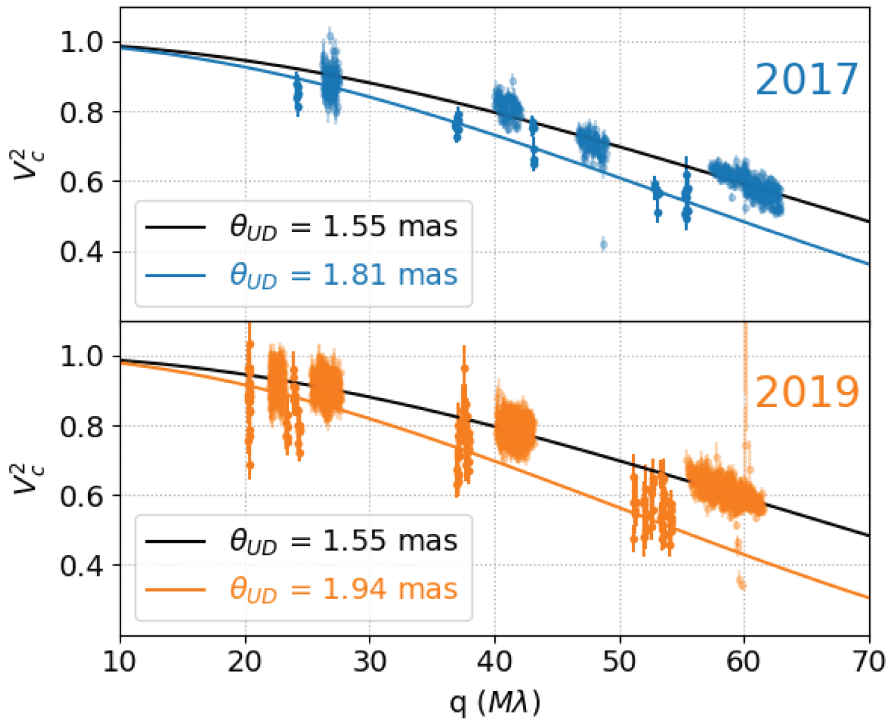

FIGURE 4.27: Visibility curves corresponding to the obtained diameter lower limits of the hypothetical shell.

4.5.2 The molecular shell

The thin layer model described in Section 4.4.3 is used to interpret the visibility curves and the spectrum. The final parameter space is the following:

- T_*: The temperature of the photosphere.
- R_*: The radius of the photosphere.
- $T_{\rm L}$: The temperature of the layer. It is assumed to be always lower than the temperature of the photosphere.
- $R_{\rm L}$: The radius of the layer. It is assumed to be always higher than the radius of the photosphere.
- τ_λ: The optical depth profile. It is assumed to be always positive (absorption)[14]. The number of τ parameters depends on the bandwidth involved.

The photosphere is assumed to be a black body whose radius is obtained using the average $\theta^*_{\rm UD}$ in the continuum, via $R_* = \theta^*_{\rm UD}/2 = 0.775$ mas. According to Figure 4.19, as the optical depths are referred to the single thin layer, the photosphere is what is visible when the value of $\tau = 0$. The physical picture is simple, if the layer is absolutely transparent, the collected light must come from the object that is inside the layer and it is the continuum, in absence of any spectral line, where this radius is defined. This is confirmed by Figures 4.25 and 4.27. Indeed, if any channel λ

[14] A negative value would imply emission lines, which are not expected in the spectrum of an evolved star.

presents $\tau = 0$, the effect of any layer parameter vanishes. Therefore, in order to study the molecular layer we can restrict the analysis to the interval [2.29-2.40 μm], corresponding to the CO molecular band. 50 channels of the total of 210 used in the MEDIUM resolution mode of GRAVITY correspond to that interval.

There is a degeneracy between the temperatures T_* and $T_{\rm L}$. As an accurate measurement of the absolute flux is not accessible (Section 4.3.1), I decided to fix the temperature of the photosphere T_* to the most recent value of the effective temperature found in the literature (Paumard et al., 2014), which is $T_{\rm eff} = 3600$ K. The free parameters and their constraints are, then:

- $R_{\rm L}$: The radius of the layer. It must be $R_{\rm L} > R_* = \theta^*_{\rm UD}/2$.
- $T_{\rm L}$: The temperature of the layer. It must be $T_{\rm L} < T_* = 3600$ K.
- τ_λ: Limited to the molecular band (50 channels) and $\tau_\lambda \geq 0$. In order to smooth limits and allow zero values I have decided to fix $\tau_{\rm min} = -0.1$.

The total number of free parameters is 52. The total number of data points is 50 (spectral channels) $\times$ 6 (baselines) $\times$ f (frames) (f=2 in 2017, f=7 in 2019). For 2019 as the frames have SPLIT polarization, there are two data sets P1 and P2 that are treated separately and averaged afterwards. This makes a total of 548 degrees of freedom for 2017 and 2048 for 2019 (each data set P) and a parameter space plenty of local minima, which makes extremely difficult to perform a χ^2 fit to find the absolute minimum. In order to simplify the fitting procedure, instead of performing a fit with 52 parameters, a fit in two steps is implemented, assuming that:

- The global free parameters for the layer are $(T_{\rm L}, R_{\rm L})$.
- For a given pair of $(T_{\rm L}, R_{\rm L})$ there is only one family of τ_λ which can explain the spectrum of the target[15].

The fitting routine is the following:

- Selecting a pair $(T_{\rm L}, R_{\rm L}) = (T_a, R_a)$ and taking Equation 4.19, the pipeline gets, for every λ involved, the τ_λ which minimizes:

$$|{\rm Res}_F|_\lambda = \left| \frac{F_{\lambda,n}(T_* = T_{eff}, T_{\rm L} = T_a, R_* = \theta^*_{\rm UD}/2, R_{\rm L} = R_a, \tau_\lambda) - F^{IRS7}_{\lambda,N}}{\sigma_{F^{IRS7}_{\lambda,N}}} \right| . \tag{4.27}$$

  The fit does not have degrees of freedom as it is performed point by point of the spectrum and all the parameters but the optical depth are fixed. Minimizing Equation 4.27 leads to a final value of $({\rm Res}_F)_\lambda = 0$ if the model is successful[16]. A value of $({\rm Res}_F)_\lambda > 0$ in any spectral channel would mean that a single layer with $(T_{\rm L}, R_{\rm L}) = (T_a, R_a)$ cannot successfully explain the observed absorption for that wavelength with any optical depths (see Section 4.4.3).

[15] This statement assumes that the single thin layer model is enough to entirely explain the data. It is not always the case as the model can reach saturation for high values of τ_λ (Figure 4.19).

[16] This is equivalent to solve τ_λ for

$$F_{\lambda,n}(T_* = T_{eff}, T_{\rm L} = t, R_* = \theta^*_{\rm UD}/2, R_{\rm L} = r, \tau_\lambda) - F^{IRS7}_{\lambda,N} = 0$$

- With the obtained optical depth profile $\tau(\lambda)$, the pipeline evaluates:

$$\chi^2_{\rm mol} = \sum_{j=0}^{N} \left(\frac{V^2_{mol}(q_j, T_* = T_{eff}, T_{\rm L} = k, R_* = \theta^*_{\rm UD}/2, R_{\rm L} = \rho, \tau(\lambda)) - V^2_{c,i}(q_j)}{\sigma_{V^2_{c,i}}(q_j)} \right)^2 . \tag{4.28}$$

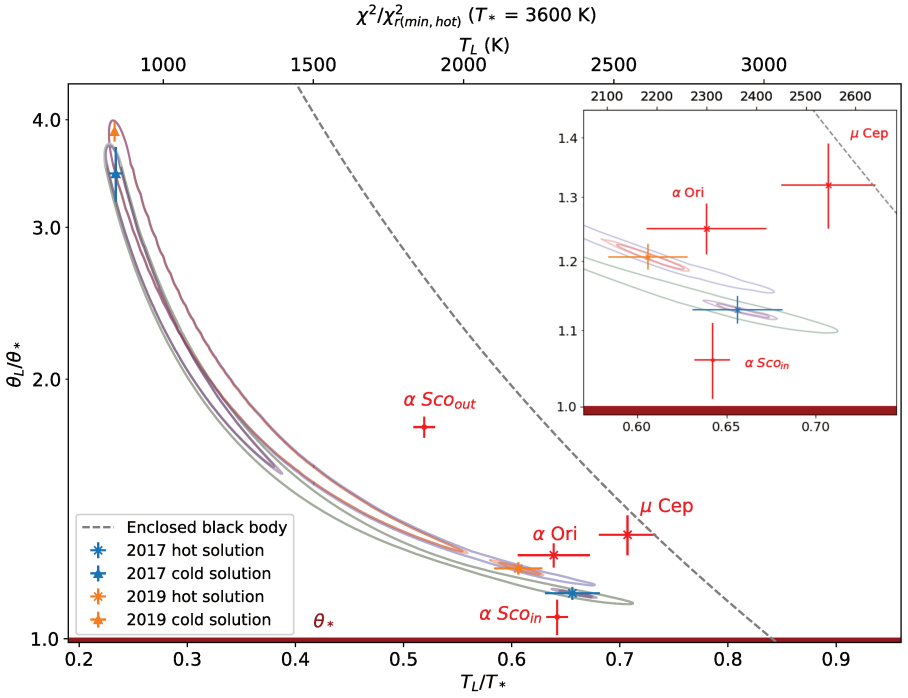

FIGURE 4.28: *Solid lines:* the contours correspond to an decrease of likelihood of 1, 3 and 5 σ relative to the hot solution minimum of each epoch considering $(T_{\rm L}, R_{\rm L})$ the two parameters of interest (Press et al., 1992). *Triangles with error bars:* the cold solution for the two epochs. *Crosses with error bars:* the hot solution for the two epochs. *Points with errorbars in red:* the CO shell physical parameters of some stars from the literature. *Grey dashed line:* temperature profile of a spherically thin shell enclosing a perfect blackbody (Equation 4.29).

The resulting $\chi^2_{\rm mol}$ map for each epoch as a contour plot is displayed in Figure 4.28, as a projection in the $(T_{\rm L}/T_*, \theta_{\rm L}/\theta_*)$ plane with $\theta_{\rm L} = 2R_{\rm L}$. Each pixel of the map corresponds to a configuration $(T_{\rm L}, \theta_{\rm L})$ with an optical depth profile defined by spectroscopy via the minimum value of Equation 4.27 for each spectral channel, and the contours trace the minimum value of Equation 4.28 defined through interferometry.

A temperature profile as a function of distance for a system made of two concentric black bodies in thermodynamic equilibrium is also shown in Figure 4.28 as the grey dashed line, obtained assuming that all the energy radiated by the photosphere is absorbed by the layer and re-emitted afterwards isotropically in all directions:

$$\frac{R_1}{R_0} = \frac{1}{\sqrt{2}} \left(\frac{T_0}{T_1} \right)^2 \tag{4.29}$$

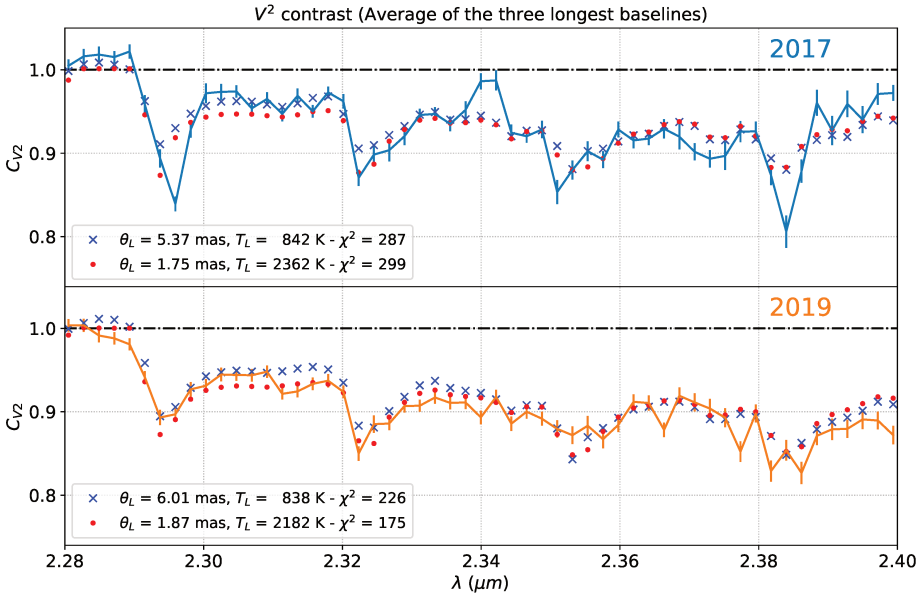

FIGURE 4.29: Visibility contrast in the CO bands. the spectral visibility of the three longest baselines have been averaged for each epoch. The χ^2 shown correspond to the squared distance between the visibility contrasts of the data and the models computed for the hot and cold solutions.

There is a trough in the map revealing a degeneracy between the temperature and the radius of the shell. For each epoch there are two minima:

- The absolute minima:

$$2017:\ (T_{\rm L}, \theta_{\rm L}) = (842 \pm 22\,{\rm K}, 5.37 \pm 0.39\,{\rm mas}), \chi^2_r = 3.73\ .$$

$$2019:\ (T_{\rm L}, \theta_{\rm L}) = (838 \pm 8\,{\rm K}, 6.01 \pm 0.16\,{\rm mas}), \chi^2_r = 1.96\ .$$

- The local minima:

$$2017:\ (T_{\rm L}, \theta_{\rm L}) = (2362 \pm 91\,{\rm K}, 1.75 \pm 0.03\,{\rm mas}), \chi^2_r = 3.93\ .$$

$$2019:\ (T_{\rm L}, \theta_{\rm L}) = (2182 \pm 80\,{\rm K}, 1.87 \pm 0.03\,{\rm mas}), \chi^2_r = 2.17\ .$$

From now on, the absolute minima will be called the *cold* solution, while the local minima will be referred as the *hot* solution. The fact that the values of $\chi^2_r > 2$ for the hot solution can be interpreted as a hint that the model is too simple to successfully reproduce the data. The contribution of the modelling errors into the statistical uncertainties is approximated by dividing the maps by the χ^2_r of the hot solutions.

With the values of both solutions, the visibility contrast is shown in Figure 4.29. For each spectral channel, the quotient defined in Equation 4.23 has been taken selecting the three longest overlapping baselines. The quantity shown is the average of the obtained values of all the frames per epoch.

Both solutions would be mathematically valid to interpret the data, but the temperature of the cold solution is below the condensation temperature of silicate dust. In the picture of the mass loss by a RSG star, CO could perfectly be detected beyond

the dust condensation radius at low temperatures, as the dust expelled by the radiation pressure of the star can drag the CO gas. Nevertheless, in principle CO is expected to form closer to the star before being dragged by the dust. As CO is a major component of the molecular shell, a CO layer with a higher column density and stronger spectroscopic signal must exist, hotter and closer to the star. In addition, the temperature profile of Equation 4.29 is much closer to the hot solution than to the cold one. For all these reasons, the hot solution makes more physical sense than the cold solution although both are compatible with the data. The cold solution cannot therefore be the dominating solution for CO around GCIRS 7.

This is confirmed by observations in other RSG stars. The locations in the χ^2 map of the shell observed in the stars Betelgeuse (Montargès et al., 2014, α Ori) and μ Cep (Perrin et al., 2005) reveal that the hot solution is much more probable to be realistically the dominating solution. A more complex model consisting in a set of 7 layers for Antares (α Sco) implemented by Hadjara et al. (2019) points to the same result (Figure 4.28 shows only the inner and the outer layer for simplicity).

The results for the hot solution of each epoch are presented in Table 4.2. The optical depth profiles corresponding to them are displayed in Figure 4.30. The error bars have been obtained through Monte-Carlo error propagation in the 1σ contour of the hot solution. The fainter values correspond to $\tau \pm \Delta\tau > 5$, where the model reaches saturation.

TABLE 4.2: Parameters of the single-layer CO shell model for the hot solution.

Parameter	2017	2019
A_0	3.27 (fixed)	3.27 (fixed)
θ_* (mas)	1.55 (fixed)	1.55 (fixed)
T_* (K)	3600 (fixed)	3600 (fixed)
θ_{L} (mas)	1.75 ± 0.03	1.87 ± 0.03
T_{L} (K)	2362 ± 91	2182 ± 80

Globally, the values of the uniform disk diameters presented on Fig. 4.25 are higher in 2019 than in 2017. The visibility contrast (Figure 4.29), significantly lower in 2019 than in 2017 beyond 2.33 μm, is another evidence of a higher shell diameter. It is also confirmed by the position of the local minima in Figure 4.28 corresponding to the hot solution, which is different at 4σ between epochs suggesting a higher diameter and a lower temperature. According to the single layer fit, these results are compatible with a shell expansion and a shell temperature decrease from 2017 to 2019. The fact that the peaks are not reproduced by the visibility contrast proves that the model saturates on the head bands. However, this does not happen in the first head band of 2019, which can be a hint of a dilution or a mechanism linked to mass loss.

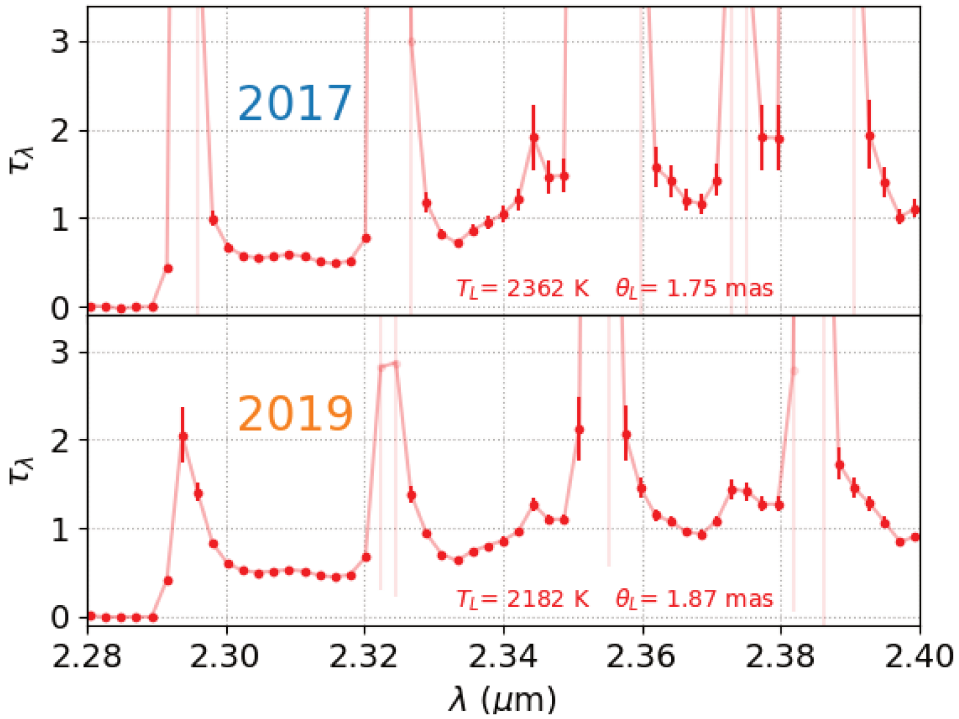

FIGURE 4.30: Optical depths computed using Equation 4.27 with the parameters of the hot solution (Table 4.2). The peaks correspond to the CO overtone lines where the single-layer model saturates as described in Section 4.4.3.

The shell density

The optical depth profiles (Fig. 4.30) are reasonably consistent in 2017 and 2019 except for the peaks, where the model saturates as described in Section 4.4.3. To obtain an estimate of the density of the shell, I have used the method described in Goorvitch (1994) by using the optical depth corresponding to the first head of the CO band. The method cannot be applied to the 2017 data as the optical depth is too high so that the thin shell model saturates. However, for 2019, there is an optical depth available for the first overtone line of CO and a column density can be estimated. This method assumes:

$$d\tau_\lambda = S\phi(\lambda - \lambda_0)Nds \ , \tag{4.30}$$

where ϕ is the profile of the line centered in λ_0 and normalized to unity, N is the density ($\mathrm{mol\,cm^{-3}}$) and S is the strength of the line ($\mathrm{cm\,mol^{-1}}$), obtained as:

$$S = \frac{\pi e^2}{m_e c^2} g_l f_l \frac{1}{Q(T)} \exp\left[-\frac{hcE_1}{k_B T}\right]\left[1 - \exp\left(-\frac{hcE_\lambda}{k_B T}\right)\right] \ , \tag{4.31}$$

where e, m_e, c, k_B, h are fundamental constants as the charge and mass of the electron, the speed of light in vacuum, the Boltzmann constant and the Planck constant, $g_l f_l$ the oscilator strengths (depending purely on each transition, tabulated in the same paper), E_1 the energy of the upper state and E_λ the energy of the lower state.

In Goorvitch (1994) the author uses a partition function obtained by fitting (and therefore tabulating) the coefficients a_i in the form from Sauval and Tatum (1984):

$$\log Q(T) = \sum_{i=0}^{3} a_i \left(\log \frac{5040}{T} \right)^i . \tag{4.32}$$

Figure 4.31 show the position of the main transitions $\Delta\nu = 2$ present in the observed molecular band of GCIRS 7. As every spectral channel λ from GRAVITY records the light collected between λ and $\lambda + \Delta\lambda$, the accuracy of this method strongly depends on the value $\Delta\lambda$, which is different depending on the observing mode of the instrument. In the observed epochs at MEDIUM resolution $\Delta\lambda = 0.0022$ μm, sometimes too large to attribute all the light collected in a specific channel to those transitions as some other minor molecular lines can be present. This is the reason why the transitions plotted in the Figure do not always correspond to a specific spectral channel.

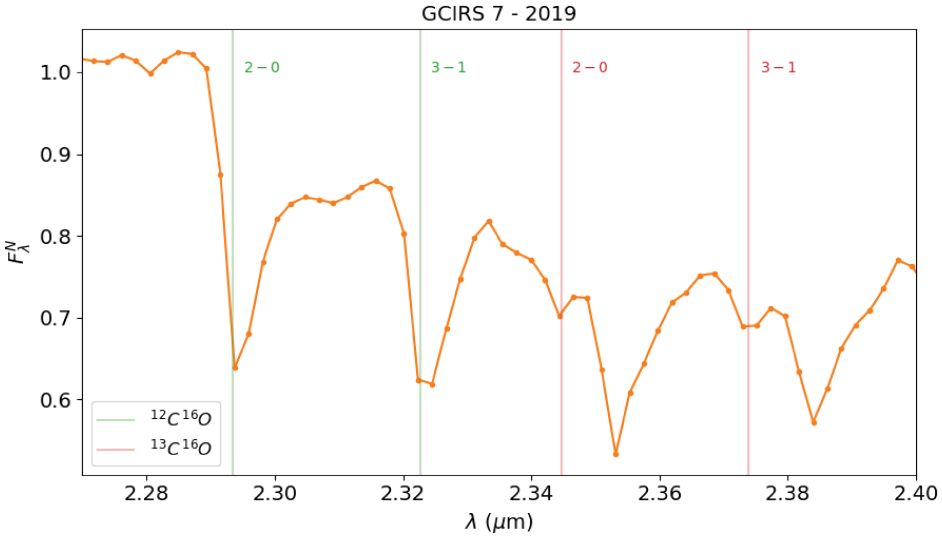

FIGURE 4.31: Spectral lines and main transitions $\Delta\nu = 2$ present in the spectra of GCIRS 7. The value of J = 51 for the transition 2-0 and $J = 50$ for the transition 3-1. Data taken from the website of NOT: http://www.not.iac.es/instruments/notcam/ReferenceInfo/

The value of the column density is computed as $dZ = Nds$ from Equation 4.30, wrapping up S and $Q(T)$. Three approximations are considered by using this method:

- I have assumed that the GRAVITY spectral channels correspond to the exact value of λ instead of $\lambda \pm \Delta\lambda$, that is, their profile is a Dirac delta. For each spectral channel λ the line profile taken is $\phi(\lambda - \lambda_0) = 1$. This approximation requires a well defined spectral line to get a somewhat meaningful result, so for this purpose I have only used the first band head of CO at 2.2935 μm (Figure 4.31). There is only one optical depth available in 2019 as this line cannot be explained in 2017 with the single layer model (Figure 4.30). This assumption, perhaps too simplistic, provides an upper limit to the column density obtained.
- The light collected in the spectral channel $\lambda \pm \Delta\lambda = 2.2937 \pm 0.0022$ μm corresponds exclusively to the first overtone line of CO ($\lambda = 2.2935$ μm). The transition corresponding to this line is $\Delta\nu = 2$ to the fundamental state $(2-0, J = 51)$ of the isotope $^{12}\mathrm{C}\,^{16}\mathrm{O}$ (Montarges, 2014).
- Wrapping up, the Equation 4.30 is simplified to $\tau_\lambda = SZ$ and then:

$$Z = \frac{\tau_\lambda}{S_\lambda(T_\mathrm{L})} \tag{4.33}$$

Using the parameter of the hot solution in 2019 and assigning the optical depth measured with the model yields a maximum column density of:

$$Z_{\mathrm{CO}}^{2019} = (2.61 \pm 0.49) \times 10^{20}\,\mathrm{mol\,cm^{-2}}\ ,$$

where the error bar has been obtained via error propagation considering σ_{T_L} (from Table 4.2) and σ_{τ_λ} (from Figure 4.30). For Betelgeuse, Montargès et al. (2014) measured, using several transitions and two isotopes ($^{12}\mathrm{C}\,^{16}\mathrm{O}$, $^{13}\mathrm{C}\,^{16}\mathrm{O}$), a column density $Z = 3.01^{+2.0}_{-0.5} \times 10^{21}\,\mathrm{mol\,cm^{-2}}$, a value higher by one order of magnitude than the shell of GCIRS 7. It is also lower than the density measured by Hadjara et al. (2019) for the first layer for Antares: $N_{\mathrm{CO}} = 3.16 \pm 1.58 \times 10^{21}\,\mathrm{mol\,cm^{-2}}$.

4.6 Discussion of the results

4.6.1 On the local interstellar extinction

In order to compare with previous measurements, the measured extinction in Brackett γ can be converted to $A_{\mathrm{K_S}}$ taking Equation 4.1 and comparing the measured flux with the de-reddened flux (inversely applying the extinction law):

$$A_{K_S} = -2.5 \log \frac{\int_{K_\mathrm{S}} T(\lambda) \times F_\lambda^{\mathrm{IRS7}} d\lambda}{\int_{K_\mathrm{S}} T(\lambda) \times F_\lambda^{\mathrm{IRS7}} 10^{+0.4 A_\lambda} d\lambda} \tag{4.34}$$

where A_λ is the power law described in Equation 4.4. The obtained result is $A_{\mathrm{K_S}} = 3.16 \pm 0.10$, identical at the two epochs. Going back to the literature (Table 4.3), Blum, Sellgren, and Depoy (1996) obtained $A_\mathrm{K} = 3.72 \pm 0.13$ via NIR photometry and an assumed intrinsic color, and later Blum et al. (2003) measured $A_\mathrm{K} = 3.48 \pm 0.09$. These values are higher than the measurement obtained by up to 3σ. Although the reason of this change might be due to any variation of the fundamental parameters of the star through any of its pulsations, it is also known (Ciurlo et al., 2016) that the interstellar medium in the central parsecs is heterogeneous. The presence of any dusty clump along a given line of sight can be responsible of a drop of up to one magnitude in K band (Paumard, Maillard, and Morris, 2004), and the motion of material during a time span of a decade can easily explain such temporal variation of the interstellar extinction.

The value $A_{\mathrm{K_S}} = 3.16$ is above average when compared to the extinction map of Schödel et al. (2010), who used stars to describe the interstellar extinction. The works Ciurlo et al. (2016, 2019), on the other side, used the interstellar medium directly probing deeper along the line-of-sight. Therefore, a large part of the extinction towards GCIRS 7 can be attributed to interstellar medium local to the central parsec, from which part of it could have circumstellar origin.

Table 4.3: K-band extinction measurements at the Galactic Center and GCIRS 7 in literature.

Reference	Measurement	Centered at
Blum, Sellgren, and Depoy (1996)	$A_\mathrm{K} = 3.72 \pm 0.13$	IRS 7
Blum et al. (2003)	$A_\mathrm{K} = 3.48 \pm 0.09$	IRS 7
Schödel et al. (2010)	$A_{\mathrm{K_S}} = 2.46 \pm 0.03$	SgrA*
Fritz et al. (2011)	$A_{\mathrm{K_S}} = 2.42 \pm 0.10$	SgrA*
This work	$A_{\mathrm{K_S}} = 3.16 \pm 0.10$	IRS 7

4.6.2 On the pulsations of the star

Using data from 4 decades, a double pulsation light curve of 470 and 2620 days respectively was fitted in Paumard et al. (2014) while this study uses observations from two runs separated 840 days. The NAOMI Adaptive optics was used in 2019 to focus the stellar flux into the GRAVITY fibres while only tip-tilt was compensated in 2017 making the flux injection highly dependent on seeing conditions, which makes extremely difficult and uncertain to compare absolute fluxes. That is the reason why the temperature from the literature is used, fitting the extinction instead.

A same photospheric size in 2017 and 2019 is measured, with a 3σ upper limit on the difference of 0.13 mas (8%). This is plausibly explained by the observational gap. With the interplay of the two periods (470 and 2620 days) revealed in Paumard et al. (2014), the size of the photosphere could well have varied during the 840 days that separate the observations performed in 2017 and in 2019 and have come back to a very similar value. However, it is also possible that the size of the star did not vary between 2017 and 2019 or varied less than expected from the 2013–2017 era. The pulsations of red supergiants are irregular and intertwined with convective mechanisms. Their periods, phases and amplitudes can vary over short timescales.

Although we observe a different fraction of coherent light, this has no effect on the absolute flux of the target. Therefore, if there is any other significant difference in the global parameters of the photosphere in K band in the studied epochs, it must be either relative to a temperature difference, assumed to be $T_* = 3600 \pm 195$ K as in the literature, or due to a large convection cell covering a significant fraction of the surface of the star, which cannot be resolved with the actual baseline coverage of VLT.

The photospheric diameter obtained is 1.547 ± 0.030 mas in 2017 and 1.549 ± 0.030 mas in 2019, rounded to $\theta^*_{\rm UD} = 1.55 \pm 0.03$ mas. The value of $\theta^*_{\rm UD}$ agrees very well with the values of $\theta^*_{\rm UD} = 1.5 - 2$ mas of Paumard et al. (2014) on K-band data obtained with AMBER in 2008, but on the other side measurements in H-band (PIONIER 2013) reveal a much smaller diameter of $\theta^*_{\rm UD} = 1.076 \pm 0.093$ mas. A priori there is no reason to consider a K-band photosphere 1.44 times larger than the H-band photosphere, confirming that GCIRS 7 has been pulsating also over the last 10 years. Using the value of $R_0 = 8246 \pm 45$ pc[17] obtained in Gravity Collaboration et al. (2020a), the radius R^* can be obtained in solar units as:

$$\tan\left(\theta^*_{\rm UD}/2\right) \approx \theta^*_{\rm UD}/2 = \frac{R_*}{R_0} \rightarrow R_* = \frac{\theta^*_{\rm UD} * R_0}{2} \tag{4.35}$$

and its uncertainty:

$$\Delta R_* = \sqrt{\left(\frac{R_*}{\theta^*_{\rm UD}}\Delta\theta^*_{\rm UD}\right)^2 + \left(\frac{R_*}{R_0}\Delta R_0\right)^2} \tag{4.36}$$

yielding $R_* = 1368 \pm 26\,R_\odot$. The same exercise for the shell diameter yields:

- 2017: $R_{\rm L} = 1544 \pm 26\,R_\odot$
- 2019: $R_{\rm L} = 1650 \pm 26\,R_\odot$

[17] The systematic error is used for this calculation as it dominates over the statistical error.

This is the first molecular shell seen in motion in the environment of a RSG star. The fact that the single layer model saturates in 2017 indicates that the density of CO was substantially higher then than in 2019. This effect can be the product of a dilution due to the expansion of the shell or a mechanism related to mass loss. Under the assumption that this decrease is exclusively due to dilution because of the expansion of the shell, it is possible to scale the density by the ratio of the surface of the shell at the two epochs to estimate what the density was in 2017. This approach reveals that the expansion of the shell predicts a density in 2017 only 14% higher than in 2019. By using again the method of Goorvitch (1994) (Equation 4.33), this density would have been reflected in an optical depth of only $\tau \approx 3$ at $\lambda = 2.293$ μm, which the single layer model would be able to reproduce without saturating. Therefore, the expansion alone is not sufficient to explain this drop in column density.

4.6.3 On the context of other evolved stars

Figure 4.32 shows the results of Perrin et al. (2005), Montargès et al. (2014), and Hadjara et al. (2019) compared to this work, and the temperature profile of two concentric blackbodies in thermal equilibrium following Equation 4.29.

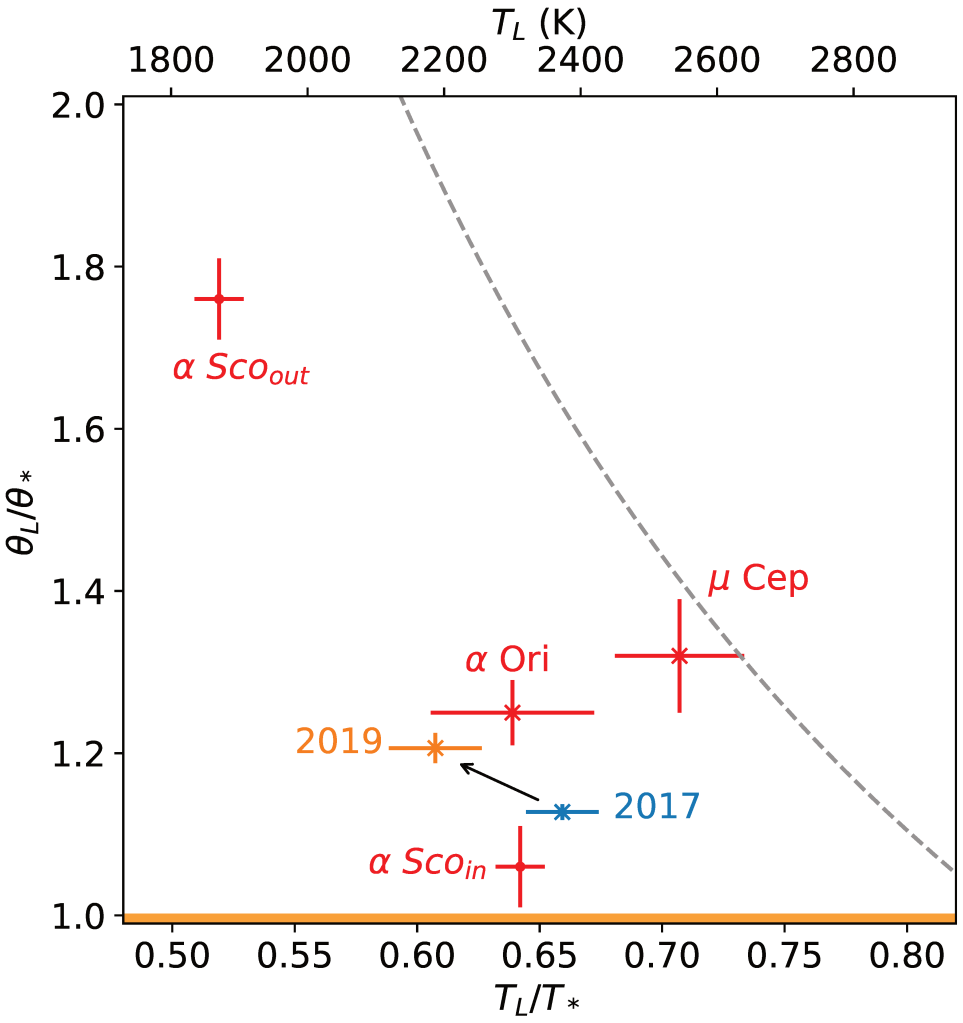

FIGURE 4.32: Status of the molecular shells of RSGs in literature and the result of this work for the two epochs.

These three stars are among the most studied RSGs in K band, and two of them (α Ori and α Sco) are the closest RSGs to Earth. Their proximity allows to characterize their structure with more detail, and any study of their molecular envelopes can be considered in parallel to GCIRS 7.

Betelgeuse (α Ori) holds the honour of being the first star different than our Sun whose apparent diameter has been measured (Michelson and Pease, 1921). An image of its surface was firstly obtained by Haubois et al. (2009). A recent measurement by Montargès et al. (2014) yields $\theta_*^{\rm UD} = 41.01 \pm 0.41$ mas and a molecular shell at $1.24R_*$. This star is located at just 220 pc (Harper et al., 2017), being the candidate to be the closest supernova in the sky in the next 10 to 100 thousand years. Currently it is being subject of a deep study due to an unprecedented dimming of 1 magnitude in V band (Levesque and Massey, 2020; Harper et al., 2020). It is true that pulsations as intense as the ones observed in GCIRS 7 have not been yet observed in Betelgeuse, but any phenomena observed in this RSG must be considered relevant for future studies involving GCIRS 7 due to their similar characteristics.

Antares is the brightest RSG in the Southern hemisphere sky. The last estimate of its diameter is 37 mas, measured with AMBER data by implementing a model consisting in several concentric shells in a sample of evolved stars by Hadjara et al. (2019). For this RSG star, the number of layers found was 7 in the interval $1.06 - 1.76\,R_*$. Up to date there is still no molecular layer found at more than $2R_*$, as opposed to less massive evolved stars as Mira class stars. Indeed the thin shell model used in my work constitutes an over simplification that must be taken as a starting point for a deeper study applying a model similar to this multiple layer approach.

When these lines are being written, GCIRS 7 is the RSG with the smallest apparent size (and the farthest one by an order of magnitude) where a structure has been observed. To illustrate this, the first image reconstruction of Betelgeuse (α Ori) by Haubois et al. (2009), the image reconstruction of the photosphere of Antares (α Sco) taken with AMBER in VLTI (Ohnaka, Weigelt, and Hofmann, 2017), the image reconstruction of CE Tauri with PIONIER (Montargès et al., 2018) and the image reconstruction with PIONIER of the up to date smallest-apparent-size RSG star V602 Car (Climent et al., 2020) are shown in Figure 4.33 together with a disk of the apparent size of GCIRS 7 in the sky. The estimated physical size is also displayed in the picture, corresponding to measurements taken in their respective works[18].

The derived physical parameters for the shell of GCIRS 7 are perfectly compatible with other molecular shells already observed in closer RSGs except for the density of CO in 2019, which appears to be an order of magnitude lower. Whether or not this low density is a result of the effect of the particular environment of GCIRS 7 in the context of the Galactic Center might be addressed by the use of a more complex model to fully characterise the outer atmosphere of GCIRS 7, such as the one of Hadjara et al. (2019) involving a multilayer model, which would be able to solve the saturation in the peaks of the CO overtone lines. It would also help to understand if the nature of the molecular shell observed for GCIRS 7 is similar to the ones of other isolated RSGs or if it is indeed less dense.

[18]The estimation of the physical size of V602 Car makes use of the distance measured by Melnik and Dambis (2020), $d = 1190$ pc.

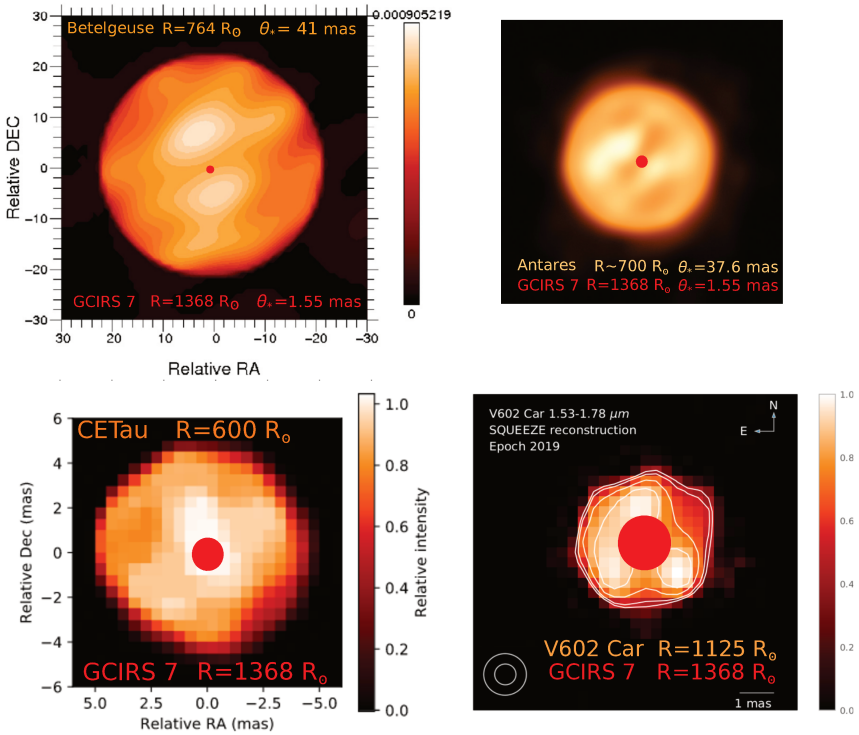

FIGURE 4.33: *Top left*: the first image reconstruction of Betelgeuse (Haubois et al., 2009). The axes unit is milliarcseconds. *Top right*: the most recent reconstructed image of Antares (O'Gorman et al., 2017). *Bottom left*: an image reconstruction of CE Tauri (Montargès et al., 2018). *Bottom right*: an image reconstruction of the RSG V602 Car (Climent et al., 2020), up to date the smallest RSG imaged. The apparent size in the sky and the corresponding physical size of these stars and GCIRS 7 are displayed over them.

Chapter 5

Conclusion and future prospects

This thesis has been written in the context of the first observations of the Galactic Center by the instrument GRAVITY. Specifically, two sources of the central parsec of the Galaxy have been explored:

- SgrA*: the supermassive black hole candidate located in the center of the Galaxy by astrometry of the star S2.
- GCIRS 7: a pulsating red supergiant known to feed the interstellar medium with expelled material of the external layers of its atmosphere.

Regarding SgrA*, I present the results of the first astrometric measurements performed by the use of optical interferometry along the orbit of the star S2 with observations conducted during 2017 and 2018, from which I have participated in four runs obtaining new data. I have processed and calibrated all the data frames used during these two epochs. Taking advantage of the proximity of the star S2 in its orbit during the months before and just after the pericenter passage, I have applied a binary source model to interpret the data with a different first guess for every night according to the latest orbital fit published. For each data frame, I have been able to obtain the relative position of the star S2 with respect to SgrA*, as well as a relative measurement of the flux of SgrA* with respect to S2 and a measurement of the incoherent background light, visually inspecting each frame to rate the quality of the data. For each night, I have obtained a best estimate position of the star S2 by averaging each fit result for that night. With the results obtained, I have produced the astrometry of S2 with an unprecedented accuracy thanks to the performance of the GRAVITY instrument, as well as I have built a light curve for SgrA* through an estimate of the flux of S2 in 2018. These data productions yield the contribution of LESIA to the Galactic Center team of the GRAVITY consortium for the early publications (2017-2018) where they have been combined with 3 other independent estimates.

The astrometry of the star S2 has been part of a wider study for the GRAVITY collaboration before and after the pericenter passage which took place in April 2018. Complementing our GRAVITY data with SINFONI data, this event allowed us to obtain the first truly dynamical measurement of the gravitational redshift around a celestial body (Gravity Collaboration et al., 2018a), and therefore the first test of General Relativity in the galactic center has been successful. The light curve of SgrA* has been included in a wider sample made of other two independent analysis to construct the GRAVITY collaboration light curve of SgrA* during the years 2017, 2018 and 2019 (Gravity Collaboration et al., 2020c), confirming the quiescent scenario with sporadic flares. Concretely, in 2018 there are three bright flares that were involved

in the exploration of orbital motions thanks to the high signal-to-noise ratio reached during those flares (Gravity Collaboration et al., 2018b). This study reveals that the observed flares can be interpreted as a hot spot orbiting near the innermost stable circular orbit of a black hole. To date, this study represents the closest empirical approach to the central source of our galaxy.

At the end of 2020, the last work of the consortium concerning the orbit of S2 is Gravity Collaboration et al. (2020a). It reports the first detection of the Schwarzschild precession in an extra solar body, another predicted effect of General Relativity. After 160 years, Observatoire de Paris has been part of the detection of the relativistic orbital precession of a body due to the curvature of space time at two different potential strengths: from a planet around a star[1] towards a star around a supermassive black hole.

The second source studied in this thesis is GCIRS 7. The work developed in this thesis takes advantage of the superb accuracy of the instrument GRAVITY to constrain the diameter profile (per spectral channel) of the star observed in 2017. The fact that the star is moderately resolved required an approach starting from the most simple model for an extended source (uniform disk) adding complexity on each new step, instead of an attempt using a complex model directly. Despite the partial resolution, a diameter significantly larger is observed in the molecular band of the spectrum of the star compared to the continuum, revealing the presence of at least one molecular shell in a similar way as other closer stars of the same spectral type. I have been able to participate in two extra runs to observe the target again in 2019, generating another dataset. For this epoch, I have repeated the analysis and found that the diameter profile returns values slightly, yet significantly, higher than in 2017 in the molecular band heads, while the continuum remains at the same diameter. By the use of a thin shell model to reproduce the data, the interpretation is compatible with a layer expansion and cooling and the density difference by itself cannot be explained by dilution only, suggesting a mass loss mechanism. This research has been presented in a Galactic Center scientific conference in Japan as well as has produced a scientific publication submitted to the journal *Astronomy & Astrophysics* which is currently in referee stage.

This thesis work proves that it is possible to track the evolution of the photosphere size and molecular shells of RSG stars with a diameter as low as 1.5 mas, without the need of fully resolved targets and with the current capabilities. The results are in agreement with the pulsation scenario proposed in Paumard et al. (2014). The null phase returned by the interferometric signal shows no significant asymmetry, which implies that the formation of the cometary tail previously observed in radio, predicted to be shaped by the interstellar winds (Yusef-Zadeh and Morris, 1991; Serabyn, Lacy, and Achtermann, 1991), does not directly involve the molecular shell at that height from the photosphere.

[1]The precession was reported by Urbain Le Verrier in 1859, but it could not be explained until 1915 by Einstein.

5.1 Perspectives on SgrA* and its close environment

For the next years to come, GRAVITY will keep tracking the orbit of S2 around SgrA*, whose apocenter passage will take place in 2026. Although it is true that the results obtained by GRAVITY during this three years already fulfill the main scientific cases what the instrument was designed for, the next years to come will provide new insights related to the upper orbit of S2.

The most recent results of the consortium (Gravity Collaboration et al., 2020a) are still compatible with an extended mass of SgrA* accounting for up to 0.1% of the total mass of the source in addition to the point source of $4 \times 10^6\ M_\odot$. A study from LESIA (Heißel, G. et al, in prep) is actually being carried out to estimate if this limit can still be reduced to better characterize the mass distribution of SgrA*. While the effect of this extended mass distribution in the half orbit of S2 closer to the pericenter cannot exclude less than 0.1 of the mass of the source, the effect on the half orbit closer to the apocenter can potentially reveal if this limit can be further lowered.

The astrometric impact of the Lense-Thirring (or frame-dragging) effect, which accounts for the influence of the rotation of the central body on the orbit of S2, is maximal in the apocenter. For this reason, the last of the parameters to measure, the angular momentum of the black hole, could then be potentially measurable during the apocenter passage by the use of orbit fitting (Grould et al., 2017) in the same way as this work does. The strategy to observe the pair, however, must be different due to the fact that S2 and SgrA* do not share the same field of view given by the fibers of GRAVITY. The model fitting cannot be a binary for the same reason, as has already been the case in 2019. A significant measurement of the angular momentum could be done earlier if a sample of flares with a period shorter than 30 minutes and with enough signal-to-noise ratio is recorded, by the exploration of orbital motions like in Gravity Collaboration et al. (2018b).

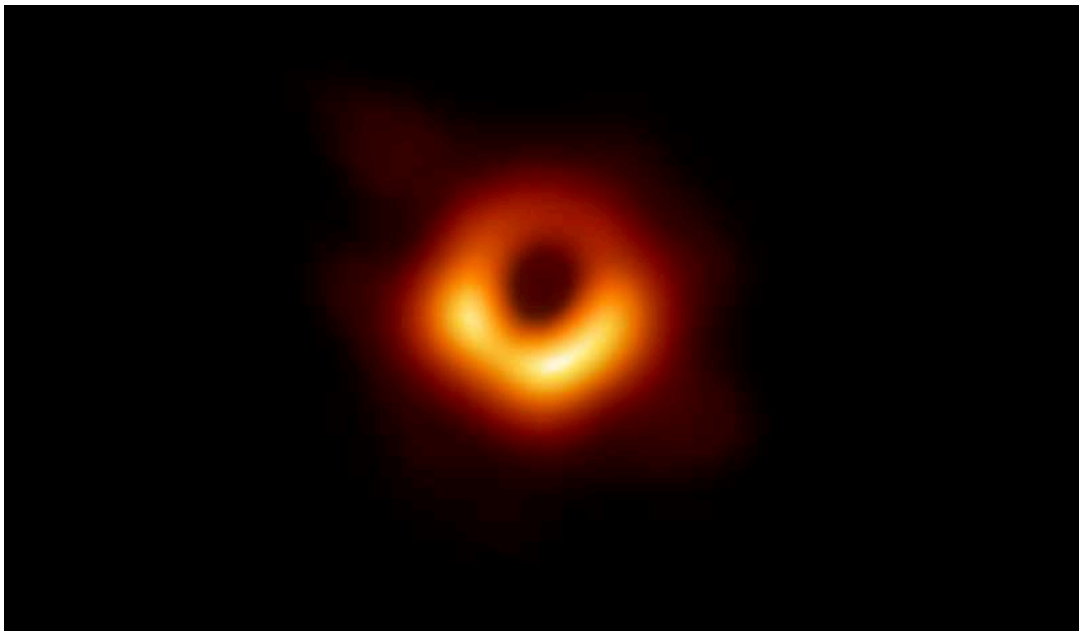

FIGURE 5.1: Image of M87* obtained by radio interferometry by EHT.
Source: eventhorizontelescope.org .

Regarding other groups, it is noteworthy to mention the release of the first image ever obtained of the accreting flow around a massive central object (Event Horizon Telescope Collaboration et al., 2019) by the Event Horizon Telescope consortium, reconstructed from the source M87* (Figure 5.1), a low luminosity AGN. This image, obtained by a competing group, required the use of an interferometer in the millimetric domain whose baseline covers the whole Earth, providing complementary results to the ones of GRAVITY. The physical implications of this image on the nature of M87* are still under investigation (Vincent et al., 2020). It is expected, in the following years, a similar image for SgrA* which will help to test potential alternative and exotic objects such as a gravastar or a boson star.

5.2 Perspectives on GCIRS 7

The results for GCIRS 7 show the typical size and temperature for a thin shell surrounding a red supergiant environment in first approximation. The molecular density obtained for 2019, however, is an order of magnitude lower than the one measured in previous works for Betelgeuse and Antares, two well studied red supergiants. The shortcoming on the model in 2017 proves that the layer density was more dense than in 2019, which could be a signature of a mass loss process. The limitation of the model is clear: a shell with negligible geometrical thickness cannot explain deep absorption lines such as the overtone lines of CO spectra in K band.

The fact that its photosphere is able to grow more than a 40% of its size makes GCIRS 7 a perfect candidate to study RSG pulsations, as well as the behaviour of the molecular layers under such large variations. The pulsations of red super giants are typically irregular, with short time-scale variations. More observations would be needed to understand the role of pulsations and to better characterize the temporal evolution of the molecular shells in the context of mass loss mechanisms. To take advantage of the full capabilities of GRAVITY, the data set for such work would be ideally taken in high resolution mode increasing the exposure time. This was part of the schedule while planning the observations in 2019 but unfortunately the weather did not allow to obtain any meaningful data. A high resolution study would give much more detail in the description of the photosphere as well as more information about the optical depths and ultimately about the density of these layers, their chemical composition and their temperature.

The location of GCIRS 7 is particular as it is located at less than 1 pc from a supermassive black hole and plenty of massive young stars (Krabbe et al., 1995) and it is known that the most external layers of GCIRS 7 are being blown away by the effect of their wind (Yusef-Zadeh and Morris, 1991; Serabyn, Lacy, and Achtermann, 1991; Tsuboi et al., 2020). The study of the mass loss of GCIRS 7 is particularly interesting in the context of the shape and nature of the nuclear interstellar environment, as it might even contribute to the existence of G2-like objects (Gillessen et al., 2012; Ciurlo et al., 2019).

GRAVITY will continue to observe and monitor the stars of the galactic center in the next years to come. I would like that the work presented in this thesis serves as a starting point for other researchers who want to profit from its impressive accuracy.

Bibliography

Abbott, B. P. et al. (Feb. 2016). "Observation of Gravitational Waves from a Binary Black Hole Merger". In: 116.6, 061102, p. 061102. DOI: 10.1103/PhysRevLett.116.061102. arXiv: 1602.03837 [gr-qc].

Adams, W. S. (Nov. 1925). "The relativity displacement of the spectral lines in the companion of Sirius". In: *The Observatory* 48, pp. 337–342.

Airapetian, V., K. G. Carpenter, and L. Ofman (Nov. 2010). "Winds from Luminous Late-type Stars. II. Broadband Frequency Distribution of Alfvén Waves". In: 723.2, pp. 1210–1218. DOI: 10.1088/0004-637X/723/2/1210. arXiv: 1008.3955 [astro-ph.SR].

Allen, D. A. and R. H. Sanders (Jan. 1986). "Is the galactic centre black hole a dwarf?" In: 319.6050, pp. 191–194. DOI: 10.1038/319191a0.

Amorim, A. et al. (Mar. 2019). "Test of the Einstein Equivalence Principle near the Galactic Center Supermassive Black Hole". In: 122.10, 101102, p. 101102. DOI: 10.1103/PhysRevLett.122.101102. arXiv: 1902.04193 [astro-ph.GA].

Amorim, Antonio et al. (July 2012). "The final design of the GRAVITY acquisition camera and associated VLTI beam monitoring strategy". In: *Optical and Infrared Interferometry III*. Vol. 8445. Society of Photo-Optical Instrumentation Engineers Conference Series, p. 844534. DOI: 10.1117/12.925993.

André, P. et al. (Jan. 2014). "From Filamentary Networks to Dense Cores in Molecular Clouds: Toward a New Paradigm for Star Formation". In: *Protostars and Planets VI*. Ed. by Henrik Beuther et al., p. 27. DOI: 10.2458/azu_uapress_9780816531240-ch002. arXiv: 1312.6232 [astro-ph.GA].

Arroyo-Torres, B. et al. (2015). "What causes the large extensions of red supergiant atmospheres?. Comparisons of interferometric observations with 1D hydrostatic, 3D convection, and 1D pulsating model atmospheres". In: 575, A50, A50. DOI: 10.1051/0004-6361/201425212. arXiv: 1501.01560 [astro-ph.SR].

Arsenault, Robin et al. (Oct. 2004). "MACAO-VLTI adaptive optics systems performance". In: ed. by Domenico Bonaccini Calia, Brent L. Ellerbroek, and Roberto Ragazzoni. Vol. 5490. Society of Photo-Optical Instrumentation Engineers Conference Series, pp. 47–58. DOI: 10.1117/12.552548.

Aurière, M. et al. (June 2010). "The magnetic field of Betelgeuse: a local dynamo from giant convection cells?" In: 516, L2, p. L2. DOI: 10.1051/0004-6361/201014925. arXiv: 1005.4845 [astro-ph.SR].

Baganoff, F. K. et al. (Sept. 2001). "Rapid X-ray flaring from the direction of the supermassive black hole at the Galactic Centre". In: 413.6851, pp. 45–48. DOI: 10.1038/35092510. arXiv: astro-ph/0109367 [astro-ph].

Baganoff, F. K. et al. (July 2003). "Chandra X-Ray Spectroscopic Imaging of Sagittarius A* and the Central Parsec of the Galaxy". In: 591.2, pp. 891–915. DOI: 10.1086/375145. arXiv: astro-ph/0102151 [astro-ph].

Balick, B. and R. L. Brown (Dec. 1974). "Intense sub-arcsecond structure in the galactic center." In: 194, pp. 265–270. DOI: 10.1086/153242.

Barstow, M. A. et al. (Oct. 2005). "Hubble Space Telescope spectroscopy of the Balmer lines in Sirius B*". In: 362.4, pp. 1134–1142. DOI: 10.1111/j.1365-2966.2005.09359.x. arXiv: astro-ph/0506600 [astro-ph].

Bartko, H. et al. (2009). "Evidence for Warped Disks of Young Stars in the Galactic Center". In: 697.2, pp. 1741–1763. DOI: 10.1088/0004-637X/697/2/1741. arXiv: 0811.3903 [astro-ph].

Bartko, H. et al. (Jan. 2010). "An Extremely Top-Heavy Initial Mass Function in the Galactic Center Stellar Disks". In: 708.1, pp. 834–840. DOI: 10.1088/0004-637X/708/1/834. arXiv: 0908.2177 [astro-ph.GA].

Bayes, T. (1763). "An essay towards solving a problem in the doctrine of chances". In: *Phil. Trans. of the Royal Soc. of London* 53, pp. 370–418.

Beasor, Emma R. et al. (Mar. 2020). "A new mass-loss rate prescription for red supergiants". In: 492.4, pp. 5994–6006. DOI: 10.1093/mnras/staa255. arXiv: 2001.07222 [astro-ph.SR].

Becklin, E. E., I. Gatley, and M. W. Werner (July 1982). "Far-infrared observations of Sagittarius A - The luminosity and dust density in the central parsec of the Galaxy". In: 258, pp. 135–142. DOI: 10.1086/160060.

Becklin, E. E. and G. Neugebauer (Jan. 1968). "Infrared Observations of the Galactic Center". In: 151, p. 145. DOI: 10.1086/149425.

– (Sept. 1975). "High-resolution maps of the galactic center at 2.2 and 10 microns." In: 200, pp. L71–L74. DOI: 10.1086/181899.

Blum, R. D., K. Sellgren, and D. L. Depoy (1996). "JHKL Photometry and the K-Band Luminosity Function at the Galactic Center". In: 470, p. 864. DOI: 10.1086/177917. arXiv: astro-ph/9604109 [astro-ph].

Blum, R. D. et al. (2003). "Really Cool Stars and the Star Formation History at the Galactic Center". In: 597.1, pp. 323–346. DOI: 10.1086/378380. arXiv: astro-ph/0307291 [astro-ph].

Boehle, A. et al. (Oct. 2016). "An Improved Distance and Mass Estimate for Sgr A* from a Multistar Orbit Analysis". In: 830.1, 17, p. 17. DOI: 10.3847/0004-637X/830/1/17. arXiv: 1607.05726 [astro-ph.GA].

Boyce, H. et al. (Feb. 2019). "Simultaneous X-Ray and Infrared Observations of Sagittarius A*'s Variability". In: 871.2, 161, p. 161. DOI: 10.3847/1538-4357/aaf71f.

Brown, R. L. and K. Y. Lo (Feb. 1982). "Variability of the compact radio source at the Galactic Center." In: 253, pp. 108–114. DOI: 10.1086/159615.

Buchholz, R. M., R. Schödel, and A. Eckart (2009). "Composition of the galactic center star cluster. Population analysis from adaptive optics narrow band spectral energy distributions". In: 499.2, pp. 483–501. DOI: 10.1051/0004-6361/200811497. arXiv: 0903.2135 [astro-ph.GA].

Chelli, A. et al. (2016). "Pseudomagnitudes and differential surface brightness: Application to the apparent diameter of stars". In: 589, A112, A112. DOI: 10.1051/0004-6361/201527484. arXiv: 1604.07700 [astro-ph.SR].

Choquet, É. et al. (Sept. 2014). "Comparison of fringe-tracking algorithms for single-mode near-infrared long-baseline interferometers". In: 569, A2, A2. DOI: 10.1051/0004-6361/201220223. arXiv: 1406.4391 [astro-ph.IM].

Chu, Devin S. et al. (Feb. 2018). "Investigating the Binarity of S0-2: Implications for Its Origins and Robustness as a Probe of the Laws of Gravity around a Supermassive Black Hole". In: 854.1, 12, p. 12. DOI: 10.3847/1538-4357/aaa3eb. arXiv: 1709.04890 [astro-ph.SR].

Ciurlo, A. et al. (Oct. 2016). "Hot molecular hydrogen in the central parsec of the Galaxy through near-infrared 3D fitting". In: 594, A113, A113. DOI: 10.1051/0004-6361/201527173. arXiv: 1606.04373 [astro-ph.GA].

– (Jan. 2019). "Clumpiness of the interstellar medium in the central parsec of the Galaxy from H_2 flux-extinction correlation". In: 621, A65, A65. DOI: 10.1051/0004-6361/201731763. arXiv: 1811.04965 [astro-ph.GA].

Climent, J. B. et al. (Mar. 2020). "VLTI-PIONIER imaging of the red supergiant V602 Carinae". In: 635, A160, A160. DOI: 10.1051/0004-6361/201936734. arXiv: 2002.09243 [astro-ph.SR].

Cohen, M. et al. (2003). "Spectral Irradiance Calibration in the Infrared. XIII. "Supertemplates" and On-Orbit Calibrators for the SIRTF Infrared Array Camera". In: 125, pp. 2645–2663. DOI: 10.1086/374362. eprint: astro-ph/0304349.

Colavita, M. M. (Jan. 1999). "Fringe Visibility Estimators for the Palomar Testbed Interferometer". In: 111.755, pp. 111–117. DOI: 10.1086/316302. arXiv: astro-ph/9810462 [astro-ph].

Colavita, M. M. et al. (Jan. 1999). "The Palomar Testbed Interferometer". In: 510.1, pp. 505–521. DOI: 10.1086/306579. arXiv: astro-ph/9810262 [astro-ph].

Cutri, R. M. et al. (June 2003). "VizieR Online Data Catalog: 2MASS All-Sky Catalog of Point Sources (Cutri+ 2003)". In: *VizieR Online Data Catalog*, II/246, pp. II/246.

Dahmen, G. et al. (Mar. 1998). "Molecular gas in the Galactic center region. II. Gas mass and N_, = H_2/I_(12)CO conversion based on a C(18)O(J = 1 -> 0) survey". In: 331, pp. 959–976. arXiv: astro-ph/9711117 [astro-ph].

de Jager, C., H. Nieuwenhuijzen, and K. A. van der Hucht (Feb. 1988). "Mass loss rates in the Hertzsprung-Russell diagram." In: 72, pp. 259–289.

Do, T. et al. (Feb. 2009). "A Near-Infrared Variability Study of the Galactic Black Hole: A Red Noise Source with NO Detected Periodicity". In: 691.2, pp. 1021–1034. DOI: 10.1088/0004-637X/691/2/1021. arXiv: 0810.0446 [astro-ph].

Do, Tuan et al. (Aug. 2019). "Relativistic redshift of the star S0-2 orbiting the Galactic Center supermassive black hole". In: *Science* 365.6454, pp. 664–668. DOI: 10.1126/science.aav8137. arXiv: 1907.10731 [astro-ph.GA].

Dodds-Eden, K. et al. (June 2009). "Evidence for X-Ray Synchrotron Emission from Simultaneous Mid-Infrared to X-Ray Observations of a Strong Sgr A* Flare". In: 698.1, pp. 676–692. DOI: 10.1088/0004-637X/698/1/676. arXiv: 0903.3416 [astro-ph.GA].

Dodds-Eden, K. et al. (Feb. 2011). "The Two States of Sgr A* in the Near-infrared: Bright Episodic Flares on Top of Low-level Continuous Variability". In: 728.1, 37, p. 37. DOI: 10.1088/0004-637X/728/1/37. arXiv: 1008.1984 [astro-ph.GA].

Eckart, A. et al. (May 1995). "High Angular Resolution Spectroscopic and Polarimetric Imaging of the Galactic Center in the Near-Infrared". In: 445, p. L23. DOI: 10.1086/187880.

Eddington, A. S. (Mar. 1919). "The total eclipse of 1919 May 29 and the influence of gravitation on light". In: *The Observatory* 42, pp. 119–122.

Einstein, A. (Jan. 1915). "Erklarung der Perihelionbewegung der Merkur aus der allgemeinen Relativitatstheorie". In: *Sitzungsber. preuss.Akad. Wiss* 47, pp. 831–839.

Eisenhauer, F. et al. (Nov. 2003). "A Geometric Determination of the Distance to the Galactic Center". In: 597.2, pp. L121–L124. DOI: 10.1086/380188. arXiv: astro-ph/0306220 [astro-ph].

Eisenhauer, F. et al. (July 2005). "SINFONI in the Galactic Center: Young Stars and Infrared Flares in the Central Light-Month". In: 628.1, pp. 246–259. DOI: 10.1086/430667. arXiv: astro-ph/0502129 [astro-ph].

Eisenhauer, F. et al. (July 2008). "GRAVITY: getting to the event horizon of Sgr A*". In: vol. 7013. Society of Photo-Optical Instrumentation Engineers Conference Series, 70132A. DOI: 10.1117/12.788407. arXiv: 0808.0063 [astro-ph].

Ekers, R. D. et al. (June 1983). "The radio structure of SGR A." In: 122, pp. 143–150.

Event Horizon Telescope Collaboration et al. (Apr. 2019). "First M87 Event Horizon Telescope Results. I. The Shadow of the Supermassive Black Hole". In: 875.1, L1, p. L1. DOI: 10.3847/2041-8213/ab0ec7. arXiv: 1906.11238 [astro-ph.GA].

Fabian, A. C. et al. (Sept. 2000). "Broad Iron Lines in Active Galactic Nuclei". In: 112.775, pp. 1145–1161. DOI: 10.1086/316610. arXiv: astro-ph/0004366 [astro-ph].

Federrath, C. et al. (Dec. 2016). "The Link between Turbulence, Magnetic Fields, Filaments, and Star Formation in the Central Molecular Zone Cloud G0.253+0.016". In: 832.2, 143, p. 143. DOI: 10.3847/0004-637X/832/2/143. arXiv: 1609.05911 [astro-ph.GA].

Finger, Gert et al. (July 2008). "Performance evaluation, readout modes, and calibration techniques of HgCdTe Hawaii-2RG mosaic arrays". In: *High Energy, Optical, and Infrared Detectors for Astronomy III*. Vol. 7021. Society of Photo-Optical Instrumentation Engineers Conference Series, 70210P. DOI: 10.1117/12.787971.

Finger, Gert et al. (July 2016). "Sub-electron read noise and millisecond full-frame readout with the near infrared eAPD array SAPHIRA". In: *Adaptive Optics Systems V*. Vol. 9909. Society of Photo-Optical Instrumentation Engineers Conference Series, p. 990912. DOI: 10.1117/12.2233079.

Foreman-Mackey, Daniel (2016). "corner.py: Scatterplot matrices in Python". In: *The Journal of Open Source Software* 1.2, p. 24. DOI: 10.21105/joss.00024. URL: https://doi.org/10.21105/joss.00024.

Foreman-Mackey, Daniel et al. (Mar. 2013). "emcee: The MCMC Hammer". In: 125.925, p. 306. DOI: 10.1086/670067. arXiv: 1202.3665 [astro-ph.IM].

Fried, D. L. (Oct. 1966). "Optical Resolution Through a Randomly Inhomogeneous Medium for Very Long and Very Short Exposures". In: *Journal of the Optical Society of America (1917-1983)* 56.10, p. 1372.

Fritz, T. K. et al. (2011). "Line Derived Infrared Extinction toward the Galactic Center". In: 737, 73, p. 73. DOI: 10.1088/0004-637X/737/2/73. arXiv: 1105.2822.

Fryer, Christopher L. et al. (Feb. 2006). "The Sgr B2 X-Ray Echo of the Galactic Center Supernova Explosion that Produced Sgr A East". In: 638.2, pp. 786–796. DOI: 10.1086/498968. arXiv: astro-ph/0506242 [astro-ph].

Genzel, R. et al. (Sept. 2000). "Stellar dynamics in the Galactic Centre: proper motions and anisotropy". In: 317.2, pp. 348–374. DOI: 10.1046/j.1365-8711.2000.03582.x. arXiv: astro-ph/0001428 [astro-ph].

Genzel, R. et al. (Oct. 2003a). "Near-infrared flares from accreting gas around the supermassive black hole at the Galactic Centre". In: 425.6961, pp. 934–937. DOI: 10.1038/nature02065. arXiv: astro-ph/0310821 [astro-ph].

Genzel, R. et al. (Sept. 2003b). "The Stellar Cusp around the Supermassive Black Hole in the Galactic Center". In: 594.2, pp. 812–832. DOI: 10.1086/377127. arXiv: astro-ph/0305423 [astro-ph].

Genzel, Reinhard, Frank Eisenhauer, and Stefan Gillessen (2010). "The Galactic Center massive black hole and nuclear star cluster". In: *Reviews of Modern Physics* 82.4, pp. 3121–3195. DOI: 10.1103/RevModPhys.82.3121. arXiv: 1006.0064 [astro-ph.GA].

Ghez, A. M. et al. (Apr. 2003). "The First Measurement of Spectral Lines in a Short-Period Star Bound to the Galaxy's Central Black Hole: A Paradox of Youth".

In: 586.2, pp. L127–L131. DOI: 10.1086/374804. arXiv: astro-ph/0302299 [astro-ph].

Ghez, A. M. et al. (Feb. 2005). "Stellar Orbits around the Galactic Center Black Hole". In: 620.2, pp. 744–757. DOI: 10.1086/427175. arXiv: astro-ph/0306130 [astro-ph].

Ghez, A. M. et al. (Dec. 2008). "Measuring Distance and Properties of the Milky Way's Central Supermassive Black Hole with Stellar Orbits". In: 689.2, pp. 1044–1062. DOI: 10.1086/592738. arXiv: 0808.2870 [astro-ph].

Gillessen, S. et al. (Feb. 2009). "Monitoring Stellar Orbits Around the Massive Black Hole in the Galactic Center". In: 692.2, pp. 1075–1109. DOI: 10.1088/0004-637X/692/2/1075. arXiv: 0810.4674 [astro-ph].

Gillessen, S. et al. (Jan. 2012). "A gas cloud on its way towards the supermassive black hole at the Galactic Centre". In: 481.7379, pp. 51–54. DOI: 10.1038/nature10652. arXiv: 1112.3264 [astro-ph.GA].

Gillessen, S. et al. (Sept. 2013). "Pericenter Passage of the Gas Cloud G2 in the Galactic Center". In: 774.1, 44, p. 44. DOI: 10.1088/0004-637X/774/1/44. arXiv: 1306.1374 [astro-ph.GA].

Gillessen, S. et al. (Mar. 2017). "An Update on Monitoring Stellar Orbits in the Galactic Center". In: 837.1, 30, p. 30. DOI: 10.3847/1538-4357/aa5c41. arXiv: 1611.09144 [astro-ph.GA].

Gitton, Philippe B. et al. (Oct. 2004). "IRIS: an infrared tilt sensor for the VLTI". In: ed. by Wesley A. Traub. Vol. 5491. Society of Photo-Optical Instrumentation Engineers Conference Series, p. 944. DOI: 10.1117/12.551377.

Goodman, Jonathan and Jonathan Weare (Jan. 2010). "Ensemble samplers with affine invariance". In: *Communications in Applied Mathematics and Computational Science* 5.1, pp. 65–80. DOI: 10.2140/camcos.2010.5.65.

Goorvitch, D. (1994). "Infrared CO Line List for the X 1 Sigma + State". In: 95, p. 535. DOI: 10.1086/192110.

Gravity Collaboration (Dec. 2017). "First Light for GRAVITY: A New Era for Optical Interferometry". In: *The Messenger* 170, pp. 10–15. DOI: 10.18727/0722-6691/5048.

Gravity Collaboration et al. (2017). "First light for GRAVITY: Phase referencing optical interferometry for the Very Large Telescope Interferometer". In: 602, A94, A94. DOI: 10.1051/0004-6361/201730838. arXiv: 1705.02345 [astro-ph.IM].

Gravity Collaboration et al. (Oct. 2018a). "Detection of orbital motions near the last stable circular orbit of the massive black hole SgrA*". In: 618, L10, p. L10. DOI: 10.1051/0004-6361/201834294. arXiv: 1810.12641 [astro-ph.GA].

Gravity Collaboration et al. (July 2018b). "Detection of the gravitational redshift in the orbit of the star S2 near the Galactic centre massive black hole". In: 615, L15, p. L15. DOI: 10.1051/0004-6361/201833718. arXiv: 1807.09409 [astro-ph.GA].

Gravity Collaboration et al. (2019). "A geometric distance measurement to the Galactic center black hole with 0.3% uncertainty". In: 625, L10, p. L10. DOI: 10.1051/0004-6361/201935656.

Gravity Collaboration et al. (Apr. 2020a). "Detection of the Schwarzschild precession in the orbit of the star S2 near the Galactic centre massive black hole". In: 636, L5, p. L5. DOI: 10.1051/0004-6361/202037813. arXiv: 2004.07187 [astro-ph.GA].

Gravity Collaboration et al. (Mar. 2020b). "Modeling the orbital motion of Sgr A*'s near-infrared flares". In: 635, A143, A143. DOI: 10.1051/0004-6361/201937233.

Gravity Collaboration et al. (June 2020c). "The flux distribution of Sgr A*". In: 638, A2, A2. DOI: 10.1051/0004-6361/202037717. arXiv: 2004.07185 [astro-ph.GA].

Greenstein, J. L., J. B. Oke, and H. L. Shipman (Nov. 1971). "Effective Temperature, Radius, and Gravitational Redshift of Sirius B". In: 169, p. 563. DOI: 10.1086/151174.

Grould, M. et al. (Dec. 2017). "General relativistic effects on the orbit of the S2 star with GRAVITY". In: 608, A60, A60. DOI: 10.1051/0004-6361/201731148. arXiv: 1709.04492 [astro-ph.HE].

Güsten, R. (Jan. 1989). "Gas and Dust in the Inner Few Degrees of the Galaxy (review)". In: *The Center of the Galaxy*. Ed. by Mark Morris. Vol. 136. IAU Symposium, p. 89.

Habibi, M. et al. (Oct. 2017). "Twelve Years of Spectroscopic Monitoring in the Galactic Center: The Closest Look at S-stars near the Black Hole". In: 847.2, 120, p. 120. DOI: 10.3847/1538-4357/aa876f. arXiv: 1708.06353 [astro-ph.SR].

Hadjara, M. et al. (2019). "A CO-multilayer outer atmosphere for eight evolved stars revealed with VLTI/AMBER". In: 489.2, pp. 2595–2614. DOI: 10.1093/mnras/stz2240. arXiv: 1909.03997 [astro-ph.SR].

Hall, D. N. B., S. G. Kleinmann, and N. Z. Scoville (Sept. 1982). "Broad helium emission in the galactic center". In: 260, pp. L53–L57. DOI: 10.1086/183869.

Hamaus, N. et al. (Feb. 2009). "Prospects for Testing the Nature of Sgr A*'s Near-Infrared Flares on the Basis of Current Very Large Telescope—and Future Very Large Telescope Interferometer—Observations". In: 692.1, pp. 902–916. DOI: 10.1088/0004-637X/692/1/902. arXiv: 0810.4947 [astro-ph].

Harper, G. M. et al. (July 2017). "An Updated 2017 Astrometric Solution for Betelgeuse". In: 154.1, 11, p. 11. DOI: 10.3847/1538-3881/aa6ff9. arXiv: 1706.06020 [astro-ph.SR].

Harper, Graham M. et al. (Apr. 2020). "SOFIA-EXES Observations of Betelgeuse during the Great Dimming of 2019/2020". In: 893.1, L23, p. L23. DOI: 10.3847/2041-8213/ab84e6. arXiv: 2003.13884 [astro-ph.SR].

Haubois, X. et al. (2009). "Imaging the spotty surface of Betelgeuse in the H band". In: 508.2, pp. 923–932. DOI: 10.1051/0004-6361/200912927. arXiv: 0910.4167 [astro-ph.SR].

Holberg, J. B. (Jan. 2010). "Sirius B and the Measurement of the Gravitational Redshift". In: *Journal for the History of Astronomy* 41.1, pp. 41–64. DOI: 10.1177/002182861004100102.

Houk, N. (1982). *Michigan Catalogue of Two-dimensional Spectral Types for the HD stars. Volume_3. Declinations -40_f0 to -26_f0.*

Houk, N. and C. Swift (1999). "Michigan catalogue of two-dimensional spectral types for the HD Stars, Vol. 5". In: *Michigan Spectral Survey* 5, p. 0.

Hulse, R. A. and J. H. Taylor (Jan. 1975). "Discovery of a pulsar in a binary system." In: 195, pp. L51–L53. DOI: 10.1086/181708.

Jansky, Karl G. (July 1933). "Radio Waves from Outside the Solar System". In: 132.3323, p. 66. DOI: 10.1038/132066a0.

Jocou, L. et al. (July 2014). "The beam combiners of Gravity VLTI instrument: concept, development, and performance in laboratory". In: *Optical and Infrared Interferometry IV*. Vol. 9146. Society of Photo-Optical Instrumentation Engineers Conference Series, 91461J. DOI: 10.1117/12.2054159.

Joyce, S. R. G. et al. (Dec. 2018). "The gravitational redshift of Sirius B". In: 481.2, pp. 2361–2370. DOI: 10.1093/mnras/sty2404. arXiv: 1809.01240 [astro-ph.SR].

Kamiński, T. (July 2019). "Massive dust clumps in the envelope of the red supergiant VY Canis Majoris". In: 627, A114, A114. DOI: 10.1051/0004-6361/201935408. arXiv: 1903.09558 [astro-ph.SR].

Kassim, N. E. et al. (June 1999). "Wide Field Radio Imaging of the Galactic Center". In: *The Central Parsecs of the Galaxy*. Ed. by Heino Falcke et al. Vol. 186. Astronomical Society of the Pacific Conference Series, p. 403.

Kendrew, S. et al. (Sept. 2012). "GRAVITY Coudé Infrared Adaptive Optics (CIAO) system for the VLT Interferometer". In: *Ground-based and Airborne Instrumentation for Astronomy IV*. Vol. 8446. Society of Photo-Optical Instrumentation Engineers Conference Series, 84467W. DOI: 10.1117/12.926558. arXiv: 1207.2945 [astro-ph.IM].

Kiss, L. L., Gy. M. Szabó, and T. R. Bedding (Nov. 2006). "Variability in red supergiant stars: pulsations, long secondary periods and convection noise". In: 372.4, pp. 1721–1734. DOI: 10.1111/j.1365-2966.2006.10973.x. arXiv: astro-ph/0608438 [astro-ph].

Krabbe, A. et al. (July 1995). "The Nuclear Cluster of the Milky Way: Star Formation and Velocity Dispersion in the Central 0.5 Parsec". In: 447, p. L95. DOI: 10.1086/309579.

Lacour, S. et al. (Apr. 2019). "The GRAVITY fringe tracker". In: 624, A99, A99. DOI: 10.1051/0004-6361/201834981. arXiv: 1901.03202 [astro-ph.IM].

Lacy, J. H. et al. (Oct. 1980). "Observations of the motion and distribution of the ionized gas in the central parsec of the Galaxy. II." In: 241, pp. 132–146. DOI: 10.1086/158324.

Lapeyrere, V. et al. (2014). "GRAVITY data reduction software". In: *Optical and Infrared Interferometry IV*. Vol. 9146. P. 91462D. DOI: 10.1117/12.2056850.

Lau, R. M. et al. (Sept. 2013). "SOFIA/FORCAST Imaging of the Circumnuclear Ring at the Galactic Center". In: 775.1, 37, p. 37. DOI: 10.1088/0004-637X/775/1/37. arXiv: 1307.8443 [astro-ph.GA].

Lawson, P.R. (Jan. 2000). *Principles of Long Baseline Stellar Interferometry*.

Le Verrier, Urbain J. (Jan. 1859). "Theorie du mouvement de Mercure". In: *Annales de l'Observatoire de Paris* 5, p. 1.

Lebofsky, M. J., G. H. Rieke, and A. T. Tokunaga (Dec. 1982). "M supergiants and star formation at the galactic center." In: 263, pp. 736–740. DOI: 10.1086/160545.

Levesque, Emily M (2017). *Astrophysics of Red Supergiants*. 2514-3433. IOP Publishing. ISBN: 978-0-7503-1329-2. DOI: 10.1088/978-0-7503-1329-2. URL: http://dx.doi.org/10.1088/978-0-7503-1329-2.

Levesque, Emily M. and Philip Massey (Mar. 2020). "Betelgeuse Just Is Not That Cool: Effective Temperature Alone Cannot Explain the Recent Dimming of Betelgeuse". In: 891.2, L37, p. L37. DOI: 10.3847/2041-8213/ab7935. arXiv: 2002.10463 [astro-ph.SR].

Levesque, Emily M. et al. (Aug. 2005). "The Effective Temperature Scale of Galactic Red Supergiants: Cool, but Not As Cool As We Thought". In: 628.2, pp. 973–985. DOI: 10.1086/430901. arXiv: astro-ph/0504337 [astro-ph].

Lippa, Magdalena et al. (Aug. 2016). "The metrology system of the VLTI instrument GRAVITY". In: *Optical and Infrared Interferometry and Imaging V*. Vol. 9907. Society of Photo-Optical Instrumentation Engineers Conference Series, p. 990722. DOI: 10.1117/12.2232272. arXiv: 1608.04888 [astro-ph.IM].

Lo, K. Y. and M. J. Claussen (Dec. 1983). "High-resolution observations of ionized gas in central 3 parsecs of the Galaxy: possible evidence for infall". In: 306.5944, pp. 647–651. DOI: 10.1038/306647a0.

Lo, K. Y. et al. (Dec. 1975). "VLBI observations of the compact radio source in the center of the Galaxy." In: 202, pp. L63–L65. DOI: 10.1086/181982.

Lo, K. Y. et al. (May 1985). "On the size of the galactic centre compact radio source: diameter <20 AU". In: 315.6015, pp. 124–126. DOI: 10.1038/315124a0.

Lu, J. R. et al. (2009). "A Disk of Young Stars at the Galactic Center as Determined by Individual Stellar Orbits". In: 690.2, pp. 1463–1487. DOI: 10.1088/0004-637X/690/2/1463. arXiv: 0808.3818 [astro-ph].

Markoff, S. et al. (Nov. 2001). "The Nature of the 10 kilosecond X-ray flare in Sgr A*". In: 379, pp. L13–L16. DOI: 10.1051/0004-6361:20011346. arXiv: astro-ph/0109081 [astro-ph].

Martins, F. et al. (2007). "Stellar and wind properties of massive stars in the central parsec of the Galaxy". In: 468.1, pp. 233–254. DOI: 10.1051/0004-6361:20066688. arXiv: astro-ph/0703211 [astro-ph].

Martins, F. et al. (Jan. 2008). "On the Nature of the Fast-Moving Star S2 in the Galactic Center". In: 672.2, p. L119. DOI: 10.1086/526768. arXiv: 0711.3344 [astro-ph].

Mauron, N. and E. Josselin (2011). "The mass-loss rates of red supergiants and the de Jager prescription". In: 526, A156, A156. DOI: 10.1051/0004-6361/201013993. arXiv: 1010.5369 [astro-ph.SR].

Melnik, A. M. and A. K. Dambis (July 2020). "Distance scale for high-luminosity stars in OB associations and in field with Gaia DR2. Spurious systematic motions". In: 365.7, 112, p. 112. DOI: 10.1007/s10509-020-03827-0. arXiv: 2006.14649 [astro-ph.GA].

Menu, J. et al. (May 2012). "Kalman-filter control schemes for fringe tracking. Development and application to VLTI/GRAVITY". In: 541, A81, A81. DOI: 10.1051/0004-6361/201218932. arXiv: 1203.4430 [astro-ph.IM].

Meyer, L. et al. (Oct. 2012). "The Shortest-Known-Period Star Orbiting Our Galaxy's Supermassive Black Hole". In: *Science* 338.6103, p. 84. DOI: 10.1126/science.1225506. arXiv: 1210.1294 [astro-ph.GA].

Michelson, A. A. (June 1920). "On the Application of Interference Methods to Astronomical Measurements". In: 51, p. 257. DOI: 10.1086/142550.

Michelson, A. A. and F. G. Pease (May 1921). "Measurement of the Diameter of α Orionis with the Interferometer." In: 53, pp. 249–259. DOI: 10.1086/142603.

Monnier, J. D. et al. (Apr. 2004). "High-Resolution Imaging of Dust Shells by Using Keck Aperture Masking and the IOTA Interferometer". In: 605.1, pp. 436–461. DOI: 10.1086/382218. arXiv: astro-ph/0401363 [astro-ph].

Montargès, M. et al. (2014). "Properties of the CO and H_2O MOLsphere of the red supergiant Betelgeuse from VLTI/AMBER observations". In: 572, A17, A17. DOI: 10.1051/0004-6361/201423538. arXiv: 1408.2994 [astro-ph.SR].

Montargès, M. et al. (Sept. 2017). "The convective surface of the red supergiant Antares. VLTI/PIONIER interferometry in the near infrared". In: 605, A108, A108. DOI: 10.1051/0004-6361/201629985. arXiv: 1705.07829 [astro-ph.SR].

Montargès, M. et al. (2018). "The convective photosphere of the red supergiant CE Tauri. I. VLTI/PIONIER H-band interferometric imaging". In: 614, A12, A12. DOI: 10.1051/0004-6361/201731471. arXiv: 1802.06086 [astro-ph.SR].

Montarges, Miguel (2014). "Perte de masse des Ã©toiles massives Ã©voluÃ©es : l'environnement circumstellaire Ã haute rÃ©solution angulaire". ThÃšse de doctorat dirigÃ©e par Kervella, Pierre et Perrin, Guy Astronomie et Astrophysique Paris 6 2014. PhD thesis. URL: http://www.theses.fr/2014PA066364.

Morris, M. et al. (Aug. 1983). "The temperature of molecular gas in the galactic center region." In: 88, pp. 1228–1235. DOI: 10.1086/113413.

Morris, Mark R., Jun-Hui Zhao, and W. M. Goss (Dec. 2017). "A Nonthermal Radio Filament Connected to the Galactic Black Hole?" In: 850.2, L23, p. L23. DOI: 10.3847/2041-8213/aa9985. arXiv: 1711.04190 [astro-ph.GA].

Mossoux, E. et al. (May 2016). "Multiwavelength study of the flaring activity of Sagittarius A in 2014 February-April". In: 589, A116, A116. DOI: 10.1051/0004-6361/201527554. arXiv: 1603.01048 [astro-ph.HE].

Najarro, F. et al. (Sept. 1997). "Quantitative spectroscopy of the HeI cluster in the Galactic center." In: 325, pp. 700–708.

Neugebauer, G. et al. (May 1976). "Late-type giants and supergiants in the galactic center." In: 205, pp. L139–L141. DOI: 10.1086/182108.

Newton, Isaac (1687). *Philosophiae Naturalis Principia Mathematica. Auctore Js. Newton*. DOI: 10.3931/e-rara-440.

O'Gorman, E. et al. (2017). "The inhomogeneous submillimeter atmosphere of Betelgeuse". In: 602, L10, p. L10. DOI: 10.1051/0004-6361/201731171. arXiv: 1706.06021 [astro-ph.SR].

Ohnaka, K., G. Weigelt, and K. H. Hofmann (2017). "Vigorous atmospheric motion in the red supergiant star Antares". In: 548.7667, pp. 310–312. DOI: 10.1038/nature23445. arXiv: 1708.06372 [astro-ph.SR].

Ott, Thomas, Andreas Eckart, and Reinhard Genzel (Sept. 1999). "Variable and Embedded Stars in the Galactic Center". In: 523.1, pp. 248–264. DOI: 10.1086/307712.

Paumard, T., J. P. Maillard, and M. Morris (Oct. 2004). "Kinematic and structural analysis of the <ASTROBJ>Minispiral</ASTROBJ> in the Galactic Center from BEAR spectro-imagery". In: 426, pp. 81–96. DOI: 10.1051/0004-6361:20034209. arXiv: astro-ph/0405197 [astro-ph].

Paumard, T. et al. (Feb. 2001). "New results on the helium stars in the galactic center using BEAR spectro-imagery". In: 366, pp. 466–480. DOI: 10.1051/0004-6361:20000227. arXiv: astro-ph/0011215 [astro-ph].

Paumard, T. et al. (2006). "The Two Young Star Disks in the Central Parsec of the Galaxy: Properties, Dynamics, and Formation". In: 643.2, pp. 1011–1035. DOI: 10.1086/503273. arXiv: astro-ph/0601268 [astro-ph].

Paumard, T. et al. (2014). "<ASTROBJ>GCIRS 7</ASTROBJ>, a pulsating M1 supergiant at the Galactic centre . Physical properties and age". In: 568, A85, A85. DOI: 10.1051/0004-6361/201423991. arXiv: 1406.5320 [astro-ph.SR].

Perrin, G. et al. (2004). "Unveiling Mira stars behind the molecules. Confirmation of the molecular layer model with narrow band near-infrared interferometry". In: 426, pp. 279–296. DOI: 10.1051/0004-6361:20041098.

Perrin, G. et al. (2005). "Study of molecular layers in the atmosphere of the supergiant star μ Cep by interferometry in the K band". In: 436, pp. 317–324. DOI: 10.1051/0004-6361:20042313. eprint: astro-ph/0502415.

Perrin, G. et al. (Nov. 2007). "The molecular and dusty composition of Betelgeuse's inner circumstellar environment". In: 474.2, pp. 599–608. DOI: 10.1051/0004-6361:20077863. arXiv: 0709.0356 [astro-ph].

Pfuhl, O. et al. (July 2014). "The fiber coupler and beam stabilization system of the GRAVITY interferometer". In: *Optical and Infrared Interferometry IV*. Vol. 9146. Society of Photo-Optical Instrumentation Engineers Conference Series, p. 914623. DOI: 10.1117/12.2055080. arXiv: 1412.1696 [astro-ph.IM].

Plewa, P. M. et al. (Nov. 2015). "Pinpointing the near-infrared location of Sgr A* by correcting optical distortion in the NACO imager". In: 453.3, pp. 3234–3244. DOI: 10.1093/mnras/stv1910. arXiv: 1509.01941 [astro-ph.GA].

Plewa, P. M. et al. (May 2017). "The Post-pericenter Evolution of the Galactic Center Source G2". In: 840.1, 50, p. 50. DOI: 10.3847/1538-4357/aa6e00. arXiv: 1704.05351 [astro-ph.GA].

Ponti, Gabriele et al. (Jan. 2013). "Traces of Past Activity in the Galactic Centre". In: *Cosmic Rays in Star-Forming Environments*. Ed. by Diego F. Torres and Olaf Reimer. Vol. 34, p. 331. DOI: 10.1007/978-3-642-35410-6_26. arXiv: 1210.3034 [astro-ph.GA].

Pott, J. U. et al. (2008). "First VLTI infrared spectro-interferometry on GCIRS 7. Characterizing the prime reference source for Galactic center observations at highest angular resolution". In: 487.1, pp. 413–418. DOI: 10.1051/0004-6361:200809829. arXiv: 0805.4408 [astro-ph].

Pound, R. V. and G. A. Rebka (Nov. 1959a). "Gravitational Red-Shift in Nuclear Resonance". In: 3.9, pp. 439–441. DOI: 10.1103/PhysRevLett.3.439.

– (Dec. 1959b). "Resonant Absorption of the 14.4-kev γ Ray from 0.10-μsec Fe^{57}". In: 3.12, pp. 554–556. DOI: 10.1103/PhysRevLett.3.554.

Press, William H. et al. (1992). *Numerical Recipes in C*. Third. Cambridge, USA: Cambridge University Press.

Rieke, G. H. and F. J. Low (Sept. 1973). "Infrared maps of the galactic nucleus." In: 184, pp. 415–425. DOI: 10.1086/152340.

Sanchez-Bermudez, J. et al. (July 2014). "Properties of bow-shock sources at the Galactic center". In: 567, A21, A21. DOI: 10.1051/0004-6361/201423657. arXiv: 1405.4528 [astro-ph.SR].

Sauval, A. J. and J. B. Tatum (Oct. 1984). "A set of partition functions and equilibrium constants for 300 diatomic molecules of astrophysical interest". In: 56, pp. 193–209. DOI: 10.1086/190980.

Schödel, R. et al. (Oct. 2002). "A star in a 15.2-year orbit around the supermassive black hole at the centre of the Milky Way". In: 419.6908, pp. 694–696. DOI: 10.1038/nature01121. arXiv: astro-ph/0210426 [astro-ph].

Schödel, R. et al. (2010). "Peering through the veil: near-infrared photometry and extinction for the Galactic nuclear star cluster. Accurate near infrared H, Ks, and L' photometry and the near-infrared extinction-law toward the central parsec of the Galaxy". In: 511, A18, A18. DOI: 10.1051/0004-6361/200913183.

Sellgren, K. et al. (June 1987). "Radial Velocities of Late-Type Stars in the Galactic Center". In: 317, p. 881. DOI: 10.1086/165338.

Serabyn, E., J. H. Lacy, and J. M. Achtermann (1991). "A Gaseous Tail Ablated from the Supergiant IRS 7 near the Galactic Center". In: 378, p. 557. DOI: 10.1086/170457.

Shapiro, Irwin I. (Dec. 1964). "Fourth Test of General Relativity". In: 13.26, pp. 789–791. DOI: 10.1103/PhysRevLett.13.789.

Shapiro, Irwin I. et al. (May 1968). "Fourth Test of General Relativity: Preliminary Results". In: 20.22, pp. 1265–1269. DOI: 10.1103/PhysRevLett.20.1265.

Sharma, Sanjib (Aug. 2017). "Markov Chain Monte Carlo Methods for Bayesian Data Analysis in Astronomy". In: 55.1, pp. 213–259. DOI: 10.1146/annurev-astro-082214-122339. arXiv: 1706.01629 [astro-ph.IM].

Skrutskie, M. F. et al. (2006). "The Two Micron All Sky Survey (2MASS)". In: 131, pp. 1163–1183. DOI: 10.1086/498708.

Smith, Nathan (Aug. 2014). "Mass Loss: Its Effect on the Evolution and Fate of High-Mass Stars". In: 52, pp. 487–528. DOI: 10.1146/annurev-astro-081913-040025. arXiv: 1402.1237 [astro-ph.SR].

Spinrad, Hyron and Robert F. Wing (Jan. 1969). "Infrared Spectra of Stars". In: 7, p. 249. DOI: 10.1146/annurev.aa.07.090169.001341.

Stark, A. A. et al. (Jan. 1989). "Molecular Line Observations of the Galactic Center Region". In: *The Center of the Galaxy*. Ed. by Mark Morris. Vol. 136. IAU Symposium, p. 129.

Storey, J. W. V. and D. A. Allen (Sept. 1983). "The Galactic nucleus." In: 204, pp. 1153–1161. DOI: 10.1093/mnras/204.4.1153.

Stothers, Richard B. (Dec. 2010). "Giant Convection Cell Turnover as an Explanation of the Long Secondary Periods in Semiregular Red Variable Stars". In: 725.1, pp. 1170–1174. DOI: 10.1088/0004-637X/725/1/1170.

Straubmeier, Christian et al. (July 2014). "The GRAVITY spectrometers: optical design and first light". In: *Optical and Infrared Interferometry IV*. Vol. 9146. Society of Photo-Optical Instrumentation Engineers Conference Series, p. 914629. DOI: 10.1117/12.2054736.

Tagger, Michel and Fulvio Melia (Jan. 2006). "A Possible Rossby Wave Instability Origin for the Flares in Sagittarius A*". In: 636.1, pp. L33–L36. DOI: 10.1086/499806. arXiv: astro-ph/0511520 [astro-ph].

Tamblyn, Peter and G. H. Rieke (Sept. 1993). "IRS 16: The Galaxy's Central Wimp?" In: 414, p. 573. DOI: 10.1086/173104.

Tanaka, Y. et al. (June 1995). "Gravitationally redshifted emission implying an accretion disk and massive black hole in the active galaxy MCG-6-30-15". In: 375.6533, pp. 659–661. DOI: 10.1038/375659a0.

Tatulli, E. et al. (Mar. 2007). "Interferometric data reduction with AMBER/VLTI. Principle, estimators, and illustration". In: 464.1, pp. 29–42. DOI: 10.1051/0004-6361:20064799. arXiv: astro-ph/0603046 [astro-ph].

Taylor, G. I. (Feb. 1938). "The Spectrum of Turbulence". In: *Proceedings of the Royal Society of London Series A* 164.919, pp. 476–490. DOI: 10.1098/rspa.1938.0032.

Taylor, J. H. and J. M. Weisberg (Feb. 1982). "A new test of general relativity - Gravitational radiation and the binary pulsar PSR 1913+16". In: 253, pp. 908–920. DOI: 10.1086/159690.

Teyssier, D. et al. (Sept. 2012). "Herschel/HIFI observations of red supergiants and yellow hypergiants. I. Molecular inventory". In: 545, A99, A99. DOI: 10.1051/0004-6361/201219545. arXiv: 1208.3143 [astro-ph.GA].

Trotta, Roberto (Mar. 2008). "Bayes in the sky: Bayesian inference and model selection in cosmology". In: *Contemporary Physics* 49.2, pp. 71–104. DOI: 10.1080/00107510802066753. arXiv: 0803.4089 [astro-ph].

Tsuboi, Masato et al. (June 2017). "ALMA View of the Galactic Center Minispiral: Ionized Gas Flows around Sagittarius A*". In: 842.2, 94, p. 94. DOI: 10.3847/1538-4357/aa74e3. arXiv: 1608.08714 [astro-ph.GA].

Tsuboi, Masato et al. (Apr. 2020). "Sub-millimeter detection of a Galactic center cool star IRS 7 by ALMA". In: 72.2, 36, p. 36. DOI: 10.1093/pasj/psaa013. arXiv: 2002.01620 [astro-ph.GA].

Tsuji, Takashi (2000). "Water in Emission in the Infrared Space Observatory Spectrum of the Early M Supergiant Star μ Cephei". In: 540.2, pp. L99–L102. DOI: 10.1086/312879. arXiv: astro-ph/0008058 [astro-ph].

van Cittert, P. H. (1934). "Die Wahrscheinliche Schwingungsverteilung in Einer von Einer Lichtquelle Direkt Oder Mittels Einer Linse Beleuchteten Ebene". In: *Physica* 1, pp. 201–210. DOI: 10.1016/S0031-8914(34)90026-4.

Vessot, R. F. C. et al. (Dec. 1980). "Test of Relativistic Gravitation with a Space-Borne Hydrogen Maser". In: 45.26, pp. 2081–2084. DOI: 10.1103/PhysRevLett.45.2081.

Vincent, F. H. et al. (July 2014). "Distinguishing an ejected blob from alternative flare models at the Galactic Centre with GRAVITY". In: 441.4, pp. 3477–3487. DOI: 10.1093/mnras/stu812. arXiv: 1404.6149 [astro-ph.HE].

Vincent, F. H. et al. (May 2016). "Imaging a boson star at the Galactic center". In: *Classical and Quantum Gravity* 33.10, 105015, p. 105015. DOI: 10.1088/0264-9381/33/10/105015. arXiv: 1510.04170 [gr-qc].

Vincent, F. H. et al. (Apr. 2019). "Multi-wavelength torus-jet model for Sagittarius A*". In: 624, A52, A52. DOI: 10.1051/0004-6361/201834946. arXiv: 1902.01175 [astro-ph.HE].

Vincent, F. H. et al. (Feb. 2020). "Geometric modeling of M87* as a Kerr black hole or a non-Kerr compact object". In: *arXiv e-prints*, arXiv:2002.09226, arXiv:2002.09226. arXiv: 2002.09226 [gr-qc].

Witzel, G. et al. (Sept. 2017). "The Post-periapsis Evolution of Galactic Center Source G1: The Second Case of a Resolved Tidal Interaction with a Supermassive Black Hole". In: 847.1, 80, p. 80. DOI: 10.3847/1538-4357/aa80ea. arXiv: 1707.02301 [astro-ph.GA].

Woillez, J. et al. (2019). "NAOMI: the adaptive optics system of the Auxiliary Telescopes of the VLTI". In: 629, A41, A41. DOI: 10.1051/0004-6361/201935890. arXiv: 1908.06651 [astro-ph.IM].

Yang, Ming and B. W. Jiang (July 2012). "The Period-Luminosity Relation of Red Supergiant Stars in the Small Magellanic Cloud". In: 754.1, 35, p. 35. DOI: 10.1088/0004-637X/754/1/35. arXiv: 1205.1275 [astro-ph.SR].

Yelda, S. et al. (2014). "Properties of the Remnant Clockwise Disk of Young Stars in the Galactic Center". In: 783.2, 131, p. 131. DOI: 10.1088/0004-637X/783/2/131. arXiv: 1401.7354 [astro-ph.GA].

Yuan, Feng, Eliot Quataert, and Ramesh Narayan (Nov. 2003). "Nonthermal Electrons in Radiatively Inefficient Accretion Flow Models of Sagittarius A*". In: 598.1, pp. 301–312. DOI: 10.1086/378716. arXiv: astro-ph/0304125 [astro-ph].

Yusef-Zadeh, F. and Mark Morris (1991). "A Windswept Cometary Tail on the Galactic Center Supergiant IRS 7". In: 371, p. L59. DOI: 10.1086/186002.

Yusef-Zadeh, F. et al. (Oct. 2006). "Flaring Activity of Sagittarius A* at 43 and 22 GHz: Evidence for Expanding Hot Plasma". In: 650.1, pp. 189–194. DOI: 10.1086/506375. arXiv: astro-ph/0603685 [astro-ph].

Zernike, F. (1938). "The concept of degree of coherence and its application to optical problems". In: *Physica* 5, pp. 785–795. DOI: 10.1016/S0031-8914(38)80203-2.

Zhao, Jun-Hui et al. (July 2009). "Dynamics of Ionized Gas at the Galactic Center: Very Large Array Observations of the Three-dimensional Velocity Field and Location of the Ionized Streams in Sagittarius A West". In: 699.1, pp. 186–214. DOI: 10.1088/0004-637X/699/1/186. arXiv: 0904.3133 [astro-ph.GA].

Appendix A

Scientific production: The molecular shell of GCIRS 7

I present here the paper submitted to the journal *Astronomy & Astrophysics* on 23 September 2020, as the first author inside the GRAVITY Collaboration. It summarizes the research work performed during the second part of the thesis, about the star GCIRS 7. The details of the work are described in Chapter 4.

Astronomy & Astrophysics manuscript no. output
March 3, 2021
©ESO 2021

MOLsphere and pulsations of the Galactic Centre red supergiant GCIRS7 from VLTI/GRAVITY⋆

GRAVITY Collaboration⋆⋆: G. Rodríguez-Coira[2], T. Paumard[2], G. Perrin[2], F. Vincent[2], R. Abuter[8], A. Amorim[6,13], M. Bauböck[1], J. P. Berger[5], H. Bonnet[8], W. Brandner[3], Y. Clénet[2], P. T. de Zeeuw[11,1], J. Dexter[1,14], A. Drescher[1], A. Eckart[4,10], F. Eisenhauer[1], N. M. Förster Schreiber[1], F. Gao[1], P. Garcia[7,13], E. Gendron[2], R. Genzel[1,12], S. Gillessen[1], M. Habibi[1], X. Haubois[9], T. Henning[3], S. Hippler[3], M. Horrobin[4], A. Jimenez-Rosales[1], L. Jochum[9], L. Jocou[5], A. Kaufer[9], P. Kervella[2], S. Lacour[2], V. Lapeyrère[2], J. B. Le Bouquin[5], P. Léna[2], M. Nowak[16,2], T. Ott[1], K. Perraut[5], O. Pfuhl[8], J. Sanchez-Bermudez[3,17], J. Shangguan[1], S. Scheithauer[3], J. Stadler[1], O. Straub,[1], C. Straubmeier[4], E. Sturm[1], L. J. Tacconi[1], T. Shimizu[1], S. von Fellenberg[1], I. Waisberg[15,1], F. Widmann[1], E. Wieprecht[1], E. Wiezorrek[1], J. Woillez[8], S. Yazici[1,4], and G. Zins[9]

(Affiliations can be found after the references)

Submitted 23 September 2020 / Accepted YYYY

ABSTRACT

Context. GCIRS 7, the brightest star in the Galactic central parsec, formed 6 ± 2 Myr ago together with dozens of massive stars in a disk orbiting the central black-hole. GCIRS 7 has been claimed to pulsate based on photometric variability arguments.
Aims. Our goal is to confirm the photospheric pulsations based on interferometric size measurements in order to better understand how the mass loss from these massive stars enrich the local interstellar medium.
Methods. We present the first medium-resolution (R = 500), K-band spectro-interferometric observations of GCIRS 7, using the GRAVITY instrument with the four Auxiliary Telescopes of the ESO VLTI. We look for variations using two epochs (2017 and 2019).
Results. GCIRS 7 is moderately resolved with a uniform-disk photospheric diameter of $\theta^*_{\rm UD} = 1.55 \pm 0.03$ mas ($R^*_{\rm UD} = 1368 \pm 26\,R_\odot$) in the K-band continuum. The narrow-band uniform-disk diameter increases above 2.3 μm with a clear correlation with the CO band heads in the spectrum. This correlation is well modelled by a hot ($T_{\rm L}$ = 2368 ± 37 K), geometrically thin molecular shell with diameter $\theta_{\rm L}$ = 1.74 ± 0.03 mas in 2017. The shell diameter increases ($\theta_{\rm L} = 1.89 \pm 0.03$ mas) while its temperature decreases ($T_{\rm L} = 2140 \pm 42$ K) in 2019. In contrast, the photospheric diameter $\theta^*_{\rm UD}$ and the extinction up to the photosphere of GCIRS 7 ($A_{\rm K_S}$ = 3.18 ± 0.16) have the same value within uncertainties at the two epochs.
Conclusions. In the context of previous interferometric and photo-spectrometric measurements, the GRAVITY data allow for an interpretation in terms of photospheric pulsations. The photospheric diameter measured in 2017 and 2019 is significantly larger than previously reported using the PIONIER instrument (θ_* = 1.076 ± 0.093 mas in 2013 in the H band). The parameters of the photosphere and molecular shell of GCIRS 7 are comparable to those of other red supergiants previously studied by interferometry. The extinction we measure is lower than previous estimates in the direction of GCIRS 7 but typical for the central parsec region.

Key words. galaxy: nucleus – supergiants – stars: individual: GCIRS 7 – stars: fundamental parameters – techniques: interferometric

1. Introduction

The stellar population of the central parsec of the Galaxy has been widely studied (Genzel et al. 2010; Morris et al. 2012, and references therein), where the presence of a disk of young stars is well known (Genzel et al. 2000, 2003; Paumard et al. 2006; Lu et al. 2009; Bartko et al. 2009; Yelda et al. 2014). Most of these stars are massive O-type supergiants and Wolf-Rayet stars (Martins et al. 2007; Bartko et al. 2010; Sanchez-Bermudez et al. 2014). GCIRS 7 is one of the few evolved late-type stars (an M1 red supergiant or RSG, Blum et al. 1996b), a SiO maser source (Menten et al. 1997) and the brightest star (in the H and K bands, with H = 9.5 and K = 6.5) of all the central parsec (Becklin & Neugebauer 1975). The works of Yusef-Zadeh & Morris (1991), and Serabyn et al. (1991) have reported a cometary tail whose origin is GCIRS 7, and more recently Tsuboi et al. (2020) revealed the presence of an ionised shell in the core of the cometary tail, estimating the mass loss of GCIRS 7 with ALMA observations.

This stellar population is soaked in a complex interstellar medium (ISM) environment and interacts with it. The central parsec is surrounded by a 2–7 pc-wide clumpy torus, the Circumnuclear Disk (CND), composed of dust and neutral gas (Becklin et al. 1982). The H II region Sgr A West (the Minispiral; e.g. Lacy et al. 1980; Lo & Claussen 1983) consists in tidally-sheared streamers and smaller patches and filaments of dust and ionised gas that orbit and penetrate the central parsec (Liszt 2003; Paumard et al. 2004; Mužić et al. 2007; Irons et al. 2012; Tsuboi et al. 2017). The volume surrounding these components inside the central cavity of the CND is not empty, but filled with a hot (≈ 1.3 keV) plasma detected in X-ray (Baganoff et al. 2003). Finally, warm H_2 (with excitation temperature $T_e \approx 2000$ K) has

⋆ Based on observations made with ESO Telescopes at the La Silla Paranal Observatory under programme IDs 098.D-0250 and 103.B-0032.
⋆⋆ GRAVITY is developed in a collaboration by the Max Planck Institute for extraterrestrial Physics, LESIA of Observatoire de Paris / Université PSL / CNRS / Sorbonne Université / Université de Paris and IPAG of Université Grenoble Alpes / CNRS, the Max Planck Institute for Astronomy, the University of Cologne, the CENTRA - Centro de Astrofisica e Gravitação, and the European Southern Observatory. Corresponding author: G. Rodríguez-Coira.

been detected throughout the central parsec, presumably at the surface of many dusty clumps (Ciurlo et al. 2016, 2019). Ferrière (2012) gives an interesting overview of the ISM content of the central parsec. The large and dense clumps that form the Minispiral are believed to be falling-in from the CND and beyond, but the origin of the lighter and less dense features (filaments, smaller clumps, X-ray plasma) is less clear. A fraction of them could originate in the feedback from the massive stars. G1 (a.k.a. Sgr A*-f, Clénet et al. 2004, 2005) and G2 (Gillessen et al. 2012) may well be extreme examples of such feedback clumplets (e.g. Meyer & Meyer-Hofmeister 2012; De Colle et al. 2014; Schartmann et al. 2015).

Thanks to the performance of stellar interferometers, the understanding of the structure and evolution of RSG has improved significantly. The closest ones have been widely studied, measuring not only their sizes but also revealing single layer atmospheres (Perrin et al. 2005, 2007; Montargès et al. 2014), multi-layer atmospheres (Ohnaka et al. 2009, 2011, 2013; Haddjara et al. 2019), complex structures in the photosphere (Haubois et al. 2009; Chiavassa et al. 2010; Ravi et al. 2011; O'Gorman et al. 2017; Ohnaka et al. 2017), or even the temporal evolution of the stellar surface (Ohnaka et al. 2011, 2013; Montargès et al. 2016, 2018; Climent et al. 2020). Moreover, imaging of RSG has been performed in Baron et al. (2014); Monnier et al. (2014) and more recently in Wittkowski et al. (2017a) and Climent et al. (2020). Although the sample of spatially resolved RSGs has been increasing within the last decade (Arroyo-Torres et al. 2013, 2015; Wittkowski et al. 2017b), this sample is still not very large due to the shortness of the RSG phase, hence only a small number of stars can be resolved by interferometers. If available, the study and characterisation of the outer atmosphere of any new RSG and its temporal evolution would add valuable knowledge to the understanding of their mass loss processes, which have not been yet fully described from first principles (Beasor et al. 2020).

Paumard et al. (2014) compiled almost 40 years of near-infrared photometric data of GCIRS 7 and exhibited two periods in the light-curves: a short "fundamental" period $P_0 \approx 470$ days and a long "secondary" period of $P_{\rm LSP} \approx 2800$ days as often seen in RSGs. Those periods are believed to be the sign of pulsations, especially for P_0 of the fundamental or first overtone radial mode (Yang & Jiang 2012, and references therein). Such pulsations should play a major role in the mass loss of RSGs. However, they have never been confirmed on the basis of direct size measurements. GCIRS 7 has been observed by interferometry on the VLTI using AMBER in the K band and PIONIER in the H band (Pott et al. 2008; Paumard et al. 2014), however the AMBER data do not have sufficient spectral resolution and (u, v)-coverage to disentangle the stellar disk from the circumstellar environment so that only the PIONIER data provide a trustworthy uniform-disk diameter ($\theta_{\rm UD}(2013) = 1.076 \pm 0.093$ mas).

The GRAVITY instrument tremendously increased the sensitivity of the VLTI (Gravity Collaboration et al. 2017), allowing us to observe GCIRS 7 at moderate spectral resolution ($R = 500$) in single-field mode using the four 1.8-m Auxiliary Telescopes (AT) at two epochs (2017 and 2019), with the goal of detecting variations in the photospheric diameter of the star and in its circumstellar environment. The data sets, the data reduction and the calibration processes are described in Sect. 2. The methods and models used to measure the parameters of the star are described in Sect. 3. The results and their implications are discussed in Sect. 4. Finally, conclusions are presented in Sect. 5.

Table 1. Observation log. HD45124 has been used for spectral calibration only. The atmospheric data has been obtained from Paranal ASM (Astronomical Site Monitoring).

Time (UT)	Target	Seeing (")	τ_0 (ms)
18-03-2017 (COMBINED mode)			
09:43:10	GCIRS 7 (SCI-SCI-SKY)	0.55-0.58	6.27
10:08:04	HD160852 (CAL-SKY)	0.71-0.64	4.48
05-07-2019 (SPLIT mode)			
04:49:38	GCIRS 7 (SCI-SCI-SKY)	0.69-0.53	4.49
05:08:29	HD161703 (CAL-CAL-SKY)	0.72-0.81	4.45
06-07-2019 (SPLIT mode)			
03:13:00	GCIRS 7 (SCI-SKY)	0.51-0.60	6.66
03:25:51	HD161703 (CAL-CAL-SKY)	0.60 -0.64	5.59
03:43:00	GCIRS 7 (SCI-SCI-SKY)	0.53-0.55	5.88
03:59:51	HD161703 (CAL-CAL-SKY)	0.72-0.88	3.68
04:17:12	GCIRS 7 (SCI-SCI-SKY)	0.91-0.75	3.55
04:33:39	HD161703 (CAL-CAL-SKY)	0.73-0.79	5.23

2. Data

The log of the data is presented in Table 1 with science on-target (SCI), calibrator on-target (CAL) and sky (SKY) frames. The data were taken at two different epochs (two SCI data frames with run ID 098.D-0250(B) corresponding to the night of 18th March 2017 and seven SCI data frames with run ID 103.B-0032(F) corresponding to the nights of the 5th and 6th July 2019) with two different baseline configurations shown in Figure 1. The maximum baseline was 132.5 m in 2017 and 129.3 m in 2019. Turbulence in the beams was corrected with the NAOMI adaptive optics (AO) system (Gonté et al. 2016; Woillez et al. 2019) on axis for the 2019 data, while only tip-tilt stabilisation using STRAP on a nearby visible star was possible in 2017. Fringe-tracking was performed on-axis at both epochs. Only the science beam combiner data were used in this study since the fringe-tracker data do not have sufficient spectral resolution for our purpose.

We chose a single target to be the calibrator for both spectroscopy and interferometry. We used this calibrator to remove the atmospheric features using the appropriate template (see Sect. 2.1.2). The calibrator is always observed at the same air mass and integration time as the science sequence (DIT = 10 s, NDIT = 30, air mass = 1.01 in 2017 and DIT = 5 s, NDIT = 30, air mass = 1.01 in 2019). We have recorded the 2017 data in combined polarisation mode and the 2019 data in split polarisation mode, making use of the Wollaston prism. For this reason, the second run in 2019 results in two simultaneously-recorded data sets, one for each polarisation (P1 and P2).

2.1. Data Reduction and calibration

2.1.1. Interferometric quantities

The data were reduced with the GRAVITY pipeline (Lapeyrere et al. 2014). As the source is moderately resolved, both the closure phase signal and the differential phase are $0° \pm 3°$ and we only used the squared visibilities (V^2) for the interferometric analysis. The pipeline was also used to produce the photometric spectra. The squared visibilities were calibrated with HD160852 ($\theta_{\rm LD} = 0.148 \pm 0.004$ mas, $V^2 = 0.997 \pm 0.001$, Chelli et al. 2016) in 2017 and HD161703 ($\theta_{\rm LD} = 0.38 \pm 0.01$

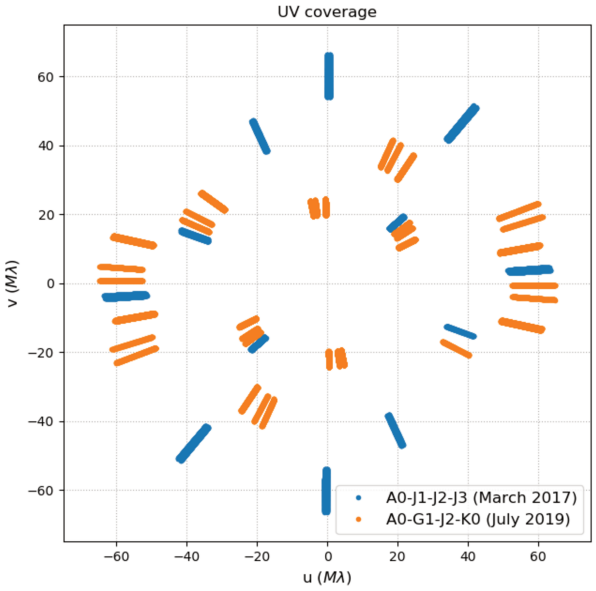

Fig. 1. (u,v) plane coverage for the two epochs 2017 and 2019. Each (u,v) point is elongated to account for the spectral range.

mas, $V^2 = 0.983 \pm 0.001$, Chelli et al. 2016) in 2019, where $\theta_{\rm LD}$ is the limb-darkened diameter, which in the original work is obtained by polynomial fitting. Both calibrators are observed at the same air mass as GCIRS 7.

2.1.2. Photometric spectra calibration

We have used several templates from Pickles (1998) to perform the absolute flux calibration of the spectra. In order to get a robust estimate of the error bars related to the template choice, we have chosen the templates A0V, A3V, F2V, F5V for 2017, and K0III, K2III, K3III for 2019. The following formula yields the calibrated flux density of GCIRS 7, measured in Wcm$^{-2}\mu$m^{-1}:

$$F_\lambda^{\rm IRS7} = \frac{F(\lambda)^{\rm IRS7}_{\rm data}}{F(\lambda)^{\rm cal}_{\rm data}} \times F(\lambda)^{\rm template}, \quad (1)$$

where $F(\lambda)^{\rm template}$ is the corresponding spectral template from Pickles (1998) for each epoch (4 templates in 2017, 3 templates in 2019). For each template a spectra $F_\lambda^{\rm IRS7}$ is obtained. We take the average of these individual estimates as our final calibrated spectrum for each epoch, and their standard deviation as the uncertainty on this calibration.

While the 2017 data have been recorded in combined polarisation mode resulting in a single spectrum, the 2019 data were recorded using the Wollaston prism, resulting in two independent spectra which are calibrated individually and then co-added into a single spectrum.

3. Modelling

3.1. Local interstellar extinction and spectrum normalisation

It is possible to measure the effect of the interstellar extinction in the direction of the source using the slope of the continuum emission and considering an extinction law. We have considered the law derived in Fritz et al. (2011):

$$A_\lambda = A_0 \times \left(\frac{\lambda}{\lambda_0}\right)^\alpha \quad (2)$$

with $\alpha = -2.11 \pm 0.06, \lambda_0 = 2.166$ μm (Brackett γ). An average value of $A_0 = 2.62 \pm 0.11$ is given in Fritz et al. (2011) for the Galactic Centre. However, it is known that extinction varies significantly throughout the central parsec, from a line-of-sight to the next and along a given line-of-sight (e.g. Ciurlo et al. 2019). We have therefore decided to derive the extinction from the source itself. Starting from a grey atmosphere approximation ($F_\lambda \propto B(\lambda, T)10^{-0.4A_\lambda}$), an expression for A_0 can be obtained by introducing A_λ from Eq. 2 and taking the derivative of the logarithm of F_λ with respect to λ:

$$A_0 = \frac{-2.5}{\alpha \log(10)} \left(\frac{\lambda}{\lambda_0}\right)^{-\alpha} \left[\lambda \frac{\partial F_\lambda}{\partial \lambda} - \frac{hc}{\lambda kT}\left(1 + \frac{1}{e^{(hc/\lambda kT)} - 1}\right) - 5\right] \quad (3)$$

where h, k, c are the Planck and Boltzmann constants and the speed of light respectively. We have used the effective temperature determined by Paumard et al. (2014) ($T = 3600 \pm 195$ K). The derivative is obtained for each spectrum in the sample (8 in 2017, 56 in 2019) through a linear regression in the continuum sub-band ($\lambda = 2.1 - 2.2$ μm), yielding as many estimates of A_0. The average of those individual estimates gives our final estimate for each epoch:

- 2017: $A_0 = 3.26 \pm 0.35$
- 2019: $A_0 = 3.28 \pm 0.26$

To estimate the uncertainties, in addition to the flux error bars we have considered the deviation of the SED of a typical RSG from a blackbody. For this purpose we have used the dereddened and absolute-calibrated spectrum of Betelgeuse from Rayner et al. (2009) to estimate the deviation. This star shares the spectral class with GCIRS 7 and was found to have a same effective temperature, which has not substantially changed in the recent decades (several measurements are presented in Sec. 4.3). An estimate of the slope for the sub-band used in our work to estimate the extinction ($\lambda = 2.1 - 2.2$ μm) gives a deviation of 11% while comparing the slope of the blackbody with a linear fit of the spectrum of Betelgeuse in the continuum sub-band. This deviation in the slope is propagated by using Eq. 3 giving an errorbar of 0.20. This value has been considered in addition to the error propagation of the fluxes to estimate the uncertainty.

The two values are compatible and can be averaged down to a single estimate of the extinction: $\bar{A}_0 = 3.27 \pm 0.20$. We can use this value to deredden $F_\lambda^{\rm IRS7}$ (Eq. 1) and integrate over the K_S band to determine the broad-band extinction specifically for the photosphere of GCIRS 7:

$$A_{K_S} = -2.5 \log \frac{\int_{K_S} F_\lambda^{\rm IRS7} d\lambda}{\int_{K_S} F_\lambda^{\rm IRS7} \times 10^{+0.4A_\lambda} d\lambda} = 3.18 \pm 0.20. \quad (4)$$

Then each spectrum is normalised separately using the average A_0 for each epoch. Finally, a weighted average of the normalised spectra is computed for each epoch, the weights being the inverse of the square of the error bars. The weighted average of the normalised spectra is noted $F_\lambda^{\rm N}$ throughout this work.

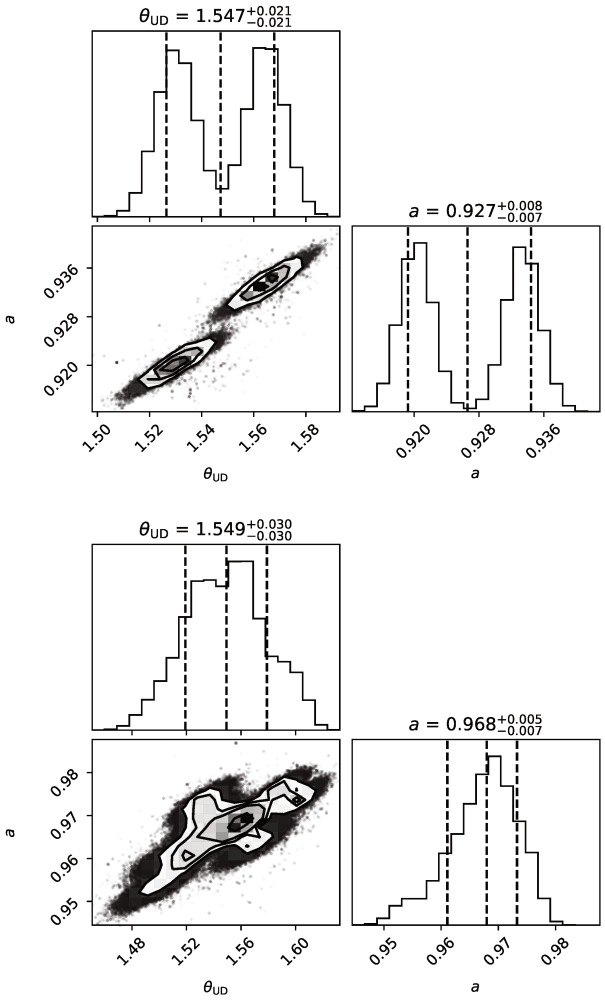

Fig. 2. Combined corner plot of the uniform-disk plus background MCMC samples on each data file for 2017 (top) and 2019 (bottom).

3.2. Squared visibilities

The target is only moderately resolved by GRAVITY ($V^2 > 0.4$) and therefore the data are not sensitive to limb darkening. We have modelled the visibility in the continuum (2.1–2.2 μm) with a uniform disk plus a spatially over-resolved background as in Perrin et al. (2007):

$$V^2_{\rm aD}(q, a, \theta^*_{\rm UD}) = a^2 V^2_{\rm UD}(q, \theta^*_{\rm UD}) \quad (5)$$

where $V_{\rm aD}(q, a, \theta^*_{\rm UD})$ is the visibility of this uniform-disk plus the spatially over-resolved background, $V_{\rm UD}(q, \theta^*_{\rm UD})$ is the usual uniform-disk visibility, $q = \sqrt{u^2 + v^2}$ is the spatial frequency (u and v are the spatial frequency components), $\theta^*_{\rm UD}$ is the angular diameter of the disk and a is the fraction of stellar flux over the total injected flux.

To explore the wavelength dependence of the parameter a, we have performed a uniform-disk plus background fit for each spectral channel in the continuum region (2.1-2.2 μm). The results for a do not reveal any significant wavelength dependency, and therefore we have assumed the stellar flux and background to have the same spectrum.

We have estimated $\theta^*_{\rm UD}$ and a using a Monte-Carlo Markov chain (MCMC) algorithm based on the Python package `emcee` (Foreman-Mackey et al. 2013). We have let 100 walkers evolve for 600 steps for each file and each polarisation state (for 2019) individually, using all wavelengths from 2.1 to 2.2 μm. The individual Monte-Carlo simulations (2 in 2017, 14 in 2019) yield distributions that are too far apart compared to their internal scatter (Fig. 2). This is a because uncalibrated instrumental errors dominate over statistical errors. For this reason, we have combined all the samples from these simulations in a single histogram per epoch. The 2017 combined histogram is clearly bimodal because there are only two individual frames, while the 2019 data set is rich enough that the 14 individual Gaussian-like histograms merge into a broad Gaussian-like peak. The two polarisation states in the 2019 data give similar distributions and are combined together. As our best estimate for the two parameters, we use the median of the 1D combined histograms (which is equivalent to taking the average of the median values of the individual 1D histograms). The 2019 data set is well suited to determine the uncertainties because it contains enough individual measurements for their scatter to make sense. Using the 16% and 84% percentiles of the 1D histogram yield uncertainties that combine statistical errors, instrumental stability, and degeneracy between the two parameters. The same approach on the 2017 data leads to a value for the uncertainty on $\theta^*_{\rm UD}$ that we deem too small, being dominated by the scatter of two individual values. We therefore adopt the 2019 error bar instead also for 2017. Our final estimates for the two years read:

- 2017: $a = 0.927 \pm 0.008$, $\theta^*_{\rm UD} = 1.547 \pm 0.030$ mas
- 2019: $a = 0.968 \pm 0.006$, $\theta^*_{\rm UD} = 1.549 \pm 0.030$ mas

It is worth noting that this uncertainty on the uniform disk diameter (30 μas) is itself quite an achievement, of the same order as the astrometric measurements performed by GRAVITY (e.g. Gravity Collaboration et al. 2020). These average best-fit models are shown in Fig. 3., compared with the best single UD fit without considering the background.

The fraction of coherent flux a means that the fibres of GRAVITY were fed with 7% incoherent light from the circumstellar background in 2017 and 3% in 2019. This decrease may

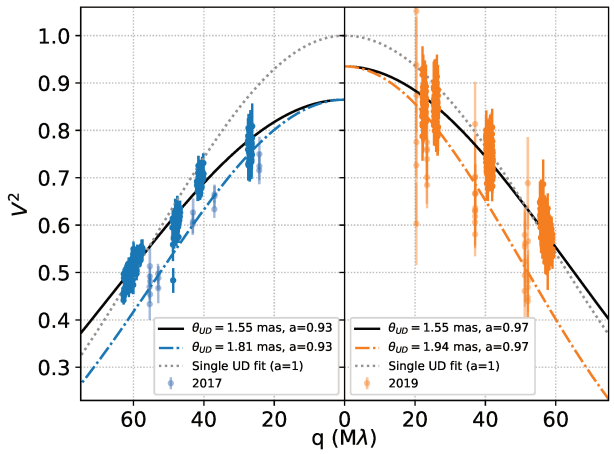

Fig. 3. V^2 measurements of 2017 and 2019. Two uniform-disk plus background models are shown: the average best-fit in the continuum (2.1–2.2 μm, black line) and the average uniform-disk diameter in the fourth CO band head (2.381–2.387 μm, coloured lines), both of them with the measured background level in parenthesis. Only the data in those two wavelength ranges are shown. The dotted line reveals the pure UD fit of the visibilities in the continuum assuming no incoherent background.

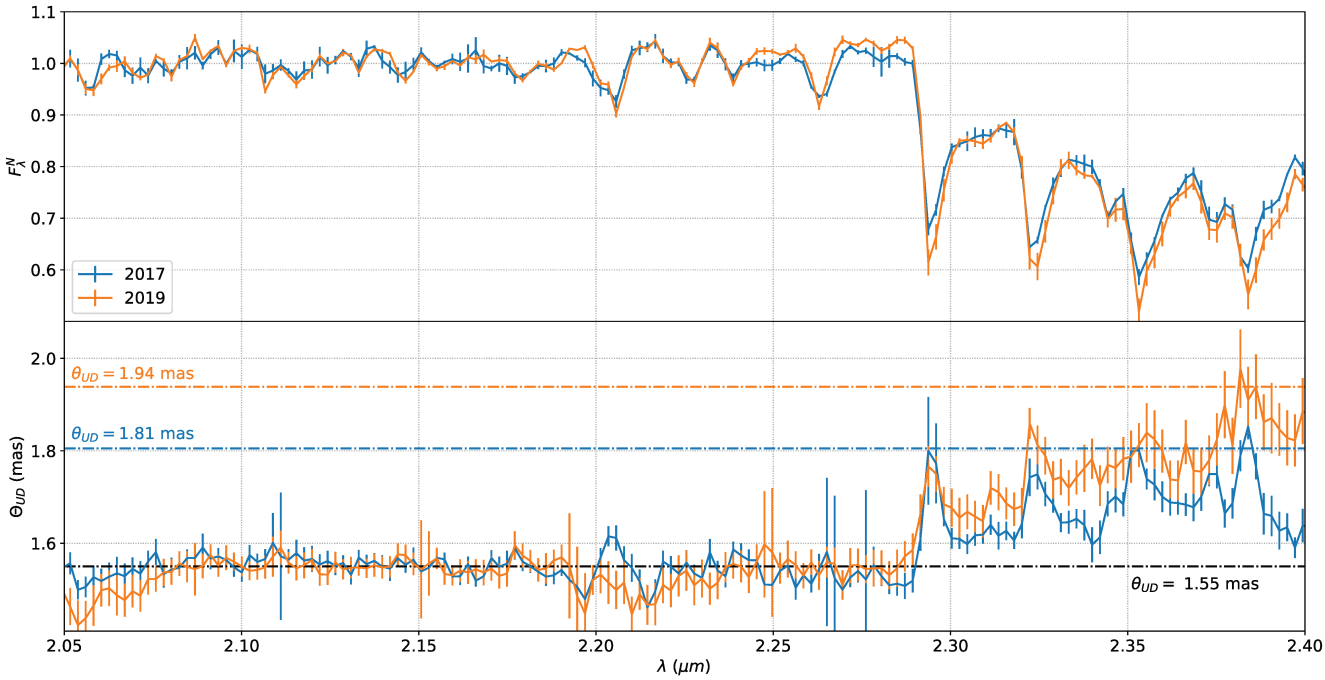

Fig. 4. Normalised spectra and Uniform Disk diameters for the two epochs. In 2019, the Uniform Disk profile is the average of the profiles of the two polarisation states.

be due to the better turbulence correction offered by the AO system NAOMI compared to tip-tilt stabilisation with STRAP, since the residuals of this correction directly translate into a widening of the fibre field-of-view (Perrin & Woillez 2019). We have removed this background from the visibilities by dividing them by a for each epoch. The use of a single value instead of a value per spectral channel is justified as the spectral resolution is moderate and the flux ratio between the emission of the circumstellar dust and stellar flux varies only slowly across the K band.

After correcting for this background, a simple uniform-disk fit is performed for each spectral channel in the interval (2.05–2.4 μm). The results are displayed in Fig. 4, showing both the normalised spectra derived in Sect. 3.1 and the chromatic uniform-disk diameter profile as a function of wavelength. The diameter is close to constant in the continuum between 2.1 and 2.2 μm, again showing that the continuum is very well fitted by a uniform-disk plus the spatially over-resolved background. The unbiased weighted standard deviation of $\theta_{\rm UD}$ through the continuum (again 2.1–2.2 μm) is 0.020 mas in 2017 and 0.018 in 2019. At this level, the main source of uncertainty on $\theta^*_{\rm UD}$ is the presence of many absorption lines in the spectrum, which form at various altitudes in the atmosphere of the star. Therefore the limitation is fundamental: it is the definition of the photosphere itself.

The average value of $\theta_{\rm UD}$ above 2.29 μm is 1.66 mas in 2017 and 1.77 mas in 2019, i.e. a 12-σ departure from the continuum level. This sharp increase follows the absorption features that can be seen in the spectrum, with local maxima matching the deep CO band heads. Such variations correlated with the CO optical depth point towards a molecular shell above the photosphere as previously evidenced e.g. by Perrin et al. (2004), Perrin et al. (2005) or Hadjara et al. (2019) for other evolved stars.

In addition to the maxima in the CO bands, the uniform disk diameter increases monotonically after 2.29 μm in 2019. Such a feature has also been observed in Betelgeuse (Montargès et al. 2014) and other RSGs (Arroyo-Torres et al. 2013, 2015), and it can be due to the presence of H2O (Montargès et al. 2014). However, this monotonic increase in the angular size is not clear in 2017, which hints at a variation in the stellar atmosphere between the two epochs.

A lower limit on the diameter of the shell is given by the maximum uniform-disk size in the molecular band: $\theta_{\rm S} \geq \theta^{\rm CO}_{\rm UD}$, which we estimated by taking the average of the three θ_{UD} values around the fourth CO band head on each epoch:

- 2017: $\theta^{\rm CO}_{\rm UD} = 1.805 \pm 0.017$ mas $= (1.166 \pm 0.027)\, \theta^*_{\rm UD}$
- 2019: $\theta^{\rm CO}_{\rm UD} = 1.939 \pm 0.019$ mas $= (1.251 \pm 0.026)\, \theta^*_{\rm UD}$

again neglecting correlated sources of error for this relative measurement.

This result is an evidence for the need for a more complex model than a grey atmosphere to describe the physics of the object. In the next section, we model the molecular features with a simple shell model, which will also allow us to give a proper interpretation to the time variability which we see.

3.2.1. The single-layer shell model

A geometrically thin molecular layer model has proven successful to reproduce the visibilities of other RSG stars (Perrin et al. 2004, 2005; Montargès et al. 2014) and is used for this study. It has allowed to interpret interferometric observations of RSG stars surrounded by a so-called MOLsphere according to the term coined by Tsuji (2000). In this model, the shell is modelled with a temperature and an optical thickness but has zero geometrical thickness.

Both the stellar photosphere and the shell are modelled with black body functions. The specific intensity at angular distance

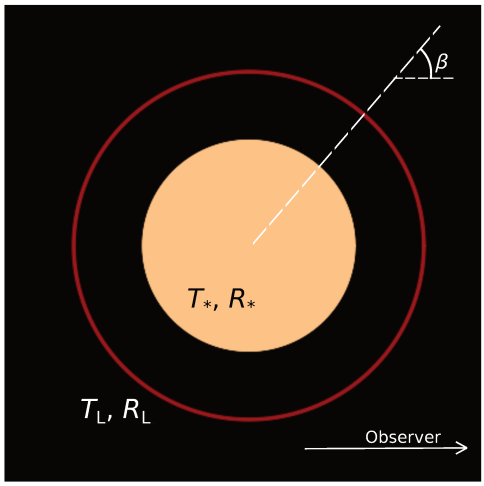

Fig. 5. Sketch of the single layer shell model.

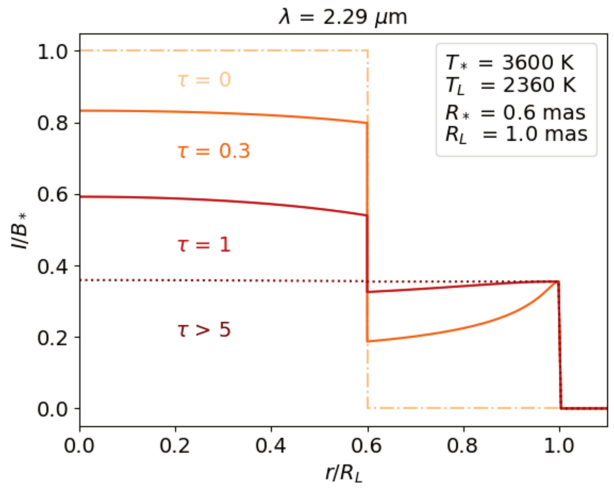

Fig. 6. Spatial intensity profile of the single layer shell model (Eq. 6) normalised by the photosphere black body function for various values of the optical depth of the shell τ. The abscissa is relative to the size of the layer. Here, the maximum attenuation reaches a factor 1.55 for a temperature of the layer $T_{\rm L} = 2360$ K.

r from the centre of the star as seen from the observer at wavelength λ is given by:

$$I^r_\lambda(T_*, T_{\rm L}, R_*, R_{\rm L}, \tau_\lambda) = \begin{cases} B_\lambda(T_*)e^{(-\tau_\lambda/\cos\beta)} & \\ +B_\lambda(T_{\rm L})[1 - e^{(-\tau_\lambda/\cos\beta)}] & \text{if } r \le R_* \\ B_\lambda(T_{\rm L})[1 - e^{(-2\tau_\lambda/\cos\beta)}] & \text{if } R_* < r \le R_{\rm L} \\ 0 & \text{otherwise,} \end{cases} \quad (6)$$

where T_* and $T_{\rm L}$ are the temperatures of the photosphere and of the molecular layer, R_* and $R_{\rm L}$ are their angular radii (hence $R_* = \theta^*_{\rm UD}/2$), τ_λ is the optical depth of the molecular layer at wavelength λ, $B_\lambda(T)$ is the Planck function at wavelength λ and temperature T, and β is the angle between the radius vector and the line-of-sight so that $\cos\beta = \sqrt{1-(r/R_{\rm L})^2}$. A sketch of the model is displayed in Fig. 5.

The centre-to-limb variation is illustrated in Fig. 6 for various optical depths. The sharp variation near $r/R_{\rm L} = 0.6$ corresponds to the edge of the photosphere, which is assumed to be a uniform disk. The increase of the projected layer optical depth with increasing r (due to the $\cos\beta$ factor) causes a slight limb darkening on the disk over the photosphere, and a limb brightening between the limb of the photosphere and the limb of the shell. The model fails to reproduce infinitely strong flux attenuation by the shell unless its temperature reaches 0 K. For example, the maximum attenuation reaches a factor 1.55 for a temperature of $T_{\rm L} = 2360$ K and is typically reached for optical depths of 5 or larger. The fact that at high optical depth the shell itself behaves as a photosphere is one of the shortcomings of this simple model for the interpretation of the surface brightness in the core of molecular lines.

We adopt the effective temperature of Paumard et al. (2014) for the photosphere: $T_* = 3600$ K. We also fix the photospheric diameter to the continuum uniform-disk diameter from Sect. 3.2: $R_* = \theta^*_{\rm UD}/2 = 0.775$ mas. In this section, we focus on the molecular features above 2.28 microns (Ohnaka & Morales Marín 2018), which includes CO bands but also water vapor to obtain measurements for $T_{\rm L}$ and $R_{\rm L}$.

A physical modelling of the wavelength-dependent optical depth of the thin layer τ_λ, although possible, would significantly add to the complexity of the model without begin necessarily accurate because of the very simplistic geometrical model. However, for a set of parameters $(T_*, T_{\rm L}, R_*, R_{\rm L})$ and for each wavelength, the relation between F^N_λ and τ_λ is bijective, except where the model saturates as explained above. For any quadruplet $(T_*, T_{\rm L}, R_*, R_{\rm L})$ and for each wavelength, we determine τ_λ univocally by finding the root of the following quantity:

$$\left| F^{\rm N}_\lambda - \frac{\int_{r=0}^{R_{\rm L}} I^r_\lambda(T_*, T_{\rm L}, R_*, R_{\rm L}, \tau_\lambda) \times 2\pi r dr}{\int_{r=0}^{R_{\rm L}} I^r_\lambda(T_*, T_{\rm L}, R_*, R_{\rm L}, \tau_\lambda = 0) \times 2\pi r dr} \right| \quad (7)$$

which is implemented by a minimization since Eq. 7 is always positive. When the model does not saturate, this minimum reaches zero. When it does saturate (this happens in a few spectral channels of the CO band heads), the exact (large) value of τ_λ does not matter as the shell is then optically thick. A visibility model of the star and the shell $V^2_{\rm shell}$ can then be built and compared to the corrected squared visibility data $V^2_{{\rm c},i} = V^2_i/a^2$, in which the effect of the incoherent background has been removed. This yields the following χ^2:

$$\chi^2 = \sum_{i=1}^{M} \left(\frac{V^2_{{\rm c},i} - V^2_{\rm shell}(q_i, T_* = T_{\rm eff}, T_{\rm L}, R_* = \theta^*_{\rm UD}/2, R_{\rm L}, \tau_\lambda)}{\sigma_i} \right)^2 \quad (8)$$

where M is the total number of data points considered for each epoch: $M = 6 \times D \times n_\lambda$ where D is the number of observations, 6 the number of baselines and n_λ the number of spectral channels in the band of interest. $T_{\rm L}$ and $R_{\rm L}$ are the only two remaining free parameters of the model. The fitting process involves then two steps:

- For each pair (T_L, R_L), τ_λ is measured from the spectrum for each wavelength by minimizing Eq. 7.
- By using the resulting set (T_L, R_L, τ_λ), the visibility squared of the model is computed and compared with the data via Eq. 8.

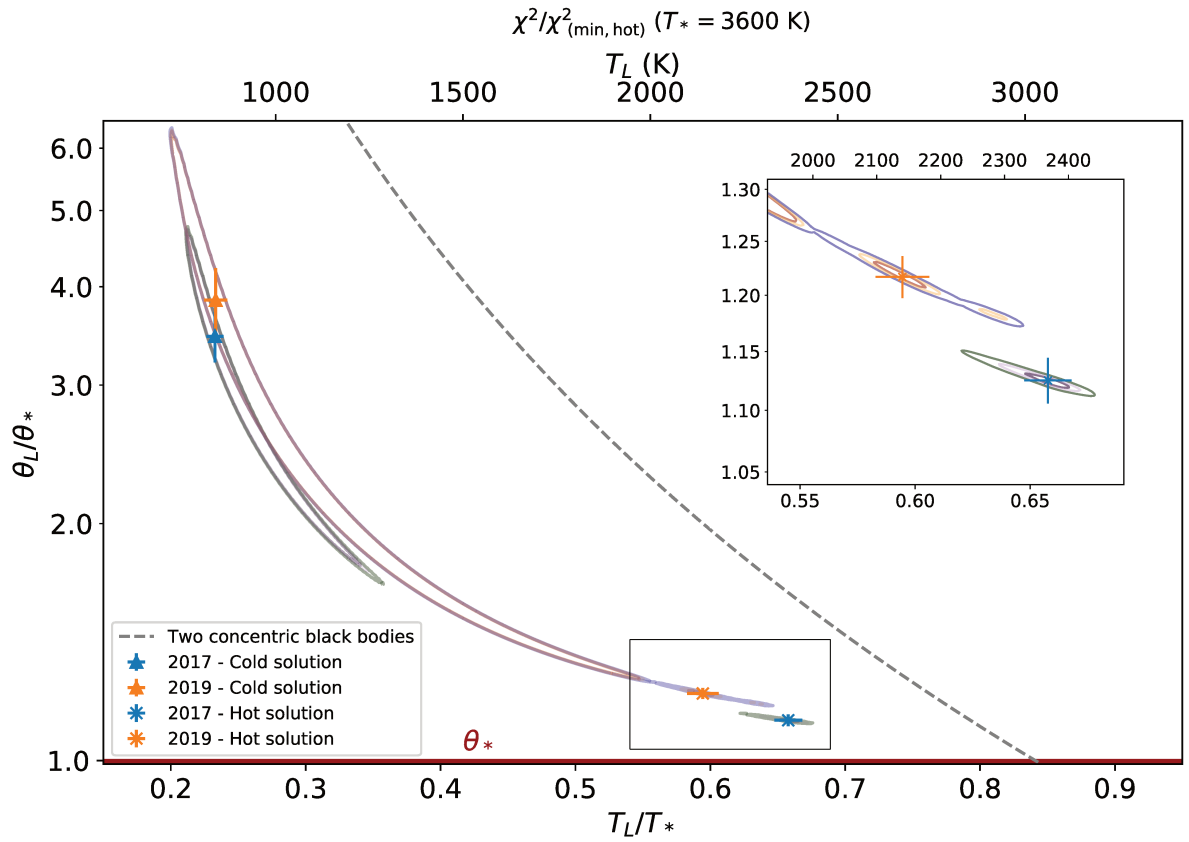

Fig. 7. *Solid lines:* contour plot of the χ^2 maps (Eq. 8). The contours shown correspond to a decrease of likelihood of 1, 3 and 5 σ relative to the hot solution minimum of each epoch considering $T_\mathrm{L}, \theta_\mathrm{L}$ the two parameters of interest (Press et al. 1992). *Grey dashed line:* temperature profile of a spherically thin shell enclosing a perfect black body (Eq. 9). *Triangles with error bars:* the cold solutions for both epochs corresponding to the absolute minima. *Crosses with error bars:* the hot solutions for both epochs (corresponding to the local minima).

Figure 7 displays a contour plot of this χ^2 for each epoch in the $(T_\mathrm{L}/T_*, \theta_\mathrm{L}/\theta_* = R_\mathrm{L}/R_*)$ plane (where $\theta_i = 2R_i$). The map does not show a single clearly defined minimum but a trough thereby showing a degeneracy between the radius and the temperature of the single layer of the shell model. For both 2017 and 2019, the trough has one global minimum at $(T_\mathrm{L}, \theta_\mathrm{L}) = (838 \pm 23\,\mathrm{K}, 5.36 \pm 0.39\,\mathrm{mas})$ with $\chi^2_r = 3.78$ in 2017 and $(T_\mathrm{L}, \theta_\mathrm{L}) = (839 \pm 31\,\mathrm{K}, 5.96 \pm 0.58\,\mathrm{mas})$ with $\chi^2_r = 1.98$ in 2019 which we call the *cold* solution and one local minimum at $(T_\mathrm{L}, \theta_\mathrm{L}) = (2368 \pm 37\,\mathrm{K}, 1.74 \pm 0.03\,\mathrm{mas})$ with $\chi^2_r = 3.93$ in 2017 and $(T_\mathrm{L}, \theta_\mathrm{L}) = (2140 \pm 42\,\mathrm{K}, 1.89 \pm 0.03\,\mathrm{mas})$ with $\chi^2_r = 2.18$ in 2019 which we call the *hot* solution. In 2017, the two solutions are incompatible at 5σ.

Despite the fact that the cold solution corresponds to the absolute minimum, it cannot be the dominating solution of the model as its temperature is below the condensation temperature of silicate dust. In the context of mass loss, CO could be detected beyond the dust condensation radius as the CO gas can be dragged by the dust set in motion by the radiation pressure of the star. However, CO is naturally a major component of the molecular shell and therefore there should be an inner region where CO must be formed before being dragged by the dust. This inner shell must present a higher column density and a stronger spectroscopic signal in the K band than the cold solution. These requirements are satisfied by the hot solution.

In addition, we have plotted in Fig. 7 the position in radius and temperature for a fully absorbing and geometrically thin shell in thermal equilibrium above the photosphere:

$$\frac{\theta_\mathrm{L}}{\theta_*} = \frac{1}{\sqrt{2}} \frac{T_*}{T_\mathrm{L}} \tag{9}$$

This model is more consistent with the hot solution than with the cold solution. For all these reasons, we believe the hot solution makes more physical sense than the cold solution although both are compatible with our data. However, the reduced χ^2 of the hot solution is not perfect which we interpret as the signature that our model is still too simple to perfectly reproduce the data. In an attempt to include these modelling errors into the statistical uncertainties, we have rescaled the errors by the square root of the χ^2 of their respective hot solution.

The optical depths obtained for the hot solution of each epoch are presented Fig. 8. The error bars have been obtained through Monte-Carlo error propagation in the 1σ contour of the hot solution. Only the values with $\tau \pm \Delta\tau < 5$ are presented as the model reaches saturation near the peaks. A summary of the parameters of the model is presented in Table 2 for the hot solution.

A visibility contrast function is introduced to better show the effect of the molecular features on the visibilities. It is the av-

Table 2. Parameters of the single-layer molecular shell model for the hot solution.

Parameter	2017	2019
A_0	3.27 (fixed)	3.27 (fixed)
θ_* (mas)	1.55 (fixed)	1.55 (fixed)
T_* (K)	3600 (fixed)	3600 (fixed)
θ_L (mas)	1.74 ± 0.03	1.89 ± 0.03
T_L (K)	2368 ± 37	2140 ± 42

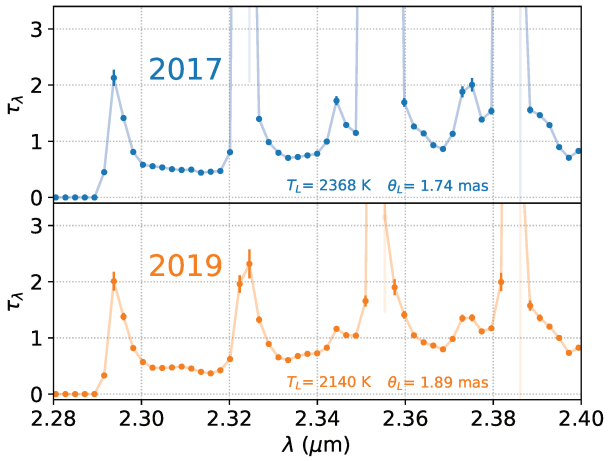

Fig. 8. Optical depths computed using Eq. 7 with the parameters of the hot solution. The peaks correspond to the CO band heads where the single-layer model saturates as described in Sect. 3.2.1.

erage of the band to continuum visibility ratio over a subset of baselines:

$$C_{V2}(\lambda) = \left\langle \frac{V_c^2(q_i, T_* = T_{\rm eff}, T_{\rm L}, R_* = \theta^*_{\rm UD}/2, R_{\rm L}, \tau_\lambda)}{V_c^2(q_i, T_* = T_{\rm eff}, T_{\rm L}, R_* = \theta^*_{\rm UD}/2, R_{\rm L}, \tau_\lambda = 0)} \right\rangle_i \quad (10)$$

This contrast function, where spectral and spatial information are combined in a synthetic way, is an interferometric counterpart to the normalised spectrum.

Figure 9 shows this function for the data of the two epochs as well as for synthetic data corresponding to the hot solution. For this plot we have chosen the three partially overlapping longest baselines for each epoch. The visibility contrasts are plotted between 2.28 and 2.4 μm to show the upper part of the continuum and the molecular features. The single-layer shell model matches the data quite well except at the bottom of the band heads where flux attenuation saturates with this simple model as explained above.

4. Discussion

4.1. Interstellar extinction

We compare our measurement of the extinction with previous ones. In Sec. 3.1 we measured the extinction from the changes incurred to the slope of the spectrum in the continuum. The extinction found in Brackett γ was then converted to $A_{\rm K_S} = 3.18 \pm 0.20$ through integration across the $\rm K_S$ band, quite stable between our two epochs. Others also estimated the extinction in the direction of GCIRS 7. Blum et al. (1996a) obtained

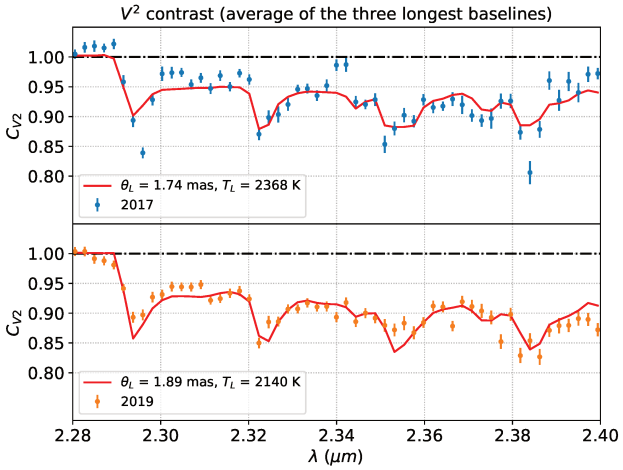

Fig. 9. Visibility contrast in the molecular features. The spectral visibility of the three longest baselines have been averaged for each epoch.

$A_{\rm K} = 3.72 \pm 0.13$ via NIR photometry and an assumed intrinsic colour, and later Blum et al. (2003) measured $A_{\rm K} = 3.48 \pm 0.09$. Both values are more than 1σ higher than our measurement. This discrepancy with archival data could be due to the better spatial filtering offered by GRAVITY thanks to the mono-mode fibres and interferometric spatial resolution, which allows to reject most of the infrared excess from the surrounding material, or to a change in the circumstellar contribution, subject to any variation of the fundamental parameters of the star as it is pulsating (Paumard et al. 2014). On the other hand, the interstellar medium (ISM) in the central parsec is known to be clumpy and heterogeneous, responsible for variations of more than one magnitude in the K band from one line-of-sight to the next and along a given line-of-sight (Ciurlo et al. 2016, and references therein). The motion of dusty clumps in the ISM over decade-long time scales could easily explain variations of the interstellar extinction by a fraction of a K-band magnitude. A value of 3.18 is above average when compared to the extinction map of Schödel et al. (2010), but rather typical in view of the extinction map of Ciurlo et al. (2016) who, by using the ISM rather than stars, probe arguably deeper along the line-of-sight. Therefore a large part of the excess extinction compared to the field average towards GCIRS 7 is attributable to ISM local to the central parsec, possibly in part of circumstellar origin.

4.2. Photospheric size

We measure a photospheric diameter of $\theta^*_{\rm UD} = 1.55 \pm 0.03$ mas, yielding $R_* = 1368 \pm 27\,R_\odot$ at 8.246 kpc (Gravity Collaboration et al. 2020). This value is in good agreement with the values of $\theta^*_{\rm UD} = 1.5 - 2$ mas of Paumard et al. (2014) on K-band data obtained with AMBER in 2008, but much larger than their H-band measurement on PIONIER 2013 data: $\theta^*_{\rm UD} = 1.076 \pm 0.093$ mas.

A possible explanation for a smaller photosphere at H-band compared to K-band is the wavelength-dependence of the opacity of negative hydrogen H^-, which determines the opacity of RSGs (Gray 2005). However, this process alone can hardly account for a factor 1.44 in size between the two bands. Therefore, these measurements provide another clue that GCIRS 7 has been pulsating over the last 10 years. Such variations in stellar diameter are also corroborated by photometric estimates using SIN-

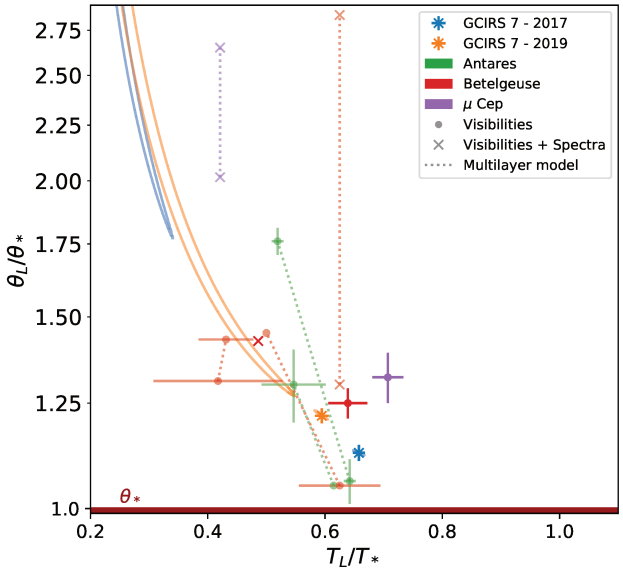

Fig. 10. The molecular shell physical parameters of a GCIRS 7 and a sample of stars from the literature derived by single-shell and multiple-shell models by using interferometric and spectroscopic measurements (Table 3). The contours shown correspond to 1 sigma from their respective hot solutions of GCIRS 7.

Table 3. MOLsphere models implemented in literature for the closest RSGs.

Single shell models			
T_* (K)	T_L (K)	θ_L/θ_*	Reference
3790	2680 ± 100	1.32 ± 0.07	Perrin+ 05
3600	1750	1.42	Verhoelst+ 06
3600	2300 ± 120	1.25 ± 0.04	Montargès+ 14
3600	2362 ± 91	1.16 ± 0.03	This work (2017)
3600	2182 ± 80	1.26 ± 0.03	This work (2019)
Multiple shell models (inner and outer layer)			
3800	1600	2.01 2.65	Tsuji 06 (μCep)
3600	2250	1.3 2.84	Tsuji 06 (αOri)
3641	1520 ± 400 1570 ± 150	1.31 1.43	Perrin+ 07
3600	2250 ± 250 1800	1.05 1.45	Ohnaka+ 09
3660 ± 120	2250 2000 ± 200	1.05 1.3 ± 0.1	Ohnaka+ 13
3660 ± 120	2350 ± 50 1900 ± 50	1.06 ± 0.05 1.76 ± 0.05	Hadjara+ 19

FONI (Paumard et al. 2014) and ALMA (Tsuboi et al. 2020). The $\theta^*_{\rm UD}$ diameters from Paumard et al. (2014), Tsuboi et al. (2020) and this work are displayed in Fig. 11, together with a model assuming the pulsation periods (470 and 2620 days) obtained by Paumard et al. (2014). The phases and amplitudes of the two modes of pulsations and the average size were semi-manually adjusted, returning a χ^2_r well below 1. However, given the little data available, too many solutions are possible to make it useful to quote the best-fit parameters. This shows that the data are consistent with pulsations but we are not able to provide further constraints at this stage.

We measure the same photospheric size in 2017 and 2019, with a 3σ upper limit on the difference of 0.13 mas ($\simeq 8\%$). This is plausibly explained by the observational gap. With the interplay of the two periods (470 and 2620 days) revealed in Paumard et al. (2014), the size of the photosphere could well have varied during the 840 days that separate the observations performed in 2017 and in 2019 and have come back to a very similar value (Fig. 11). However, it is also possible that the size of the star did not vary between 2017 and 2019 or varied less than expected from the 2013–2017 era. The pulsations of red supergiants are irregular and intertwined with convective mechanisms. Their periods, phases and amplitudes can vary over short time-scales.

4.3. The MOLsphere of GCIRS 7 in context

The results of this work are compared with the parameters of the MOLspheres of Antares, Betelgeuse and μCep as derived in various works following similar approaches as ours.

A single thin shell, similar at the one used in this work, has been modelled in Perrin et al. (2005) for μCep via interferometry in the K band. The work of Verhoelst et al. (2006) combined spectroscopy in NIR, MIR and FIR with interferometry in the K and L bands to characterize the extended atmosphere of Betelgeuse revealing the presence of alumina, while Ryde et al. (2006) presented new MIR spectroscopic data which could not rule out a scenario based only on a cool photosphere ($T = 3250$ K). For the same star, the most recent work involving a thin shell model was presented by Montargès et al. (2014), who used H- and K-band interferometry to estimate the temperature, diameter and density of the thin shell.

Several multi layer models have been also proposed for RSGs. Tsuji (2006) used NIR and MIR spectroscopy, together with K-band interferometry, to constrain a two-layer model (inner and outer) for μCep and Betelgeuse. A year later, Perrin et al. (2007) used N-band interferometry to model the close stellar environment of Betelgeuse with the use of another two-layer model estimating the density of the H_2O, SiO and Al_2O_3 molecules in the MOLsphere. Ohnaka et al. (2009) also resolved spatially the structure of the atmosphere of Betelgeuse and characterized a MOLsphere by using two layers and K-band interferometry. This extended component was also observed by Ohnaka et al. (2011) (K-band interferometry) who found a significant variation of the visibilities and phases in the CO overtone lines between two different epochs, but no significant variation in the continuum. For the star Antares, Ohnaka et al. (2013) used a similar approach (K-band interferometry) characterizing a double layer model at two different epochs, but without any significant variations in temperature or size. A model consisting in several concentric layers was used in Hadjara et al. (2019) to characterize a sample of M stars via K-band interferometry. In the case of Antares, they modelled 7 layers between 1.06 and 1.76 stellar radii.

These measurements are listed in Table 3 and displayed in Fig. 10, as well as the results of this work. The properties of GCIRS 7 are compatible in 2019 within one sigma with all the single shell models except Verhoelst et al. (2006), and are compatible also with the outer shell of Antares from Ohnaka et al. (2013). On the other hand, 2017 reveals a smaller shell, close to the inner layer of Antares from Hadjara et al. (2019).

In addition, considering the multiple shell models, both the inner and the outer shell of Perrin et al. (2007) and the outer shell of Ohnaka et al. (2013) are also compatible within 1σ to

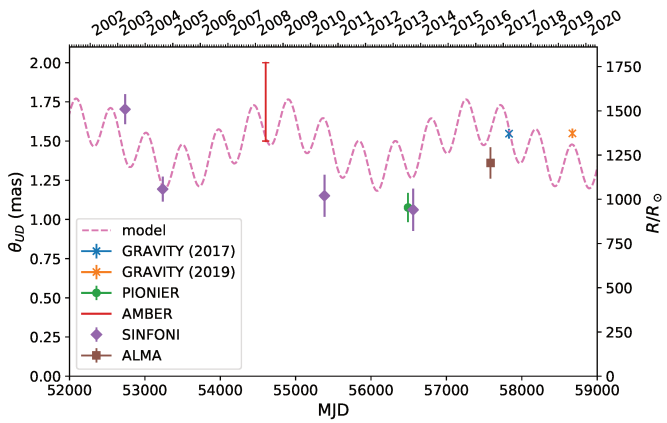

Fig. 11. Photospheric uniform-disk and limb-darkened (in the case of SINFONI) diameter estimates from Paumard et al. (2014), Tsuboi et al. (2020) and this work. Only the AMBER (K-band), PIONIER (H-band) and GRAVITY (K-band) points are interferometric measurements. The SINFONI (H/K-band) and ALMA (340 GHz) points are spectro-photometric estimates. We display a sample model using the two periods in Paumard et al. (2014).

the through pointing to the cold solution in 2019. This is an indication of the shortcomings of the single shell model to interpret 2019 data for GCIRS 7.

4.4. Size and expansion of the molecular shell

The ratio of the shell diameter to the photospheric diameter (1.16–1.26) is very similar to previous findings. Perrin et al. (2005) found a ratio of 1.32 for μ Cep, Montargès et al. (2014) found 1.25 for Betelgeuse. This is still compatible with the lower altitude layers of α Sco for which Hadjara et al. (2019) found ratios in the range 1.06 to 1.76, and temperatures between 2360 and 1900 K using a multi-layer model (see the next section for the discussion of the temperature). In addition, Wittkowski et al. (2017b) measured a ratio 1.49 for V766 Cen between the photospheric radius and the radius of a layer of Na I causing a line in emission at 2.205 μm.

The uniform disk diameters for the molecular band presented on Fig. 4 show globally higher values in 2019 than in 2017. This is also evidenced by the significantly lower visibility contrast in 2019 beyond 2.33 μm (Fig. 9). This is confirmed by the analysis with the single-layer model where the hot solutions found in 2017 and 2019 in Fig. 7 are different by 4σ. Our results are compatible with a layer expansion of 8% leading to a layer temperature decrease from 2017 to 2019.

However, the single shell model constitutes a simplified approach for a MOLsphere. Indeed, although a strong contribution of the shell due to a larger size or a lower temperature is found in 2019, the apparent difference in the shell between the two epochs may be a consequence of the degeneracies of the parameters. A more complex model would be needed to solve the degeneracies, and therefore to be able to conclude about a possible shell expansion.

4.5. Column density of CO

The optical depth profiles shown in Fig. 8 are consistent in 2017 and 2019 except for the peaks where the model saturates. With these optical depth profiles we have used the method of Goorvitch (1994) to estimate the column density of CO. The method uses the first band head of CO at 2.293 μm and the temperature of the shell T_L measured for each epoch. Using the parameter of the hot solution and assigning the optical depth measured with the model in the 2.293 μm channel to the first band head of the CO overtone yields, for each epoch:

- $N_{\rm CO}^{2017} = (2.68 \pm 0.38) \times 10^{20}$ mol cm^{-2}.
- $N_{\rm CO}^{2019} = (2.15 \pm 0.26) \times 10^{20}$ mol cm^{-2}.

These values are similar to what Tsuji (2006) measured for μCep and Betelgeuse: $N_{\rm CO} \approx 10^{20}$ mol cm^{-2}. Also for Betelgeuse, by using several isotopes Montargès et al. (2014) measured a higher density: $N_{\rm CO} = 3.01^{+2.0}_{-0.5} \times 10^{21}$ mol cm^{-2}. Relative to Antares, our densities are compatible with the value measured by Ohnaka et al. (2013): $N_{\rm CO} \approx 10^{19-20}$ mol cm^{-2} at 1.3 R_*, and in the range of values found by Hadjara et al. (2019) ($10^{21.5} - 10^{19.2}$ mol cm^{-2}).

The optical depths of Fig. 8 reveal values slightly larger for 2017 than for 2019 as long as the wavelength increases, except for the first head band, which is the same at the two epochs. This is the effect of the monotonic increase of the diameter mentioned in the uniform disk approach (Fig. 4). In addition, in 2017 none the head bands except for the first one can be reproduced by the optical depths of the thin shell due to saturation, while the first two band heads are reproduced in 2019. This is an indicator that the density of the MOLsphere of GCIRS 7 might have decreased.

It is possible to test if this decrease can be due to an expansion of the molecular shell by scaling the measured density by the ratio of the surface of the shell at the two epochs. Assuming no sudden mass loss episode, if the shell has expanded since 2017 at the measured diameter (from 1.74 to 1.89 mas), the column density of CO in 2019 would be $N_{\rm CO} = 2.27$, which is 1σ compatible with the measured value. Therefore, our single-shell interpretation allows a possible expansion of the molecular envelope, but the fact that the model is simplified does not allow to fully confirm it without a deeper study involving an extended atmosphere approach.

Indeed, although CO is the main component of the molecular shell, other molecular species such as water have also been observed in the MOLspheres of other RSGs (Verhoelst et al. 2006; Ryde et al. 2006; Perrin et al. 2007; Montargès et al. 2014), and the decrease of the temperature of the molecular shell may also play a role in the density variation. For GCIRS 7, the molecular shell in 2017 could have been warm enough for water to dissociate ($T = 2400$ K), although it may still have existed at $T = 2200$ K in 2019.

The location of GCIRS 7 is particular as it is located at less than 1 pc from a supermassive black hole and plenty of massive young stars (Krabbe et al. 1995) and it is known that the most external layers are being blown away by the effect of their wind (Tsuboi et al. 2020; Yusef-Zadeh & Morris 1991; Serabyn et al. 1991). Whether or not their presence affects the observed molecular shell of GCIRS 7 could be addressed by the use of a more complex model to fully characterise the outer atmosphere of GCIRS 7, such as the one of Hadjara et al. (2019) as a column density is needed for 2017. It would help to understand the nature of the molecular shell observed for GCIRS 7, as well as its temporal evolution.

5. Conclusion

We report on spectro-interferometry of GCIRS 7 in the K band using GRAVITY at ESO/VLTI. With the sensitivity of current interferometers, we proved that wavelength-dependent structures can be observed in evolved stars even if they are not fully resolved.

We find that GCIRS 7 presents the behaviour of a typical RSG. We detect a molecular shell above the photosphere and estimate the sizes and temperatures for the photosphere and the shell as well as the column density for CO based on optical depths constrained with a single-layer model. This is, to date, the RSG star with the smallest apparent size and the farthest for which a molecular shell has been spatially resolved from the star and characterised. We have also obtained an estimate of the local interstellar extinction with the spectral data.

The extinction ($A_{K_S} = 3.18 \pm 0.16$) and size of the photosphere ($\theta^*_{UD} = 1.55 \pm 0.03$) were the same within uncertainties at the two epochs in 2017 and 2019.

However, the photospheric size must have changed from > 1.5 mas in 2008 to 1.1 ± 0.1 mas in 2013 (Paumard et al. 2014) and back to 1.55 ± 0.03 mas in 2017–2019.

The spectro-differential visibility signal demonstrate the presence of CO above the photosphere. In the context of a thin spherical shell model, the temperature (≈ 2200–2400 K) and diameter (10–20% larger than the photosphere) of this shell are in line with what has been found for other similar RSG stars.

The size and temperature of the shell have significantly changed between the two epochs and are compatible with an expansion.

The column density for the molecular shell presents a value in the same line than the column density of the shells for other RSGs measured with similar methods. The model fails to reproduce all the band heads in 2017 except the first, while in 2019 the first two band heads are reproduced. This suggests that the density must have been higher in 2017. An intepretation based on a shell expansion from 2017 to 2019 is compatible with our data.

This work corresponds to a first order description of the outer atmosphere of GCIRS 7. Overall, our results support the interpretation in terms of stellar pulsations proposed by Paumard et al. (2014) and hint at an expansion of a molecular shell. Follow-up observations over a good fraction of the ≈ 2800-day period with contemporaneous H and K photometry, spectroscopic effective temperature and interferometric size measurements, together with a more detailed multi-layer model made relevant by the spectral resolution of GRAVITY, would be needed to further confirm the pulsations and study the associated mass loss processes.

References

Arroyo-Torres, B., Wittkowski, M., Chiavassa, A., et al. 2015, A&A, 575, A50
Arroyo-Torres, B., Wittkowski, M., Marcaide, J. M., & Hauschildt, P. H. 2013, A&A, 554, A76
Baganoff, F. K., Maeda, Y., Morris, M., et al. 2003, ApJ, 591, 891
Baron, F., Monnier, J. D., Kiss, L. L., et al. 2014, ApJ, 785, 46
Bartko, H., Martins, F., Fritz, T. K., et al. 2009, ApJ, 697, 1741
Bartko, H., Martins, F., Trippe, S., et al. 2010, ApJ, 708, 834
Beasor, E. R., Davies, B., Smith, N., et al. 2020, MNRAS, 492, 5994
Becklin, E. E., Gatley, I., & Werner, M. W. 1982, ApJ, 258, 135
Becklin, E. E. & Neugebauer, G. 1975, ApJ, 200, L71
Blum, R. D., Ramírez, S. V., Sellgren, K., & Olsen, K. 2003, ApJ, 597, 323
Blum, R. D., Sellgren, K., & Depoy, D. L. 1996a, ApJ, 470, 864
Blum, R. D., Sellgren, K., & Depoy, D. L. 1996b, AJ, 112, 1988
Chelli, A., Duvert, G., Bourgès, L., et al. 2016, A&A, 589, A112
Chiavassa, A., Lacour, S., Millour, F., et al. 2010, A&A, 511, A51
Ciurlo, A., Paumard, T., Rouan, D., & Clénet, Y. 2016, A&A, 594, A113
Ciurlo, A., Paumard, T., Rouan, D., & Clénet, Y. 2019, A&A, 621, A65
Clénet, Y., Rouan, D., Gendron, E., et al. 2004, A&A, 417, L15
Clénet, Y., Rouan, D., Gratadour, D., et al. 2005, A&A, 439, L9
Climent, J. B., Wittkowski, M., Chiavassa, A., et al. 2020, A&A, 635, A160
De Colle, F., Raga, A. C., Contreras-Torres, F. F., & Toledo-Roy, J. C. 2014, ApJ, 789, L33
Ferrière, K. 2012, A&A, 540, A50
Foreman-Mackey, D., Hogg, D. W., Lang, D., & Goodman, J. 2013, PASP, 125, 306
Fritz, T. K., Gillessen, S., Dodds-Eden, K., et al. 2011, ApJ, 737, 73
Genzel, R., Eisenhauer, F., & Gillessen, S. 2010, Reviews of Modern Physics, 82, 3121
Genzel, R., Pichon, C., Eckart, A., Gerhard, O. E., & Ott, T. 2000, MNRAS, 317, 348
Genzel, R., Schödel, R., Ott, T., et al. 2003, ApJ, 594, 812
Gillessen, S., Genzel, R., Fritz, T. K., et al. 2012, Nature, 481, 51
Gonté, F. Y. J., Alonso, J., Aller-Carpentier, E., et al. 2016, in Society of Photo-Optical Instrumentation Engineers (SPIE) Conference Series, Vol. 9907, Proc. SPIE, 990720
Goorvitch, D. 1994, ApJS, 95, 535
Gravity Collaboration, Abuter, R., Accardo, M., et al. 2017, A&A, 602, A94
Gravity Collaboration, Abuter, R., Amorim, A., et al. 2020, A&A, 636, L5
Gray, D. F. 2005, The Observation and Analysis of Stellar Photospheres, 3rd edn. (Cambridge University Press)
Hadjara, M., Cruzalèbes, P., Nitschelm, C., et al. 2019, MNRAS, 489, 2595
Haubois, X., Perrin, G., Lacour, S., et al. 2009, A&A, 508, 923
Irons, W. T., Lacy, J. H., & Richter, M. J. 2012, ApJ, 755, 90
Krabbe, A., Genzel, R., Eckart, A., et al. 1995, ApJ, 447, L95
Lacy, J. H., Townes, C. H., Geballe, T. R., & Hollenbach, D. J. 1980, ApJ, 241, 132
Lapeyrere, V., Kervella, P., Lacour, S., et al. 2014, in Proc. SPIE, Vol. 9146, Optical and Infrared Interferometry IV, 91462D
Liszt, H. S. 2003, A&A, 408, 1009
Lo, K. Y. & Claussen, M. J. 1983, Nature, 306, 647
Lu, J. R., Ghez, A. M., Hornstein, S. D., et al. 2009, ApJ, 690, 1463
Martins, F., Genzel, R., Hillier, D. J., et al. 2007, A&A, 468, 233
Menten, K. M., Reid, M. J., Eckart, A., & Genzel, R. 1997, ApJ, 475, L111
Meyer, F. & Meyer-Hofmeister, E. 2012, A&A, 546, L2
Monnier, J. D., Berger, J.-P., Le Bouquin, J.-B., et al. 2014, in Society of Photo-Optical Instrumentation Engineers (SPIE) Conference Series, Vol. 9146, Optical and Infrared Interferometry IV, ed. J. K. Rajagopal, M. J. Creech-Eakman, & F. Malbet, 91461Q
Montargès, M., Kervella, P., Perrin, G., et al. 2016, A&A, 588, A130
Montargès, M., Kervella, P., Perrin, G., et al. 2014, A&A, 572, A17
Montargès, M., Norris, R., Chiavassa, A., et al. 2018, A&A, 614, A12
Morris, M. R., Meyer, L., & Ghez, A. M. 2012, Research in Astronomy and Astrophysics, 12, 995
Mužić, K., Eckart, A., Schödel, R., Meyer, L., & Zensus, A. 2007, A&A, 469, 993
O'Gorman, E., Kervella, P., Harper, G. M., et al. 2017, A&A, 602, L10
Ohnaka, K., Hofmann, K. H., Benisty, M., et al. 2009, A&A, 503, 183
Ohnaka, K., Hofmann, K. H., Schertl, D., et al. 2013, A&A, 555, A24
Ohnaka, K. & Morales Marín, C. A. L. 2018, A&A, 620, A23
Ohnaka, K., Weigelt, G., & Hofmann, K. H. 2017, Nature, 548, 310
Ohnaka, K., Weigelt, G., Millour, F., et al. 2011, A&A, 529, A163
Paumard, T., Genzel, R., Martins, F., et al. 2006, ApJ, 643, 1011
Paumard, T., Maillard, J. P., & Morris, M. 2004, A&A, 426, 81
Paumard, T., Pfuhl, O., Martins, F., et al. 2014, A&A, 568, A85
Perrin, G., Ridgway, S. T., Mennesson, B., et al. 2004, A&A, 426, 279
Perrin, G., Ridgway, S. T., Verhoelst, T., et al. 2005, A&A, 436, 317
Perrin, G., Verhoelst, T., Ridgway, S. T., et al. 2007, A&A, 474, 599
Perrin, G. & Woillez, J. 2019, A&A, 625, A48
Pickles, A. J. 1998, PASP, 110, 863
Pott, J. U., Eckart, A., Glindemann, A., et al. 2008, A&A, 487, 413
Press, W. H., Teukolsky, S. A., Vetterling, W. T., & Flannery, B. P. 1992, Numerical Recipes in C, 3rd edn. (Cambridge, USA: Cambridge University Press)
Ravi, V., Wishnow, E. H., Townes, C. H., et al. 2011, ApJ, 740, 24
Rayner, J. T., Cushing, M. C., & Vacca, W. D. 2009, ApJS, 185, 289
Ryde, N., Harper, G. M., Richter, M. J., Greathouse, T. K., & Lacy, J. H. 2006, ApJ, 637, 1040
Sanchez-Bermudez, J., Schödel, R., Alberdi, A., et al. 2014, A&A, 567, A21
Schartmann, M., Ballone, A., Burkert, A., et al. 2015, ApJ, 811, 155
Schödel, R., Najarro, F., Muzic, K., & Eckart, A. 2010, A&A, 511, A18
Serabyn, E., Lacy, J. H., & Achtermann, J. M. 1991, ApJ, 378, 557
Tsuboi, M., Kitamura, Y., Tsutsumi, T., et al. 2020, PASJ
Tsuboi, M., Kitamura, Y., Uehara, K., et al. 2017, ApJ, 842, 94
Tsuji, T. 2000, ApJ, 538, 801
Tsuji, T. 2006, ApJ, 645, 1448
Verhoelst, T., Decin, L., van Malderen, R., et al. 2006, A&A, 447, 311

Wittkowski, M., Abellán, F. J., Arroyo-Torres, B., et al. 2017a, A&A, 606, L1
Wittkowski, M., Arroyo-Torres, B., Marcaide, J. M., et al. 2017b, A&A, 597, A9
Woillez, J., Abad, J. A., Abuter, R., et al. 2019, A&A, 629, A41
Yang, M. & Jiang, B. W. 2012, ApJ, 754, 35
Yelda, S., Ghez, A. M., Lu, J. R., et al. 2014, ApJ, 783, 131
Yusef-Zadeh, F. & Morris, M. 1991, ApJ, 371, L59

[1] Max Planck Institut fur Exterterrestrische Physik (MPE), Giessenbachstr.1, D-85748 Garching, Germany
[2] LESIA, Observatoire de Paris, Universite PSL, CNRS, Sorbonne Université, Université de Paris, 5 place Jules Janssen, F-92195 Meudon, France
[3] Max Planck Institute for Astronomy, Königstuhl 17, 69117 Heidelberg, Germany
[4] 1. Physikalisches Institut, Universitat zu Köln, Zülpicher Straße 77, 50937 Cologne, Germany
[5] CNRS, IPAG, Univ.Grenoble Alpes, F-38000, Grenoble, France
[6] Universidade de Lisboa - Faculdade de Ciências, Campo Grande, P-1749-016 Lisboa, Portugal
[7] Faculdade de Engenharia, Universidade do Porto, Rua Dr. Roberto Frias, P-4200-465 Porto, Portugal
[8] European Southern Observatory, Karl-Schwarzschild-Straße 2, 85748 Garching, Germany
[9] European Southern Observatory, Santiago 19, Casilla 19001, Chile
[10] Max Planck Institute for Radio Astronomy, Auf dem Hügel 69, 53121 Bonn, Germany,
[11] Sterrewacht Leiden, Leiden University, Postbus 9513, NL-2300 RA Leiden, the Netherlands
[12] Departments of Physics and Astronomy, Le Conte Hall, University of California, Berkeley, CA 94720, USA
[13] CENTRA, Centro de Astrofísica e Gravitação, Instituto Superior Técnico, Avenida Rovisco Pais 1, P-1049 Lisboa, Portugal
[14] Department of Astrophisical & Planetary Sciences, JILA, Duane Physics Bldg., 2000 Colorado Ave, University of Colorado, Boulder, CO 80309, USA
[15] Department of Particle Physics & Astrophysics, Weizmann Institute of Science, Rehovot 76100, Israel
[16] Institute of Astronomy, Madingley Road, Cambridge CB3 0HA, UK
[17] Instituto de Astronomía, Universidad Nacional Autónoma de México, Apdo. Postal 70264, Ciudad de México 04510, Mexico

Acknowledgements. This research has made use of the Jean-Marie Mariotti Centre `LITpro` service co-developed by CRAL, IPAG and Lagrange, [1] `OifitsExplorer` service [2], `Aspro2` service [3], , `SearchCal` service [4] co-developed by LAGRANGE and IPAG, and of CDS Astronomical Databases SIMBAD and VIZIER [5]. This publication makes use of data products from the Two Micron All Sky Survey, which is a joint project of the University of Massachusetts and the Infrared Processing and Analysis Center/California Institute of Technology, funded by the National Aeronautics and Space Administration and the National Science Foundation. A.A. and P.G. were supported by Fundação para a Ciência e a Tecnologia, with grants reference UIDB/00099/2020 and SFRH/BSAB/142940/2018. The corresponding author would also like to thank all the support astronomers, the operations team, the logistics and service staff of Paranal Observatory for their help during the observations. SvF, FW & AJ-R acknowledge support by the MaxPlanck International Research School.

[1] LITpro software available at http://www.jmmc.fr/litpro
[2] Available at http://www.jmmc.fr/oifitsExplorer
[3] Available at http://www.jmmc.fr/aspro2
[4] Available at http://www.jmmc.fr/searchcal
[5] Available at http://cdsweb.u-strasbg.fr/

Appendix B

Proceedings: New Horizons in Galactic Center Astronomy and Beyond

I present here the contribution to the proceedings of the conference *New Horizons in Galactic Center Astronomy and Beyond* held in Yokohama, Japan, on October 21st – 24th, 2019. The contribution consists in a poster presented on October 23rd which includes some preliminary results described in the submitted paper about GCIRS 7 (Appendix A).

The molecular layer of GCIRS7

Rodríguez-Coira, G.[1]; Amorim, A.[5,6]; Bauböck, M.[2]; Benisty, M.[3]; Berger, J. -P.[3]; Clénet, Y.[1]; Coudé Du Foresto, V.[1]; de Zeeuw[2,11], T.; Dexter[2], J.; Duvert, G.[3]; Eckart, A.[4]; Eisenhauer, F.[2]; Ferreira, Miguel C.[5]; Gao, F.[2]; Garcia, Paulo J. V.[5,7,9]; Gendron, E.[1]; Genzel, R.[2,12]; Gillessen, S.[2]; Gordo, P.[5,6]; Habibi, M.[2]; Horrobin, M.[4]; Jimenez-Rosales, A.[2]; Jocou, L.[3]; Kervella, P.[1]; Lacour, S.[1,2]; Le Bouquin, J. -B.[3]; Léna, P.[1]; Ott, T.[2]; Pössel, M. [8]; Paumard, T.[1]; Perraut, K.[3]; Perrin, G.[1]; Pfuhl, O.[2]; Rousset, G.[1]; Straub, O.[2]; Straubmeier, C.[4]; Sturm, E.[2]; Vincent, F.[1]; von Fellenberg, S.[2]; Waisberg, I.[2] and Widmann, F. [2] (GRAVITY Collaboration)

[1]*LESIA, Observatoire de Paris, Universite PSL, CNRS, Sorbonne Université, Université de Paris, 5 place Jules Janssen, F-92195 Meudon, France*

[2]*Max Planck Institut fur Exterterrestrische Physik (MPE), Giessenbachstr.1, D-85748 Garching, Germany*

[3]*CNRS, IPAG, Univ.Grenoble Alpes, F-38000, Grenoble, France*

[4]*Physikalisches Institut, Universitat zu Koln, Zulpicher Str. 77, D-50937 Koln, Germany*

[5]*CENTRA, Centro de Astrofísica e Gravitação, Instituto Superior Técnico, Avenida Rovisco Pais 1, P-1049 Lisboa, Portugal*

[6]*Universidade de Lisboa - Faculdade de Ciências, Campo Grande, P-1749-016 Lisboa, Portugal*

[7]*Faculdade de Engenharia, Universidade do Porto, Rua Dr. Roberto Frias, P-4200-465 Porto, Portugal*

[8]*Max Planck Institute for Astronomy (MPIA) and Haus der Astronomie, Konigstuhl 17, D-69117 Heidelberg, Germany*

[9]*European Southern Observatory, Santiago 19, Casilla 19001, Chile*

[10]*Max-Plank-Institut fur Radioastronomie, Auf dem Hugel 69, 53121 Bonn, Germany*

[11]*Sterrewacht Leiden, Leiden University, Postbus 9513, NL-2300 RA Leiden, the Netherlands*

[12]*Departments of Physics and Astronomy, Le Conte Hall, University of California, Berkeley, CA 94720, USA*

Abstract. From all the stars formed inside the disk of young stars in the Galactic Centre, GCIRS7, a variable red supergiant in H and K bands, is by far the brightest of all of them. Using K band interferometric data (VLTI-GRAVITY), we measure uniform disk diameters around 20% times higher for wavelengths inside the CO absorption band compared to the continuum wavelengths, showing that a grey uniform disk model is not enough to reproduce the visibility curves of this star. A model based on a molecular spherical thin layer, already proven successful in other supergiant stars with similar spectral features, is implemented.

1. The brightest star of the central parsec

GCIRS7 has been classified as a M1 red supergiant star, pulsating in H and K bands with $< m_K >= 6.8$ (Paumard et al. 2014) making it an interesting target to study the morphology of evolved stars as well as the History of the Galactic Centre. With the interferometer VLTI-GRAVITY[1] (GRAVITY Collaboration 2017) it is possible to fit a uniform disk visibility curve per spectral channel, revealing a complex structure (Fig. 1) with a larger diameter corresponding to the CO and H2O molecular bands. Via Levenberg-Marquardt least square optimization, we implement a model based on a blackbody for the photosphere and another blackbody for a large, thin molecular layer surrounding it, responsible for the observed absorption band.

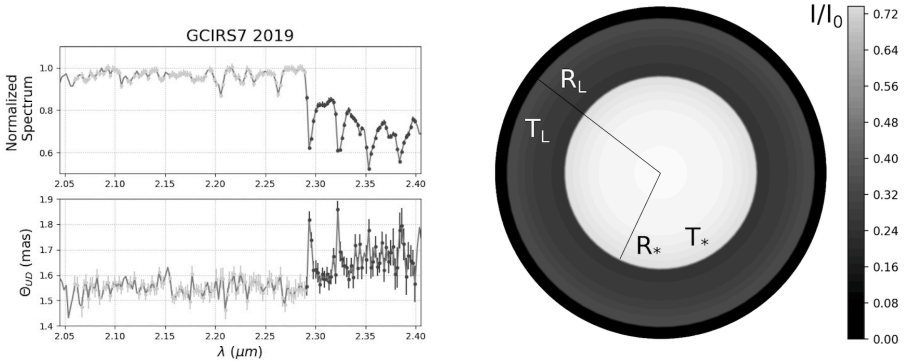

Figure 1. *Left:* Uniform disk fit per spectral channel, 2019 data. *Right:* Model as seen by the observer. The space between R_L and R_* is assumed empty in principle.

2. Preliminary Results

The size of the photosphere is compatible with a same value for 2017 and 2019 of $R_* = 0.8 \pm 0.1$ mas (1368 solar radii at $R_0 = 8178$ pc). The layer is poorly constrained, with $T_L < 2850$ K and $R_L > 0.95$ mas ($R_L/R_* > 20\%$), similar to other RSGs (Perrin et al. 2005). The full results will be presented in GRAVITY Collaboration (in prep).

References

T. Paumard, O. Pfuhl, F. Martins, P. Kervella, T. Ott, J.-U. Pott, J. B. Le Bouquin, J. Breitfelder, S. Gillessen, G. Perrin, L. Burtscher, X. Haubois, and W. Brandner 2014: GCIRS 7, a pulsating M1 supergiant at the Galactic centre. Astronomy & Astrophysics, Volume 568, id.A85, 10 pp.

GRAVITY Collaboration, 2017: First light for GRAVITY: Phase referencing optical interferometry for the Very Large Telescope Interferometer. Astronomy & Astrophysics, Volume 602, id.A94, 23 pp.

G.Perrin, S.T. Ridgway, T. Verhoelst, P.A. Schuller, V. Coudé du Foresto, W.A.Traub, R. Millan-Gabet and M.G.Lacasse 2005: Study of molecular layers in the atmosphere of the supergiant star μ Cep by interferometry in the K band Astronomy & Astrophysics, Volume 436, 1, 7 pp.

[1]Based on observations collected at the European Southern Observatory under ESO programmes 098.D-0250(B) and 103.B-0032(F).

Appendix C

Proceedings: XIII Scientific Meeting of the Spanish Astronomical Society

I present here the contribution to the proceedings of the *XIII Meeting of the Spanish Astronomical Society* held on July 16$^{\text{th}}$ to 20$^{\text{th}}$, 2018 in Salamanca, Spain. The contribution consists in a poster presented on July 18$^{\text{th}}$. The aim of the poster was to give an introduction to the Spanish Astronomical community about the GRAVITY instrument right after the first results of the Galactic Center team, published in Gravity Collaboration et al. (2018b).

Highlights on Spanish Astrophysics X, Proceedings of the XIII Scientific Meeting of the Spanish Astronomical Society held on July 16 – 20, 2018, in Salamanca, Spain. B. Montesinos, A. Asensio Ramos, F. Buitrago, R. Schödel, E. Villaver, S. Pérez-Hoyos, I. Ordóñez-Etxeberria (eds.), 2019

GRAVITY – Reaching out to SgrA* with VLTI.

GRAVITY Collaboration - R. Abuter[8], A. Amorim[6,14], N. Anugu[7], M. Bauböck[1], M. Benisty[5], J. P. Berger[5,8], N. Blind[10], H. Bonnet[8], W. Brandner[3], A. Buron[1], C. Collin[2], F. Chapron[2], Y. Clénet[2], V. Coudé du Foresto[2], P. T. de Zeeuw[12,1], C. Deen[1], F. Delplancke-Ströbele[8], R. Dembet[8,2], J. Dexter[1], G. Duvert[5], A. Eckart[4,11], F. Eisenhauer[1], G. Finger[8], N. M. Förster Schreiber[1], P. Fédou[2], P. Garcia[7,14], R. Garcia Lopez[15,3], F. Gao[1], E. Gendron[2], R. Genzel[1,13], S. Gillessen[1], P. Gordo[6,14], M. Habibi[1], X. Haubois[9], M. Haug[8], F. Haußmann[1], Th. Henning[3], S. Hippler[3], M. Horrobin[4], Z. Hubert[2,3], N. Hubin[8], A. Jimenez Rosales[1], L. Jochum[8], L. Jocou[5], A. Kaufer[9], S. Kellner[11], S. Kendrew[16,3], P. Kervella[2], Y. Kok[1], M. Kulas[3], S. Lacour[2], V. Lapeyrère[2], B. Lazareff[5], J.-B. Le Bouquin[5], P. Léna[2], M. Lippa[1], R. Lenzen[3], A. Mérand[8], E. Müler[8,3], U. Neumann[3], T. Ott[1], L. Palanca[9], T. Paumard[2], L. Pasquini[8], K. Perraut[5], G. Perrin[2], O. Pfuhl[1], P. M. Plewa[1], S. Rabien[1], A. Ramírez[9], J. Ramos[3], C. Rau[1], G. Rodríguez-Coira[2], R.-R. Rohloff[3], G. Rousset[2], J. Sanchez-Bermudez[9,3], S. Scheithauer[3], M. Schöller[8], N. Schuler[9], J. Spyromilio[8], O. Straub[2], C. Straubmeier[4], E. Sturm[1], L. J. Tacconi[1], K. R. W. Tristram[9], F. Vincent[2], S. von Fellenberg[1], I. Wank[4], I. Waisberg[1], F. Widmann[1], E. Wieprecht[1], M. Wiest[4], E. Wiezorrek[1], J. Woillez[8], S. Yazici[1,4], D. Ziegler[2] and G. Zins[9]

[1] Max Planck Institute for extraterrestrial Physics, Giessenbachstraße 1, 85748 Garching, Germany
[2] LESIA, Observatoire de Paris, Université PSL, CNRS, Sorbonne Université, Univ. Paris Diderot, Sorbonne Paris Cité, 5 place Jules Janssen, 92195 Meudon, France
[3] Max Planck Institute for Astronomy, Königstuhl 17, 69117 Heidelberg, Germany
[4] 1 st Institute of Physics, University of Cologne, Zülpicher Straße 77, 50937 Cologne, Germany
[5] Univ. Grenoble Alpes, CNRS, IPAG, 38000 Grenoble, France
[6] Universidade de Lisboa – Faculdade de Ciências, Campo Grande, 1749-016 Lisboa, Portugal
[7] Faculdade de Engenharia, Universidade do Porto, rua Dr. Roberto Frias, 4200-465 Porto, Portugal
[8] European Southern Observatory, Karl-Schwarzschild-Straße 2, 85748 Garching, Germany
[9] European Southern Observatory, Casilla, 19001 Santiago 19, Chile
[10] Observatoire de Genève, Université de Genève, 51 Ch. des Maillettes, 1290 Versoix, Switzerland
[11] Max Planck Institute for Radio Astronomy, Auf dem Hügel 69, 53121 Bonn, Germany

[12] Sterrewacht Leiden, Leiden University, Postbus 9513, 2300 RA Leiden, The Netherlands
[13] Departments of Physics and Astronomy, Le Conte Hall, University of California, Berkeley, CA, 94720 USA
[14] CENTRA – Centro de Astrofísica e Gravitação, IST, Universidade de Lisboa, 1049-001 Lisboa, Portugal
[15] Dublin Institute for Advanced Studies, 31 Fitzwilliam Place, Dublin 2, Ireland
[16] European Space Agency, Space Telescope Science Institute, 3700 San Martin Drive, Baltimore, MD 21218, USA

Abstract

As one of the 2nd generation of interferometric instruments in VLTI, GRAVITY was installed at the end of 2015 and has been observing the Galactic Center since May 2016. With the goal to reach an accuracy of tens of micro arcseconds, it is able to perform the most precise astrometric measurement of SgrA* to date. For that purpose, GRAVITY combines the light collected (coherently) from of all the 8 m UTs or the four 1.8 m ATs providing infrared wavefront sensing to control the telescope adaptive optics, two interferometric beam combiners (one for fringe-tracking and one for the science object), an acquisition camera and various laser guiding systems for beam stabilization, as well as a dedicated laser metrology to trace the optical path length differences for narrow angle astrometry. Operating in K band with an active stabilization of the science channel, GRAVITY is able to increase the typical integration time from a few milliseconds (the typical atmospheric coherence time) to minutes, which implies a big leap in sensitivity allowing to observe fainter objects (K=19 in science detector) with the power of a 130m baseline interferometer, as it is the close environment of the supermassive black hole located in the center of our Galaxy. (See poster).

RÉSUMÉ

Le parsec central est l'une des régions les plus intéressantes de notre Galaxie. Il est peuplé d'un amas stellaire nucléaire où coexistent des étoiles massives, énergétiques et jeunes, des étoiles évoluées plus froides, du plasma chaud et des flux de matière interstellaire. Un objet compact appelé SgrA*, d'une masse de plusieurs millions de masses solaires, se trouve en son centre, devenant ainsi le plus proche candidat au trou noir supermassif, mais étant plus faible dans toutes les longueurs d'onde que les autres noyaux galactiques. L'une des étoiles les plus proches de SgrA*, S2, effectue une orbite autour d'elle en 16 ans seulement et est suffisamment brillante pour être utilisée comme une sonde robuste du potentiel gravitationnel de la source centrale par suivi d'orbite. Dans l'infrarouge, SgrA* présente une émission quiescente avec de courts épisodes aléatoires appelés sursauts où sa luminosité augmente fortement jusqu'à un facteur 4, durant plusieurs heures avant de s'affaiblir. L'origine de ces éruptions est probablement due à la présence de processus d'accrétion dans l'environnement proche du trou noir et leur étude peut fournir des informations essentielles sur la nature exotique de SgrA*. Malheureusement, ces événements sont aléatoires et nécessitent un suivi suffisamment échantillonné dans le temps. L'instrument GRAVITY, qui fait partie de la deuxième génération de VLTI, permet d'utiliser l'interférométrie optique pour étudier le Centre Galactique. Il est capable de suivre l'orbite de l'étoile S2 avec une précision sans précédent, jusqu'à 10 microsecondes d'arc. Ce travail de thèse est axé sur l'analyse des données des premiers produits de l'instrument GRAVITY au Centre Galactique. Dans la première partie de la thèse, l'astrométrie de l'étoile S2 est obtenue par l'utilisation des deux premières années d'observations de la GRAVITY, auxquelles j'ai participé activement. Pour cela, un modèle d'étoile binaire est utilisé pour reproduire les données interférométriques. Juste avant et après le passage du péricentre, qui a eu lieu en 2018, j'ai obtenu les positions de S2 par rapport à SgrA* atteignant une précision astrométrique de 30 microsecondes d'arc, comparable à la taille attendue de l'ombre du trou noir supermassif. En outre, j'ai obtenu une nouvelle courbe de lumière de SgrA* qui complète les données déjà publiées et confirme le comportement quiescent avec des sursauts. Les résultats obtenus font partie d'une étude plus large impliquant l'ajustement de l'orbite où plusieurs tests de relativité générale ont été effectués avec succès, ainsi que des interprétations des sursauts comme produit des processus d'accrétion dans l'orbite proche de SgrA*. La deuxième partie de la thèse est centrée sur une étoile évoluée appelée GCIRS 7, qui est également située dans le parsec central. Cette étoile, qui présente une grande variabilité dans l'infrarouge est connue pour contribuer au milieu interstellaire du Centre Galactique. En complétant les données de GRAVITY de 2017 par des observations que j'ai effectuées en 2019, j'ai mis en place un modèle d'atmosphère qui s'agit d'une photosphère et d'une fine couche moléculaire afin d'expliquer les données de GCIRS 7 obtenues par GRAVITY. Les résultats montrent que les données peuvent être interprétées comme une photosphère avec le même diamètre pour les deux époques, mais la couche étant plus froide et plus grande en 2019 par rapport à 2017. Une estimation de la densité de la couche révèle une saturation du modèle pour 2017 en raison d'une densité élevée, mais les données de 2019 sont partiellement reproduites. Les résultats peuvent être expliqués par une expansion et un refroidissement de la couche probablement dus à un épisode de perte de masse.

MOTS CLÉS

Interférométrie, GRAVITY, Sursauts, Trou noir, Astrométrie.

ABSTRACT

The central parsec is one of the most interesting regions of our Galaxy. It is populated by a nuclear stellar cluster where massive, energetic and young stars coexist with colder evolved stars, hot plasma and streams of interstellar matter. A compact object called SgrA* with a mass of several million solar masses lies in its center becoming the closest supermassive black hole candidate, but being fainter in all wavelengths than other galactic nuclei. One of the closest stars to SgrA*, S2, completes an orbit around it in just 16 years and is bright enough to be used as a robust probe the gravitational potential of the central source by orbit tracking. In the infrared, SgrA* presents a quiescent emission with random short episodes called flares where its brightness sharply increases up to a factor 4, lasting several hours before dimming. The origin of these flares is likely due to the presence of accretion processes in the close environment of the black hole and their study can provide essential information about the exotic nature of SgrA*. Unfortunately, these events are random and require a sufficiently sampled monitoring over time. The GRAVITY instrument, part of the second generation of VLTI, enables the use of optical interferometry to study the Galactic Center. It is able to track the orbit of the star S2 with unprecedented accuracy, up to 10 micro-arcseconds. This thesis work is focused on the data analysis of the first products of the GRAVITY instrument in the Galactic Center. In the first part of the thesis, the astrometry of the star S2 is obtained by the use of the first two years of GRAVITY observations, in which I have actively participated. For that purpose, a binary star model is used to reproduce the interferometric data. Right before and after the pericenter passage, who took place in 2018, I have obtained the positions of S2 with respect to SgrA* reaching an astrometric accuracy of 30 micro-arcseconds, comparable with the expected size of the shadow of the supermassive black hole. In addition, I have obtained a new light curve of SgrA* which complements the data already published and confirms the quiescent-flare scenario. The results obtained are part of a larger study involving orbit fitting where several tests of General Relativity have been successfully performed, as well as interpretations of the flares as a product of accretion processes in the near SgrA* orbit. The second part of the thesis is focused on an evolved star called GCIRS 7, which is also located in the central parsec and serves as a reference for GRAVITY observations. This star, which has a large variability in the infrared, is known to contribute to the interstellar medium of the Galactic Center. By complementing GRAVITY archival data from 2017 with observations I have taken in 2019, I have implemented an atmosphere model, widely used for the study of other advanced stars, to explain the visibility curves of GCIRS 7 obtained by GRAVITY. The model consists of a photosphere and a thin molecular shell. The results show that the data can be interpreted as a photosphere with the same diameter for both epochs, but with a shell being colder and larger in 2019 compared to 2017. An estimation of the density of the thin shell reveals a saturation of the model for 2017 due to a high density, but 2019 data is partially reproduced. The results can be explained by a layer expansion and cooling likely due to an episode of mass loss.

KEYWORDS

Flares, GRAVITY, Astrometry, Interferometry, Black hole.